UNIVERSITY OF OXFORD

Functional Lung Assessment using Hyperpolarised Xenon Gas Magnetic Resonance Imaging

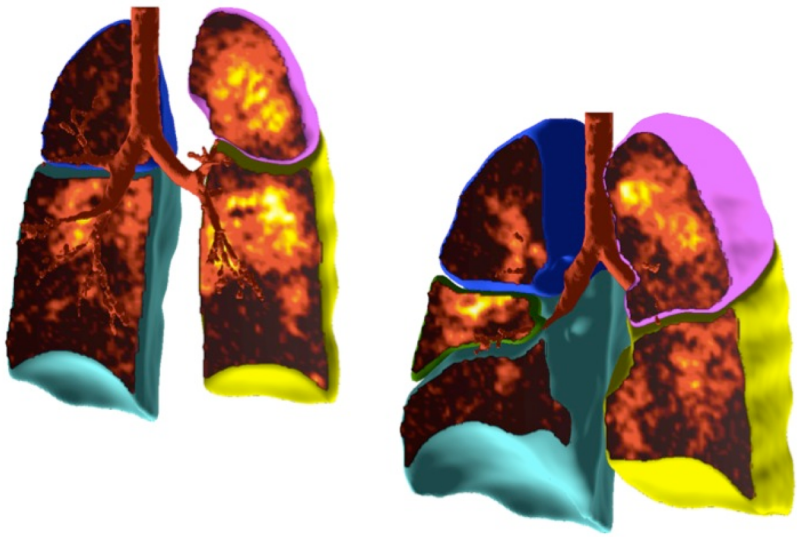

Submitted in fulfilment of the requirements for the degree of Doctor of Philosophy at the University of Oxford

Tahreema N H Matin

BSc (Hons), MBBS, FRCR

Green Templeton College

Trinity Term 2016

Supervisor: Professor Fergus V Gleeson

Declaration

I, Tahreema N H Matin declare that the work presented in this thesis is my own, unless stated otherwise, and is in accordance with the University of Oxford's regulations for the degree of Doctor of Philosophy.

October 2016

The Churchill Hospital
Oxford University Hospitals NHS Foundation Trust
Old Road
Headington
Oxford
OX3 7LE

Abstract

Functional lung assessment using hyperpolarised xenon gas magnetic resonance imaging

Tahreema N H Matin, Green Templeton College, Trinity Term 2016
Submitted in fulfilment of the requirements for the degree of Doctor of Philosophy at the University of Oxford

Purpose

Chronic obstructive pulmonary disease (COPD) is a leading cause of mortality worldwide. The standard method for assessing lung function in COPD is spirometry, which provides *global* lung function information but is a poor predictor of disability and quality of life. The overall aim of this thesis is to develop utility of hyperpolarised xenon gas magnetic resonance imaging (HP ^{129}Xe-MRI) as a technique to evaluate *regional* lung function.

Methods

Studies were approved by the National Research Ethics Service (NRES). Eleven volunteers and 25 patients with COPD underwent HP ^{129}Xe-MRI, pulmonary function tests (PFTs) and quantitative computerised tomography (QCT). Gravitational-dependent gradients of HP ^{129}Xe-MRI were compared between prone and supine postures in healthy volunteers. Lobar quantification of HP ^{129}Xe-MRI was completed in COPD patients, who also underwent time-resolved HP ^{129}Xe-MRI and HP ^{129}Xe-MRI pre- and post-salbutamol to determine feasibility of detecting regional delayed ventilation and post-intervention change. The relationship between study measures was assessed using Pearson's correlation coefficient.

Results

HP ^{129}Xe-MR ventilation gradients were more marked in the supine than prone posture in healthy volunteers, whereas diffusion-weighted gradients were more uniform. HP ^{129}Xe-MRI was successfully quantified according to pulmonary lobes and correlated with lobar lung anatomy (QCT) and global functional transfer capability (TLCO) (r=-0.61, $p<0.005$). Delayed ventilation was observed with time-resolved breath-hold HP ^{129}Xe-MRI. Differential regional ventilation change was detected with HP ^{129}Xe-MRI post-salbutamol.

Conclusion

These data demonstrate technical optimisation of HP ^{129}Xe-MRI in healthy volunteers and COPD patients. Successful generation of lobar HP ^{129}Xe-MRI parameters offers an automated analysis method that can be adopted into the clinical workflow. Finally proof-of-principle data have identified roles for HP ^{129}Xe-MRI in evaluating regional treatments and assessing therapeutic response. Future work will evaluate the role of HP ^{129}Xe-MRI in patient selection for lung volume reduction therapy and as a surrogate end-point in drug development studies.

Acknowledgment

There are a many people, without whom this thesis would not have been possible and I am sincerely grateful to each and every one. First, I would like to thank my Supervisor, Professor Fergus V Gleeson for giving me the opportunity to embark on an Academic Radiology career, for his kind guidance and continued support to achieve academic excellence, for his unparalleled work ethic and encouragement to become an independent researcher.

I am indebted to the Oxford Respiratory Trials Unit (ORTU) in particular the research nurses Tara Harris-Wright and Andrea Byles for their endless hard-work and for the kindness they have shown me on a daily basis throughout my DPhil. I also thank Dr Annabel Nickol and Professor Naj Rahman for their guidance, support and valuable feedback on my work.

I am grateful to Anthony McIntyre for bringing humour, for his unwavering "can do" attitude and help to accommodate research patients despite clinical pressures. I thank Kenneth Jacob and the other MRI radiographers for help with xenon gas administration and patient scanning. I thank Jenni Lee and the Xenon gas production team for their assistance with gas manufacture. I would also like to thank the Churchill Nuclear Medicine and CT radiographers, particularly Carole Duncan for accommodating and scanning study patients. I thank Daniel McGowan for help with nuclear medicine scan protocol development.

I thank Xiaojun Xu (Peggy) for her kindness while teaching me to perform hyperpolarised xenon MR scanning and to complete data analysis using Matlab. I am indebted to Peggy for sharing her wealth of MR physics knowledge and for her friendship during enduring times. I am grateful to Mitchell Chen for his help with Matlab.

I would like to thank Vicente Grau for his computing expertise and Tom Doel for his endless patience and help resolving the many computer error messages experienced during data analysis. I am indebted to Tom for teaching me how to use the Pulmonary Toolkit and for his continued IT support. I am also grateful to Professor Jim Wild and Neil J Stewart for helping to establish hyperpolarised xenon MRI sequences on the MR scanner.

Finally, I dedicate this thesis to my family; to my father who continues to be right by my side supporting and encouraging me through all my academic endeavours and whose advice to avoid too much stress at work continues to be a lifelong lesson; to my mother who has taught me to be determined, an independent thinker and self-sufficient – all skills that I have needed to draw upon in large scores throughout this DPhil; and last but by no means least my elder sister who continues to be my academic inspiration, my mentor and my best friend –whose endless support and advice has made completing this thesis possible.

Table of contents

List of chapters

Appendices

List of figures

List of tables

Abbreviations

%LAA	Percentage low-attenuation areas less than -950 HU
^{129}Xe	Xenon-129 gas
^{19}F-MRI	Fluorine-19 magnetic resonance imaging
^{1}H	Proton
^{1}H-MRI	Conventional/anatomic proton magnetic resonance imaging
2-D	Two-dimensional
3-D	Three-dimensional
^{3}He	Helium-3 gas
ADC	Apparent diffusion coefficient
AMCs	Age-matched healthy controls
AP	Antero-posterior
ARDS	Acute respiratory distress syndrome
ASL-FAIRER	Arterial spin-labeling-flow sensitive alternating inversion recovery with extra radiofrequency pulse
BODE	Body mass index, airflow obstruction, dyspnoea, exercise capacity
BW	Bandwidth
cm	Centimetre
COPD	Chronic obstructive pulmonary disease
CT	Computerised tomography
Δ	Absolute difference
DECT	Dual-energy computerised tomography
DICE	Volume overlap index
DLCO	Diffusion capacity of the lungs for carbon monoxide
ESRD	End-stage renal disease
FD	Fourier decomposition
FDA	Food and drug administration
FEV_1	Forced expiratory volume in 1 second
FOV	Field of view
FRC	Functional residual volume
FVC	Forced vital capacity
GOLD	Global initiative for chronic obstructive lung disease
GUI	Graphic user interface
HP	Hyperpolarised
HRCT	High resolution computerised tomography
ILD	Interstitial lung disease
IR-SSFSE	Inversion recovery single-shot fast spin echo
L	Litre
LEHR	Low energy high resolution
LVRS	Lung volume reduction surgery

LVRT	Lung volume reduction therapy
MDCTA	Pulmonary multi-detector computerised tomography angiography
MHRA	Medicines and healthcare products regulatory authority
mmol	millimole
MR	Magnetic resonance
MRC	Medical Research Council
MRI	Magnetic resonance imaging
NETT	National emphysema treatment trial
NHS	National health service
NICE	National institute for health and care excellence
NM	Nuclear medicine
NM-Q	Nuclear medicine perfusion
NM-V	Nuclear medicine ventilation
O_2-MRI	Oxygen-enhanced magnetic resonance imaging
OSEM	Ordered subset expectation maximisation
PaO_2	Partial pressure of oxygen in arterial blood
P_AO_2	Partial pressure of oxygen in alveolar gas
PE	Pulmonary emboli
PET	Positron emission tomography
PFTs	Pulmonary function tests
Pi10	Square root of bronchial wall area for a theoretical airway with an internal perimeter of 10 mm
PO_2	Partial pressure of oxygen
PSE	Percentage signal enhancement
PTK	Pulmonary toolkit
QCT	Quantitative computed tomography
RCT	Randomised controlled trial
RF	Radiofrequency
ROI	Region-of-interest
RV	Residual volume
S/V	Alveolar surface area per unit volume of gas
SaO_2	Arterial oxygen saturation
sec	Second
SEOP	Spin exchange and optical pumping
SNR	Signal-to-noise ratio
SPECT	Single photon emission computerised tomography
T_1	Longitudinal relaxation
T_2	Transverse relaxation
T_2^*	Combination of "true" T_2 relaxation and relaxation caused by magnetic field inhomogeneities
TE	Echo time
TLC	Total lung capacity
TLCO	Transfer factor of the lungs for carbon monoxide

TR	Repetition time
UTE	Ultrashort echo time
V/Q	Ventilation-perfusion
Va	Alveolar volume
VDP	Ventilation defect percentage
VDS	Ventilation defects per slice
VDS%	Ventilation defect score percentage
VDV	Ventilation defect volume
VENT	Endobronchial valve for emphysema palliation trial
VOI	Volume-of-interest
VSI	Ventilation signal intensity
WHO	World health organisation
Xe-CT	Xenon-enhanced computerised tomography
XTC	Xenon polarisation transfer contrast

Publications and presentations

Publications

Matin TN, Rahman N, Nickol A *et al.* Lobar analysis of hyperpolarised xenon magnetic resonance lung imaging (HP ^{129}Xe-MRI) in chronic obstructive pulmonary disease (COPD). *Radiology* 2017 Mar;282(3):857-868. doi: 10.1148/radiol.2016152299.

Matin TN, Xu X, McGowan DR, Doel T, Grau V *et al.* Novel single photon emission tomography/computed tomography (SPECT/CT) methodology for accurate determination of lobar lung function in chronic obstructive pulmonary disease (COPD) Submitted to *Clinical Radiology* (October 2016)

Scientific presentations (oral)

Oct 2014	Regional lung assessment using nuclear medicine perfusion imaging and quantitative CT in COPD. European Association of Nuclear Medicine Congress, Gothenburg.
Dec 2014	Imaging derived regional lung function using hyperpolarised xenon MRI and quantitative CT in COPD. British Thoracic Society Winter meeting, London.
Mar 2015	Regional image-derived lung function and structure in COPD and non-small cell lung cancer. European Congress of Radiology, Vienna.
Mar 2015	Quantitative regional analysis of functional lung imaging in COPD. European Congress of Radiology, Vienna.
Dec 2015	Lobar analysis of hyperpolarised xenon lung imaging in COPD. Radiological Society of North America (RSNA) Annual Meeting, Chicago.
Dec 2016	Time-resolved hyperpolarised xenon lung imaging (HP ^{129}Xe-MRI) for evaluation of collateral ventilation in chronic obstructive pulmonary disease (COPD). Accepted for presentation at RSNA Annual Meeting, Chicago.

Scientific presentations (poster)

March 2016	The use of hyperpolarised xenon (HP ^{129}Xe-MRI) for assessing collateral ventilation. EPOS, European Congress of Radiology, Vienna.
Dec 2015	Hyperpolarised xenon MRI – a new functional imaging technique in respiratory medicine. RSNA, Chicago.
Dec 2015	Demonstrating utility of hyperpolarised xenon MRI and quantitative CT in COPD. RSNA, Chicago.

1 Introduction

In this chapter, Part 1 provides an overview of chronic respiratory disease and the standard methods for lung function assessment. Part 2 provides a review of lung function evaluation using clinical imaging modalities. Part 3 introduces the background to hyperpolarised noble gas magnetic resonance imaging (MRI) using helium-3 and xenon-129 and provides a review of research functional pulmonary MRI techniques.

1.1 Part 1

1.1.1 The burden of chronic respiratory disease

Respiratory disease is responsible for one in five of all UK deaths(1). The estimated annual National Health Service (NHS) cost for respiratory disease is £6.6 billion(1). Chronic respiratory disease such as chronic obstructive pulmonary disease (COPD) leads to disabling symptoms that impair quality of life, with breathlessness, reduced exercise tolerance and social isolation.

COPD accounts for more than one fifth (23%) of all respiratory deaths(1), making it the fifth leading cause of death in the UK and fourth worldwide(2, 3). It is characterised by progressive airflow limitation caused by a combination of small airways disease (obstructive bronchiolitis) and parenchymal destruction (emphysema)(4). It is currently estimated that over three million people in the

UK are affected by COPD, although 2 million remain undiagnosed(5). In contrast to other chronic diseases, the prevalence of COPD continues to rise, with a steady increase in females(5) making it a disease of equal importance in both men and women. COPD places a significant burden on the NHS accounting for approximately 1.4 million GP consultations and greater than 1 million hospital bed days each year(1). One in eight (130, 000) emergency admissions to hospital are due to COPD, making it the greatest cause of emergency admission in the UK(5). The estimated direct cost of COPD to the NHS is between £810-£930m per annum(1). Indirect costs of COPD are also significant with approximately 24 million lost work-days each year(6).

1.1.2 Standard methods for assessment of pulmonary function in COPD

The standard method for assessing lung function in COPD is spirometry, which combined with anatomical imaging (computed tomography, CT) can provide structural information. Spirometry alone provides information on *global* lung function. It does not provide information about the support 'framework' of the lung itself (the parenchyma) or specific regions within the lung. The independent contributions of airway(7) and parenchymal(8) abnormalities may be obscured by whole lung measures, particularly in early stage disease.

Most importantly, changes measured by spirometric indices do not correlate with patient symptoms, nor reflect deteriorating disease. This is particularly disappointing, since symptomatic disability is a stronger predictor of mortality

from COPD than spirometry alone(9). Current guidelines for COPD severity assessment(5) have been updated in recognition that a combination of multidimensional indices is a better predictor of clinical outcomes than the forced expiratory volume in 1 second (FEV_1) alone(9, 10).

CT can provide morphological information at high resolution but exposure to ionising radiation renders it an unfavourable modality for multiple follow-up scans. Nuclear medicine is able to provide functional information regarding lung ventilation and perfusion but also exposes patients to radiation, is expensive and time consuming, has limited availability, and has limitations in spatial and temporal resolution.

Conventional MRI has limited use in respiratory disease since the lungs are largely composed of air, which does not generate an MR signal. Emerging state-of-the art functional MRI techniques using gas contrast agents include hyperpolarised gas MRI, oxygen-enhanced MRI and fluorinated gas MRI, none of which have been adopted into clinical practice. MRI using hyperpolarised xenon gas (HP ^{129}Xe-MRI) provides a unique strategy for evaluating regional lung function by permitting direct visualisation of the lung airspaces. HP ^{129}Xe-MRI is free from ionizing radiation making it safe and practical for diseases such as chronic respiratory disease where repeat scans are necessary.

1.2 Part 2

1.2.1 Assessment of pulmonary function with clinical imaging modalities

1.2.1.1 Chest Radiograph

Chest radiographs form part of the standard diagnostic pathway for patients with COPD(5) since they are easily obtained, inexpensive and involve minimal exposure to ionising radiation. Chest radiography is performed primarily to exclude other pathology since the accuracy and sensitivity for diagnosing emphysema radiographically remains controversial(11-13). Previous work compared radiographic appearances with post-mortem histology to determine the sensitivity of chest radiography for emphysema detection(14-18). While some of these studies demonstrated excellent(14, 15, 17) agreement between radiographic and necroscopic findings, others reported a poor correlation(16, 18).

A variety of radiographic criteria have been proposed to aid the diagnosis of emphysema; up to 90% accuracy was reported with the criterion over-inflation(17) whereas arterial deficiency was deemed less useful(18). Consensus of previous research(19-22) has suggested utility of the following radiographic criteria in emphysema detection: -

- Increased radiolucency of the lung fields(23)
- Flattening of the diaphragms(24, 25)

- Pruning of the peripheral vasculature
- Increased retrosternal airspace
- Widening of the intercostal spaces
- Narrowed and more vertical cardiac silhouette.

Despite the proposed radiographic criteria, there remains debate about the usefulness of chest radiography to evaluate lung function impairment in patients with COPD. Previous investigators have concluded that a radiological diagnosis of emphysema can only be made in the presence of at least two criteria i.e. pulmonary vessel attenuation and over-inflation (flattened diaphragm, increased retrosternal space)(26). In contrast, other researchers have reported that radiological evidence of over-inflation alone was sufficient for emphysema diagnosis(17).

Whilst moderate and severe emphysema may be identified on chest radiographs(27), early/mild emphysema is much more difficult to detect. Furthermore the functional significance of localised changes on chest radiographs cannot be determined. For these reasons, historical literature supporting the use of all available clinical, radiological and functional data for evaluation of emphysema(28, 29) likely still holds true.

It is now widely accepted that computed tomography (CT) is the most accurate imaging method for diagnosing emphysema *in vivo*(30-37). Direct comparison of chest radiography and CT for emphysema assessment demonstrated increased sensitivity of CT over chest radiographs(34, 38, 39). Assessment of pulmonary

vascularity(40) and pulmonary artery-bronchus ratios(41) on chest radiographs may provide physiologic information about pulmonary vascular congestion, however the radiographic evaluation of regional lung ventilation and perfusion is not possible.

1.2.1.2 Quantitative Computed Tomography (QCT)

Quantitative CT (QCT) can provide reliable and valid measures of lung structure including parenchymal attenuation, air trapping and airway dimensions(42-47). These structural changes are important to the pathophysiology of many lung disorders, such as COPD and asthma(48, 49). Co-registration of QCT with functional modalities, for example HP ^{129}Xe-MRI, offers the potential for comprehensive evaluation of both lung structure and function.

1.2.1.2.1 QCT-derived emphysema measurement

QCT has been most widely adopted for evaluation of emphysema in COPD using the density mask technique with a threshold of -950 Hounsfield units (HU). Muller *et al.*(45) initially validated the density mask technique, in which CT pixels with attenuation below -910HU correlated with emphysematous holes >5mm in diameter on pathology. Recent evaluation with thin-section, multi-detector CT showed better correlation at lower thresholds(50). The threshold most commonly employed in the literature is -950(51).

An alternative method is to determine the CT attenuation at a given percentile along the frequency histogram of lung attenuation, most commonly the 15th

percentile(52, 53). It has been reported that the percentile method is less sensitive to changes in lung volume(53). Unfortunately the depth of inspiration, scanner type and technical parameters may all influence both techniques and are sources of variation that should be considered when evaluating images.

On expiratory CT, air trapping may be quantified by the percentage of lung volume less than a given threshold (e.g. -856HU). Quantification of air trapping using this method correlated significantly with spirometry(54). Other indices of air trapping include: -

- Inspiratory to expiratory lung volume ratio
- Inspiratory to expiratory lung attenuation ratio (provided strongest correlation with physiological air trapping(55))
- Expiratory to inspiratory relative volume change of voxels with attenuation values between -860 and -950HU.

1.2.1.2.2 QCT-derived airway measurement

Radiologic assessment of the airways provides useful information about bronchial inflammation and remodelling. There have been substantial recent advances in quantitative evaluation of the segmental and subsegmental airways. Three-dimensional airways can be reconstructed from volumetric CT to measure dimensions e.g. external and internal diameters and airway wall thickness of airways orthogonal to their long axes. Measurement of airway parameters

correlated with the severity of airflow obstruction and history of COPD exacerbation(56, 57).

1.2.1.3 Dual energy Computed Tomography (DECT)

Dual-energy CT (DECT) of the lungs can provide both anatomical and functional information but has not yet been widely adopted into clinical practice(58). This is largely due to concerns regarding associated radiation exposure, although this is not supported by the published literature(58, 59). The technique involves the simultaneous acquisition of data at two different tube voltages e.g. 140 kVP and 80 kVP/100 kVP. Various contrast materials and tissue components can be selectively analysed via image reconstruction.

1.2.1.4 Dual-energy CT based assessment of lung perfusion

DECT-based pulmonary multi-detector CT angiography (MDCTA) has been predominantly evaluated in the detection of pulmonary embolic disease, with less focus on whole lung perfusion, although, in emphysema, it may have the potential to assess regional lung perfusion changes and quantify disease severity(60, 61).

1.2.1.5 Dual-energy CT-based assessment of lung ventilation

Ventilation in patients with various pulmonary diseases has been assessed using xenon as an inhaled contrast agent using dual-energy CT (Xe-CT).

Peripheral ventilation defects were demonstrated in 16 of 22 asthmatics who underwent Xe-CT(62). The extent of ventilation defects correlated with lower FEV_1 values and thicker airway wall measurements in this cohort(62).

A recent study suggested that the ventilation abnormalities detected by Xe-CT in asthma could be used as a novel parameter to reflect disease status and severity(63). In a cohort of 43 asthmatic adults, Xe-CT demonstrated ventilation defects and xenon trapping which increased and decreased after methacholine and salbutamol inhalation, respectively(63). The ventilation abnormalities did not correlate with spirometric indices but showed significant correlation with asthma symptoms(63).

Goo *et al.*(64) evaluated Xe-CT in seventeen children with bronchiolitis obliterans by comparing density values and ventilation defect volumes from the xenon images with corresponding measurements from hyperlucent lung regions in conventional CT. Xenon and CT density values correlated positively in the whole lung in 16 children and for hyperlucent regions in 13 children(64). The volume percentages of xenon ventilation defects were not significantly different to those of CT hyperlucent regions but demonstrated variability of up to 33.3%(64).

The inherent disadvantages of DECT include radiation exposure and CT artefacts due to motion and the contrast media itself.

1.2.2 Nuclear medicine

Nuclear medicine lung scintigraphy (NM-V/Q) is an established modality for assessing pulmonary ventilation and perfusion. It is routinely used in clinical practice for detecting pulmonary emboli and has an evolving role in other respiratory diseases(65, 66). Three-dimensional (3-D) ventilation/perfusion single photon emission tomography (NM-V/Q SPECT) has largely replaced planar scintigraphy and with the introduction of hybrid NM-V/Q SPECT/CT, ventilation and perfusion SPECT data may now be combined with anatomical information from CT acquired in a single session(67). NM-V/Q SPECT/CT has been shown to improve the diagnostic accuracy for pulmonary emboli (PE)(68, 69). The addition of low-dose CT was reported to increase specificity of NM-V/Q SPECT from 88% to 100%(68). A recent meta-analysis showed no difference in performance between NM-V/Q SPECT and CT pulmonary angiography (CTPA) for PE detection(70). The review stated that although CTPA was more cost effective, NM-V/Q SPECT should still be considered when radiation dose is of concern(70).

Application of NM-V/Q SPECT/CT as a clinical and research tool has been described in the assessment of: -

- Ventilation post-lung resection(71)
- COPD ventilation heterogeneity(72)
- Regional change in asthma(73)
- Regional lung function in interstitial lung disease(74).

1.2.2.1 NM-V/Q SPECT in COPD

NM-V/Q SPECT is not routinely used in the assessment of COPD, but has been recommended in patients considered for lung volume reduction therapy (LVRT)(75). NM-V/Q SPECT features previously described to represent functional lung abnormality in keeping with COPD include: -

- An uneven distribution of radiopharmaceutical
- Central and peripheral "hot spots"
- Mismatch (Q<V)
- Reverse mismatch (V<Q)
- Matched defects (reduction in V=reduction in Q)(76, 77).

The central and peripheral "hot spots" relate to increased resistance in the main and small peripheral pulmonary airways, respectively that commonly occurs in COPD(77). Obstruction to conductive airflow leads to impaction of radiopharmaceutical particles, appreciated on imaging as "hot spots". Although a radiological feature associated with COPD, "hot spots" may also present with asthma. In severe COPD, well-functioning lung regions have been previously interpreted as relative "hot spots" but actually represent areas of preserved matched ventilation and perfusion.

Regions of matched ventilation and perfusion reduction may be due to emphysema or secondary to hypoxic vasoconstriction and blood flow diversion from poorly ventilated lung. Mild COPD may be appreciated on NM-V/Q SPECT by reverse mismatch (V<Q) defects(78) due to airway disease with incomplete hypoxic vasoconstriction leading to shunting and hypoxaemia(79).

NM-V/Q SPECT has also been reported to help identify comorbid disease in COPD, for example PE and congestive heart failure. Redistribution of perfusion to non-dependent lung zones may represent congestive heart failure(80). Segmental mismatch (Q<V) is the well-recognised criterion for PE diagnosis(65). In COPD, smaller areas of mismatch may indicate subsegmental PE or be caused by local vascular remodelling or vascular obliteration, which also occurs in COPD.

Conventionally, altered NM-V/Q SPECT patterns were considered to confound image interpretation(81). However, the potential for identification of different phenotypes in COPD has inspired renewed interest in the modality(82). Previous studies have suggested that NM-V/Q SPECT is more sensitive to small airway disease and emphysema than spirometry(76) and HRCT(83). The correlation between NM-V/Q SPECT with symptoms, spirometry and QCT-derived emphysema has been previously investigated in thirty patients with moderate to very severe COPD(78). Whilst significant correlations between NM-V/Q SPECT and emphysema and spirometry were reported, no correlation was found with the Medical Research Council (MRC) dyspnoea questionnaire or clinical COPD questionnaire(78).

1.2.2.2 Measurement of ventilation-perfusion (V/Q) distribution

Although complex, invasive and time-consuming, the multiple inert gas elimination test remains the gold standard measure of V/Q in the lungs. Principally used as a research tool, the technique involves analysis of the

retention and excretion data of six inert gases as they pass through the pulmonary circulation to provide a global measure of the V/Q relationship. NM-V/Q SPECT provides data about the relative distribution of V/Q tracers. NM-V/Q SPECT is limited by spatial resolution and has been reported as less sensitive than the multiple inert gas elimination test in early disease(84). However, it does provide regional topographic information and arguably V/Q inequalities appreciated with NM-V/Q SPECT would relate to clinically significant disruptions in gas exchange.

Extraction of regional functional information from NM-V/Q SPECT requires universal analysis methods for defect volume and heterogeneity quantification not yet fully developed. Abnormal distribution of ventilation may represent early stage disease with NM-V heterogeneity quantification offering a potential disease biomarker in COPD(85) and bronchiolitis obliterans(86). NM-V heterogeneity may be measured using the coefficient of variation or textural image processing methods, for example, the fractal dimension(87). Despite strong correlation between fractal dimension and spirometry, this measure has been criticised for lacking spatial information(88).

1.2.2.3 New roles for NM-V/Q SPECT/CT

An emerging role for NM-V/Q SPECT/CT, outside of pulmonary embolus detection includes radiotherapy field planning for lung cancer treatment and preoperative lung function assessment before surgery(82). In patients with lung cancer and frequently co-existent emphysema, NM-Q SPECT/CT may be used to

identify lung regions with preserved function and subsequently modify radiotherapy fields. This enables well-functioning lung areas to be spared(89-92) and more targeted administration of high dose radiotherapy to diseased lung, aiming to reduce the risk of radiation pneumonitis and fibrosis in healthy lung tissue(93, 94) whilst improving survival(95).

NM-Q SPECT/CT has utility in patients considered for lung reduction surgery by estimating the impact of resection on pulmonary status. Conventional nuclear medicine methods for assessing the contribution of individual lobes to overall lung perfusion have been based largely on radiological scores and planar scintigraphy(96-100). These are subject to interpretation errors, lack accuracy and are not based on anatomical landmarks.

The most widely adopted method for regional analysis of nuclear medicine perfusion (NM-Q) imaging uses two-dimensional (2-D) planar perfusion scintigraphy (Figure 1.1). The 2-D method simply divides each lung into three equally sized regions-of-interest (ROIs) corresponding to upper, middle and lower lung zones without any reference to anatomic landmarks. Since the left lung consists of two lobes, the left middle lung zone ROI is commonly divided equally and added to the upper and lower lung zone ROIs respectively. This results in five ROIs corresponding to the five lobes of the lung. The relative perfusion contribution of each zone is considered representative of the different lobes of the lung and is used to predict the effect of lobar resection.

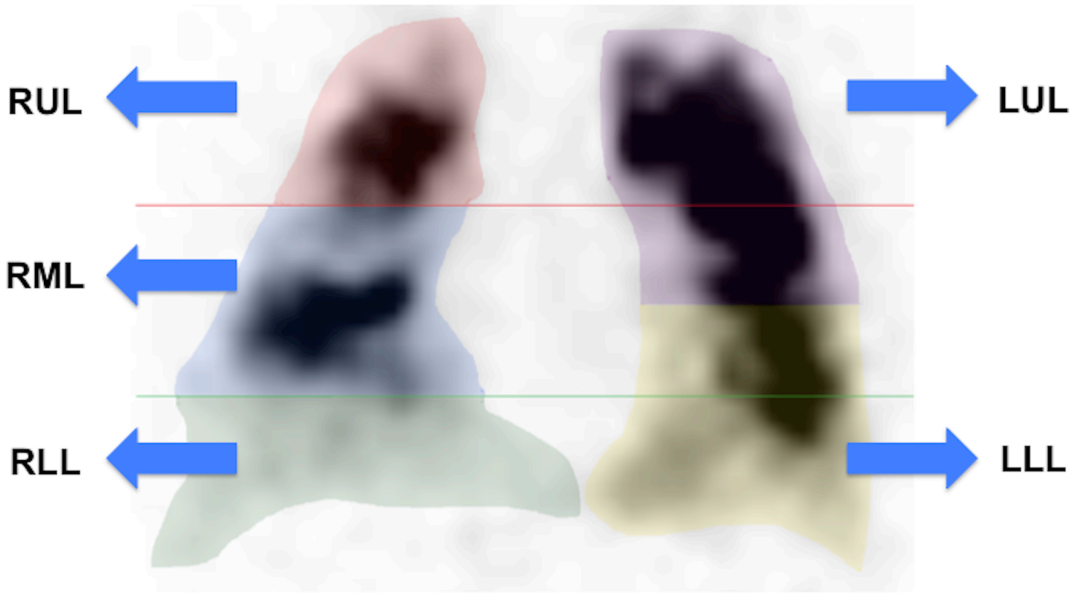

Figure 1.1: The 2-D method for regional analysis of planar perfusion scintigraphy. The lung is divided into five regions-of-interest (ROIs) without any reference to anatomic landmarks. The relative perfusion contribution of each coloured ROI is considered representative of the different lobes of the lung and is used to predict the effect of lobar resection.

Combined NM-Q SPECT/CT can provide 3-D images of the lung but even using this technique, 3-D methods employed to analyse lobar perfusion have largely been based on manual segmentation and drawing of 2-D ROIs which are summed to provide a 3-D volume-of-interest (VOI)(101). Preliminary work completed during this DPhil involved testing a newly available semi-automated software analysis tool for combined NM-Q SPECT/CT, which allows precise definition of lobar boundaries and anatomically accurate regional relative percentage perfusion measurements (Hermes Medical Solutions, AB, Stockholm) (Figure 1.2). The preliminary research confirmed that lobar lung function can be

calculated from hybrid NM-Q SPECT/CT and correlated with QCT-derived emphysema in patients with COPD(102).

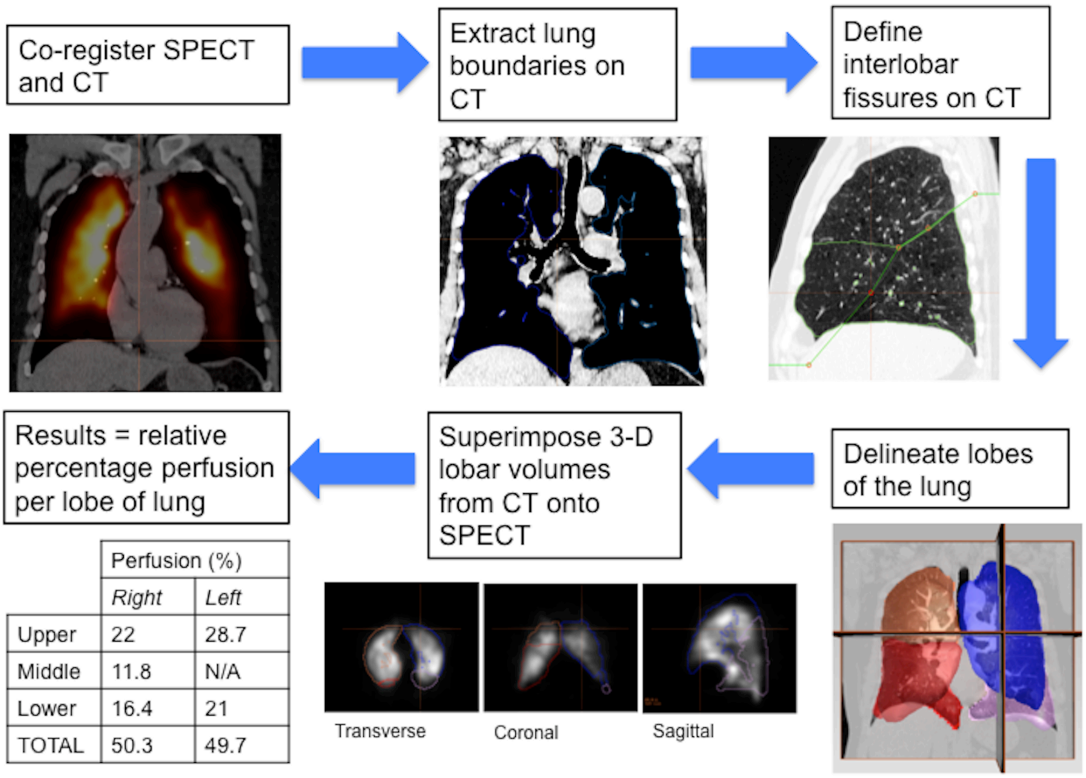

	Perfusion (%)	
	Right	*Left*
Upper	22	28.7
Middle	11.8	N/A
Lower	16.4	21
TOTAL	50.3	49.7

Figure 1.2: The 3-D method of regional analysis of nuclear medicine perfusion SPECT co-registered to CT.

Advances in regional analysis of NM-V/Q SPECT/CT presents an opportunity for more accurate prediction of post-treatment lung function in patients considered for lobar treatments. Further research is required to investigate the feasibility and correlation between predicted NM-V/Q SPECT/CT and actual post-treatment lung function.

1.2.2.4 NM-V/Q SPECT compared with hyperpolarised gas MRI

Subjective, qualitative analysis of NM-V SPECT has been previously reported to be comparable to hyperpolarised helium gas MRI (HP ^{3}H-MRI) for evaluation of regional ventilation in COPD(103). However, quantitative analysis showed approximate two-fold greater ventilation signal with HP ^{3}He-MRI than NM-V SPECT(103). The discrepancy was suggested to relate to differences in gas delivery methods, i.e. single breath-hold for HP ^{3}He-MRI and normal tidal breathing for NM-V SPECT(103).

The ventilation radiotracer used in NM-V SPECT should be taken into account. The distribution of ^{99m}Tc-labelled Technegas is chiefly via convective flow (along pressure gradients) rather than along ventilation paths governed by diffusive flow (diffusion gradients)(104). In gas exchanging compartments, at the lung periphery, airflow is predominantly along diffusion gradients(105) secondary to Brownian motion. This is particularly relevant in COPD, where emphysema and airway narrowing results in large regions of ventilation occurring mainly via diffusive flow. SPECT studies using inert gas radionuclides instead of ^{99m}Tc-labelled Technegas, for example ^{133}Xe may help overcome this problem by offering improved imaging of diffusive flow, including via collateral pathways(106).

In comparison with NM-V/Q SPECT/CT, potential advantages of functional lung assessment with HP ^{129}Xe-MRI include improved spatial resolution, no ionising radiation exposure, the possibility for temporal/dynamic imaging and provision

of complementary information about pulmonary microstructure and gas transfer in addition to static ventilation.

1.2.3 Conventional MRI

Conventional (^{1}H) MRI has limited use in respiratory disease since the lung is largely composed of airspaces that do not generate MR signal(107). Multiple air-tissue interfaces within the lung create significant magnetic susceptibility differences contributing to poor image quality. New optimised MR sequences, for example ultrashort echo time (UTE) may enable imaging of the lungs(108) but do not provide any functional information. Research into functional lung imaging using conventional (^{1}H) MR-based techniques, for example Fourier-decomposition MRI(109), is still at a relative early stage and are only indirectly sensitive to pulmonary ventilation(110).

1.2.4 Ultrashort echo time (UTE) MRI

UTE pulse sequences are capable of improving pulmonary MR signal to provide information about lung structure(111). In patients with COPD, regions of emphysema may be identified based on the difference between MR signal from normal lung parenchyma and areas of tissue destruction (emphysematous bullae)(112). Previous investigation of UTE sequences has shown correlation between MR signal intensity and pulmonary tissue density(113). UTE methods have been successfully applied to patients with emphysema to demonstrate a relationship with histology(114). Further studies in patients with COPD reported

UTE pulmonary signal intensity to correlate with pulmonary function tests and CT-derived density measurements(115). Development of zero echo time MR pulse strategies(116) aim to further minimise the effects of rapid MR signal decay, compensating for inherent low pulmonary ^{1}H abundance and generating pulmonary images similar to CT(108, 117).

1.2.5 Fourier decomposition MRI

Fourier decomposition (FD) MRI is another approach that has been developed to overcome the challenge of low pulmonary ^{1}H signal(109, 118). The technique is dependent upon ^{1}H MRI signal oscillations that occur with differences in lung volume during normal tidal breathing. The oscillation of ^{1}H MRI signal intensity related to the compression and expansion of lung parenchyma and blood flow generates very weak but native contrast enabling ventilation and perfusion images to be acquired(109). Successful acquisition of FD MRI has been previously reported in animal studies(119) and patients with COPD(115). FD MRI ventilation maps acquired in patients with COPD showed 'ventilation defects' spatially correlated with those from HP ^{3}He-MRI(115). FD MRI is acquired during free breathing and therefore requires complex non-rigid registration and analysis to generate ventilation/perfusion images. This coupled with the inherent weak ^{1}H MRI contrast are disadvantages associated with FD MRI. Furthermore adoption of the technique is currently limited due to the lack of validation.

Inhalation of hyperpolarised xenon (^{129}Xe), an inert noble gas, can resolve the problem of inherent low pulmonary ^{1}H signal by enabling direct visualisation of the lung airspaces on MRI. In addition, the high solubility of ^{129}Xe in biological tissues(120) and associated chemical shifts(121), make hyperpolarised ^{129}Xe ideal for evaluating gas exchange in the lung(122-130). The inherent properties of ^{129}Xe may be exploited to regionally quantify ventilation, diffusion and gas transfer within the lung and provide comprehensive *in vivo* assessment of lung function.

1.3 Part 3

1.3.1 Hyperpolarised gas magnetic resonance imaging

The first hyperpolarised gas MR images were obtained using ^{129}Xe in a mouse heart-lung preparation by Albert *et al.*(131), followed shortly by hyperpolarised helium (^{3}He) images of human lungs by MacFall *et al.*(132). In subsequent years, hyperpolarised ^{3}He MR imaging (HP ^{3}He-MRI) became the focus of investigation primarily because ^{3}He provides a stronger MR signal due to a larger magnetic moment than ^{129}Xe. ^{3}He has a gyromagnetic ratio of 203.782 MHz rad T^{-1} or 76% of ^{1}H, while ^{129}Xe has a gyromagnetic ratio of 74.521 MHz rad T^{-1} or 28% of ^{1}H. Availability of ^{3}He is limited by its production (only possible via the radioactive decay of tritium(133)) and government sequestering of the isotope for use in neutron detectors(133, 134). Until recently, polarisation methods were capable of achieving 30-50% polarisation levels for ^{3}He but only 10% for ^{129}Xe(124, 135).

However, recently new modified polarisation methods have been described which achieve up to 55% polarisation levels of ^{129}Xe(136, 137). These levels of polarisation are comparable to those previously published for ^{3}He. With demand for ^{3}He far exceeding supply(138) and high associated costs, ^{129}Xe is an increasingly attractive alternative, given its natural abundance and wider availability.

1.3.2 Xenon (^{129}Xe)

Xenon (Xe) is an inert, non-toxic noble gas. ^{129}Xe has a nuclear spin of ½, but in contrast to protons, the nuclear spin arises from an unpaired neutron. Atmospheric air contains approximately 0.04 mol% of xenon. The xenon isotope ^{129}Xe is employed for hyperpolarised xenon MR imaging. The natural abundance of ^{129}Xe in atmospheric Xe is 26%, and it can be extracted relatively easily.

Previous applications of xenon include use as an anaesthetic at much higher concentrations (> 3 times, and at larger volumes) than employed in this thesis. Xenon has also been used in scintigraphic and CT brain perfusion studies and as an inhaled contrast agent in CT(139, 140).

The pioneering techniques employed to characterise lung function using HP ^{3}He-MRI(141-145) may be translated to HP ^{129}Xe-MRI(128, 129, 146-149). A summary of progress to date with HP ^{129}Xe-MRI is provided in the context of previous HP ^{3}He-MRI research.

1.3.3 Ventilation imaging

Ventilation imaging is performed by acquiring images following inhalation of hyperpolarised noble gas. Ventilation images typically show homogeneously distributed high signal in normally functioning regions of the lung. Regions of absent or relatively low signal are known as "ventilation defects" and correspond to regions of obstructed airflow(132, 150).

1.3.3.1 Hyperpolarised ^{3}He-MR ventilation imaging

Ventilation imaging with HP ^{3}He-MRI has shown utility in detection of functional abnormalities in a range of obstructive lung pathologies e.g. chronic obstructive pulmonary disease (COPD), cystic fibrosis (CF)(151, 152), asthma(150, 153, 154) and bronchiolitis obliterans(155, 156). The size and extent of HP ^{3}He-MRI ventilation defects correlated with spirometry(151, 157). Furthermore, HP ^{3}He-MRI has shown increased sensitivity in detecting ventilation abnormalities compared with spirometry and lung ventilation scintigraphy(135, 158).

Several methods for quantitative measurement of regional lung ventilation using HP ^{3}He-MRI have been suggested in experimental animal studies(159-161) (162). In a rat model of emphysema, the ventilation abnormalities detected preceded the histological changes seen in lung alveoli(163). This study supports a role for hyperpolarised gas MR imaging in earlier detection of lung pathology. Preliminary results in humans also have been reported(164, 165).

1.3.3.2 Hyperpolarised ^{129}Xe-MR ventilation imaging

Albert *et al.* initially demonstrated imaging of lung airspaces using hyperpolarised ^{129}Xe introduced into the trachea of a mouse heart-lung model(131). This was followed by a combined imaging and spectroscopic approach by Mugler *et al.*(166). Ventilation imaging acquired using ^{129}Xe clearly depicts ventilation defects associated with functional lung abnormalities(147, 149, 167). HP ^{129}Xe-MRI is safe and well tolerated. To date, no serious adverse effects have been reported in small cohorts of healthy volunteers and patients with respiratory disease imaged using HP ^{129}Xe-MRI(128, 147, 167).

1.3.4 Diffusion-weighted imaging

The diffusion coefficient of a particular gas determines the average distance its atoms move in a given period of time. The lung microstructure acts to restrict diffusion of hyperpolarised noble gas atoms enabling the average short time diffusion coefficient, (apparent diffusion coefficient, ADC) to be measured with MRI(168).

1.3.4.1 Hyperpolarised ^{3}He-MR diffusion-weighted imaging

Increased ADC values have been reported with HP ^{3}He-MRI in emphysema, reflecting increased free movement of ^{3}He gas atoms permitted by alveolar tissue destruction(168-171). In this way, regional ADC values can be used as a surrogate measure of alveolar airspace size. Precise correlations between hyperpolarised gas MRI ADC measurements and histological measurements of

alveolar size have been reported(172-174). ADC values with HP ^{3}He-MRI have proven highly reproducible(175, 176), and been shown to closely correlate with lung function tests(169).

Subclinical smoking–related emphysematous changes might be revealed with ADC measurements before they are demonstrated on high resolution CT(HRCT)(177). In addition, gravity-dependent gradients and age-related changes in alveolar size can be detected with diffusion imaging(178, 179). Detailed analysis of the signal from diffusion imaging provides additional information about lung structure. Model based(180, 181) and "q-space"(145, 182) techniques enable the estimation of underlying structural dimensions and closely correlate with histological measurements.

1.3.4.2 Hyperpolarised ^{129}Xe-MR diffusion-weighted imaging

ADC values may also be determined using HP ^{129}Xe-MRI. However, ^{129}Xe has a much lower diffusivity than ^{3}He and demonstrates a lower diffusion coefficient. This may offer an advantage for assessment of the distal small airways and alveoli(183).

The mean ADC value of ^{129}Xe in eight patients with COPD was reported as significantly elevated compared to those for ten age-matched healthy controls(146). A gravity-dependent gradient in alveolar size and age-related changes in ADC was also demonstrated in this study(146).

Preliminary research findings support the utility of ^{129}Xe diffusion imaging for the assessment of lung microstructure(146, 149).

1.3.5 Hyperpolarised gas MRI to measure intrapulmonary partial pressure of oxygen

In the presence of oxygen within the lung, hyperpolarised noble gases undergo hastened loss of polarisation resulting in a predicted reduced MR signal(184). This known paramagnetic effect of oxygen on ^{3}He gas may therefore be utilized to quantitatively measure intrapulmonary partial pressure of oxygen (PO_2)(159, 185). Reproducibility of intrapulmonary PO_2 measurements has been confirmed. Regional ventilation-to-perfusion ratios may also be calculated from the partial pressure data(186).

Hyperpolarised ^{129}Xe is also susceptible to the paramagnetic effect of oxygen within the pulmonary airspaces. The resultant loss of polarisation and predicted decay in MR signal may be used to measure intrapulmonary PO_2(149, 187, 188). However, this is slightly more complex than when measuring with ^{3}He because additional signal loss due to diffusion of ^{129}Xe into alveolar tissue needs to be taken into account(136). A correction for the effects of gas exchange and uptake can be applied to PO_2 measurements with HP ^{129}Xe-MRI(128).

1.3.6 Other hyperpolarised gas MR imaging sequences

“Dynamic ventilation images” may be obtained with hyperpolarised gas MRI by

employing ultrafast pulse sequences(141, 189-191). Dynamic ventilation imaging allows the distribution and severity of air trapping to be assessed directly(190, 191) and has been performed to evaluate air trapping in patients with bronchial asthma(190) and CF(191). The optimisation of multiple breath HP ^{3}He-MRI techniques will enable wash-in/wash-out time constants and fractional ventilation to be measured, which may prove complementary to information from diffusion-weighted imaging and partial pressure of oxygen in alveolar gas (P_AO_2) mapping(192).

1.3.7 Dissolved phase imaging

Following inhalation, 2% of hyperpolarised ^{129}Xe dissolves through the alveolar membrane into the parenchyma and blood. This results in an MR spectrum with multiple peaks(122, 123, 193, 194) i.e. a single large peak corresponding to the gas-phase of ^{129}Xe in the lung airspaces and two smaller peaks with chemical shifts of about 200 ppm from the gas-phase, corresponding to the dissolved-phase of ^{129}Xe in the lung parenchyma and blood(122, 123, 193, 194). This chemical shift difference between gas- and dissolved- phase enable characterisation of gas exchange with HP ^{129}Xe-MRI. Spectroscopic acquisitions of dissolved-phase ^{129}Xe have been produced in the human lung(128, 129).

The xenon polarisation transfer contrast (XTC) is a technique that uses the rapid, diffusion driven exchange of ^{129}Xe between the airspaces and dissolved-phase compartments, to indirectly image the otherwise limited dissolved-phase signal(124, 195). XTC data may be used to derive values of alveolar surface area

per unit volume of gas (S/V)(136, 196). In addition, the XTC method has been used successfully to measure lung septal thickness in animals(125, 197) and humans(136).

Preliminary results have shown that direct dissolved-phase imaging in humans is feasible with HP ^{129}Xe-MRI(198-200). Mugler *et al.*(199) simultaneously acquired HP ^{129}Xe-MRI ventilation and dissolved-phase images in six healthy and five subjects with lung disease. Distributions of gas- and dissolved-phase signal were uniform in healthy subjects. However, a gradient in dissolved-phase signal intensity was demonstrated along the anterior-posterior direction, likely due to the gravity dependent gradient in lung tissue density occurring in a supine posture. In contrast, heterogeneous distribution of gas-phase and dissolved-phase signal was observed in subjects with lung disease. Interestingly, the variations in dissolved-phase signal did not match the variations in ventilation in these subjects, highlighting the potential for HP ^{129}Xe-MRI to detect underlying pathology relating to lung tissue or regional blood flow.

1.3.8 Fluorine-19 magnetic resonance imaging of the lungs (^{19}F-MRI)

Functional MR images of the lungs may be acquired using inhaled inert fluorinated gases (^{19}F-MRI)(201-203). This technique is of particular interest to the functional lung imaging community because unlike HP noble gas MRI, inert fluorinated gases do not require hyperpolarisation prior to imaging. The high natural abundance (100%) and gyromagnetic ratio (251.662 MHz rad T^{-1}) of ^{19}F,

coupled with short longitudinal relaxation times (T_1)(204) allows signal averaging and thus acquisition of ^{19}F-MR images with reasonable signal-to-noise ratio (SNR) within a single breath-hold. ^{19}F-MRI can be performed with various fluorinated gases; tetrafluoromethane (CF_4), sulfur hexafluoride (SF_6) hexafluoroethane (C_2F_6) and perfluoropropane (C_3F_8 or PFP), all of which are non-toxic and tolerated safely.

Wolf *et al.* obtained the first inert fluorinated gas MR images of human lungs in 2008 using a mixture of SF_6 and O_2(205). Despite very poor image quality, the feasibility and safety of ^{19}F-MRI was demonstrated. Subsequently, ^{19}F-MRI has been reported in healthy volunteers(201) and patients with respiratory disease(202). ^{19}F-MR ventilation images obtained from a healthy volunteer showed fairly homogeneous distribution of signal throughout the lungs but with substantial T_2* blurring and phase artifacts around the lung edges(201).

1.3.8.1 Static ^{19}F-MR ventilation imaging

^{19}F-MR ventilation images have recently been acquired in a small number of patients with COPD, asthma and lung transplant recipients(202). Signal voids, qualitatively similar to HP noble gas MRI ventilation defects were demonstrated in COPD. Further quantification and direct comparison with HP noble gas MRI would be necessary for validation.

1.3.8.2 Dynamic ^{19}F-MR ventilation imaging

Inert fluorinated gases may be mixed with O_2 without significant detriment to image quality enabling continuous breathing of gas mixtures and the opportunity for dynamic imaging(206). Dynamic ^{19}F-MRI uses a wash in/wash out approach to quantify regional gas replacement and gas trapping and has been completed in animals(206-208), healthy volunteers, patients with asthma and COPD(209). The distribution of ^{19}F-MR ventilation signal was reported as homogeneous in healthy volunteers, with similar wash-in/wash-out curves to those obtained with Xe-CT(210). In contrast, patients with respiratory disease showed heterogeneous ^{19}F signal distribution and variable wash in/wash out curves, potentially indicative of gas trapping.

1.3.8.3 ^{19}F-MR diffusion-weighted imaging

The very short T_2* values associated with inert fluorinated gases make diffusion-weighted imaging particularly challenging. However, the use of a UTE sequence has demonstrated significant differences in C_2F_6 ADC values between healthy and emphysematous excised human lungs(211).

The substantially lower ^{19}F-MR image quality compared with HP noble gas imaging and significant research efforts being made to advance HP ^{3}He-MR and ^{129}Xe-MRI suggests ^{19}F-MRI is still an emerging technique and currently not optimised to a level comparable with HP noble gas MRI. Nonetheless, the viability of ^{19}F-MRI provides supplementary evidence that gas phase MRI may play an important role in pulmonary imaging technology in the not too distant

future(203).

1.3.9 Oxygen-enhanced MRI (O_2-MRI)

Oxygen-enhanced MRI (O_2-MRI)(212) offers an alternative method for pulmonary ventilation-imaging using molecular oxygen as an inhaled contrast agent. Oxygen has the advantage of being relatively inexpensive, readily available and safely tolerated during short-term inhalation. O_2-MRI can be performed with conventional proton MR sequences on commercially available scanners. O_2-MRI was first proposed over a decade ago and is based on the paramagnetic properties of oxygen(213). Inhalation of pure O_2 increases pulmonary partial pressure of oxygen in arterial blood (PaO_2) resulting in shortening of the T_1 time and subsequent increased signal of T_1-weighted images(214).

Subtraction of images acquired while breathing room air (21% O_2) from those acquired while breathing 100% oxygen generate typical O_2-MR ventilation images. Although the change in T_1 signal intensity between the two conditions is generally considered to be predominantly ventilation-weighted, free diffusion of O_2 into blood suggests that there is a perfusion component unaccounted for(215). The complex interaction between ventilation, diffusion and perfusion makes accurate interpretation of O_2-MRI challenging.

1.3.9.1 Steady state O_2-MR imaging

Preliminary O_2-MR images were acquired using a 2-D inversion recovery single-

shot fast spin echo (IR-SSFSE) sequence(213). Incomplete lung coverage, susceptibility to cardiac and diaphragmatic motion artefacts and the relatively small T_1 shortening effect of oxygen (10%) resulted in poor image quality and SNR. Despite these limitations, oxygen-enhanced signal was evident in healthy lung regions, whereas signal was reduced in areas corresponding to emphysema(216).

Advances in O_2-MR sequence development include multislice imaging with dual respiratory and cardiac gating(217) and 3D radial ultrashort echo time (UTE) sequences(218). These O_2-MR sequences offer the potential for complete lung coverage, improved spatial resolution and higher SNR.

1.3.9.2 Dynamic O_2-MR imaging

Quantitative measures that can be determined from dynamic O_2-MR ventilation imaging include wash-in/wash-out time constants(219) and the percentage signal enhancement (PSE) relative to baseline.

1.3.9.3 V/Q assessment with O_2-MRI

By combining O_2-MRI with two other conventional (^{1}H) MR-based techniques, regional V/Q(220) may be assessed: -

1) Arterial spin labelling – flow-sensitive alternating inversion recovery with an extra radiofrequency pulse (ASL-FAIRER) sequence for measurement of regional perfusion(221)
2) O_2-MRI to quantify regional specific ventilation

3) ^{1}H-MRI to measure regional lung density.

This combined triple MRI technique was used to demonstrate more uniform V/Q distributions in the prone compared with supine posture in a healthy volunteer(222). In addition to the highly complex analysis required, the technique only allows limited coverage of a single sagittal image slice.

ASL involves two acquisitions of a single pulmonary image slice approximately 5 seconds apart using an ultrafast spin echo pulse sequence. Before acquiring the first image, slice-selective saturation is performed to diminish the imaged slice MR signal. The time elapsed between this "tagging" preparation and actual image acquisition is one systolic ejection period. Untagged blood from outside the selected slice flows in during this time generating a blood-bright image. The process is repeated but for the second image the tagging is spatially non-selective resulting in diminished MR signal of the blood flowing into the imaged slice and consequently generating a blood-dark image. MR signal from static components are eliminated by subtraction of the blood-dark from the blood-bright image yielding a final image of blood delivered to the pulmonary slice in one systolic ejection period.

V/Q assessment with the triple MRI technique requires approximately 18 minutes to acquire a single pulmonary image slice. The slice-selective nature of ASL tag preparation limits simultaneous application to multiple image slices and the wash-in nature of O_2-MRI requires lengthy observation times to measure specific ventilation in a given region. Until the technique is further developed to

enable volumetric coverage of the whole lung within a reasonable scan time, it will remain largely within the domain of physiological research.

1.3.9.4 Clinical applications of O_2-MRI

O_2-MRI remains predominantly a research technique despite promising results from early clinical studies. Lower and more heterogeneous O_2-MRI PSE was reported in patients with emphysema compared to healthy volunteers(212). In comparison to CT, O_2-MRI PSE showed a stronger correlation with pulmonary function tests(223).

Ohno *et al.* used O_2-MRI to demonstrate a lower PSE in patients with lung cancer compared to healthy volunteers(219). A further finding from this study was significantly lower PSE in patients with co-existent lung cancer and emphysema compared with those diagnosed with lung cancer alone.

For prediction of post-surgical FEV_1 in lung cancer patients undergoing resection, O_2-MRI was reported as equivalent to QCT(224). For COPD clinical stage assessment, dynamic O_2-MRI was also reported to be equivalent to QCT(225, 226), whereas in asthma, mean O_2-MRI wash-in times were shown to correlate more strongly with disease severity than QCT(227). In addition, O_2-MRI-derived measures have been reported to decrease in asthma patients after an allergen challenge(228). The ability of O_2-MRI to differentiate between patients with and without interstitial lung disease related to connective tissue disease was reported as comparable to thin-section CT(229).

The availability of oxygen and lack of required dedicated hardware makes O_2-

MRI a potentially accessible technique for ventilation imaging. However, much more research is needed to untangle the signal related specifically to ventilation, diffusion and perfusion before O_2-MRI can be considered for clinical use.

1.4 Hypothesis

Current methods for assessing lung function are inadequate. HP ^{129}Xe-MRI potentially offers comprehensive evaluation of regional lung function and quantification of the relationship between gas delivery, exchange and transport. Establishing this new technique will broaden our understanding of regional lung disease pathophysiology and enable individual-tailored treatments by improved assessment and potentially prediction of therapeutic response.

The utility of HP ^{129}Xe-MRI may only be realised following rigorous validation of the technique, comparison with current assessment tools to demonstrate its advantages and identification of roles where the HP ^{129}Xe-MRI can complement or enhance clinical practice. To this end, the hypotheses of this thesis are that HP ^{129}Xe-MRI: -

1) Is sensitive to gravitational effects on lung function and therefore an imaging technique robust to normal physiology
2) Can be used to generate lobar measures of lung function following automated non-rigid co-registration with ^{1}H-MRI and CT
3) Is capable of demonstrating delayed/collateral ventilation indicating a potential role in the assessment pathway for LVRT candidates

4) Is capable of demonstrating regional lung function change post-therapeutic intervention supporting a potential role in drug development studies as a surrogate end-point.

1.5 Aims

This thesis therefore aims to systematically investigate: -

1) The normal range of HP ^{129}Xe-MRI parameters and sensitivity to gravitational effects in healthy volunteers
2) The generation of lobar HP ^{129}Xe-MRI-dervied measures in patients with COPD
3) The feasibility of time-resolved breath-hold HP ^{129}Xe-MRI for detecting delayed/collateral ventilation
4) The ability of HP ^{129}Xe-MRI to detect regional lung function change post-therapeutic intervention.

2 Chapter 2: Materials and methods

2.1 Practical considerations - hardware

MRI scanners with broadband multinuclear capabilities may be used to perform hyperpolarised gas imaging, provided the following additional pieces of hardware are available: -

1. A polariser
2. Scanner modifications to operate at the resonance frequency of ^{129}Xe (at 1.5T is ~17.7 MHz, compared to 63.9 MHz for protons)
3. A dedicated radiofrequency (RF) coil to permit imaging.

   RF chest coils for hyperpolarised gases are not widely available from scanner manufacturers and remain custom made for research purposes(165).

2.2 Performing HP ^{129}Xe-MRI

All clinical research was carried out at the Radiology department, Churchill Hospital, Oxford. Figure 2.1 is a flow diagram of a typical HP ^{129}Xe-MRI scan.

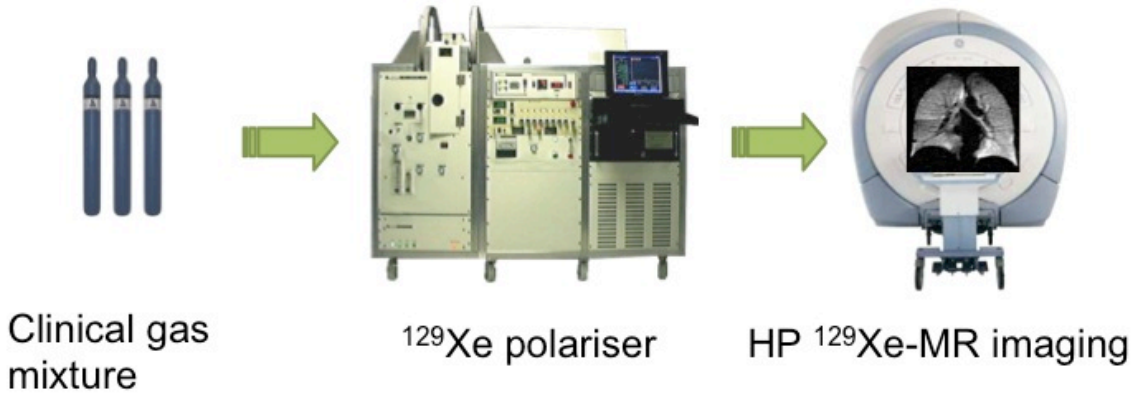

Figure 2.1: **Flow diagram of HP ^{129}Xe-MRI examination.**

2.3 Hyperpolarisation

In their natural form, noble gases (^{129}Xe and ^{3}He) have low magnetic moments generating a weak MR signal. The nuclear polarisation of noble gases can be increased dramatically using a method called optical pumping and spin exchange (SEOP). This technique was developed over 50 years ago and has been extensively applied within the field of physics research(230, 231).

Comprehensive details of hyperpolarisation methods have been previously published(232-237). In brief, SEOP involves illuminating a heated glass cell containing ^{129}Xe and rubidium metal with circularly polarised laser light [Figure 2.2] SEOP results in a large net polarisation of ^{129}Xe, in turn giving rise to a large MR signal.

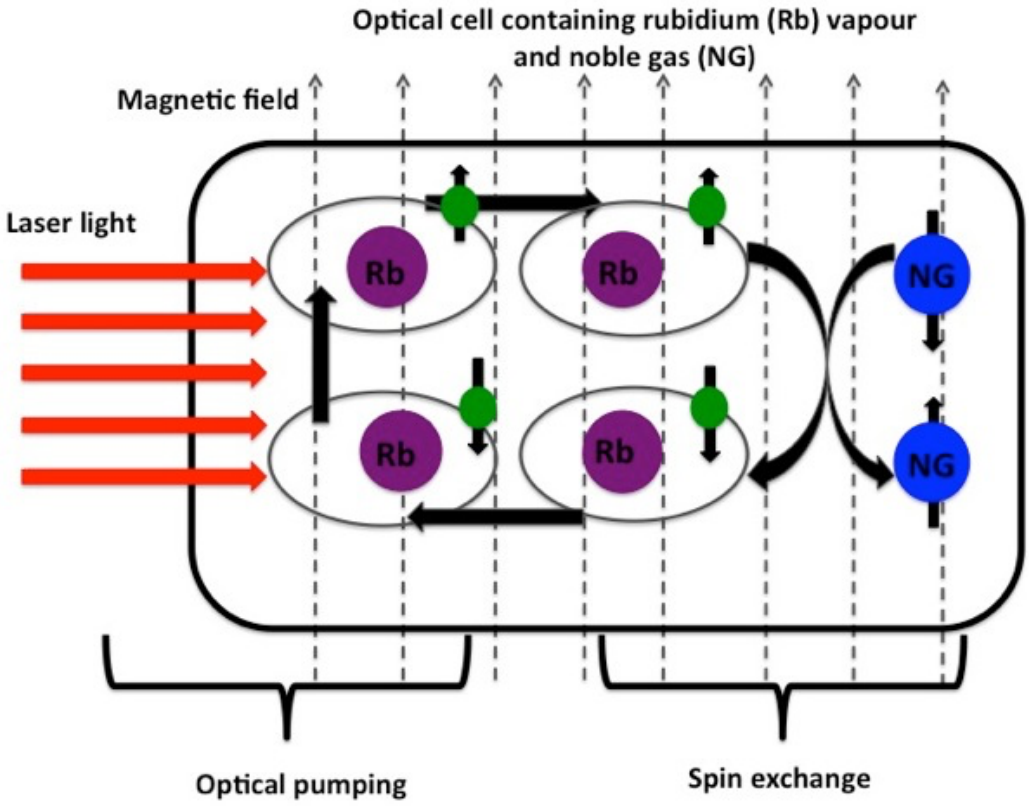

Figure 2.2: **Simplified conceptual diagram of SEOP.** Adapted from Mugler *et al.*(238).

Challenges faced when imaging hyperpolarised noble gases include the following: -

1. The hyperpolarisation generating the MR signal is "non-renewable". Some polarisation will be consumed during image acquisition and may only be replenished by the introduction of additional hyperpolarised gas.
2. The paramagnetic properties of oxygen within the lungs lead to a loss of polarisation and decay of MR signal. However, this characteristic can be utilized beneficially to measure intrapulmonary PO_2.
3. Noble gases are highly diffusive resulting in MR signal loss.

Low flip angle gradient echo MR sequences have been developed to account for the above factors. These MR pulse sequences only consume a small fraction of the longitudinal magnetisation each repetition.

2.4 ^{129}Xe polarisation and delivery

Isotopically enriched ^{129}Xe gas (80% ^{129}Xe, Spectra Gases Inc., Alpha NJ, USA, supplied by Littleport, Cambridgeshire, UK) was polarised to 4-12% by rubidium vapour spin-exchange optical pumping (SEOP, Figure 4), and cryogenically accumulated in 1 L doses using a commercial polariser (Polarean 9800, Durham, NC, USA). Hyperpolarised ^{129}Xe was then thawed into a Tedlar bag (Jensen Inert Products, Coral Springs, FL, USA), and the polarisation determined using a polarisation measurement station (Polarean 2881). Hyperpolarised ^{129}Xe was administered by first instructing patients, who were lying supine in the MRI scanner, to exhale to functional residual capacity (FRC) and then inhale the 1 L contents of the Tedlar bag through 0.95 cm inner diameter Tygon tubing (Cole-Palmer Instrument Co Ltd., Hanwell, London, UK). Patients were then instructed to hold their breath for up to 25 seconds for image acquisition. Study participants were provided training and instruction for breath-hold imaging, performing practice breath holds beforehand, to ensure lung volumes were as reproducible as possible for all imaging.

2.5 Calibration dose

Prior to acquisition of any HP ^{129}Xe-MR imaging, all participants underwent a calibration scan. This involved administration of a small volume (approximately 100 mL) of hyperpolarised ^{129}Xe gas mixed with medical grade nitrogen for a total volume of 1 L. Patients were instructed to perform a standard breath-hold for only a short period of time; 2 seconds. Calibration pulse sequence parameters were: single slice thickness of 20 mm, FOV of 40 cm x 40 cm, resolution of 96 x 96 matrix, BW of 3.97 kHz, TE/TR of 3.1/20 ms, flip angle of 90°.

The calibration scan outputs are patient-specific control variables. These enable optimisation of subsequent HP ^{129}Xe-MR scanning sequences according to the patient's height and weight to ensure high quality image acquisition.

2.6 MRI

All MR scans were performed on a 1.5 T Signa HDx whole body MR system (GE Healthcare, Milwaukee, WI, USA). Subjects were fitted with a flexible twin Helmholtz quadrature transmit-receive coil (Clinical MR solutions, Brookfield, WI) resonating at the ^{129}Xe Larmor frequency (17.7 MHz). Scans were acquired in the prone and supine position in healthy volunteers [Section 3] and supine alone in patients with COPD [Section 4-6].

2.6.1 Static HP ^{129}Xe-MR ventilation imaging

Following initial ^{1}H MRI localisers, HP ^{129}Xe-MR ventilation images were acquired during an approximate 25-second breath-hold, in the anterior-to-posterior direction using a broadbanded 2-D spoiled gradient echo sequence. Pulse sequence parameters were: 15 mm coronal slices covering the whole lung, field of view (FOV) of 40 cm x 40 cm, resolution of 96 x 96 matrix, bandwidth (BW) of 4 kHz, echo time/repetition time (TE/TR) of 4.2/20 ms, flip angle of 9°.

2.6.2 HP ^{129}Xe-MR diffusion-weighted imaging

HP ^{129}Xe-MR diffusion-weighted images were acquired using an interleaved 2-D gradient echo sequence with two b-values (b=0, 20.855 sec/cm^2). Pulse sequence parameters were: 30 mm coronal slices covering the whole lung in the anterior-posterior direction, FOV of 40 cm x 40 cm, resolution of 96 x 96 matrix, BW of 4 kHz, TE/TR of 13.2/20ms, flip angle of 7°.

2.6.3 Time-resolved HP ^{129}Xe-MR ventilation imaging

This sequence was used in patients with chronic obstructive pulmonary disease (COPD) who were investigated for delayed ventilation [Section 5]. All participants who completed this HP ^{129}Xe-MR sequence had previously undergone static HP ^{129}Xe-MR ventilation imaging which, enabled identification of up to 3 coronal slices containing ventilation defects.

Time-resolved HP ^{129}Xe-MR ventilation imaging adopted the same sequence

parameters as static imaging (15 mm coronal slices, FOV of 40 cm x 40 cm, resolution of 96 x 96 matrix, BW of 4 kHz, TE/TR of 4.2/20 ms) with 3-second delays; the selected coronal slices were imaged up to five times during a single breath-hold with a flip angle of 4°.

2.6.4 Proton MR imaging

Anatomical proton (^{1}H) MR images were acquired during a separate 15-second breath-hold after each set of HP ^{129}Xe-MR ventilation and diffusion-weighted images. Subjects inhaled 1 L oxygen via a Tedlar bag from FRC prior to breath-hold. These images were acquired using a multislice balanced steady-state free precession sequence and image location copied from the preceding HP ^{129}Xe-MRI for co-registration purposes. Pulse sequence parameters were: 15 mm coronal slices covering the whole lung, FOV of 40 x 40 cm, resolution of 128 x 128 matrix, BW of 125 kHz, TE/TR=2.8/1.2 ms, flip angle 45°.

2.6.5 HP ^{129}Xe-MRI reproducibility

A subgroup of patients with COPD [Section 4] returned within 6 weeks of initial baseline imaging for repeat acquisition of HP ^{129}Xe-MR imaging to enable assessment of reproducibility. Reproducibility imaging (HP ^{129}Xe-MRI_R) was only completed in patients with stable disease who remained exacerbation free since initial imaging. Reproducibility HP ^{129}Xe-MR ventilation and diffusion-weighted MR images were acquired in exactly the same way as described above.

2.6.6 MRI analysis

HP ^{129}Xe-MRI analysis was performed using Pulmonary Toolkit (PTK)(239), an open-source image processing kit that runs in the Matlab® environment (Mathworks, Natick, MA). PTK builds on previous techniques developed in our group(240) and is capable of fully automated lobar analysis of HP ^{129}Xe-MR ventilation and diffusion-weighted imaging. The output from PTK includes whole lung and lobar HP ^{129}Xe-MRI parameters; ventilated volume (%) and mean ADC values. Key steps in the pipeline involving PTK are illustrated in Figure 2.3.

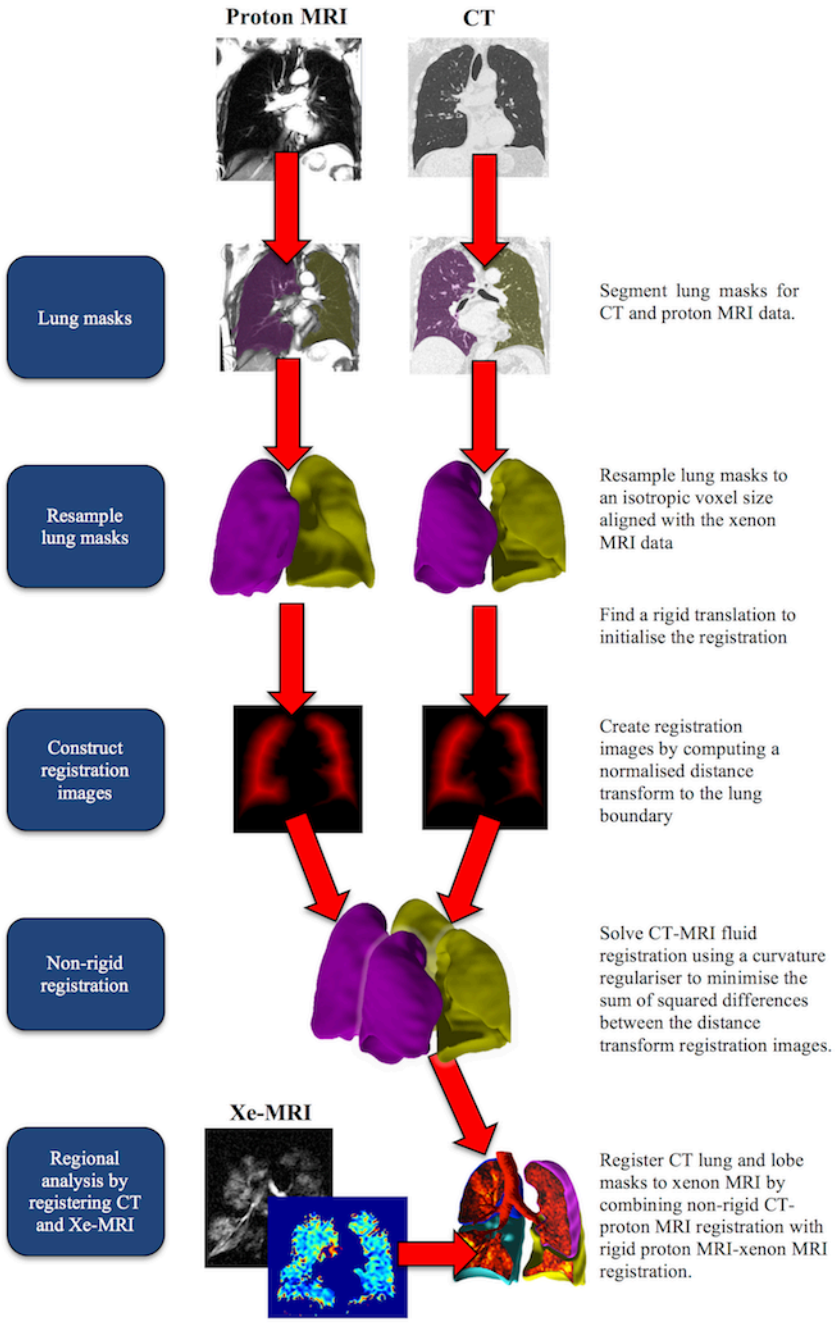

Figure 2.3: **Schematic of pipeline for regional HP ^{129}Xe-MR image analysis using pulmonary toolkit (PTK).** Reproduced from (241).

Regional analysis is performed by using image registration to apply lung and lobar boundaries from CT data to ^{129}Xe-MRI. Direct registration between CT and HP ^{129}Xe-MRI is challenging due to the difficulty in identifying lung boundaries

and other anatomical features from HP ^{129}Xe-MRI data. For this reason, registration is performed in two steps, using proton MRI as an intermediate stage. Proton MRI provides an ideal intermediate stage, since the lung inflation protocol can be matched, allowing images to be rigidly registered to HP ^{129}Xe-MRI data using image metadata, and the visible lung boundaries can be used to perform a non-rigid registration with CT data.

HP ^{129}Xe-MRI ventilation and ADC scan data were saved onto a dedicated workstation for analysis. ADC values per pixel were calculated according to published formula(242). PTK incorporates a graphic user interface (GUI) that first completes automated segmentation of the lungs on CT and proton MRI, and the lobes on CT data. The segmented lung masks are used to perform an inter-modal registration allowing the CT lobe masks to be registered to proton and HP ^{129}Xe-MRI. This enables the computation of lobar masks on proton MRI and subsequently HP ^{129}Xe-MRI, which were then used to establish lobar ventilation and ADC maps. The accuracy of image registration was ensured by confirming a volume overlap index (DICE) value of >0.8.

For analysis of time-resolved HP ^{129}Xe-MR ventilation data, PTK was used to measure the ventilation level (signal intensity) per pulmonary lobe for each time point. HP ^{129}Xe signal decay due to the imaging procedure and natural T_1 relaxation processes were accounted for by normalisation of images at each time point using a region of fully ventilated lung (243). Delayed ventilation was defined as the quantifiable increase in ventilation level (signal intensity) in a lobe showing ventilation defects at baseline.

The method for automated segmentation of the lungs from proton MRI comprises an initialisation based on 3-D region-growing with an adaptive threshold. Contour refinement is then performed for each coronal slice using a 2-D level-set algorithm with an image-gradient force, region-based speed term and curvature regulariser.

The algorithm employed for automated CT lung segmentation is based on a region-growing method with a global threshold to extract the initial lung region(244) followed by left and right lung separation and boundary refinement(245) both of which have been validated in the literature.

The automated algorithm for CT lobe segmentation combines a Hessian-based filter for detecting pulmonary fissures with anatomical cues from segmented lungs, airways and pulmonary vessels. This method is robust to small vessels crossing the lobar boundary, requires no training or prior data and is robust to incomplete fissures(246).

Registration between the CT and proton MRI is performed by first generating normalised distance transforms to the lung boundaries for each lung mask. A deformation field is computed by using a curvature regulariser to minimise the sum of squared differences between the normalised distance transforms for each modality. Non-linear fluid registration of multi-modality pulmonary imaging has been previously reported to be superior to rigid registration(247).

2.7 Quantitative computed tomography (QCT)

QCT was acquired on a 64-slice GE Lightspeed scanner (GE, Milwaukee, USA). Images were taken 60 seconds post-administration of 100 mL of intravenous iohexol contrast (equivalent to 300 mg of organic iodine per mL) with the following CT parameters; 0.625 mm slice thickness, current 60 mA, voltage 120kV, tube collimation 40 mm and beam pitch 0.984:1, scan type helical full, rotation time 0.5 seconds. QCT images were acquired post-intravenous contrast as part of the patient's clinical work-up according to local standard protocols.

QCT was acquired during suspended inspiration following inhalation of 1 L oxygen via a Tedlar bag from FRC to ensure lung volumes were as similar to HP ^{129}Xe-MRI as possible. Subjects underwent breath-hold training by radiographer instruction to ensure reproducibility. No data were acquired in expiration.

2.7.1 QCT analysis

QCT was analysed using Pulmonary Toolkit (PTK), to determine percentage emphysema on a whole lung and lobar basis [Figure 2.4]. QCT-derived emphysema was derived from the percentage of lung voxels with attenuation less than -950 HU (%LAA).

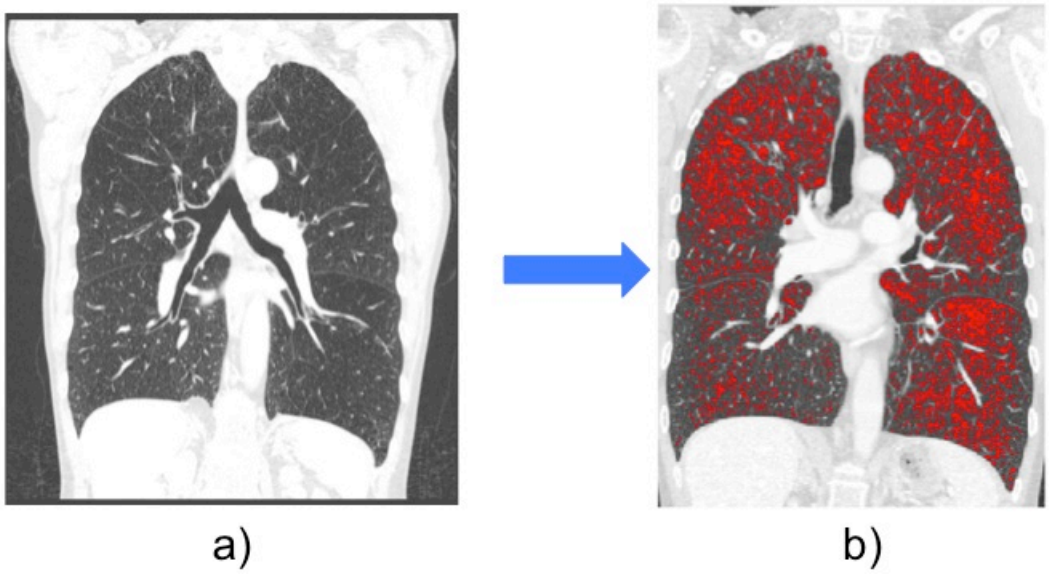

Figure 2.4: **Method used to quantify lobar percentage emphysema from QCT.** a) Coronal CT chest in lung windows. b) PTK determines the percentage of lung tissue with attenuation below the threshold -950 HU (red areas) corresponding to emphysema.

QCT was also analysed using commercially available software (GE Thoracic VCAR) to measure average lumen diameter and wall area for 3rd to 6th generation airways [Figure 2.5]. To reduce technical errors associated with small airways, only airways with an internal perimeter greater than 6 mm were included. To avoid potential inter-subject bias from different airway size distribution, a standardised measure for airway wall thickness (Pi10) was derived for each subject by plotting the square root of airway wall area against the internal perimeter of each measured airway(248). The resulting regression line was used to calculate the square root of bronchial wall area for a "theoretical airway" with an internal perimeter of 10 mm (Pi10) within each lobe(249). This methodology has been previously employed and is described elsewhere(248).

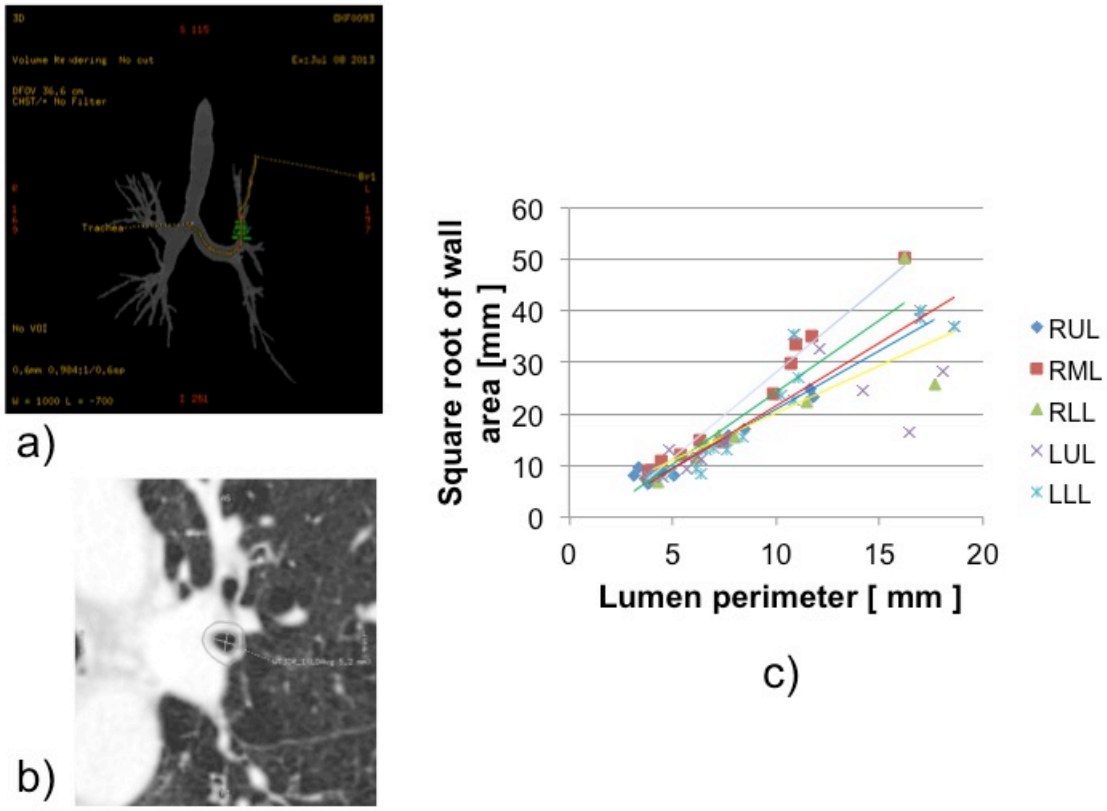

Figure 2.5: **Method used to quantify lobar airway wall thickness from QCT using Pi10.** Pi10 is the square root of wall area for a "hypothetical" airway with internal luminal perimeter of 10 mm. a) 3-D airway segmentation from volumetric CT data. b) Axial CT showing measurement of average airway diameter and wall area. c) Regression line used to determine Pi10 for each pulmonary lobe.

2.8 Nuclear medicine single-photon emission computed tomography (NM SPECT)

Patients with COPD [Section 4] completed combined nuclear medicine perfusion SPECT and quantitative CT (NM-Q SPECT/CT) on a 16-slice GE Discovery 670 SPECT/CT scanner (GE Healthcare, Milwaukee, USA). A subgroup of patients with COPD who were investigated for delayed HP ^{129}Xe-MR ventilation [Section

5] also completed combined nuclear medicine ventilation SPECT and CT (NM-V SPECT/CT) on the same GE Discovery 670 SPECT/CT scanner. Patients who completed NM SPECT/CT did not undergo separate QCT on the 64-slice GE Lightspeed scanner as detailed above [Section 2.7].

2.8.1 Nuclear medicine ventilation (NM-V SPECT)

For NM-V SPECT, patients were administered technetium-99 diethylene-triamine-pentaacetate (^{99m}Tc-DTPA) aerosol produced by a SmartVent™ delivery system (Diagnostic Imaging Ltd, Welford, UK). The dose used was 500 MBq ^{99m}Tc-DTPA in a volume of 0.8 mL. Patients were instructed to inhale ^{99m}Tc-DTPA aerosol via a mouthpiece, whilst wearing a nose-clip to prevent escape of the inhaled gas through the nose. Patients practised breathing through the tube beforehand to improve technique. Images were acquired for 20 seconds per step using low energy high-resolution (LEHR) collimators. The SPECT images were reconstructed onto a 64 x 64 matrix size using ordered subset expectation maximisation (OSEM) using the CT for attenuation correction (Xeleris 3 GE Healthcare, Milwaukee, USA). OSEM was performed with 2 iterations, 10 subsets using a Butterworth filter with critical frequency 0.55 cycles/cm and power 10.

2.8.2 Nuclear medicine perfusion (NM-Q SPECT)

For the NM-Q SPECT, subjects were injected with 200 MBq Technetium labelled macro-aggregated albumin (^{99m}Tc-MAA) and images acquired for 30 seconds per step using LEHR collimators. The SPECT images were reconstructed onto a 128

x 128 matrix size using ordered subset expectation maximisation (OSEM) using the CT for attenuation correction (Xeleris 3 GE Healthcare, Milwaukee, USA). OSEM was performed as described for NM-V SPECT above.

2.8.3 SPECT/CT

For QCT, images were acquired 60 seconds post-administration of 100 mL of intravenous iohexol contrast (equivalent to 300 mg of organic iodine per mL) with the following CT parameters: 1.25 mm slice thickness, current 50-400 smart mA, voltage 120kV, tube collimation 1.25 mm and beam pitch 0.938:1. QCT images were acquired post-intravenous contrast as part of the patient's clinical work-up according to local standard protocols.

NM-V/Q SPECT was acquired during tidal breathing and QCT was acquired during suspended inspiration following inhalation of 1 L oxygen via a Tedlar bag from FRC. Subjects underwent breath-hold training by radiographer instruction to ensure reproducibility.

2.8.4 NM-V/Q SPECT/CT analysis

NM-V/Q SPECT was analysed to determine lobar relative percentage ventilation and perfusion using newly available semi-automated software analysis tool (Hermes Medical Solutions, AB, Stockholm). Details of the 3-D method for regional analysis of combined NM-Q SPECT/CT are provided in Section 1 [Figure 1.2]. NM-V SPECT/CT was analysed in exactly the same way. The software

performed automated registration of CT and NM-V/Q and extraction of the lung boundaries on CT. Delineation of the pulmonary fissures was completed in a semi-automated fashion, whereby the operator (T. M.) placed markers on the fissures in up to 5 image slices. The software used the markers to generate an automated volume-of-interest (VOI) for each pulmonary lobe. The 3-D lobar volumes from CT were superimposed onto SPECT to determine the relative percentage of ventilation and perfusion respectively per lobe. The precise definition of lobar boundaries by localisation of the interlobar fissures enabled anatomically accurate regional relative percentage perfusion and ventilation measurements to be generated.

The QCT component of the examination was analysed as detailed in Section 2.7.1 to derive lobar %LAA and Pi10. To enable direct correlation with NM-V/Q SPECT lobar *relative* percentages, QCT-derived lobar percentage emphysema was converted to lobar *relative* percentage emphysema by expressing this as a percentage of total lung volume. Similarly for direct correlation between NM-V/Q SPECT and HP ^{129}Xe-MRI, HP ^{129}Xe-MRI lobar percentage ventilated volume was converted to lobar *relative* percentage ventilated volume by expressing this as a percentage of total lung volume.

2.9 Pulmonary function tests (PFTs)

Subjects completed pulmonary function tests (PFTs) on a Hypair compact plus flowmeter pulmonary function testing station (Medisoft group, Sorinnes, Belgium) and Masterscreen™ Body gold standard body plethysmography using

Sentry Suite® software (Jaeger™, Carefusion, Hoechberg, Germany). PFTs included spirometry (FEV_1, FEV_1/forced vital capacity - FVC) and plethysmography (residual volume expressed as a percentage of total lung capacity (RV/TLC), functional residual capacity - FRC and transfer factor of the lungs for carbon monoxide - TLCO). Individual recordings were compared to predicted values from standard published data.

For measuring the effects of intervention on HP ^{129}Xe-MRI [Section 6], only spirometry was performed i.e. plethysmography was excluded.

2.10 Dyspnoea-12 questionnaire

Participants completed the dyspneoa-12 questionnaire in reference to current level of breathlessness according to standard methodology(250, 251). The dyspneoa-12 questionnaire consists of 12 descriptor items on a scale of none (0), mild (1), moderate (2), or severe (3). An example questionnaire has been included [Appendix 1]. The questionnaire provides an overall score for breathlessness severity that includes seven physical items and five affective items. Total scores from the dyspnea-12 range from 0 to 36, with higher scores corresponding to greater severity of breathlessness currently experienced.

The time reference period for “these days” captures the current level of breathlessness experienced by patients as opposed to specifically on the day of the test or in response to a specific activity.

3 Chapter 3: Generating an atlas of normal lung function with HP ^{129}Xe-MRI

3.1 Background

3.1.1 Gravitational distribution of ventilation and perfusion within the lung

The primary function of the lung is gas exchange. Under normal conditions, passive mechanisms including the effects of gravity and pulmonary vascular branching structures(252) are considered most important. These factors achieve efficient ventilation-perfusion (V/Q) matching and gas exchange in the healthy lung(253). The distribution of regional ventilation and perfusion, and their dependence on gravity is an on-going area of research, primarily to improve the understanding of V/Q matching in respiratory disease states. Previous pulmonary modelling studies predicted that the gradient of intrapleural pressure would be more uniform in the prone position compared with the supine posture due to the shape of the lungs within the thorax(254). Therefore, it would follow, that the gravitational distribution of ventilation and potentially V/Q matching would also show greater uniformity when lying prone(255).

The underlying mechanism for improved gas exchange in the prone posture has not been fully elucidated(255, 256). Alternative factors excluding the effects of gravity have been suggested, including dorso-ventral differences in lung structure that balance out the gravitation forces in the prone posture(257). Emerging evidence suggests that the underlying structure of the bronchial and pulmonary vascular anatomy is a significant factor. The role of a non-symmetrical bronchovascular branching pattern in the lung may be more important than the gravitational influence on gas exchange. Despite the contentious debate(258-260), the general consensus remains that the predominant influence on ventilation and perfusion is gravity(256).

Several animal and human studies have demonstrated a dramatic difference in regional ventilation between prone and supine postures. Predominant dorsal ventilation was demonstrated when supine compared with more uniform ventilation distribution when prone(255, 257, 261-266). However, there are conflicting reports within the literature stating that there is no difference between the gravitational gradient of ventilation in the prone or supine position(267-269).

Gravitational gradients in pulmonary perfusion have also been reported in both postures, but was larger in the supine compared with prone posture(267, 268, 270-272). Conflicting studies have shown pulmonary perfusion to conform to a uniform distribution(255, 273), to follow similar gradients in both postures(270, 271) and produce a greater gradient(267, 274) in the prone than in the supine posture. The gravitation influence on pulmonary perfusion varies with lung

volume, being most significant at total lung capacity and least at residual volume(275).

In addition to ventilation and perfusion, the effect of gravity extends to other physiological factors including lung density and alveolar size(276, 277). Patient posture alters pulmonary function tests, due to position-dependent changes in respiratory dynamics(278). The gravitational influence on pulmonary ventilation and perfusion, and its dependence on posture(279) are clearly pertinent to imaging acquisition and interpretation. Cross-sectional imaging is commonly acquired in supine and prone postures, which differ from one another and also from the normal physiological upright position(279).

The application of HP ^{129}Xe-MRI for evaluation of regional lung function requires the definition of normal imaging parameters in healthy volunteers. It is important to demonstrate the sensitivity of HP ^{129}Xe-MRI to gravitational influences on the distribution of ventilation to provide evidence that the technique is robust and can be used in the clinical setting. Accurate interpretation of HP ^{129}Xe-MRI in respiratory disease requires the consideration of normal parameters and the presence gravitational gradients. This is particularly relevant when imaging respiratory diseases such as interstitial lung disease (ILD) where the disease process itself may predominate in the dependent lung regions. The potential to observe gravitational-dependent gradients in ventilation and ADC using HP ^{129}Xe-MRI in healthy individuals, may also allow assessment of disease states where gradients are altered, for example left-sided heart failure(280).

3.1.2 Imaging methods to determine V/Q distribution

The vast majority of studies that previously demonstrated altered distribution of ventilation and perfusion according to posture employed nuclear medicine(281-283) or wash-in/wash-out techniques. Ventilation assessment with radioisotope imaging is limited by spatial and temporal resolution. Xenon-enhanced CT (Xe-CT) provides improved spatial resolution and enables determination of ventilation from the wash-in and wash-out of stable ^{133}Xe(263, 284, 285).

Xe-CT was previously used to determine the distribution of xenon wash-out in the lungs of supine pigs(286). This study demonstrated increased ventilation in the more dependent lung regions, despite pulmonary gas content being reduced in these areas(286). Investigation of ventilation gradient in the antero-posterior (AP) direction using Xe-CT in humans confirmed these findings, showing higher ventilation in the dependent lung regions(287, 288).

Human studies involving nuclear medicine techniques, for example positron emission tomography (PET)(267) and single-photon emission computed tomography (SPECT)(268, 269) reported that the ventilation gradient due to gravitational effect was not significantly different between supine and prone postures. This conflicts with a large body of evidence and prior animal studies concluding that ventilation and perfusion is more uniform in the prone posture(255). The limited spatial and temporal resolution of nuclear medicine in evaluation of ventilation may have contributed to these inconsistent findings.

More recently, Henderson *et al.*(222) employed a novel functional lung MR technique [Section 1.3.9.3] involving arterial spin labelling for quantification of pulmonary blood flow(289-291) and inhaled 100% oxygen as a contrast agent to measure ventilation(213, 292). Single sagittal slice images were acquired for seven healthy volunteers and demonstrated the gravitational distribution of ventilation-perfusion ratio to be more uniform in the prone than supine posture.

3.1.3 Gravitational gradient in CT-derived lung density

A gravitational gradient in lung tissue density was reported in humans to be reduced in the prone compared to the supine posture, although present in both positions(254, 272). Using CT, Albert *et al.*(293) demonstrated up to 42% of the left lung and 13% of the right lung are subject to compression by the heart when lying supine. This effect was significantly reduced to less than 4% in both lungs when lying prone(293) consistent with a lung tissue AP gradient that is greater when adopting the supine rather than prone posture.

The observed lung tissue gradient is generally considered to be a result of heart and mediastinal compression on dependent lung(272). However, even when the heart and mediastinum are excluded in modelling studies, the effect remains present(254). Alternative explanations for the difference in lung tissue gradient between postures includes the shape of the lungs, which causes a larger volume of dependent lung in the supine compared with prone position(254).

CT-derived attenuation measurements demonstrated marked AP gradients on imaging acquired in full expiration(294), which are significantly diminished on imaging acquired at full inspiration(295). In a recent study, there was no significant difference in lung density gradient related to posture, however this only evaluated a single lateral sagittal lung slice(222). Collectively, these studies highlight the inherent limitations in lung tissue gradient evaluation with cross-sectional imaging, specifically that lung volume/inspiratory level must be controlled and full lung coverage acquired to ensure reliable results.

3.1.4 Gravitational distribution of ventilation in hyperpolarised ^{3}He-MRI

The dependence of ventilation on posture has been previously investigated in small cohorts of animals and humans using HP ^{3}He-MRI. Acquisition of a 3-D HP ^{3}He-MR ventilation sequence in rats demonstrated a linear ventilation gradient with elevated signal in the dependent regions when lying supine, whereas in the prone position the ventilation distribution was more uniform(160).

Small gravity dependent ventilation defects were observed in healthy volunteers in the most inferior, dependent regions of the lung when imaged supine with HP ^{3}He-MRI. These ventilation defects subsequently resolved on prone imaging(296). Similar findings have been reported in other small cohorts of healthy volunteers and patients with asthma(154).

Initial application of HP ^{3}He-MR ventilation imaging in subjects with and without respiratory disease showed a tendency towards higher signal intensities in the lower and posterior lung fields, although these were not quantified(153). These findings have been confirmed in twelve healthy volunteers including both smokers and non-smokers(297). Significantly higher HP ^{3}He-MRI ventilation signal was demonstrated in posterior compared to anterior lung quadrants in this cohort(297).

3.1.5 Gravitational distribution of ventilation in hyperpolarised ^{129}Xe-MRI

Early dissolved-phase HP ^{129}Xe-MR images in healthy volunteers showed increased signal intensity towards the dependent lung(199, 200). In contrast, three subjects with asthma and two with COPD showed spatially varied distribution of ventilation and gas transfer using HP ^{129}Xe-MRI(199). Kaushik *et al.* reported on signal intensity gradients in nine healthy volunteers imaged with an interleaved 3-D radial sequence both prone and supine(198). This ^{129}Xe-MR sequence enabled gaseous- and dissolved-phase image acquisition during the same breath-hold. Similar to previous trends, gaseous- and dissolved-phase signal intensities were greatest in the dependent, posterior lung and diminished in the anterior lung(198). However, contrary to the uniform distribution of ventilation shown with HP ^{3}He-MRI in animals imaged prone(160), in healthy volunteers the gaseous-phase ^{129}Xe-MR signal showed an intensity gradient that favoured the dependent lung even when prone(198).

3.1.6 Gravitational distribution of ADC values in HP ^{3}He-MRI

The distribution of ADC values relating to posture has been investigated in healthy volunteers and subjects with respiratory disease using HP ^{3}He-MRI(176, 298, 299). In the supine position, gravity appears to exert influence with consistent findings of an AP gradient and lower ^{3}He-MR ADC values in the dorsal regions in healthy volunteers (176, 298, 299). Further investigation demonstrated a larger AP gradient on scans obtained at full expiration(300), which reduced significantly on full inspiration(176, 301). Fichele *et al.*(298) evaluated the variation of ADC values in six healthy subjects in four postures: supine, prone, left-lateral decubitus and right-lateral decubitus. For all postures, lower ADC values were found in the dependent lung regions compared with non-dependent lung regions, the largest variation present in the left-lateral decubitus position(298). Comparison of healthy volunteers and subjects with COPD has shown a reduced(299) or even absent(176) AP gradient of ADC values in the presence of emphysema, presumed due to disease heterogeneity and gas-trapping. Even in the absence of airflow limitation, AP gradients of HP ^{3}He-MRI ADC are smaller in ex-smokers with abnormal TLCO compared with normal TLCO suggesting a high sensitivity of the imaging technique to regional gas trapping.

3.1.7 Gravitational distribution of ADC values in HP ^{129}Xe-MRI

The AP gradient of HP ^{129}Xe-MR diffusion-weighted imaging has been investigated in 7 healthy volunteers when supine only(242). This study including nine subjects with COPD, reported a decrease in ADC values in the AP direction

for healthy volunteers but nearly absent AP ADC gradient in COPD subjects(242). There are no reports within the literature regarding the distribution of HP ^{129}Xe-MRI ADC values in healthy volunteers when prone.

3.2 Hypothesis

To date, HP ^{129}Xe-MRI has only been acquired in small cohorts of predominantly healthy volunteers primarily to determine the safety and tolerability of the technique(147, 167). HP ^{129}Xe-MRI offers the potential for regional evaluation of ventilation, diffusion and gas transfer down to pulmonary lobe and segmental level. Accurate HP ^{129}Xe-MRI interpretation requires definition of the normal imaging parameters and demonstration that the technique is sensitive to the gravitational effects on lung function and therefore normal physiology. This will enable an atlas of normal lung function to be generated, against which imaging from other respiratory diseases can be directly compared to.

The hypothesis of this chapter is that HP ^{129}Xe-MR ventilation and diffusion-weighted imaging is sensitive to gravitational effects and shows a more uniform distribution of ventilation signal intensity level and ADC values in the prone compared to supine posture.

3.3 Aims

There are limited HP ^{129}Xe-MRI data in healthy volunteers and systematic evaluation of AP gradients for both ventilation and ADC in the same subjects is

sparse. HP ^{129}Xe-MR ventilation and ADC gradients have not previously been compared with CT-derived lung density gradients in healthy volunteers using imaging acquired at a single time-point.

The aims of this chapter are therefore: -

1. To establish the range of quantitative HP ^{129}Xe-MR imaging parameters (ventilation level and ADC) in healthy volunteers
2. To determine the AP gradient of HP ^{129}Xe-MR ventilation in supine and prone postures
3. To determine the AP gradient of HP ^{129}Xe-MR ADC values in supine and prone postures
4. To correlate the supine AP gradient of lung tissue density from QCT with the supine AP gradients of HP ^{129}Xe-MR ventilation and diffusion-weighted imaging in healthy volunteers.

3.4 Materials and Methods

3.4.1 Subjects

The study was approved by the National Research Ethics Service (NRES) South Central Committee (Berkshire) [Research ethics committee (REC) reference 11/SC/0487] and written informed patient consent was obtained.

Eleven adult males were enrolled into the study from a tertiary referral centre over a 20-month period between November 2013 and June 2015. The study

population were male (mean age 36.45±8.24 years, range 24-53 years, Table 3.1).

The study population consisted of healthy volunteers who had previous surgical resection of testicular germ cell cancer but no other associated comorbidity. Patients had not received chemotherapy or thoracic radiotherapy prior to study entry, did not have a significant smoking (≤10 pack years) or respiratory history, and had normal spirometry (FEV_1 ≥80% predicted for age and height), normal arterial oxygen saturations (SaO_2), no reported exercise limitation and a normal thoracic CT. Patients were recruited from this cohort as they were fit and healthy candidates who had already completed thoracic CT as part of their routine clinical care avoiding the requirement for additional exposure to ionising radiation.

The study inclusion criteria were: -

- Patients with previous histologically verified testicular germ cell tumour who have successfully undergone resection with no evidence of metastatic disease.
- Normal chest CT, confirmed subjectively by a Consultant thoracic radiologist with 15 years of experience and no evidence of emphysema on CT lung density mapping (≤8%)(302-304).
- Normal spirometry indices (>80% predicted FEV_1 for age and height), normal arterial oxygen saturations (SaO_2), normal carbon monoxide transfer factor, and no subjective exercise limitation.

- Current non-smokers with no significant smoking history (≤10 pack years) and no history of respiratory disease.
- World health organisation (WHO) performance status 0 [Appendix 2].
- Over the age of 18 and able to give informed consent.

Study exclusion criteria included a prior history of significant chest trauma or thoracic surgery, contraindications to MRI and epilepsy requiring on-going medical treatment or a seizure within the year prior to completion of study measures. The approved study protocol is appended [Appendix 3].

Participants completed pulmonary function tests (PFTs) and HP ^{129}Xe-MRI at a single time point. Thoracic QCT was acquired on a 64-slice GE Lightspeed scanner (GE, Milwaukee, USA) only if not previously obtained for routine clinical care within the last 12 months.

Full details regarding QCT [Section 2.7] and HP ^{129}Xe-MRI [Section 2.6] acquisition including ^{129}Xe polarisation and delivery [Section 2.4] are provided in Section 2.

3.4.2 HP ^{129}Xe-MRI analysis

The orientation and position of the flexible xenon chest coil remained at the same position relative to the magnet for all experiments. HP ^{129}Xe-MR ventilation and diffusion-weighted images were acquired in the cranial-to-caudal direction

in the axial plane, using a 15 mm and 30 mm slice thickness respectively to cover the whole lung. All other sequence parameters are as described in Section 2.6. HP ^{129}Xe-MRI was acquired in the axial plane to account for natural T_1 decay occurring during imaging acquisition, which would otherwise contribute to inaccurate analysis since the last image slice acquired would have lower signal intensity than the first. By reformatting axially acquired images to perform analysis in the coronal plane, T_1 decay is averaged throughout the coronal slices. This allows the effect of gravity to be determined without the loss of signal due to T_1 influencing the results.

The normal HP ^{129}Xe-MRI parameters were established by measuring the mean whole lung ventilation signal intensity level (VSI) and mean whole lung ADC value for each healthy volunteer.

Analysis of antero-posterior (AP) gradients in HP ^{129}Xe-MR ventilation and diffusion-weighted imaging were performed using the automated PTK software. PTK reformatted images acquired in the axial plane by dividing each image slice into 10 equal regions-of-interest (ROI) in the AP direction to generate 10 coronal bins [Figure 3.1]. Coronal bins were then summed in the cranio-caudal direction to generate coronal slices i.e. all coronal bins labelled A were summed to generate the most anterior coronal slice, coronal bins labelled B summed to generate the second coronal slice and the process repeated until coronal slices for full lung coverage had been generated.

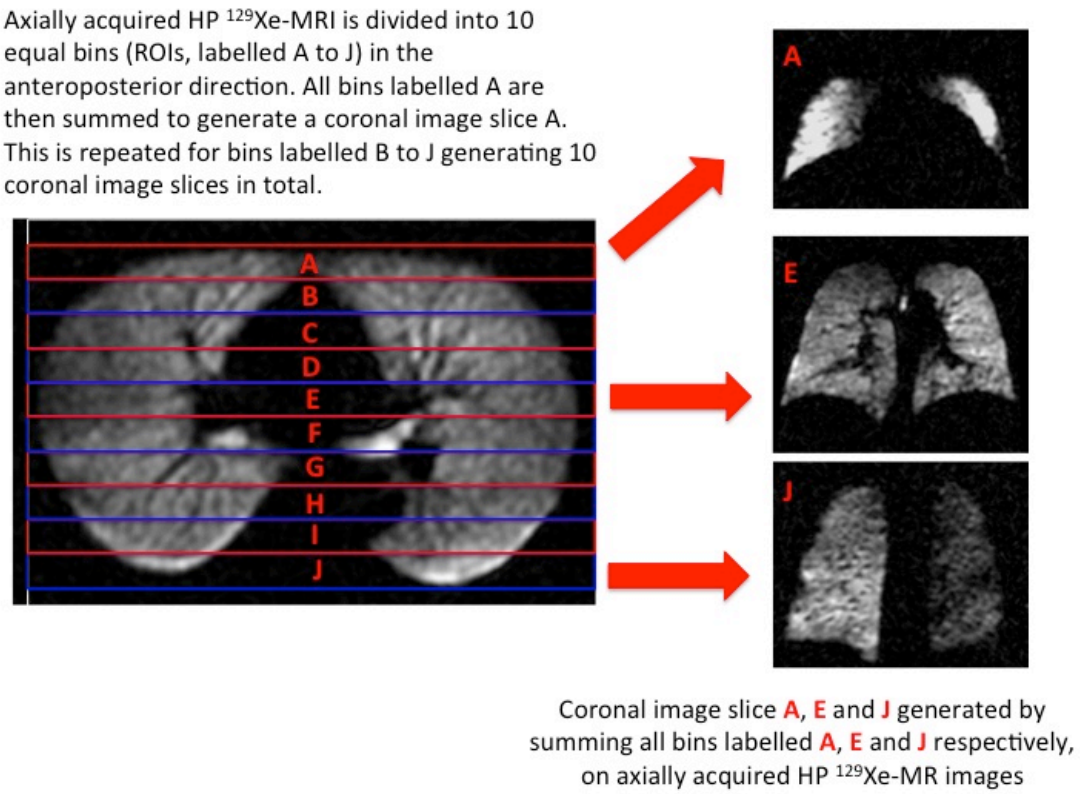

Figure 3.1: **Schematic of the PTK reformatting process for axially acquired HP ^{129}Xe-MRI to generate coronal image slices for analysis.**

For HP ^{129}Xe-MR ventilation imaging, PTK calculated the total VSI for each coronal slice generated in the AP direction for imaging acquired in the prone and supine posture. Irrespective of patient posture, ventilation signal intensity level per coronal slice was plotted against distance from lung edge in the AP direction i.e. most anterior (non-dependent) lung region to most posterior (dependent) regions. Regression analysis and the slope of the line of best fit were used to determine AP gradient values. The absolute difference in ventilation level in the AP direction (ΔVSI) was calculated by subtracting the ventilation signal intensity level of the most posterior (dependent) from the most anterior (non-dependent) coronal slice. This was completed for both supine and prone imaging.

Analysis of HP ^{129}Xe-MR diffusion-weighted imaging was completed in exactly the same way as described above but PTK calculated mean ADC values per coronal slice generated rather than ventilation level. ADC values per pixel were calculated according to published formula(242). The absolute difference of ADC in the AP direction (ΔADC) was calculated by subtracting the ADC value of the most posterior (dependent) from the most anterior (non-dependent) coronal slice.

3.4.3 QCT Analysis

QCT was acquired only in the supine posture. PTK was used to analyse lung density from QCT, in addition to percentage emphysema on a whole lung basis (%LAA) as detailed in the Section 2.7.1.

Mean whole lung density was determined. In addition, mean lung density (g/mL) was calculated for reformatted coronal image slices generated to match the ROIs used for HP ^{129}Xe-MRI gradient analysis. Mean lung density per coronal slice was plotted against distance from lung edge in the AP direction and the slope of the resulting regression line used to determine the AP gradient. The absolute difference in lung density in the AP direction (ΔCT density) was calculated by subtracting the mean density of the most posterior (dependent) from the most anterior (non-dependent) coronal slice.

3.4.4 Statistical Analysis

A priori analyses were completed to evaluate the influence of posture on HP ^{129}Xe-MR ventilation and diffusion-weighted imaging. To evaluate statistically significant differences between prone and supine postures (gradients), p values were calculated according to Student's paired t-test (Excel 2011, Microsoft) for: -

1. HP ^{129}Xe-MR ventilation signal intensity and ADC gradients in the supine compared with prone posture
2. HP ^{129}Xe-MR mean whole lung ADC and ΔADC supine compared with prone parameters
3. HP ^{129}Xe-MR mean whole lung ventilation signal intensity (VSI) and ΔVSI supine compared with prone parameters

A priori analyses using linear least squares regression and the Pearson's correlation coefficient were undertaken to determine the relationship between: -

1. HP ^{129}Xe-MRI VSI and ADC gradients and CT density gradients in the supine posture only
2. Mean whole lung HP ^{129}Xe-MRI VSI and PFTs
3. Mean whole lung HP ^{129}Xe-MRI ADC and PFTs.

P values less than 0.05 were considered significant.

3.5 Results

3.5.1 Subject demographics

In total, 11 subjects underwent HP ^{129}Xe-MR ventilation and diffusion-weighted imaging over a 20-month period. The demographics of the study population are shown in Table 3.1. HP ^{129}Xe-MRI was well tolerated by all subjects with no serious adverse events.

HP ^{129}Xe-MR ventilation imaging was successfully acquired both supine and prone in 10 subjects. HP ^{129}Xe-MR diffusion-weighted imaging was successfully acquired in 11 subjects in the supine posture and 9 subjects in the prone posture. Failure for acquisition of HP ^{129}Xe-MRI in these 3 subjects was due to technical issues relating to the MR sequence acquisition and co-ordination of subject breath-hold resulting in poor image quality not suitable for analysis. For this reason comparative analysis for imaging gradients was performed in 10 subjects for ventilation imaging and 9 for diffusion-weighted imaging. Descriptive statistics were completed for all data acquired.

QCT had been acquired in all 11 subjects within the preceding 12 months for routine clinical purposes. As such, repeat acquisition with breath-hold volume control i.e. FRC + 1 L could not be performed due to the additional exposure to ionising radiation involved. QCT had been acquired at suspended full inspiration according to standard local protocols. QCT was included in analysis with the acknowledgement of significant variability in lung inflation level between

imaging modalities. For one healthy volunteer (OXN011), the QCT had been acquired at a different regional NHS Trust within the preceding 12 months. The images were therefore analysed for %LAA to confirm inclusion criteria and study eligibility but not for QCT density, ΔQCT density or QCT density AP gradient as the CT scanner, image acquisition parameters and lung inflation level were not equivalent to standard departmental protocols.

Pulmonary function tests were completed in 11 volunteers. The plethysmography equipment was broken on the study visit day for one subject (OXN014). Therefore, all pulmonary function parameters excluding RV/TLC and FRC were obtained in this individual.

Table 3.1: **Characteristics of study population**

Demographic	Characteristics of study population Mean (SD)
Sex	Male
Age (years)	36.5 (8.2)
Height (m)	1.81 (0.04)
Weight (kg)	96.2 (22.0)
FEV_1 (L, % predicted)	106.4 (16.2)
FVC	114.9 (15.2)
FEV_1/FVC (%)	81.5 (12.2)
RV/TLC (%)	36.5 (24.7)
FRC (L, % predicted)	115.3 (16.3)
TLCO (mmol/min/kPa, % predicted)	99.5 (9.1)
%LAA	0.7 (0.2/2.1)

If not otherwise stated, the figures are mean (SD)
FEV_1 = Forced expiratory volume in 1 second, FVC = Forced expiratory vital capacity, RV/TLC = Residual volume expressed as percentage of total lung capacity, FRC = Functional residual capacity, TLCO = Transfer factor of the lung for carbon monoxide, %LAA = Percentage low-attenuation areas less than -950 HU

Table 3.2: **Pulmonary function test results and %LAA for each healthy volunteer included in the study**

Patient ID	Age	FEV_1	FEV_1/FVC	RV/TLC	FRC	TLCO	%LAA
OXN002	37	73	65	32	80	108	2.08
OXN004	44	107	71	23	99	94	6.09
OXN005	53	108	72	29	132	109	0.29
OXN006	24	115	85	16	118	92	0.25
OXN007	32	142	92	22	140	96	3.98
OXN008	30	113	79	28	128	113	2.12
OXN011	41	109	64	27	113	101	0.72
OXN012	29	107	90	18	108	79	0.16
OXN014	32	90	105	-	-	100	0
OXN015	33	110	92	22	114	97	1.42
OXN016	46	96	81	28	121	105	1.09
Group Mean (SD)	36.5 (8.2)	106.4 (16.2)	81.5 (12.2)	36.5 (24.7)	115.3 (16.3)	99.5 (9.1)	1.56 (1.85)

FEV_1 = Forced expiratory volume in 1 second (L, % predicted), FEV_1/FVC = FEV_1/Forced expiratory vital capacity (% predicted), RV/TLC = Residual volume expressed as percentage of total lung capacity, FRC = Functional residual capacity, TLCO = Transfer factor of the lung for carbon monoxide, %LAA = Percentage low-attenuation areas less than -950 HU

Table 3.3: **HP ^{129}Xe-MR ventilation and diffusion-weighted imaging mean whole lung parameters in the prone posture**

Patient ID	VSI	ΔVSI	VSI AP gradient	ADC (cm^2sec^{-1})	ΔADC (cm^2sec^{-1})	ADC AP gradient
OXN002	_	_	_	0.022 (0.008)	0.048 (0.034)	-0.0007
OXN004	1.26 (0.65)	0.42 (0.30)	0.010	0.017 (0.003)	0.004 (0.003)	6×10^{-5}
OXN005	0.31 (0.06)	-0.10 (0.07)	0.006	0.038 (0.013)	-0.035 (0.025)	0.0011
OXN006	0.96 (0.41)	-0.44 (0.31)	0.027	0.025 (0.007)	0.020 (0.014)	-0.0004
OXN007	0.95 (0.31)	-0.58 (0.41)	0.028	0.022 (0.006)	0.035 (0.025)	-0.0002
OXN008	1.02 (0.40)	-0.79 (0.56)	0.038	0.029 (0.007)	-0.019 (0.014)	0.0002
OXN011	1.25 (0.54)	-1.00 (0.71)	0.057	0.032 (0.006)	-0.038 (0.027)	0.0003
OXN012	1.06 (0.44)	-1.16 (0.82)	0.057	_	_	_
OXN014	1.21 (0.72)	-1.78 (1.26)	0.103	0.033 (0.003)	-0.012 (0.008)	0.0001
OXN015	1.33 (0.67)	-0.91 (0.65)	0.060	0.035 (0.009)	-0.045 (0.032)	9×10^{-5}
OXN016	0.93 (0.38)	-0.85 (0.60)	0.052	_		_
Group mean	1.03 (0.27)	-0.72 (0.57)	0.044 (0.027)	0.028 (0.007)	-0.005 (0.032)	6.11×10^{-5} (0.0005)

Figures are mean (SD)
VSI = Ventilation signal intensity, ADC = apparent diffusion coefficient, AP = Antero-posterior, Δ = absolute change

Table 3.4: **HP ^{129}Xe-MRI and QCT mean whole lung parameters in the supine posture**

Patient ID	VSI	ΔVSI	VSI AP gradient	ADC (cm^2sec^{-1})	ΔADC (cm^2sec^{-1})	ADC AP gradient	QCT density	ΔQCT density	QCT density AP gradient
OXN002	_	_	_	0.019 (0.004)	-0.026 (0.018)	-4×10^{-5}	0.210 (0.025)	0.02 (0.014)	0.0005
OXN004	1.75 (1.00)	-2.47 (1.75)	0.134	0.019 (0.004)	0.002 (0.001)	-0.0004	0.167 (0.032)	0.07 (0.049)	0.0038
OXN005	1.03 (0.46)	-1.17 (0.83)	0.055	0.036 (0.007)	0.035 (0.025)	-0.0008	0.186 (0.030)	0.01 (0.008)	0.0045
OXN006	1.21 (0.44)	-0.79 (0.56)	0.054	0.021 (0.005)	0.006 (0.004)	-0.0003	0.185 (0.025)	-0.02 (0.014)	0.0037
OXN007	1.42 (0.54)	-1.18 (0.83)	0.084	0.023 (0.005)	-0.001 (0.001)	-0.0004	0.192 (0.030)	-0.01 (0.008)	0.0058
OXN008	1.22 (0.50)	-1.33 (0.94)	0.074	0.031 (0.005)	0.013 (0.010)	-0.0006	0.223 (0.031)	-0.06 (0.042)	0.0058
OXN011	1.87 (1.02)	-3.44 (2.44)	0.176	0.033 (0.006)	-0.014 (0.010)	-0.0003	_	_	_
OXN012	0.94	-1.22	0.043	0.033	-0.023	-0.0001	0.197	0.02	0.0046

	(0.33)	(0.87)		(0.005)	(0.016)		(0.031)	(0.013)	
OXN014	0.93 (0.32)	-1.04 (0.73)	0.044	0.030 (0.003)	0.011 (0.008)	-1×10^{-5}	0.258 (0.036)	-0.09 (0.060)	0.0059
OXN015	1.28 (0.74)	-1.87 (1.32)	0.101	0.033 (0.007)	0.016 (0.011)	-0.0007	0.153 (0.033)	0.01 (0.009)	0.0036
OXN016	0.92 (0.45)	-1.33 (0.88)	0.062	0.030 (0.004)	-0.015 (0.011)	3×10^{-5}	0.186 (0.028)	-0.003 (0.002)	0.0028
Group Mean	1.26 (0.32)	-1.59 (0.77)	0.082 (0.041)	0.028 (0.006)	0.0003 (0.018)	-3.29×10^{-4} (0.0003)	0.196 (0.028)	-0.005 (0.041)	0.0041 (0.0016)

Figures are mean (SD)

VSI = Ventilation signal intensity, ADC = apparent diffusion coefficient, AP = Antero-posterior, QCT = Quantitative computed tomography, Δ = absolute change

Table 3.5: **Pearson's correlation of whole lung HP ^{129}Xe-MR parameters and pulmonary function tests**

Pearson correlation coefficient (*r*=)	**HP ^{129}Xe-MRI mean VSI**		**HP ^{129}Xe-MRI mean ADC (cm^2sec^{-1})**		**QCT-derived mean lung density**
	Prone	Supine	Prone	Supine	Supine
QCT-derived mean %LAA	0.27 (p=0.45)	0.63 (p=0.05)*	-0.77 (p=0.01)*	-0.62 (p=0.04)*	-0.32 (0.37)
FEV_1 (L, % predicted)	-0.14 (p=0.71)	0.37 (p=0.29)	-0.07 (p=0.85)	0.05 (p=0.89)	-0.34 (p=0.34)
FVC (L, % predicted)	-0.06 (p=0.87)	0.62 (p=0.06)	0.17 (p=0.67)	0.37 (p=0.27)	-0.60 (0.06)
FEV_1/FVC (%)	0.22 (p=0.54)	-0.60 (p=0.07)	0.21 (p=0.59)	0.17 (p=0.61)	0.33 (p=0.35)
RV/TLC (%)ξ	0.16 (p=0.65)	-0.30 (p=0.40)	0.50 (p=0.17)	0.32 (p=0.34)	-0.0003 (p=0.99)
FRC (L, % predicted)ξ	-0.62 (p=0.05)*	-0.32 (p=0.37)	0.40 (p=0.29)	0.43 (p=0.18)	0.01 (p=0.97)
TLCO (mmol/min/kPa, % predicted)	-0.35 (p=0.32)	-0.003 (p=0.99)	0.36 (p=0.34)	0.11 (p=0.75)	0.26 (p=0.46)

ξ Data available in n=10, * Statistically significant p value, FEV_1 = Forced expiratory volume in 1 second, FVC = Forced expiratory vital capacity, RV/TLC = Residual volume expressed as percentage of total lung capacity, FRC = Functional residual capacity, TLCO = Transfer factor of the lung for carbon monoxide, %LAA = Percentage low-attenuation areas less than -950 HU, VSI = Ventilation signal intensity, ADC = Apparent diffusion coefficient.

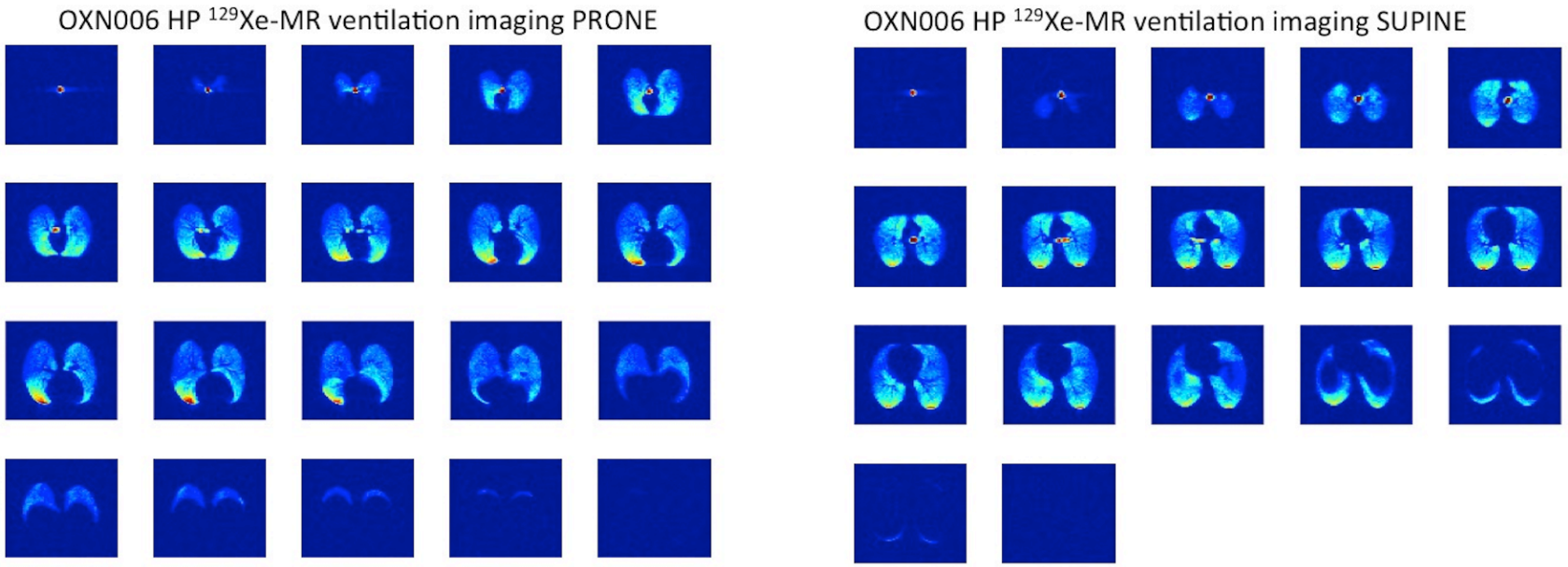

Figure 3.2: **Axial HP ^{129}Xe-MR ventilation imaging from OXN006 in the prone and supine posture.**

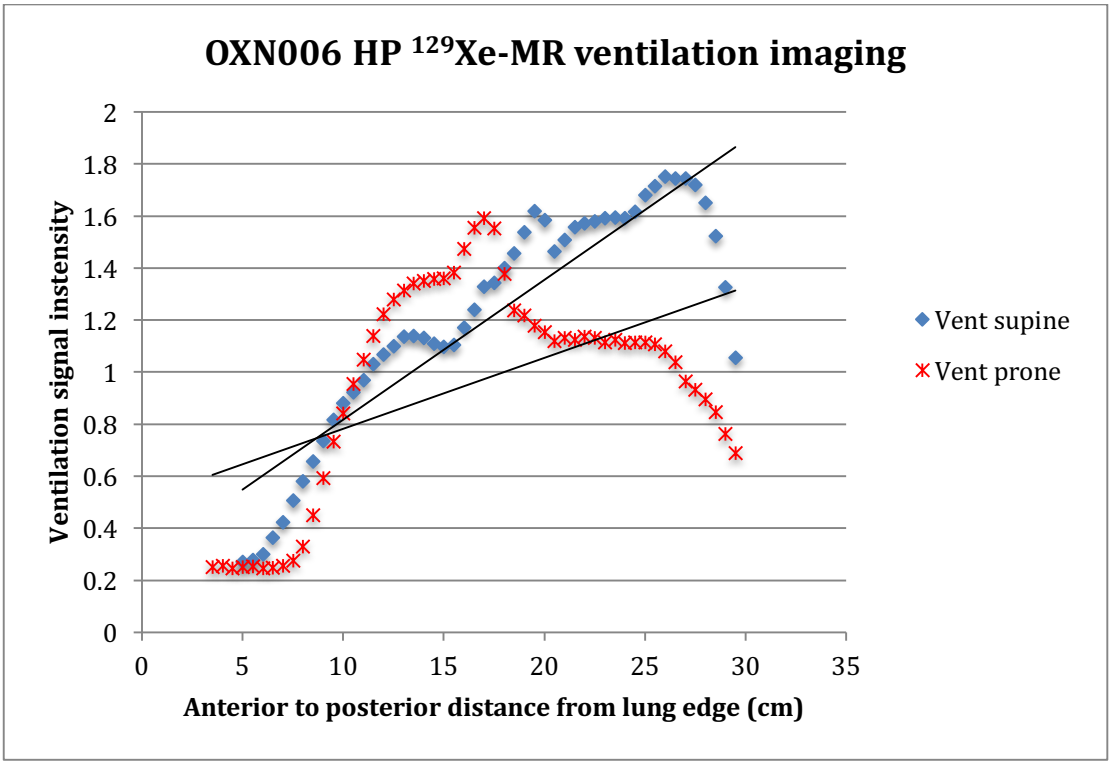

Figure 3.3: Graph showing ventilation signal intensity in the AP direction for HP ^{129}Xe-MR ventilation imaging acquired from OXN006 in the prone and supine posture.

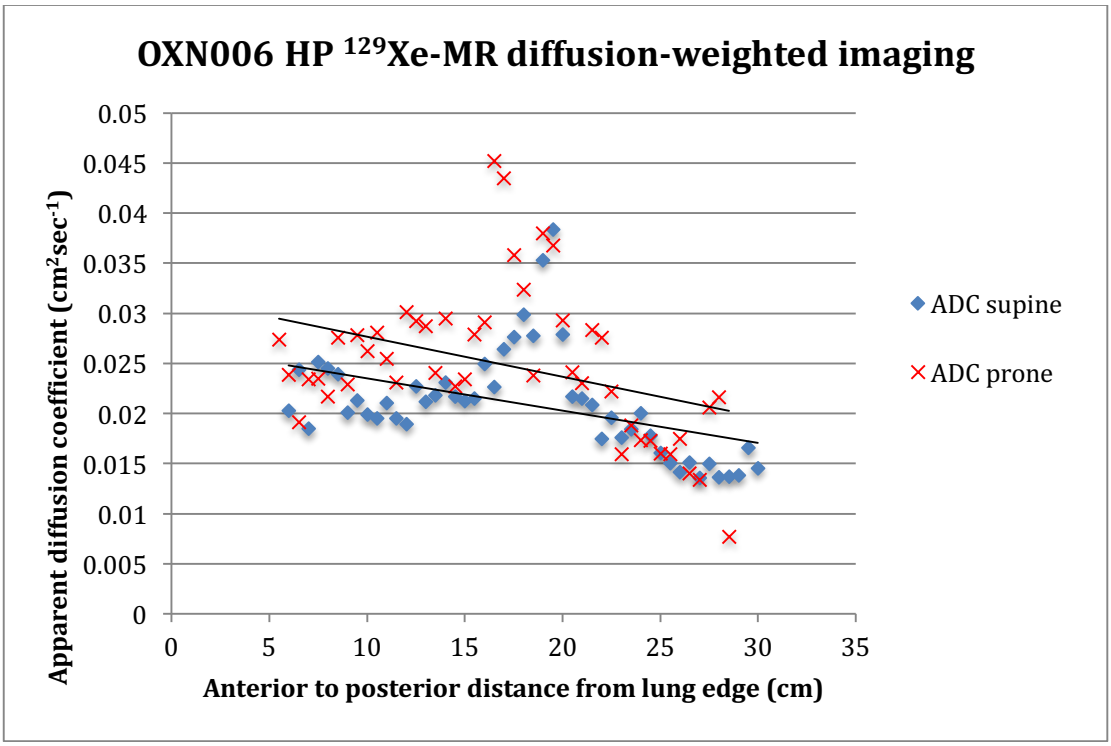

Figure 3.4: Graph showing mean ADC values in the AP direction for HP ^{129}Xe-MR diffusion-weighted imaging acquired from OXN006 in the prone and supine posture.

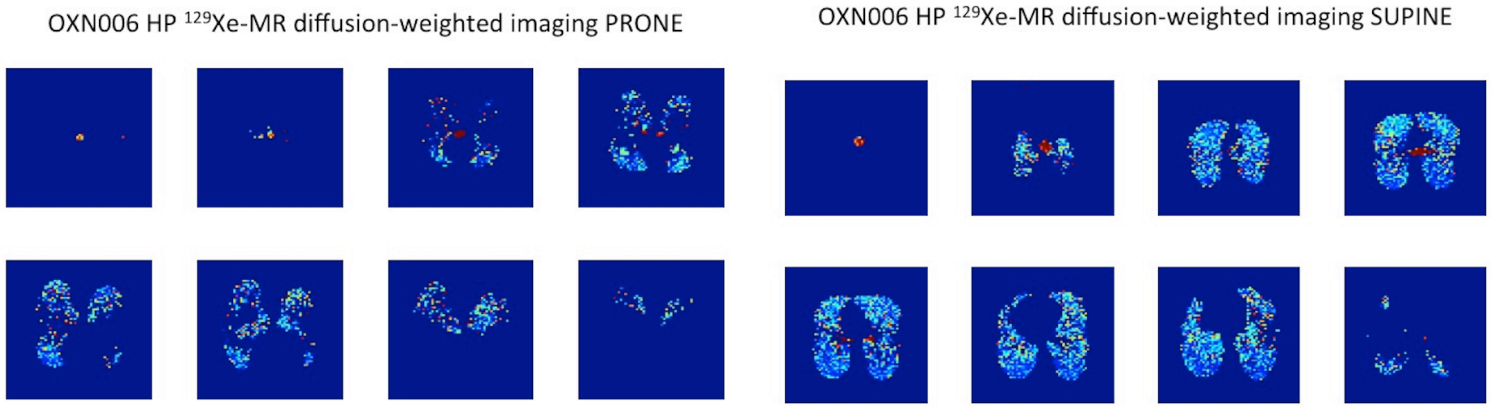

Figure 3.5: **Axial HP ^{129}Xe-MR diffusion-weighted imaging from OXN006 in the prone and supine posture.**

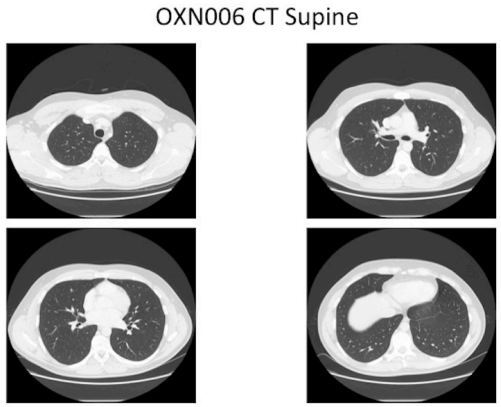

Figure 3.6: **Axial thoracic QCT (supine) from OXN006.**

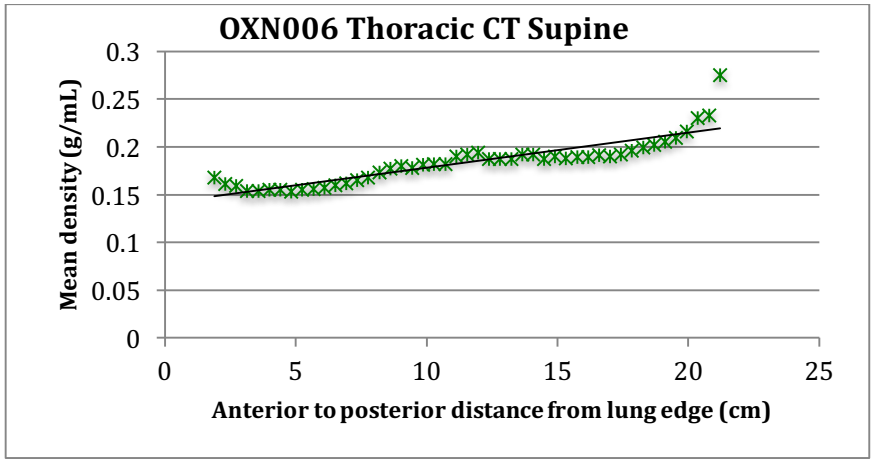

Figure 3.7: **Graph showing mean density in the AP direction for QCT acquired from OXN006 in the supine posture.**

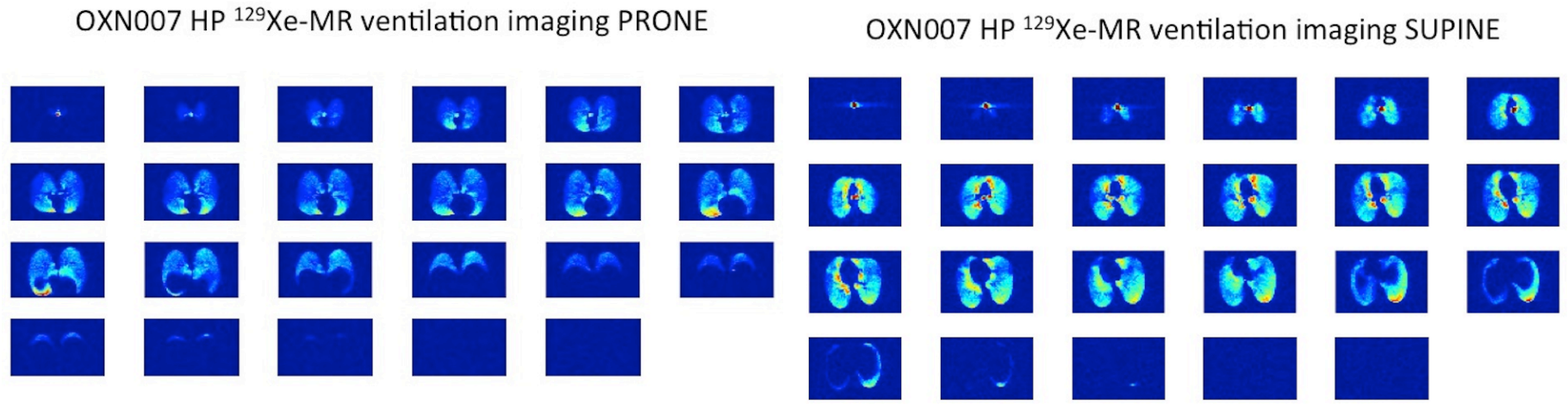

Figure 3.8: **Axial HP ^{129}Xe-MR ventilation imaging from OXN007 in the prone and supine posture.**

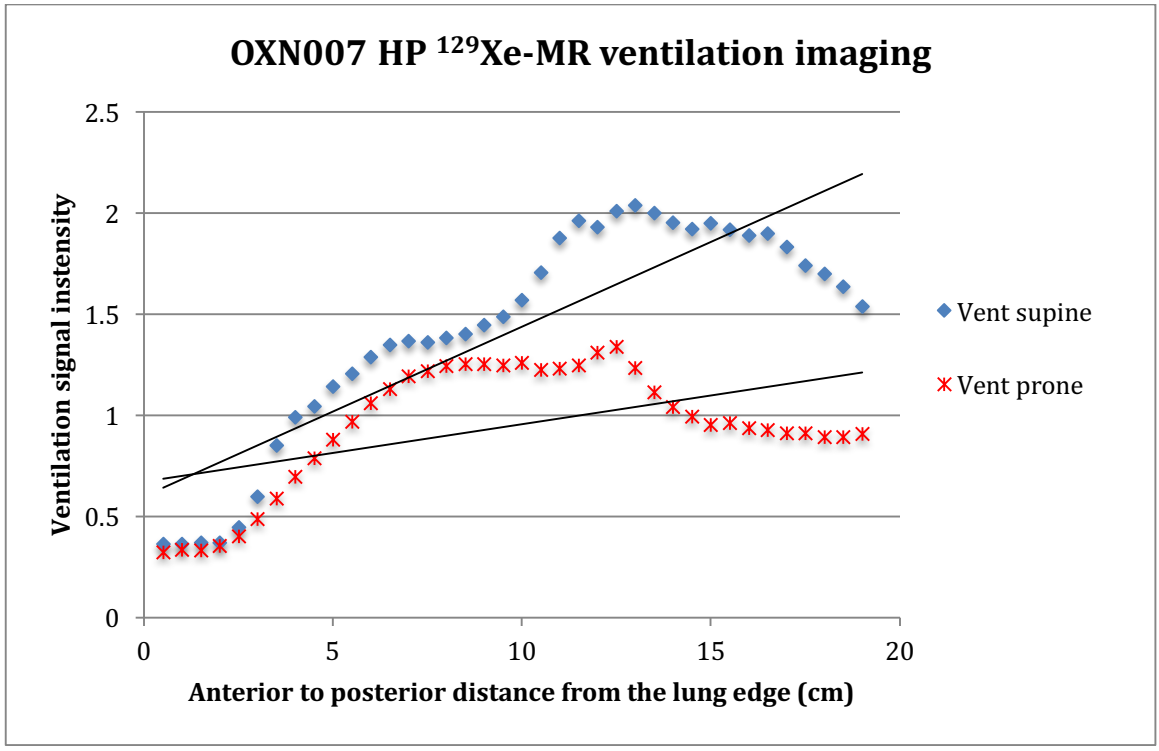

Figure 3.9: Graph showing ventilation signal intensity in the AP direction for HP ^{129}Xe-MR ventilation imaging acquired from OXN007 in the prone and supine posture.

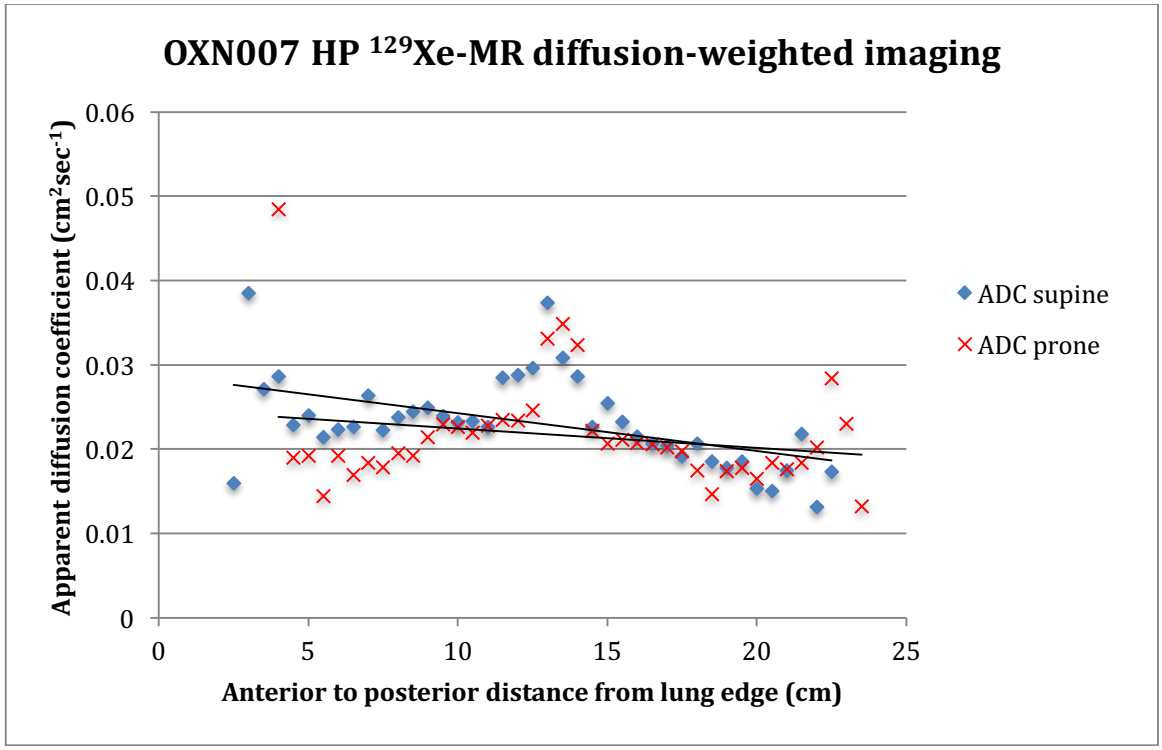

Figure 3.10: Graph showing mean ADC values in the AP direction for HP ^{129}Xe-MR diffusion-weighted imaging acquired from OXN007 in the prone and supine posture.

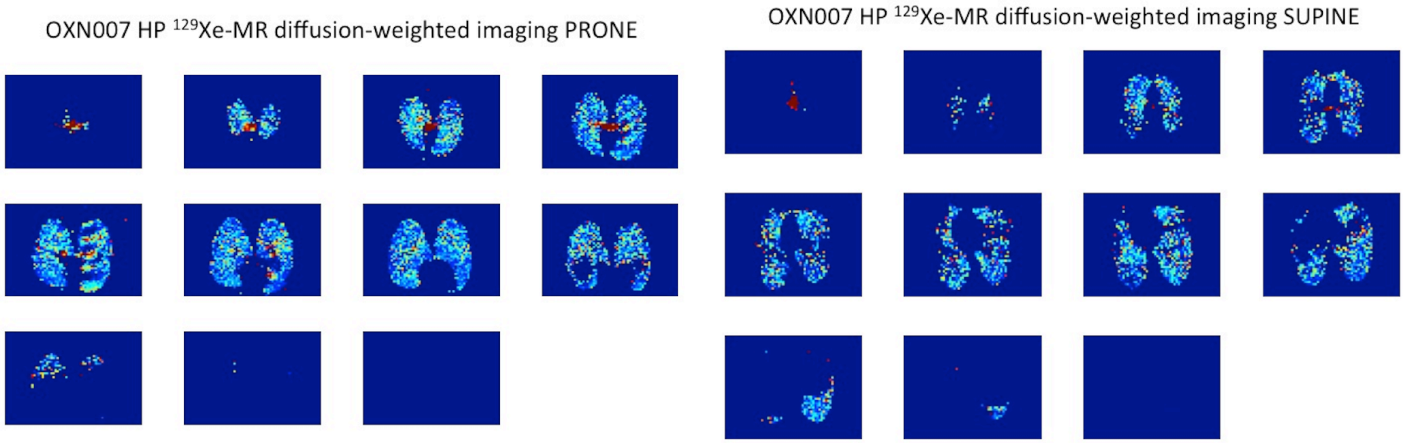

Figure 3.11: **Axial HP ^{129}Xe-MR diffusion-weighted imaging from OXN007 in the prone and supine posture.**

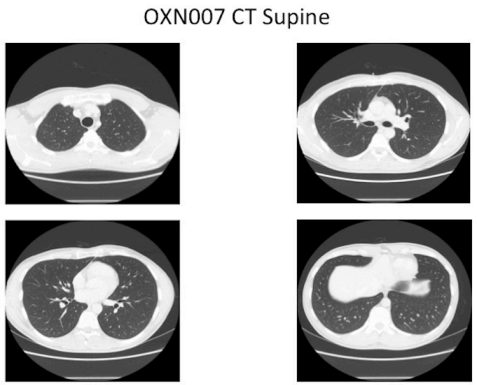

Figure 3.12: **Axial thoracic QCT (supine) from OXN007.**

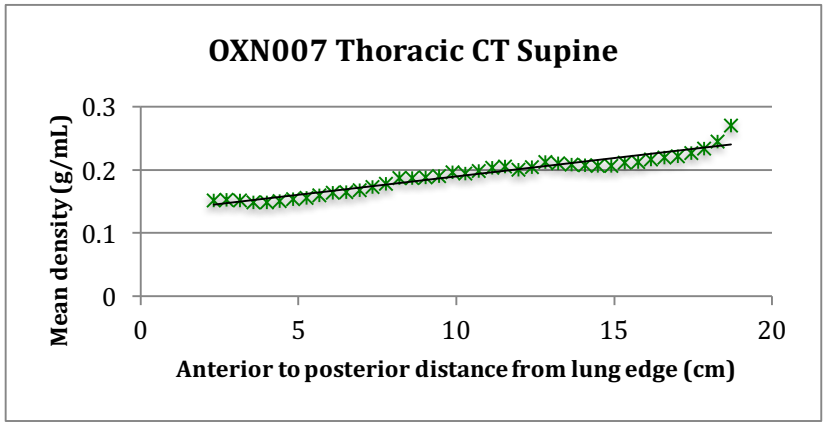

Figure 3.13: **Graph showing mean density in the AP direction for QCT acquired from OXN007 in the supine posture.**

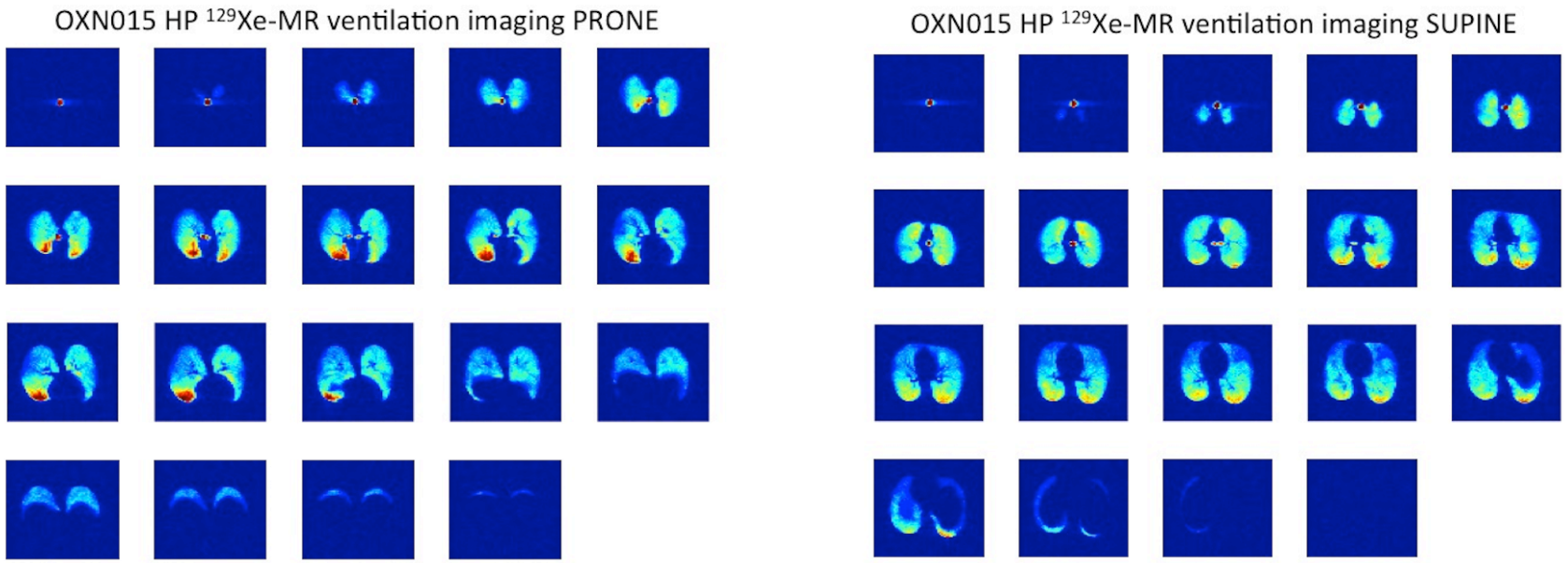

Figure 3.14: Axial HP ^{129}Xe-MR ventilation imaging from OXN015 in the prone and supine posture.

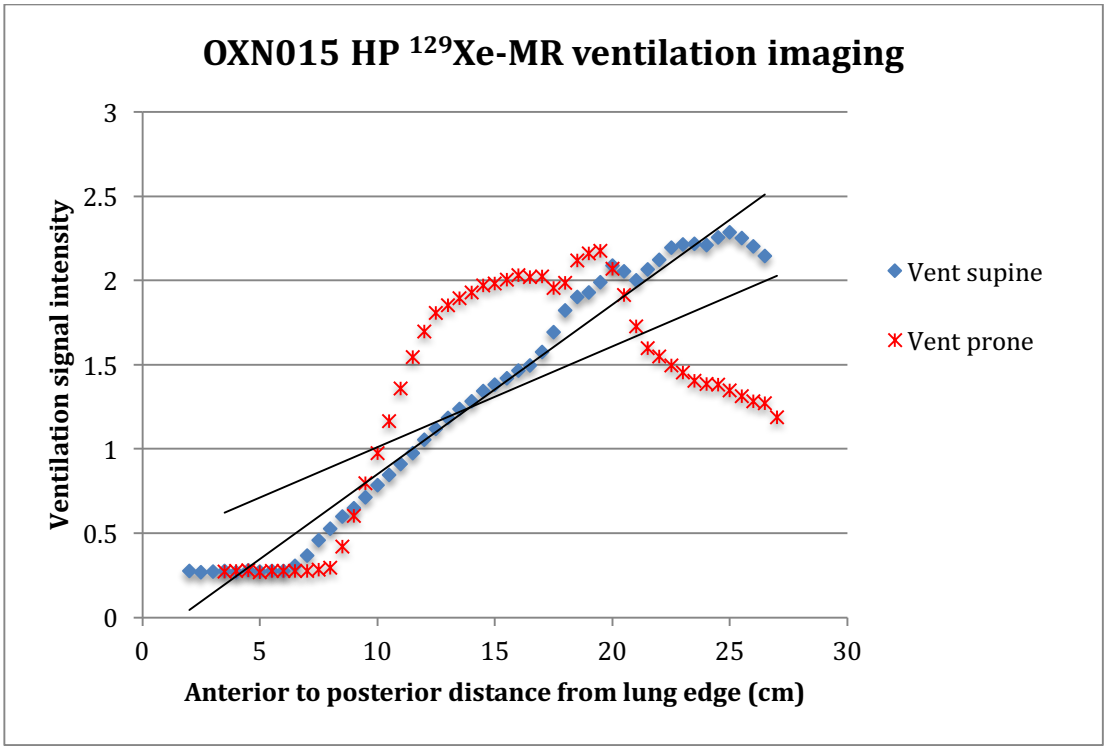

Figure 3.15: Graph showing ventilation signal intensity in the AP direction for HP ^{129}Xe-MR ventilation imaging acquired from OXN015 in the prone and supine posture.

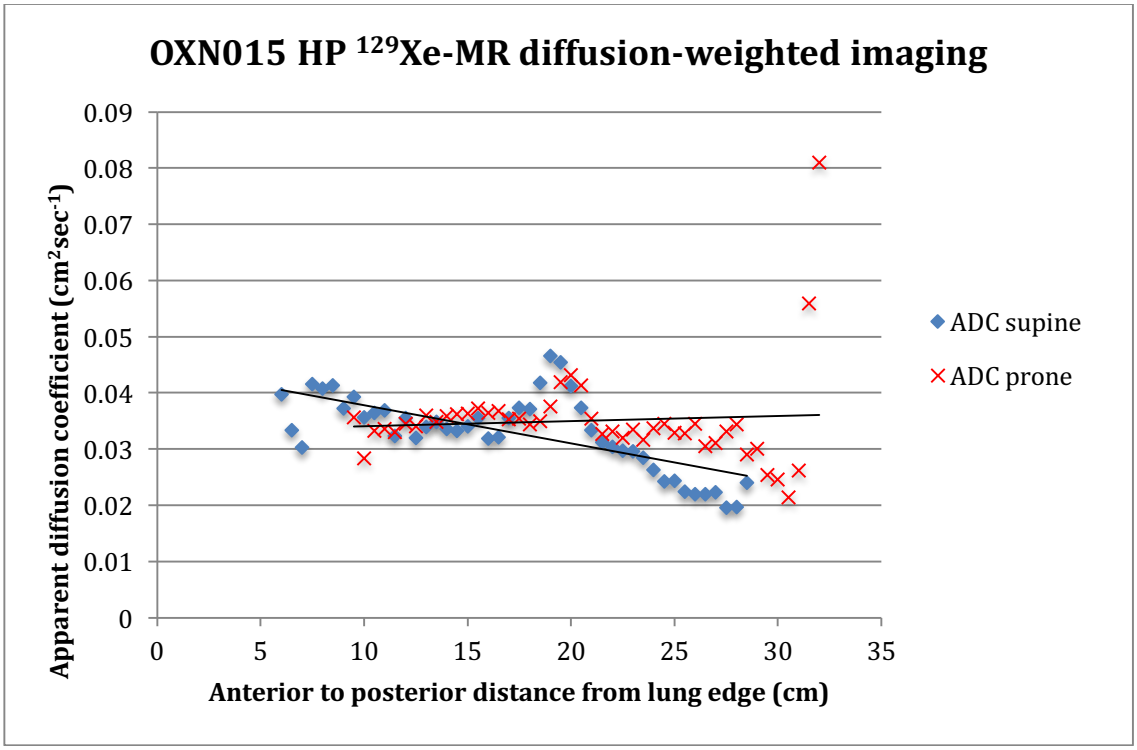

Figure 3.16: Graph showing mean ADC values in the AP direction for HP ^{129}Xe-MR diffusion-weighted imaging acquired from OXN015 in the prone and supine posture.

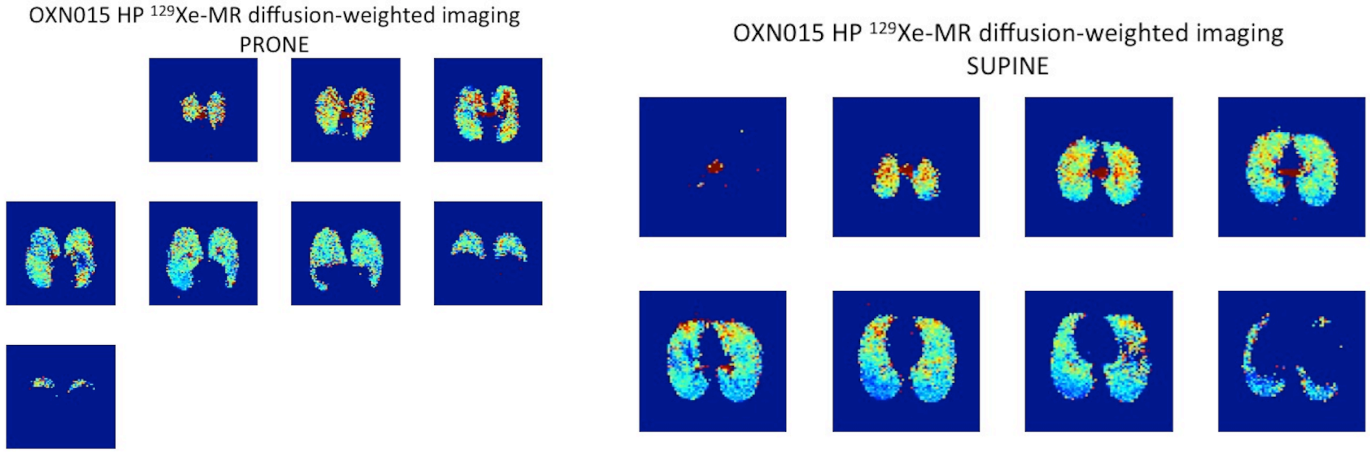

Figure 3.17: Axial HP ^{129}Xe-MR diffusion-weighted imaging from OXN015 in the prone and supine posture.

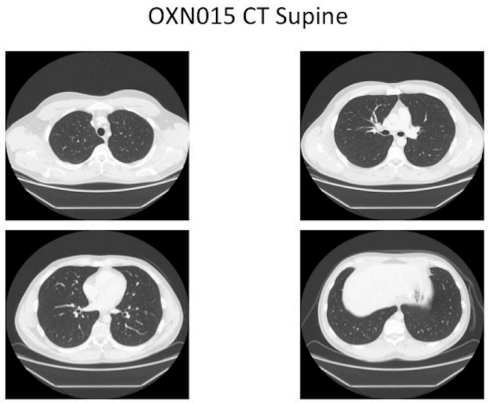

Figure 3.18: Axial thoracic QCT (supine) from OXN015.

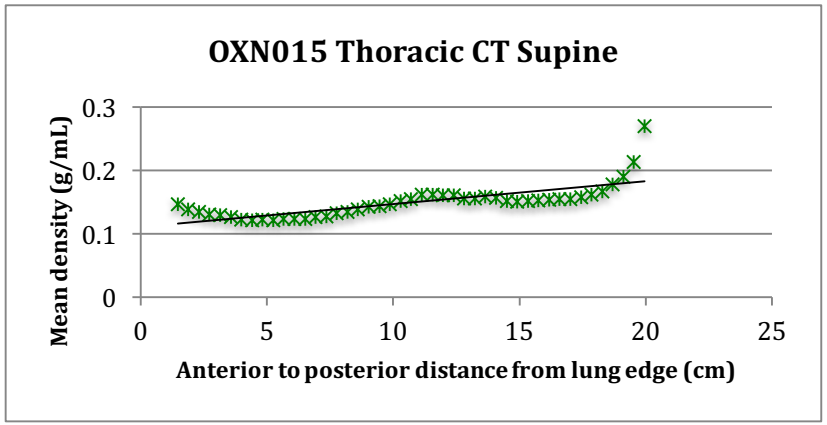

Figure 3.19: Graph showing mean density in the AP direction for QCT acquired from OXN015 (supine).

3.5.2 Whole lung HP ^{129}Xe-MRI VSI and ADC

Representative QCT, HP ^{129}Xe-MR ventilation and diffusion-weighted images acquired from three subjects and corresponding gradient data analyses are shown in Figures 3.2 – 3.4. Images and corresponding graphs for the other subjects are appended [Appendix 4].

The mean whole lung HP ^{129}Xe-MR ventilation signal intensity, ADC, QCT-derived density and percentage emphysema for each subject are shown in Table 3.3 for the prone position and Table 3.4 for the supine position. PFT results for each subject are included in Table 3.2.

There was no significant difference between the mean whole lung HP ^{129}Xe-MR VSI or ADC in supine and prone positions ($t(9)=2.12$, $p=0.063$ and $t(8)=0.64$, $p=0.54$ respectively).

3.5.3 Correlation between whole lung HP ^{129}Xe-MRI and QCT-derived emphysema

The correlation between mean whole lung imaging parameters, QCT-derived %LAA and PFTs are shown in Table 3.5.

There was moderate correlation between whole lung HP ^{129}Xe-MRI mean VSI with QCT-derived %LAA in the supine position ($r=0.63$, $p=0.05$) but no correlation in the prone position. There was moderate negative correlation

between whole lung HP ^{129}Xe-MRI mean ADC and QCT-derived %LAA in both prone and supine postures (r=-0.77, p=0.01 and r=-0.62, p=0.04 respectively).

Whole lung HP ^{129}Xe-MRI mean VSI correlated with FRC (r=-0.62, p=0.05) and showed a trend towards correlation with the PFTs; FVC (r=0.62, p=0.06) and FEV_1/FVC (r=-0.60, p=0.07). Whole lung HP ^{129}Xe-MRI mean ADC did not correlate with any PFTs. Although not statistically significant, mean whole lung QCT-derived density showed a trend towards correlation with FVC (r=-0.60, p=0.06).

3.5.4 HP ^{129}Xe-MRI antero-posterior (AP) gradients

The supine gradient and absolute difference in the AP direction for HP ^{129}Xe-MR ventilation signal intensity, ADC and QCT-derived density for each healthy volunteer are shown in Table 3.4. The prone gradient and absolute difference in the AP direction for HP ^{129}Xe-MR ventilation signal intensity and ADC values are shown in Table 3.3.

A trend for HP ^{129}Xe-MR ventilation signal intensity to increase from the anterior to posterior lung resulting in positive gradient was demonstrated for both supine and prone postures. However, the AP VSI gradient was more marked in the supine posture (mean=0.082, SD=0.041) compared with the prone posture (mean=0.044, SD=0.027). HP ^{129}Xe-MR AP ΔVSI was similarly larger in the supine compared with prone position. There was significant difference between the HP

^{129}Xe-MR AP VSI gradient when supine and prone (t(9)=2.23, p=0.027) and between HP ^{129}Xe-MR AP ΔVSI when supine and prone (t(9)=2.53, p=0.016).

For HP ^{129}Xe-MR diffusion-weighted imaging in the supine position, a common trend of decreasing ADC values and subsequent negative ADC gradients (mean=-3.29x10^{-4}, SD=0.00027) was shown in the AP direction for all subjects. In contrast, when prone, a general trend of more uniform ADC values and small positive ADC gradients (mean=6.11x10^{-5}, SD=0.00047) was shown in the AP direction. In the prone position, although the study population mean HP ^{129}Xe-MR AP ADC gradient was positive, three subjects (OXN002, OXN006 and OXN007) demonstrated a small negative HP ^{129}Xe-MR AP ADC gradient. Similarly, HP ^{129}Xe-MR ΔADC confirmed on average, a lower ADC value in the dependent lung regions when supine and higher ADC value when prone. There was no significant difference between HP ^{129}Xe-MR AP ADC gradients or AP ΔADC in the supine and prone posture (t(8)=1.65, p=0.069 and t(8)= 0.33, p=0.37 respectively).

There was no correlation between the supine HP ^{129}Xe-MR VSI or ADC gradient with QCT density gradient in the AP direction (*r*=-0.088, p=0.809 and *r*=-0.42, p=0.23 respectively).

3.6 Discussion

In this chapter, the normal parameters for HP ^{129}Xe-MR ventilation signal and diffusion-weighted imaging in healthy volunteers have been established. Antero-posterior gradients demonstrated with HP ^{129}Xe-MR ventilation imaging are significantly different in the supine and prone posture. In contrast, HP ^{129}Xe-MR ADC values appear to be more uniform within the lung. Although, an overall trend for negative HP ^{129}Xe-MR ADC AP gradients when supine and positive gradients when prone was found, the difference between postures did not reach statistical significance.

3.6.1 Whole lung HP ^{129}Xe-MR VSI and ADC are unchanged by posture

There was no difference in the study population mean whole lung HP ^{129}Xe-MR VSI in supine (mean= 1.26, SD=0.32) and prone positions (mean=1.03, SD=0.27). Previously published cohorts of healthy volunteers imaged with HP ^{129}Xe-MR ventilation imaging include 24 subjects during a technical run-in phase(167), investigated primarily for safety and tolerability of ^{129}Xe gas inhalation. The ventilation images were analysed using a visual score by thoracic radiologists (ventilation defect score percentage, VDS%) and automated segmentation (ventilation defect percentage, VDP) to quantify absence of ventilation signal. The reported mean VDS% was 3.03±5.17 and VDP% was 2.72±2.39 for healthy subjects (Male:Female - 8:16, mean age 32.2±11.4 years)(167). In a further small cohort of 8 healthy volunteers(305), the mean VDS% and VDP% (±SD) were

calculated to be 3.65±6.07 and 2.41±2.55 respectively, consistent with previous reports.

Image analysis of HP ^{129}Xe-MR requires optimisation and currently no standardised method has been widely adopted. The semi-automated segmentation approach used to analyse HP ^{129}Xe-MR ventilation imaging in this chapter, provides voxel signal intensity level values quantifying the degree of ventilation. Previous methodology has adopted a binary approach to ventilation signal i.e. a threshold is established above which voxels are deemed ventilated and below which voxels are deemed not ventilated. The current method uses a linear scale to capture the level of ventilation within each voxel. Whilst accounting for background image noise, the current method allows a more comprehensive and accurate analysis, since each voxel is given a specific level of ventilation rather than a binary outcome. Unfortunately this precludes direct comparison to previously reported ventilation defect scores or percentages. In the next chapter, the automated segmentation method presented is extended to provide ventilated volume percentage within the whole lung and per pulmonary lobe.

No statistical difference was observed between the group mean HP ^{129}Xe-MR ADC value in supine and prone positions ($t(8)=0.64$, $p=0.54$). The mean HP ^{129}Xe-MR ADC value obtained for this cohort when supine, although slightly lower, overlaps with the same standard deviation range reported by Kaushik *et al.*(146) (0.036±0.003 cm^2sec^{-1})(242). This would be expected since Kaushik *et al.* imaged a group of seven healthy volunteers (M:F - 3:4; mean age=32.9±11.3 years, range

24-56 years) with similar demographic data to the eleven subjects included in this chapter. The slight discrepancy observed is likely due to the different HP ^{129}Xe-MR diffusion-weighted MR pulse sequences used. A slightly higher diffusion-weighted b-value (b = 20.855 sec/cm^2) was used in this chapter and higher b-values have been previously reported to give lower ADC values(180).

The different imaging protocol employed by Kaushik *et al.*(146) may also provide an explanation for the observed difference. Kaushik *et al.*(146) acquired images limited to 10 slices in the coronal plane generally excluding the most anterior and posterior lung. In contrast, the method presented involves acquiring images in the axial plane (full lung coverage in the cranio-caudal direction) and then generating coronal bins for analysis. This ensures that the natural T_1 decay of ^{129}Xe gas within the lungs (~20 seconds) occurring during breath-hold image acquisition is taken into account during data analysis.

3.6.2 Whole lung HP ^{129}Xe-MRI correlates with QCT-derived emphysema

QCT-derived %LAA correlated moderately with whole lung HP ^{129}Xe-MRI mean VSI in the supine posture and mean ADC in both postures. Whole lung HP ^{129}Xe-MRI mean VSI correlated with FRC whereas mean ADC did not correlate with any PFTs. The relationship between HP gas MRI and %LAA and PFTs has been described in respiratory disease(169, 306-309) but literature in healthy volunteers is lacking. Direct comparison with previous HP gas MR studies is therefore not possible.

In a previous study comparing HP ^{129}Xe-MRI with HP ^{3}He-MRI in patients with COPD and healthy volunteers, both modalities showed significant correlation with FEV_1, FEV1/FVC and diffusion capacity of the lungs for carbon monoxide (DLCO)(310). However, differential results for healthy volunteers were not separately reported. A strong correlation between ^{3}He and ^{129}Xe ADC values and %LAA was also demonstrated in this study but only reported in patients with COPD(310). The relationship between HP gas MRI and QCT-derived emphysema in COPD has been corroborated by further studies(306, 308).

Moderate correlation between mean HP ^{129}Xe-MRI ADC values and three pulmonary function metrics; DLCO/alveolar volume (Va), FEV_1 (% predicted) and FEV_1/FVC in patients with COPD and ten age-matched healthy controls (AMCs) has been reported(146). Although not consistent with the current findings, the mean age (62.9 ± 7.6 years) of AMCs was considerably higher than participants included in this chapter.

3.6.3 The HP ^{129}Xe-MR ventilation antero-posterior (AP) gradient is more pronounced in the supine posture

A clear increase in HP ^{129}Xe-MR ventilation signal intensity was shown in the AP direction for both supine and prone postures. The results also demonstrated significantly greater HP ^{129}Xe-MR VSI AP gradient and ΔVSI in the supine compared to prone position. This is consistent with the general consensus of

increased ventilation in dependent lung regions when supine and a more uniform ventilation distribution when prone(255, 257, 261-266).

The gradient in pulmonary ventilation has been extensively reported and explained by the gradient of pleural pressure caused predominantly by the effects of gravity. The regional difference has been attributed to both the weight of the lung itself and differences between the shape of the lung tissue and surrounding pleural space(311). The spring-like self-deformation of the lung(312) considered the main determinant of ventilation gravitational gradient has been previously described as the 'slinky effect'(312, 313). In dependent regions of the lung, the transpulmonary pressure is reduced and lung tissue less expanded compared with non-dependent lung regions. The less expanded dependent lung tissue has greater compliance and consequently greater ventilation(312) when inspiration starts from FRC and measurements are made under static conditions(311), similar to the current study.

During quiet spontaneous breathing in the supine posture, the dependent lung is preferentially ventilated compared with anterior lung regions(314). This occurs despite the compression of dependent lung and consequent reduced size of air spaces. It would follow that the volume of gas and oxygen concentration within the compressed dependent lung is also reduced. The predicted rate of ^{129}Xe polarisation loss would therefore be lower in the presence of reduced oxygen(184, 315) and this may be a contributory factor to higher HP ^{129}Xe-MR signal in dependent lung regions. However, this factor alone would not explain the observed VSI gradients since the T_1 relaxation time of ^{129}Xe in alveolar air is

greater than the breath-hold required for image acquisition (~20 seconds). In addition to the 'slinky effect' and gradient in regional pulmonary compliance, other factors including dependent airways closure(292), the nonlinear nature of the lung pressure-volume curve and pulmonary vascular anatomy(256) have been proposed to contribute to regional ventilation distribution.

The gravitational gradient exhibited by pulmonary ventilation has been previously demonstrated with a variety of imaging techniques including nuclear medicine studies with ^{133}Xe(271), krypton isotopes(274), PET(267) and more recently with xenon-enhanced CT(288), oxygen-enhanced ^{1}H-MRI(292), and HP noble gas MRI in animals (160, 316).

Previous animal studies of HP ^{3}He-MR ventilation imaging demonstrated greater AP gradients in the supine compared to prone posture(160), in keeping with current findings. HP ^{3}He-MR ventilation imaging in 12 healthy volunteers also showed higher signal in posterior compared with anterior lung regions(297).

The distribution of ventilation signal relating to posture has not previously been specifically investigated with HP ^{129}Xe-MRI. However, HP ^{129}Xe-MR dissolved phase imaging has been employed to determine gas transfer within the lung. Dissolved-phase protocols involve an interleaved, three-dimensional radial MR sequence to image both gaseous- and dissolved-phase ^{129}Xe distributions within the same breath-hold. Gas-phase imaging enables assessment of ventilation distribution and therefore comparison with the current study findings. Kaushik *et al.* determined HP ^{129}Xe-MR gas-phase AP gradients in nine healthy

volunteers(198). Similar results to this study were shown, including increased gas-phase signal in the dependent lung regions and a significantly diminished AP gradient when prone(198).

3.6.4 HP ^{129}Xe-MR ADC values are more uniform within the lung

This study demonstrated a general trend for decreasing HP ^{129}Xe-MR ADC values in the AP direction when lying supine. This is consistent with reported findings in seven healthy volunteers by Kaushik *et al.*(146). This chapter extends previous reports by quantifying the HP ^{129}Xe-MR ADC AP gradient in the prone as well as the supine posture. The prone ADC AP gradient was smaller than the supine gradient and showed a general trend towards more uniform ADC values throughout the lung. However, the difference between AP ADC gradients in the supine and prone posture did not reach statistical significance.

The presence of AP gradients in ADC has been contributed to gravitational-dependent compression of the lung(271). The weight of the overlying lung parenchyma(271) and heart(293) result in compression of the dependent regions. In the healthy lung, this compression results in smaller airspaces in the most dependent areas of lung and consequently lower HP ^{129}Xe-MR ADC values in these regions. It is widely acknowledged that this effect is more pronounced in the supine compared with the prone posture(255, 257, 317).

Similar gravitational-dependent AP gradients have been previously confirmed in healthy volunteers using HP ^{3}He-MRI(176, 298, 299). The influence of four different postures; supine, prone, right lateral decubitus and left lateral decubitus on distribution of ADC values was investigated in six healthy volunteers using HP ^{3}He-MRI(298). In this study, the difference in mean ADC of two regions-of-interest (ROIs) comprising the uppermost, non-dependent and lowermost dependent lung was determined. The greatest variation between ROIs was demonstrated in the left lateral decubitus posture. A significant difference in ADC values was shown in the AP direction for supine posture whereas in the prone position within the left lung, although the mean ADC for the dependent ROI was lower than the non-dependent ROI, the difference was not statistically significant. These findings are consistent with the observed results in this chapter.

A further study determined the distribution of HP ^{3}He-MR ADC values in four centremost coronal slices of the lungs in 8 healthy volunteers and 9 subjects with COPD when supine(299). The absolute difference between anterior and posterior image slices, and ADC AP gradient was significantly greater in healthy volunteers than subjects with COPD(299). Regional gas trapping and heterogeneity of emphysematous tissue destruction in COPD is thought to counteract the gravitational compression of dependent lung regions and thus cause smaller ADC AP gradients in these subjects.

A similar negligible ADC AP gradient was observed by Diaz *et al.* in sixteen subjects with emphysema using HP ^{3}He-MRI(176). Comparison of HP ^{3}He-MR

ADC AP gradients in subjects with normal or abnormal TLCO, but no airflow limitation, demonstrated a significantly smaller gradient in those with abnormal TLCO(318). For this abnormal TLCO group, the AP gradient was similar to that in subjects with COPD, suggesting regional gas-trapping is present in subjects with abnormal TLCO despite the absence of airflow limitation(318). The potential for HP noble gas MRI ADC AP gradients to reveal regional gas trapping prior to abnormal spirometry may indicate a role for HP ^{129}Xe-MRI in early pulmonary disease detection.

Although HP ^{129}Xe-MR VSI and ADC AP gradients demonstrated an overall trend comparable between all subjects, they were unique to each individual and distinctly nonmonotonic (Figures 3.2-3.4b, c). A prominent increase in VSI and ADC value appears to be present in central image slices, likely representing the presence of ^{129}Xe in the conducting airways. Both VSI and ADC values would be expected to be higher in the trachea and main bronchi and cause the central peak observed. Nonmonotonic distribution of HP ^{3}He-MR ventilation and HP ^{129}Xe-MR gas-transfer has been previously reported in animal studies(160) and healthy volunteers(198) respectively.

3.6.5 QCT density increases in the AP direction

Only small AP gradients were shown for QCT density and although the trend for increasing density in the dependent lung regions parallels findings with HP ^{129}Xe-MR VSI and ADC when supine, there was no significant correlation. This is due to the different lung volumes the imaging modalities were acquired at; QCT

at suspended full inspiration and HP ^{129}Xe-MRI at FRC+1 L. Unfortunately, QCT had already been acquired according to standard protocols as part of the patient's clinical work-up and could not therefore be repeated due to additional exposure to ionising radiation. These data are supported by previous density measurements on CT(319), with observed AP gradients being marked on images acquired in full expiration(294) and much less prominent on images acquired in full inspiration(295). Similarly, HP ^{3}He-MR ADC AP gradients in eight healthy volunteers were significantly decreased at a larger inhaled lung volumes(176).

3.6.6 Limitations

The small number of healthy volunteers included in the study is a limitation. However, where previous human imaging studies have focussed on a single sagittal slice(222, 292) or incomplete pulmonary coverage(146), the current study involves complete lung coverage and therefore presents a more comprehensive analysis of gravitational gradients. Furthermore, the distribution of HP ^{129}Xe-MR ventilation and ADC values has been determined in the same healthy individuals when lying prone and supine.

Supine QCT had been previously acquired in all subjects at suspended full inspiration and therefore not at the same lung volume as HP ^{129}Xe-MRI. This limitation prevented meaningful comparative analysis between HP ^{129}Xe-MRI and QCT gravitational gradients. Despite this, a general trend for increased QCT-derived lung density in the AP direction was demonstrated. The breath-hold volume was controlled for in HP ^{129}Xe-MRI by practice breath-holds prior to and

radiographer coaching during imaging acquisition. As healthy volunteers completed both prone and supine imaging, for comparative posture analysis they acted as their own controls.

The analysis was completed using open source software (PTK) not commercially available, which may be considered another limitation. The lack of established HP ^{129}Xe-MRI analysis methodology presents a challenge when comparing the current findings with previous HP noble gas MR studies that used different parameters e.g. VDP. Despite the use of different imaging parameters, the results were consistent with expected gravitational effects.

Another potential limitation of image analysis was the inclusion of ^{129}Xe signal from the trachea and main bronchi in the central image slices. Although systematically included for all patients, the elevated ventilation and ADC values in the centre of the lung could have been accounted for by applying a quadratic rather than linear fit function to determine AP gradients. Alternatively, imaging could have been segmented to exclude the trachea and main bronchi.

3.6.7 Future work

The presented work could be extended to HP ^{129}Xe-MR dissolved phase imaging to determine ventilation and dissolved phase AP gradients in healthy volunteers. This would provide detailed *in vivo* information about regional ventilation and gas transfer within the lung. Evaluation of these functional parameters in states where normal physiological gradients are altered, for example, in congestive

cardiac failure, will improve the understanding of how ventilation, gas transfer and perfusion are affected in pulmonary disease at a regional level.

Current findings corroborate previous reports, suggesting that HP ^{129}Xe-MRI is a technique sensitive to normal physiology, hence is able to detect the expected gravitational gradients in supine and prone postures. The ability for HP ^{129}Xe-MRI to reflect normal physiology provides evidence to support its use in pulmonary disease and suggests it will be a reliable imaging modality to detect regional physiological disturbance.

3.6.8 Conclusion

In conclusion, this chapter has established normal parameters for HP ^{129}Xe-MR ventilation and diffusion-weighted imaging. HP ^{129}Xe-MR ventilation AP gradients were more marked in the supine than prone posture, whereas ADC AP gradients were more uniform. The gravitational-dependent trends observed with HP ^{129}Xe-MRI are consistent with the classic model of West and Dollery(317), predicting increased ventilation in the dependent lung regions. Future work should explore the potential for HP ^{129}Xe-MRI to improve our understanding of disease processes where normal gravitational-dependent gradients are disturbed, for example, heart failure and pulmonary congestion in end-stage renal disease.

4 Chapter 4: Lobar analysis of HP ^{129}Xe-MRI in chronic obstructive pulmonary disease (COPD)

4.1 Background

Chronic obstructive pulmonary disease (COPD) is a leading cause of morbidity and mortality(4), accounting for a significant economic and social burden worldwide(320). COPD is characterised by progressive but not fully reversible airflow obstruction and is caused predominantly by smoking(5). The diagnosis of COPD(5) is considered in patients over the age of 35 years with a risk factor including a smoking history and one or more of the following symptoms: -

1. Exertional breathlessness
2. Chronic cough
3. Regular sputum production
4. Frequent winter bronchitis
5. Wheeze.

The standard method for assessing lung function in COPD is spirometry, which combined with anatomical imaging (CT) can provide structural information. Spirometry remains pivotal in establishing a diagnosis and assessing severity in COPD despite being a poor predictor of disability and quality of life(321).

Current guidelines(5) recognise the limitations of spirometry, specifically FEV_1 in the assessment of COPD severity and recommend calculation of the multidimensional BODE index (body mass index, airflow obstruction, dyspnoea and exercise capacity). Previous studies demonstrated superiority of the BODE index compared with FEV_1 in: -

1. Prediction of acute exacerbations(322)
2. Prediction of number of hospital admissions(10)
3. Prediction of mortality in patients with COPD(9, 10, 323).

The provision of an accurate, robust regional imaging technique that can quantify heterogeneous disease severity and determine treatment response within different pulmonary lobes is needed. Emerging state-of-the art functional MRI techniques using gas contrast agents to address this need, include hyperpolarised gas MRI, oxygen-enhanced MRI and fluorinated gas MRI. Unfortunately, despite recent advances in gradient performance and sequence acquisition strategy, none of these functional pulmonary MRI techniques have been adopted into clinical practice. However, efforts to improve accessibility and development of regional analysis tools would help to bridge the gap required for translation.

4.1.1 HP ^{3}He-MRI in COPD

Previous investigation of COPD with HP gas MRI has been predominantly with ^{3}He(306, 307, 324-329). An initial study with HP ^{3}He-MR ventilation imaging demonstrated increased ventilation defects per slice (VDS) and ventilation defect

volume (VDV) in patients with COPD compared with healthy volunteers(326). HP ^{3}He-MRI has subsequently been used in a prospective multicentre study to identify patients with COPD and α_1-antitrypsin deficiency from age-matched never smokers(330). HP ^{3}He-MRI ADC values were reported more effective than HRCT-derived mean lung density measurements in distinguishing COPD patients from healthy controls(330).

It has been suggested that HP ^{3}He-MR ventilation imaging parameters may be useful for COPD severity(324) and longitudinal assessment(307, 331). Longitudinal changes in COPD have been evaluated with HP ^{3}He-MRI(307). Over an approximate 2-year period a significant increase was demonstrated in all HP ^{3}He-MRI parameters; VDV, ventilation defect percentage (VDP) and ADC values, whereas FEV_1 remained stable(307). The findings suggest that HP ^{3}He-MRI is sensitive tool for assessing COPD changes over time.

The strong correlation previously shown between HP ^{3}He-MR ADC values and TLCO in patients with COPD(306) and α_1-antitrypsin deficiency(332) indicate that diffusion-weighted imaging may provide a biomarker for detecting emphysema progression.

The simultaneous acquisition of regional HP ^{3}He-MRI pO_2 and diffusion-weighted imaging in a patient with severe COPD showed higher oxygen depletion rates in a region-of-interest with elevated ADC values(329). The accurate regional mapping of pO_2 and oxygen depletion rates and correlation

with degree of tissue destruction with HP ^{3}He-MRI may offer new insights into the efficiency of oxygen exchange.

Further studies have reported the sensitivity of HP ^{3}He-MRI to early lung microstructure changes(168, 169, 177, 178, 180, 181), correlation of HP ^{3}He-MR parameters with established measurements of pulmonary function(169, 306) and histologic measurements of emphysema(333). The reproducibility of HP ^{3}He-MRI in COPD has also been previously investigated(175, 176, 324, 326) with excellent same-day and 1-week follow-up repeated ADC measurements but more variable measures of ventilation distribution(324). HP ^{3}He-MRI has also shown regional improvements after bronchodilator use in COPD(334, 335).

4.1.2 HP ^{129}Xe-MRI in COPD

The previous use of HP ^{129}Xe-MRI in patients with COPD has been primarily to demonstrate safety and tolerability of the technique(147, 167). Ten patients with COPD (GOLD criteria I-III) demonstrated no serious adverse events or changes in vital signs after administration of 1 L hyperpolarised ^{129}Xe for breath-hold MRI(167). Similar to the other healthy volunteers and age-matched control subjects included in the study, 80% of patients with COPD experienced transient xenon-related symptoms, most commonly dizziness, paraesthesia, euphoria and hypoesthesia(167). These symptoms spontaneous resolved without clinical intervention, lasting approximately 2 minutes(167). The tolerability of HP ^{129}Xe-MRI was also evaluated in healthy volunteers and patients with respiratory disease following administration of 500 mL hyperpolarised ^{129}Xe gas mixed with

500 mL ^{4}He gas(147). The cohort included ten patients with COPD, who like other participants had no severe adverse events or withdrawals(147). The lower 500 mL hyperpolarised ^{129}Xe gas dose administered resulted in much fewer adverse events with only one transient-xenon related episode of light-headedness occurring in a patient with asthma(147).

High resolution imaging of pulmonary ventilation is possible with HP ^{129}Xe-MRI(147, 167, 238). Quantitative comparison of HP ^{3}He- and ^{129}Xe-MRI obtained within five minutes in ten patients with COPD showed significantly greater VDP obtained with ^{129}Xe(310). Greater HP ^{129}Xe-MRI VDP was speculated to arise from incomplete or delayed filling of distal lung regions due to the lower diffusion coefficient of ^{129}Xe relative to ^{3}He(310). The findings would suggest that airway narrowing preferentially limits the passage of ^{129}Xe gas compared with ^{3}He and implies HP ^{129}Xe-MRI is more sensitive biomarker for early disease. Subsequent investigation of the same patient cohort demonstrated a significant increase in pulmonary emphysema spatially correlated with ventilation defects detected by HP ^{129}Xe-MRI but not appreciated with HP ^{3}He-MRI(308).

HP ^{129}Xe-MR diffusion-weighted imaging has also shown utility in the assessment of lung microstructure(146, 238), with elevated whole lung mean apparent diffusion co-efficient (ADC) values present in COPD subjects corresponding to emphysematous tissue destruction.

4.1.3 HP ^{129}Xe-MRI analysis

A variety of ventilation scoring metrics have been developed for analysis of whole lung HP gas MR ventilation images, ranging from reader-based scoring(157), manual segmentation(325), semi-automated(334) to fully automated segmentation(336).

Initial analysis of hyperpolarised gas MRI focussed on reader-based scoring techniques. However, it has become clear that robust and automated quantification is required to enable extraction of functional lung imaging information and improve efficiency of data analysis. Woodhouse *et al.*(309) introduced ventilation defect percentage (VDP), the simplest parameter for quantification of hyperpolarised gas MR ventilation imaging. The method for calculating this established parameter involved delineation of ventilation defect boundaries, using a seeded region-growing algorithm to segment a proton MR image and confine analysis to the thoracic cavity(334, 335, 337). Kirby *et al.*(310, 334) extended analysis of whole lung HP ^{3}He-MR ventilation imaging by employing a k-means cluster technique. This allowed classification of HP ^{3}He-MRI voxel intensity values into clusters ranging from 1 to 5, representing gradations of signal intensity from no signal (cluster 1) to hyperintense signal (cluster 5). Although this technique considered spatial and contextual information on a whole lung basis, the ventilation signal per lobe was not defined.

Virgincar *et al.*(338) validated the semi-automated segmentation-based VDP analysis method in HP ^{129}Xe-MRI by showing significant correlation with an expert reader-based ventilation defect score percentage (VDS%). This chapter aims to extend previously described semi-automated segmentation methods by determining ventilation and ADC per lobe following automated non-rigid co-registration to proton MRI and QCT for delineation of lung fissure boundaries.

The feasibility of lobar and bronchopulmonary segmental ventilation assessment using HP ^{3}He-MRI has been reported in healthy volunteers and subjects with asthma(339, 340). However, methods specifically for lobar quantification of HP ^{129}Xe-MRI in subjects with COPD have not been reported, and it is in these patients that regional analysis may be of benefit when considering their suitability for treatments such as lung volume reduction surgery (LVRS), and endobronchial valve placement.

4.2 Hypothesis

The motivation for this chapter was to generate lobar measurements of HP ^{129}Xe-MRI ventilation and ADC using an automated analysis tool, which could then potentially be incorporated into the clinical workflow for treatment evaluation in patients with obstructive pulmonary disease.

Against this background, the hypothesis that lobar measurements of HP ^{129}Xe-MRI can be derived following automated non-rigid registration with ^{1}H-MRI and CT will be tested.

4.3 Aims

The aims of this chapter are: -

1. To generate lobar measures of HP ^{129}Xe-MR ventilation and diffusion-weighted imaging
2. To demonstrate reproducibility of the lobar HP ^{129}Xe-MRI measures generated
3. To compare lobar HP ^{129}Xe-MRI parameters with lobar QCT-derived emphysema and airway wall thickness
4. To compare whole lung HP ^{129}Xe-MRI parameters with PFTs in patients with COPD.

4.4 Materials and Methods

4.4.1 Subjects

The study was approved by the NRES South Central Committee (Berkshire) [REC reference 11/SC/0488], and written informed patient consent was obtained.

Between July 2013 and January 2015, twenty-two participants diagnosed with COPD were prospectively enrolled from a tertiary referral centre with the following inclusion criteria: -

- At least mild disease (stage II-IV on GOLD criteria classification [Appendix 5], FEV_1<80% predicted and FEV_1/FVC<70%)
- Significant smoking history (>15 pack years)
- Over the age of 18 and able to give informed consent.

Study exclusion criteria included the presence of co-existent cardio-pulmonary disease that predominated over COPD and might confound result interpretation (e.g. asthma, bronchiectasis, cystic fibrosis, lung cancer, uncontrolled heart failure, frequent unstable angina, respiratory muscle weakness). During the study period 15 patients did not fulfil the inclusion criteria; 6 patients were classified as stage I on GOLD criteria, 3 patients had a smoking history <15 pack years, 5 patients had predominant asthma and 1 patient had uncontrolled heart failure. The approved study protocol has been appended [Appendix 6].

The study population included fifteen males and seven females. The mean ± standard deviation and range of age in all participants was 66.5±7.3 years (51-77 years); in males, 65.7±7.8 years (51-77 years); and in females, 68.2±5.6 years (56-74 years). A Student's *t*-test was performed and demonstrated no significant difference in age between males and females (p=0.47).

Patients completed baseline multi-modality imaging at a single time point, including HP ^{129}Xe-MRI and NM-Q SPECT/CT, PFTs and dyspnoea-12 questionnaires. Static HP ^{129}Xe-MR ventilation and diffusion-weighted imaging was acquired. Study measures were completed during disease stability as defined by participants remaining exacerbation free for at least 4-weeks with no change to their regular medications prior to completion of study measures. All study measures, specifically imaging and PFTs were completed pre-bronchodilator to allow for direct comparison.

Image analysis was completed blinded to clinical data and PFTs. Full details regarding study measures and analysis are provided in [Section 2].

4.4.2 HP ^{129}Xe-MRI reproducibility

A subgroup of patients returned within 91.5±67.2 days (mean±SD) of initial baseline imaging for repeat acquisition of HP ^{129}Xe-MRI to enable assessment of reproducibility. Reproducibility imaging (HP ^{129}Xe-MRI$_R$) [Section 2.6.5] was only completed in patients with stable disease who remained exacerbation free since baseline imaging. HP ^{129}Xe-MR$_R$ ventilation imaging was acquired in 11 patients and HP ^{129}Xe-MR$_R$ diffusion-weighted imaging in 10 patients.

4.4.3 Statistical Analysis

A priori analyses were completed to evaluate the relationship between imaging parameters and PFTs. The Pearson's correlation coefficient was calculated between: -

1. HP ^{129}Xe-MRI lobar parameters and QCT-derived lobar %LAA
2. HP ^{129}Xe-MRI lobar parameters and QCT-derived lobar Pi10
3. HP ^{129}Xe-MRI lobar parameters and NM-Q SPECT lobar relative % perfusion
4. Whole lung HP ^{129}Xe-MRI parameters and PFTs
5. Whole lung HP ^{129}Xe-MRI parameters and dyspnoea-12 scores
6. Whole lung QCT-derived %LAA and PFTs
7. Whole lung QCT-derived Pi10 and PFTs.

For computation of lobar correlation coefficients, data from the five pulmonary lobes were included per patient. For HP ^{129}Xe-MR ventilation imaging, 110 lobar pairs were included and for HP ^{129}Xe-MR diffusion-weight imaging, 105 lobar pairs were included. All inference (p values) were completed on a per-pair basis and not per-patient. P values less than 0.05 were considered significant.

Bland Altman statistics were used to determine the reproducibility of static HP ^{129}Xe-MR ventilation and diffusion-weighted imaging. The mean, standard deviation, mean difference, 95% limits of agreement and coefficient of repeatability (CR) for HP ^{129}Xe-MR$_R$ lobar ventilated volume (%) and HP ^{129}Xe-MR$_R$ average lobar ADC (cm^2sec^{-1}) were established for the 11 and 10 patients who completed reproducibility imaging.

4.5 Results

HP ^{129}Xe-MRI was well tolerated by all patients with no serious adverse events. The demographics of the study population are shown in Table 4.1. Individual study measures are shown in Table 4.2. HP ^{129}Xe-MR diffusion-weighted imaging was not acquired in one patient due to xenon coil failure. Data analysis for HP ^{129}Xe-MR diffusion-weighted imaging was therefore completed in 21 patients. NM-Q SPECT was declined and not acquired in four patients. NM-Q SPECT correlations with HP ^{129}Xe-MRI were therefore completed in 18 patients. HP ^{129}Xe-MR ventilation imaging and other study measures were successfully acquired in all patients. Reproducibility HP ^{129}Xe-MR$_R$ ventilation and diffusion-weighted imaging was completed in 11 and 10 patients respectively. Images and

data analyses from each patient are shown in Section 4.5.1 – 4.5.3 and Appendix 7.

Table 4.1: Characteristics of study population

Demographic	Characteristics of study population Mean (SD)
Sex	Male 15, Female 7
Age (years)	66.6 (7.3)
Smoking pack-years	66.3 (47.3)
Smoking status	Current smoker 8, Ex-smoker 14
FEV_1 (L, % predicted)	54 (17.3)
FEV_1/FVC (%)	43.0 (11.0)
RV/TLC (%)	52.7 (9.4)
FRC (L, % predicted)	149.5 (26.9)
TLCO (mmol/min/kPa, % predicted)	56.7 (16.9)
GOLD stage II (%)	59.1
GOLD stage III (%)	36.4
GOLD stage IV (%)	4.5
%LAA	6.4 (1.6/15.5)
Pi10 (mm)	6.2 (0.8)
HP ^{129}Xe-MRI ventilated volume (%)	72.5 (14.5)
HP ^{129}Xe-MRI average ADC (cm^2sec^{-1})	0.052 (0.014)ξ

If not otherwise stated, the figures are mean (SD)

ξ Data only available for n=21

FEV_1 = Forced expiratory volume in 1 second, FVC = Forced expiratory vital capacity, RV/TLC = Residual volume expressed as percentage of total lung capacity, FRC = Functional residual capacity, TLCO = Transfer factor of the lung for carbon monoxide, GOLD = Global initiative for chronic obstructive lung disease, %LAA = Percentage low-attenuation areas less than -950 HU, given as median (25/75 percentile), Pi10 = Square root of bronchial wall area for a "theoretical airway" with an internal perimeter of 10 mm

Table 4.2: Whole lung imaging parameters and PFT results in patients with COPD

Patient	HP ^{129}Xe-MRI ventilated volume %	Mean HP ^{129}Xe-MRI ADC ξ (cm^2sec^{-1})	QCT-derived %LAA	QCT-derived Pi10 (mm)	FEV_1 % predicted	FEV_1/FVC (%)	RV/TLC (%)	FRC % predicted	TLCO	Dyspnoea-12 score
OXF0093	62.45	0.069	25.6	5.4	37	44	68	183	30	4
OXF0139	79.12	0.057	16.5	4.6	63	51	46	152	54	4
OXF0127	84.19	0.055	20.8	5.0	59	37	49	188	60	0
OXF0131	83.22	0.055	20.4	4.6	38	39	55	142	36	9
OXF0121	92.05	0.034	0.2	6.7	56	55	60	117	81	6
OXF0104	89.75	0.081	34	6.4	61	40	46	189	30	0
OXF0068	83.85	0.052	0.8	6.2	42	41	62	151	63	3
OXF0069	76.21	0.070	41.2	6.4	35	37	54	146	46	6
OXF0106	93.13	0.070	11.4	5.8	71	51	58	165	57	19
OXF0109	85.97	0.051	4.2	6.5	34	25	54	179	76	3
OXF0141	42.53	0.049	5.7	6.0	19	21	68	163	49	19
OXF0129	83.36	0.044	0.6	5.9	64	52	45	116	71	3
OXF0041	78.03	0.038	0.3	5.9	32	33	65	164	91	8
OXF0113	84.14	0.049	1.6	6.5	79	54	41	123	62	1
OXF0144	63.68	0.059	5.1	6.3	55	36	47	160	55	3
OXF0086	62.64	0.067	9.8	7.0	71	42	42	123	66	3
OXF0136	45.98	0.031	7.1	6.9	78	55	49	118	64	6
OXF0052	65.80	-	12.7	7.9	46	30	42	155	29	13
OXF0151	63.14	0.030	1.7	6.3	74	67	46	121	48	5
OXF0098	63.57	0.058	8.1	6.1	60	43	39	119	39	10
OXF0009	54.73	0.047	4.1	6.1	36	37	71	200	61	21
OXF0153	58.04	0.039	0.2	7.1	78	57	52	116	79	13

ξ Data available in n=21, FEV_1 = Forced expiratory volume in 1 second, FVC = Forced expiratory vital capacity, RV/TLC = Residual volume expressed as percentage of total lung capacity, FRC = Functional residual capacity, TLCO = Transfer factor of the lung for carbon monoxide, %LAA = Percentage low-attenuation areas less than -950 HU, given as median (25/75 percentile), Pi10 = Square root of bronchial wall area for a "theoretical airway" with an internal perimeter of 10 mm

4.5.1 Data analysis from COPD patient OXF0139

Table 4.3: **Lobar imaging parameters acquired from OXF0139**

Imaging parameter	Pulmonary lobe				
	RUL	RML	RLL	LUL	LLL
HP ^{129}Xe-MRI % ventilated volume	74.18	73.59	77.04	50.82	58.19
HP ^{129}Xe-MRI$_R$ % ventilated volume	66.63	69.06	85.23	47.25	65.99
HP ^{129}Xe-MRI ADC (cm^{2}sec^{-1})	0.054	0.040	0.043	0.038	0.053
HP ^{129}Xe-MRI$_R$ ADC (cm^{2}sec^{-1})	0.057	0.040	0.045	0.041	0.054
QCT-derived % LAA	19.4	10.9	13.0	16.8	21.6
QCT-derived Pi10 (mm)	4.7	5.3	4.2	5.0	4.4
NM-Q SPECT relative % perfusion	13.3	17.2	34.6	11.6	23.3

R Repeat HP ^{129}Xe-MRI measures to evaluate reproducibility
RUL = Right upper lobe, RML = Right middle lobe, RLL = Right lower lobe, LUL = Left upper lobe, LLL = Left lower lobe, %LAA = Percentage low-attenuation areas less than -950 HU, Pi10 = Square root of bronchial wall area for a "theoretical airway" with an internal perimeter of 10 mm

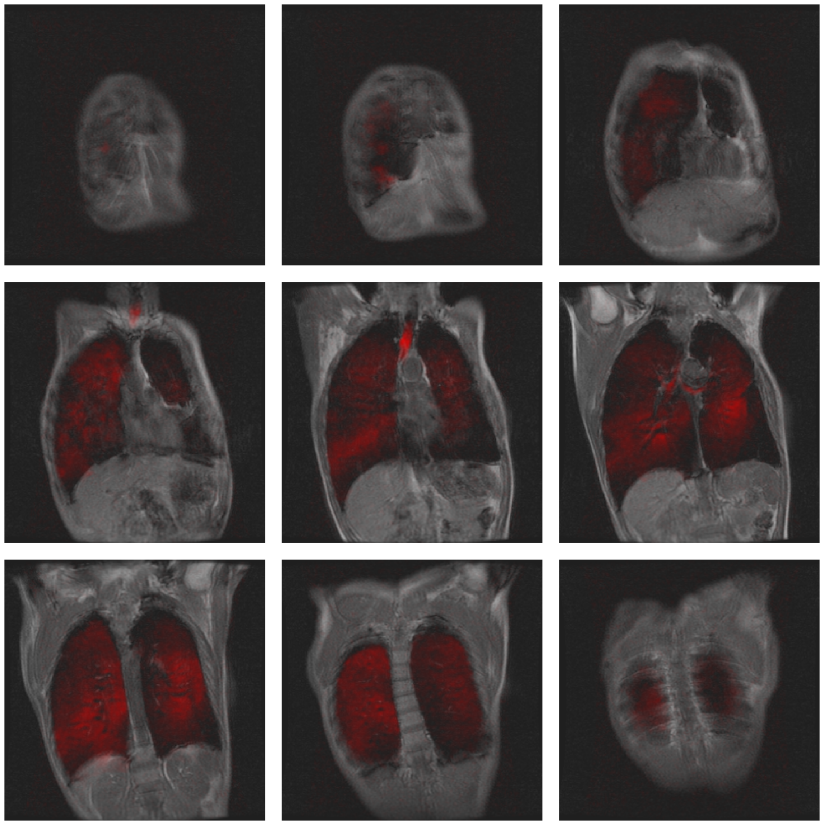

Figure 4.1: Coronal co-registered HP ^{129}Xe-MR ventilation imaging and proton MRI acquired from OXF0139. Co-registration to proton MRI enables the lung boundaries to be defined.

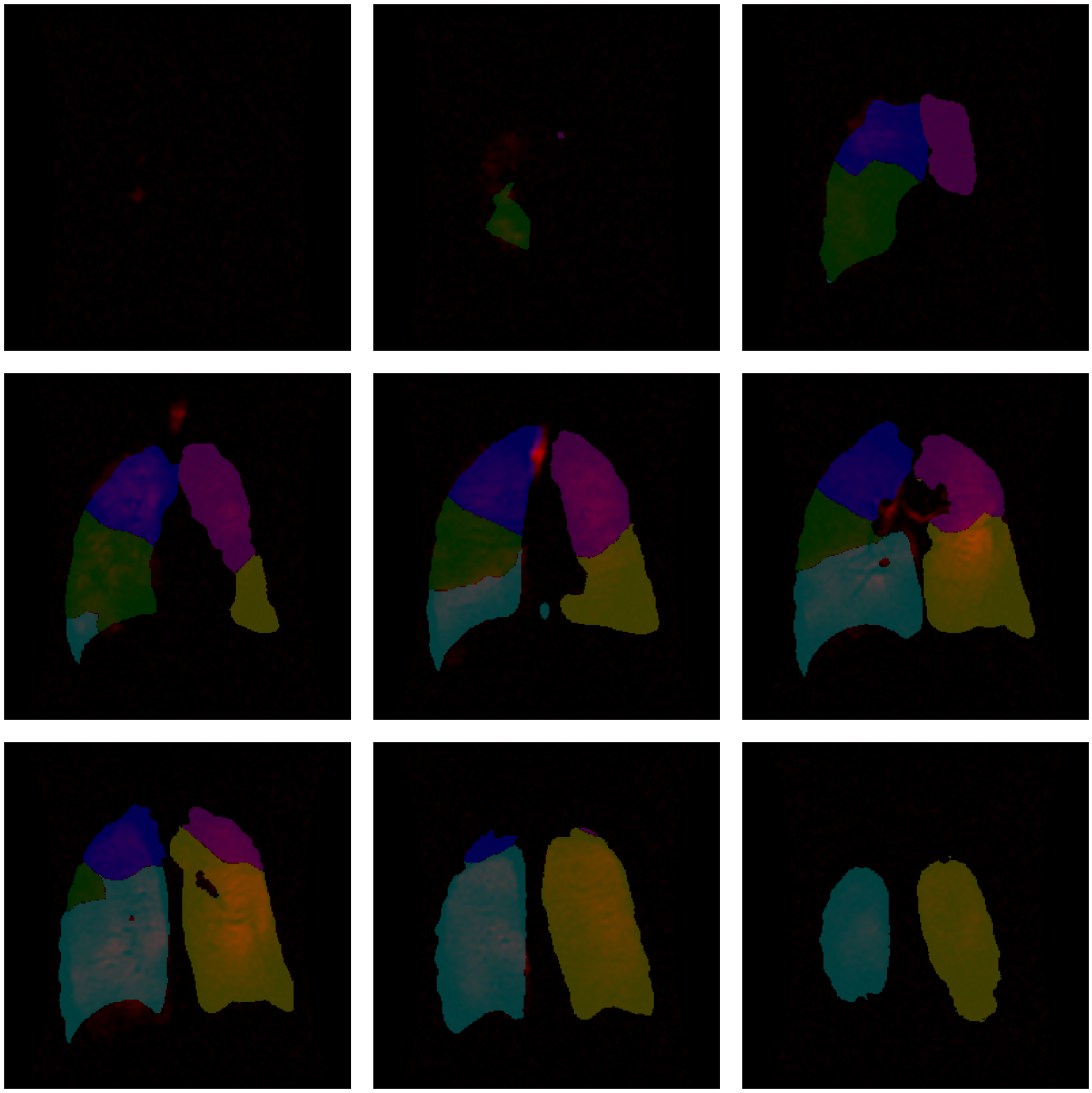

Figure 4.2: Non-rigid co-registration of coronal QCT to HP ^{129}Xe-MR ventilation imaging acquired from OXF0139. Co-registration to QCT enables the lobar boundaries (pulmonary fissures) to be defined.

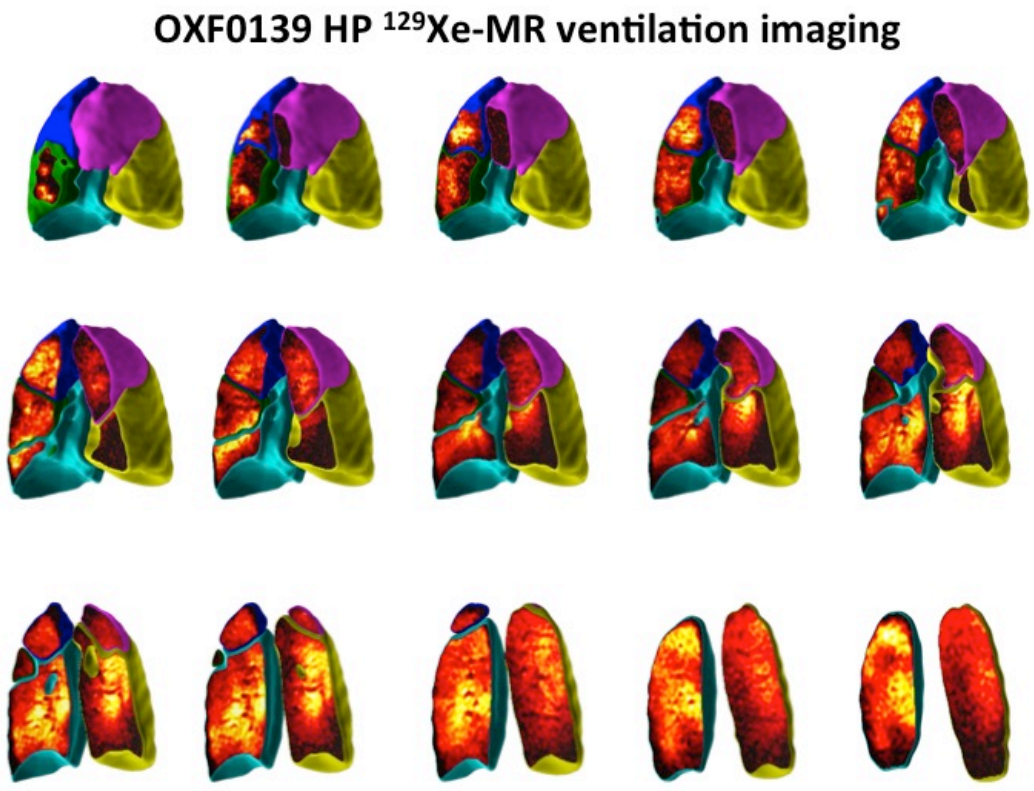

Figure 4.3: 3-D lobar HP ^{129}Xe-MRI ventilation imaging from OXF0139. Low signal intensity in the left upper lobe (pink) anteriorly indicates relatively poor ventilation in this region. In contrast, high signal intensity in the right lower lobe (cyan) is consistent with good ventilation in this region.

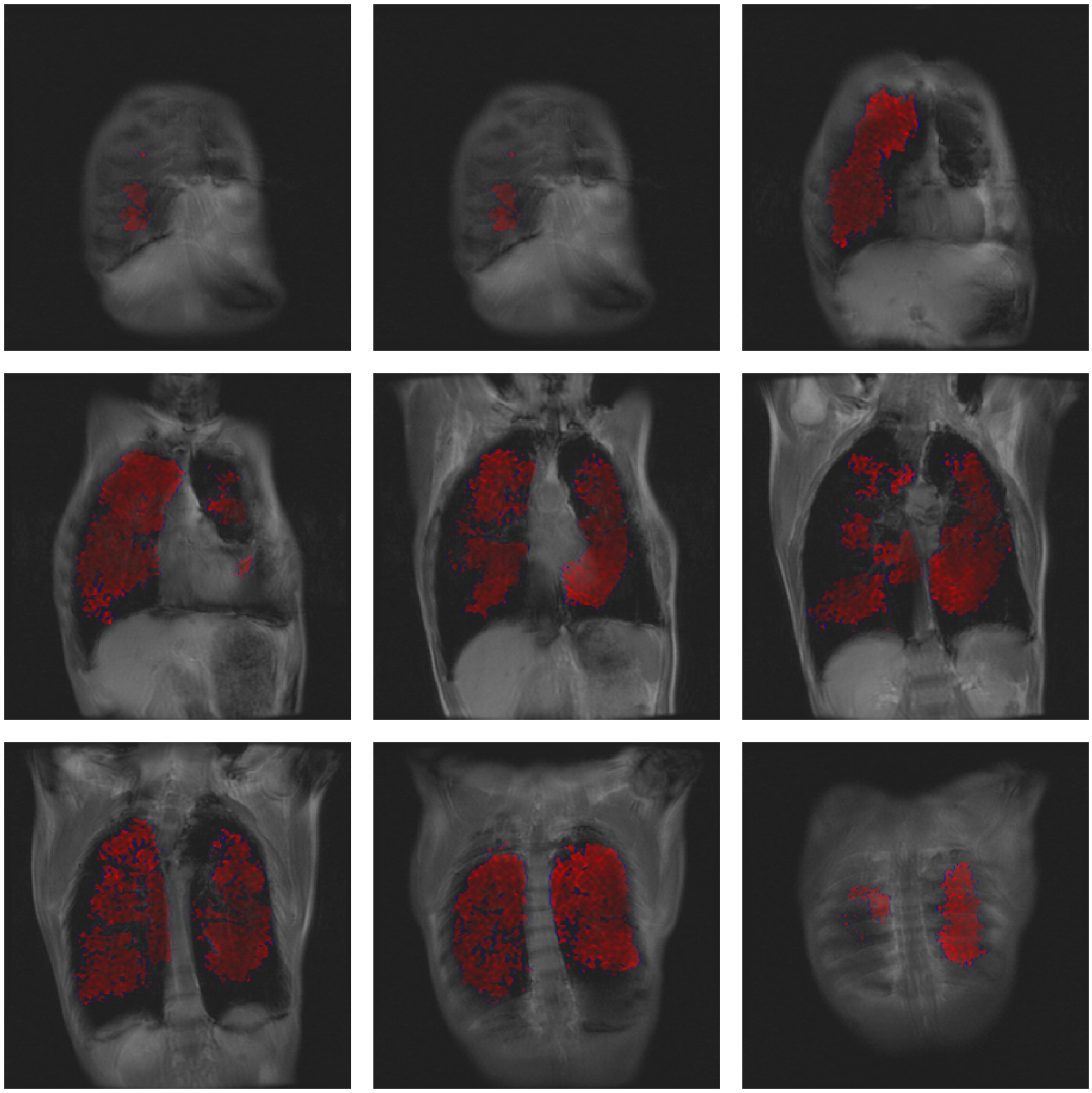

Figure 4.4: Coronal HP ^{129}Xe-MR diffusion-weighted imaging co-registered to proton MRI acquired from OXF0139.

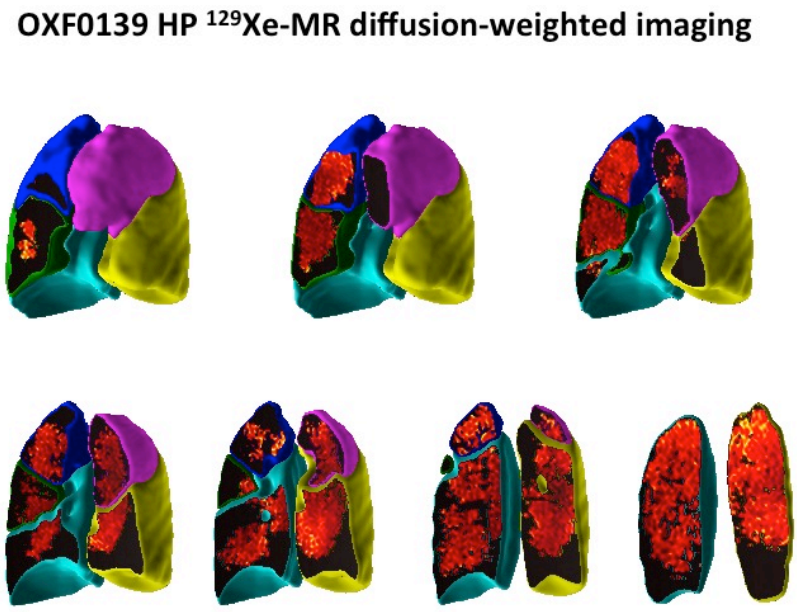

Figure 4.5: 3-D lobar HP ^{129}Xe-MRI diffusion-weighted imaging from OXF0139. High signal intensity in the left lower lobe (yellow) posteriorly corresponds to elevated HP ^{129}Xe-MRI ADC values and indicates emphysematous tissue destruction.

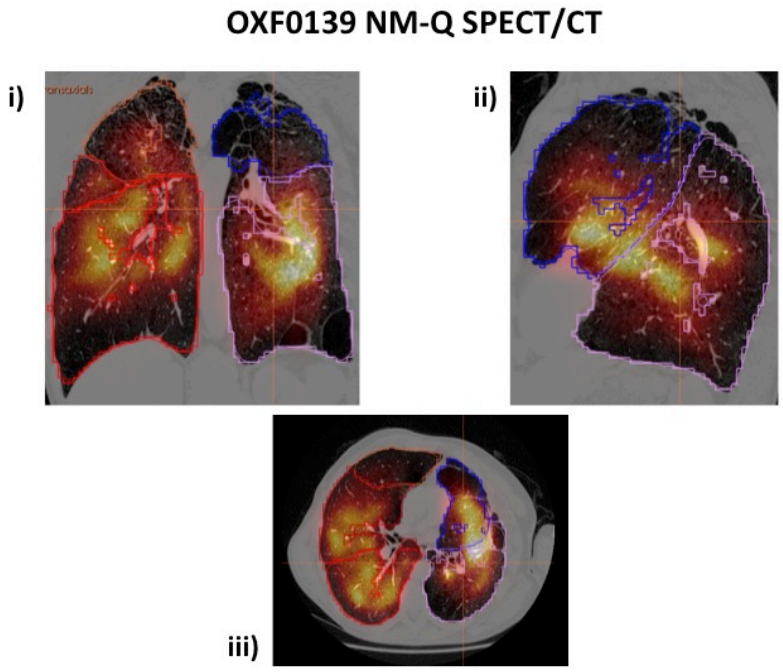

Figure 4.6: Selected images of NM-Q SPECT/CT acquired from OXF0139. Images are in the i) coronal, ii) sagittal and iii) axial plane.

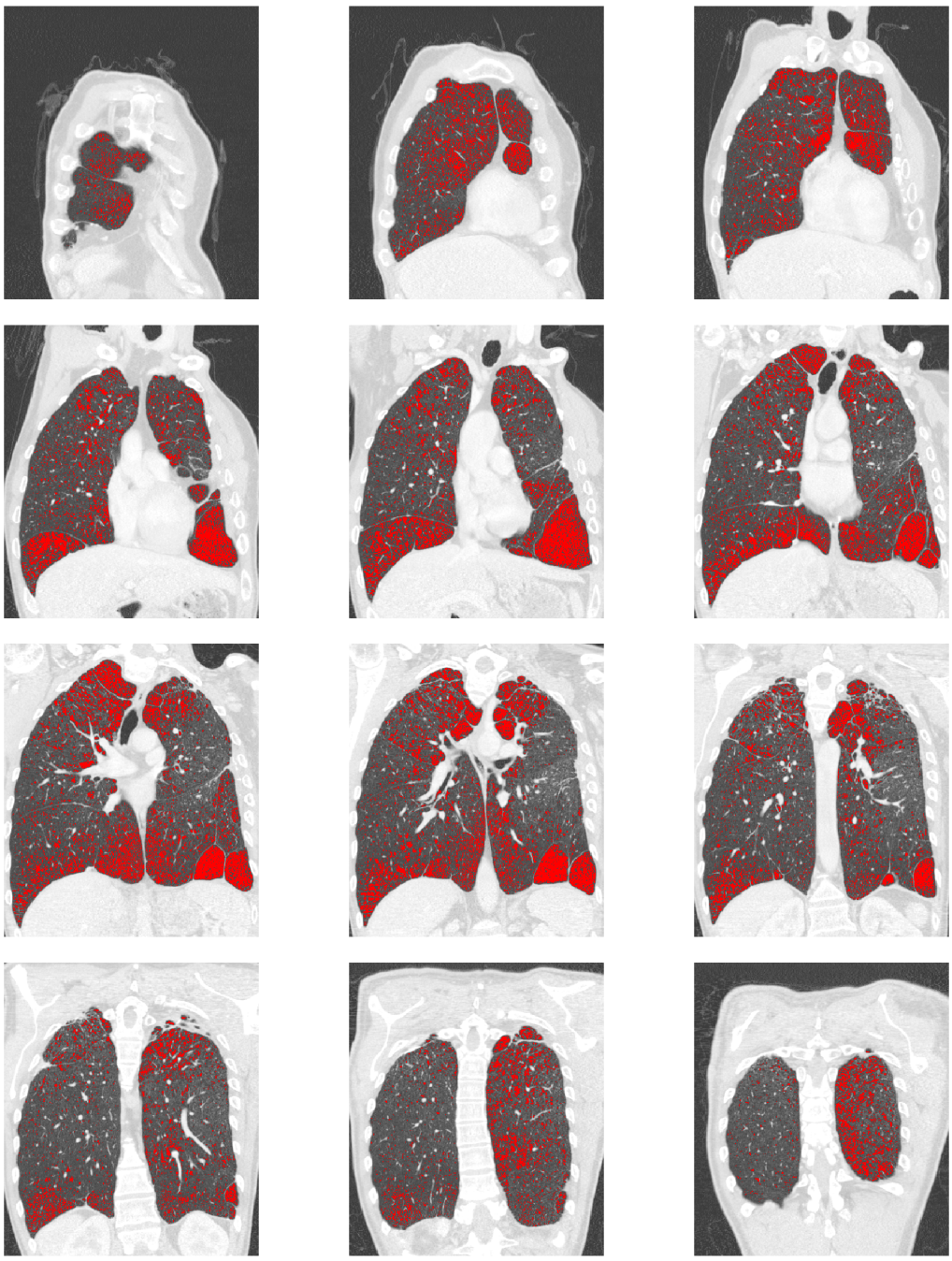

Figure 4.7: QCT-derived emphysema (% LAA) from patient OXF0139. Red areas correspond to regions with attenuation less than -950 HU. Images show moderate paraseptal emphysema.

4.5.2 Data analysis from COPD patient OXF0068

Table 4.4: Lobar imaging parameters acquired from OXF0068

Imaging parameter	Pulmonary lobe				
	RUL	RML	RLL	LUL	LLL
HP ^{129}Xe-MRI % ventilated volume	75.77	79.92	86.30	86.19	90.70
HP ^{129}Xe-MRI$_R$ % ventilated volume	84.98	86.59	95.93	85.98	95.80
HP ^{129}Xe-MRI ADC (cm^2sec^{-1})	0.042	0.036	0.050	0.043	0.042
QCT-derived % LAA	0.9	0.5	0.9	1.1	0.5
QCT-derived Pi10 (mm)	5.6	4.9	6.2	7.5	5.7
NM-Q SPECT relative % perfusion	17.1	5.8	29.2	22	25.9

R Repeat HP ^{129}Xe-MRI measures to evaluate reproducibility
RUL = Right upper lobe, RML = Right middle lobe, RLL = Right lower lobe, LUL = Left upper lobe, LLL = Left lower lobe, %LAA = Percentage low-attenuation areas less than -950 HU, Pi10 = Square root of bronchial wall area for a "theoretical airway" with an internal perimeter of 10 mm

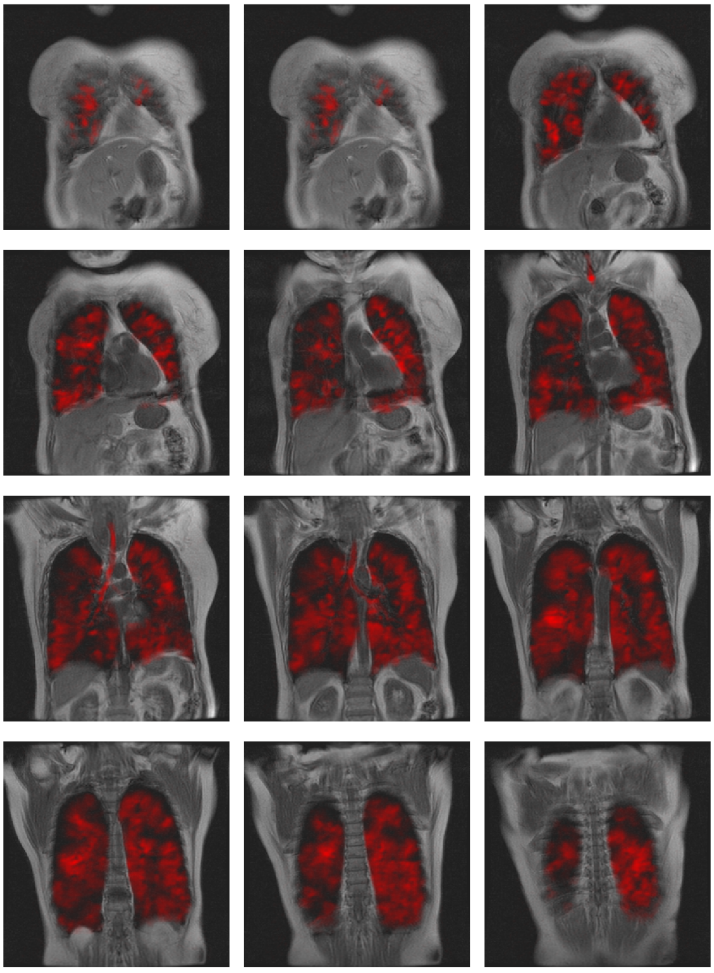

Figure 4.8: Coronal co-registered HP ^{129}Xe-MR ventilation imaging (red) and proton MRI acquired from OXF0068. Co-registration to proton MRI enables the lung boundaries to be defined.

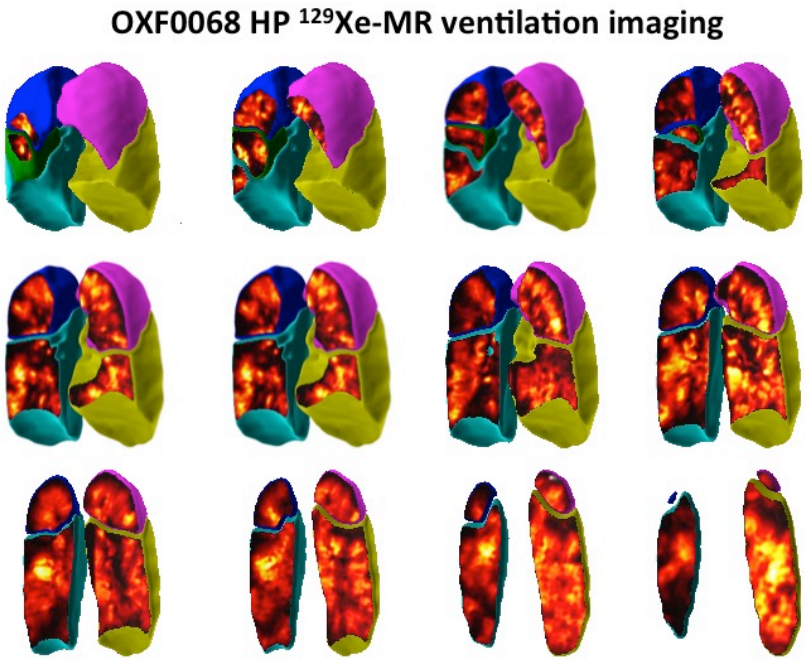

Figure 4.9: 3-D lobar HP ^{129}Xe-MR ventilation imaging from OXF0068. Images show patchy heterogeneous ventilation signal throughout the lungs with ventilation defects more pronounced in the right lung.

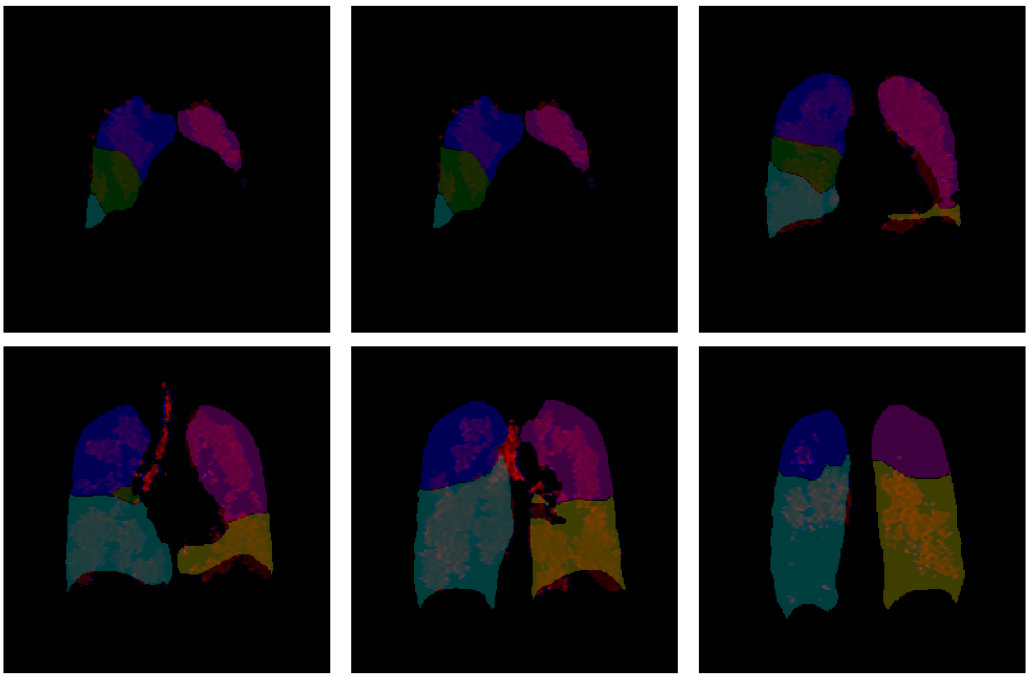

Figure 4.10: Non-rigid co-registration of HP ^{129}Xe-MR diffusion-weighted imaging and QCT from OXF0068. QCT enables definition of the lobar boundaries (pulmonary fissures) to allow lobar quantification of HP ^{129}Xe-MR ADC values.

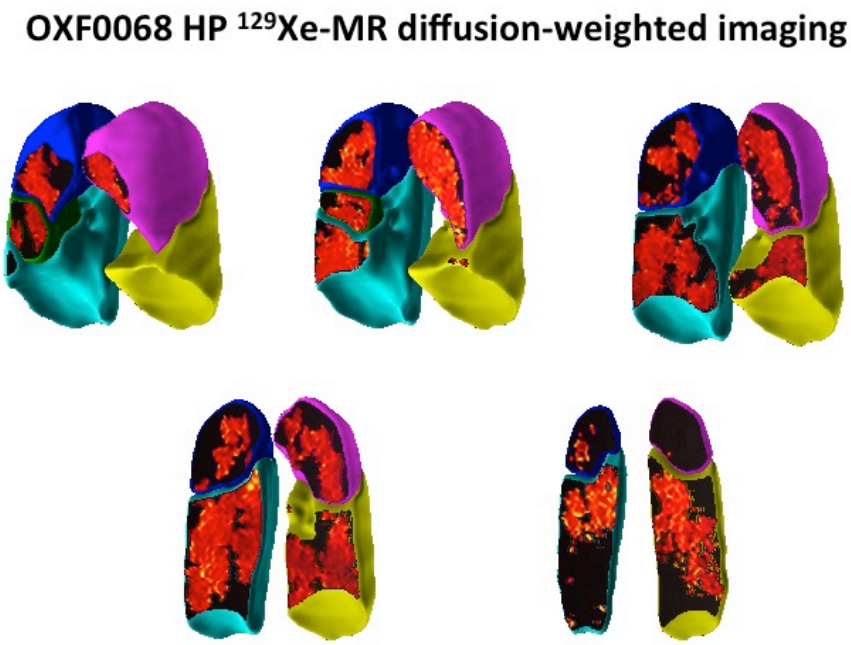

Figure 4.11: 3-D lobar HP ^{129}Xe-MR diffusion-weighted imaging from OXF0068. There is increased signal intensity in the posterior right lower lobe (cyan) corresponding to higher ADC values and increased emphysema.

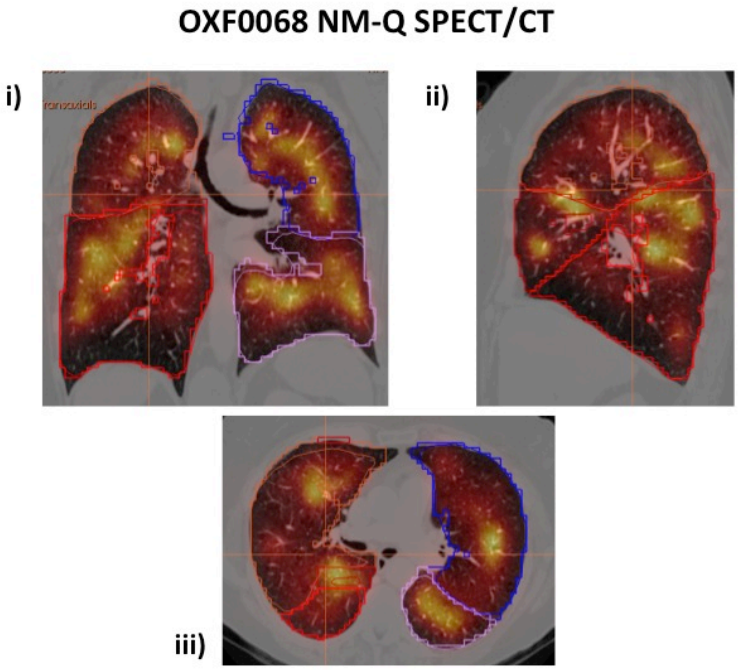

Figure 4.12: Selected NM-Q SPECT/CT images from OXF0068. Images are in the i) coronal, ii) sagittal and iii) axial plane and demonstrate relatively homogeneous perfusion signal in all pulmonary lobes.

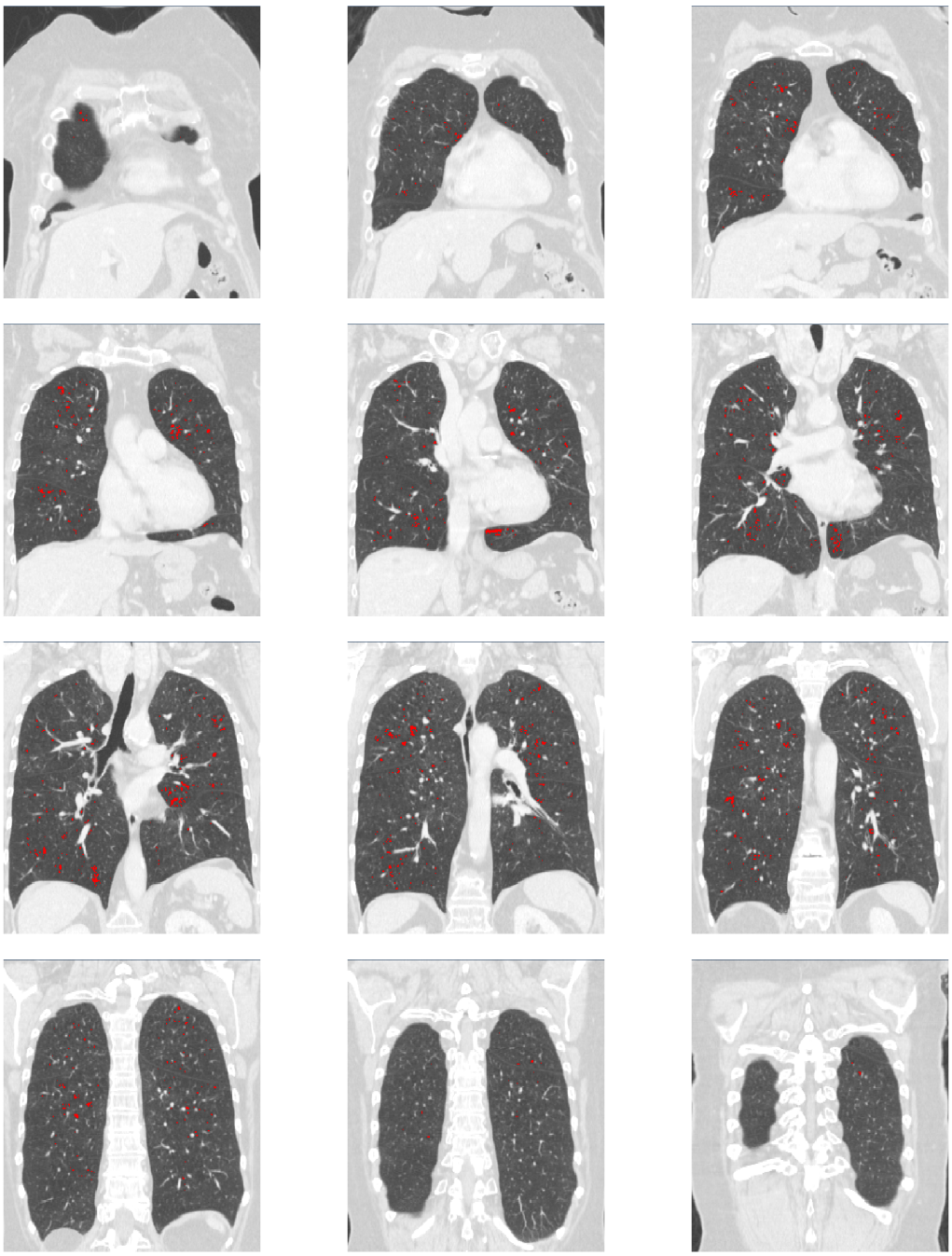

Figure 4.13: QCT-derived emphysema (% LAA) from COPD patient OXF0068. Red areas correspond to regions with attenuation less than -950 HU. Images show mild emphysematous changes only.

4.5.3 Data analysis from COPD patient OXF0069

Table 4.5: Lobar imaging parameters acquired from OXF0069

Imaging parameter	Pulmonary lobe				
	RUL	RML	RLL	LUL	LLL
HP ^{129}Xe-MRI % ventilated volume	51.44	90.96	87.12	50.83	95.24
HP ^{129}Xe-MRI$_R$ % ventilated volume	32.77	63.82	72.96	54.03	90.12
HP ^{129}Xe-MRI ADC (cm^2sec^{-1})	0.073	0.058	0.066	0.086	0.058
QCT-derived % LAA	54.9	19.4	25.1	61.9	8.1
QCT-derived Pi10 (mm)	7.5	11.1	6.2	5.8	5.8
NM-Q SPECT relative % perfusion	1	9.2	30.3	29.4	30

R Repeat HP ^{129}Xe-MRI measures to evaluate reproducibility
RUL = Right upper lobe, RML = Right middle lobe, RLL = Right lower lobe, LUL = Left upper lobe, LLL = Left lower lobe, %LAA = Percentage low-attenuation areas less than -950 HU, Pi10 = Square root of bronchial wall area for a "theoretical airway" with an internal perimeter of 10 mm

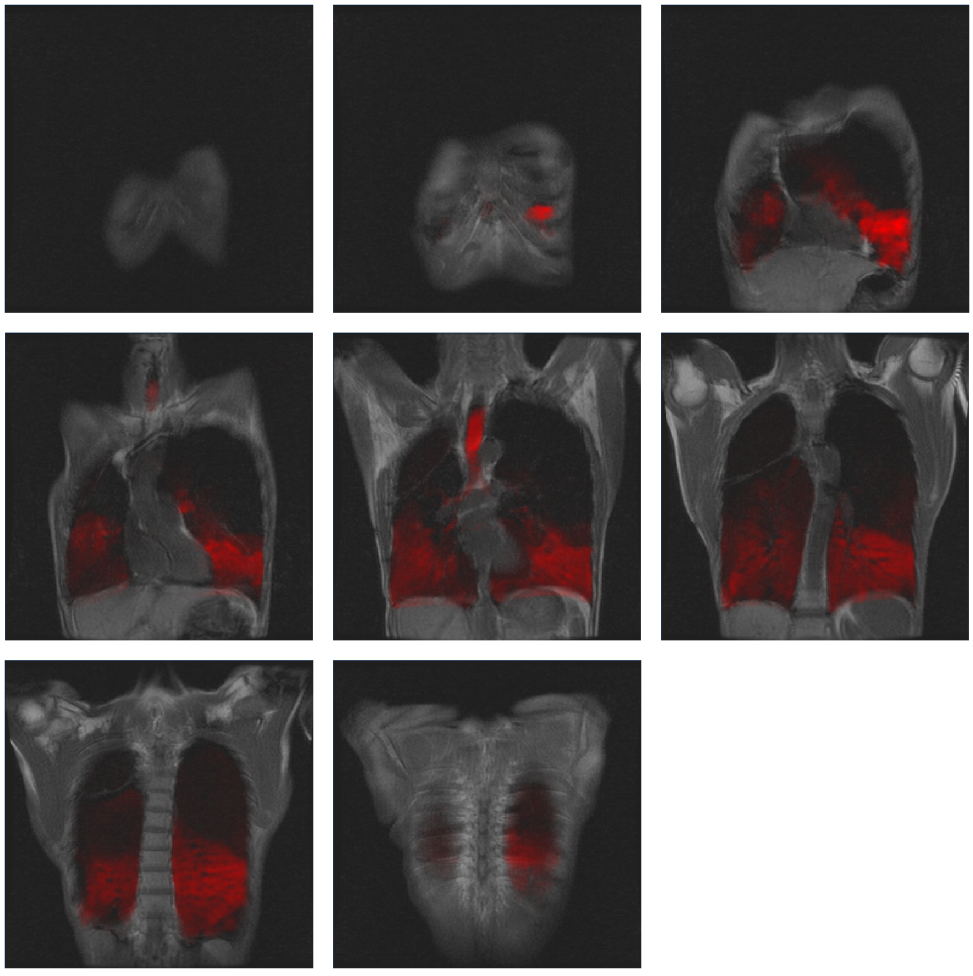

Figure 4.14: Coronal co-registered HP ^{129}Xe-MR ventilation imaging (red) and proton MRI from OXF0069. Co-registration to proton MRI enables the lung boundaries to be defined which is particularly important in the upper lobes where large HP ^{129}Xe-MR ventilation defects are present.

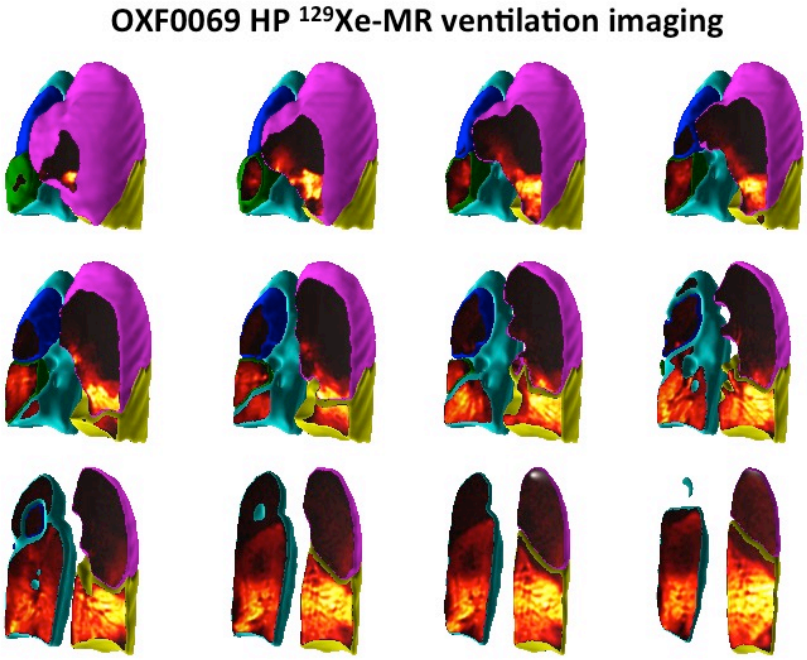

Figure 4.15: 3-D lobar HP ^{129}Xe-MR ventilation imaging from OXF0069. Images demonstrate large ventilation defects in the right upper (blue) and left upper (pink) lobes.

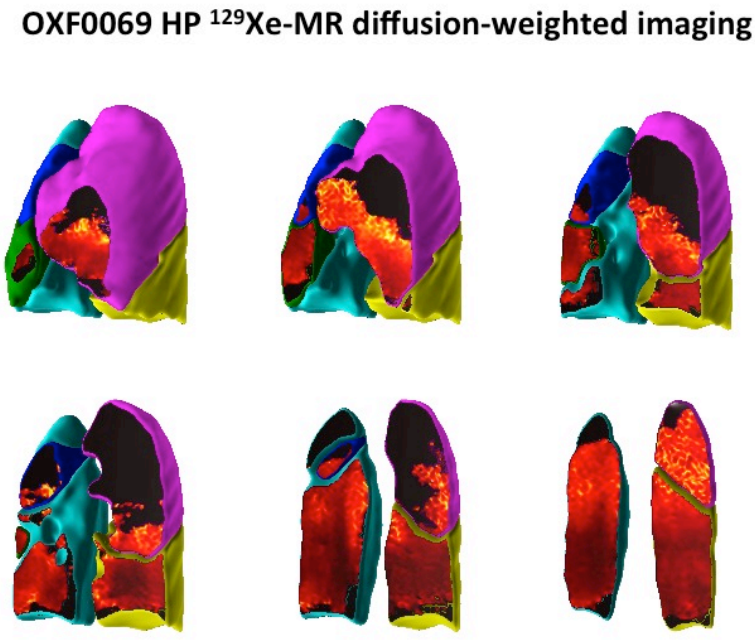

Figure 4.16: 3-D lobar HP ^{129}Xe-MR diffusion-weighted imaging in OXF0069. There is increased signal intensity in the left upper (pink) lobe corresponding to higher ADC values and relative increased emphysema compared to other lobes.

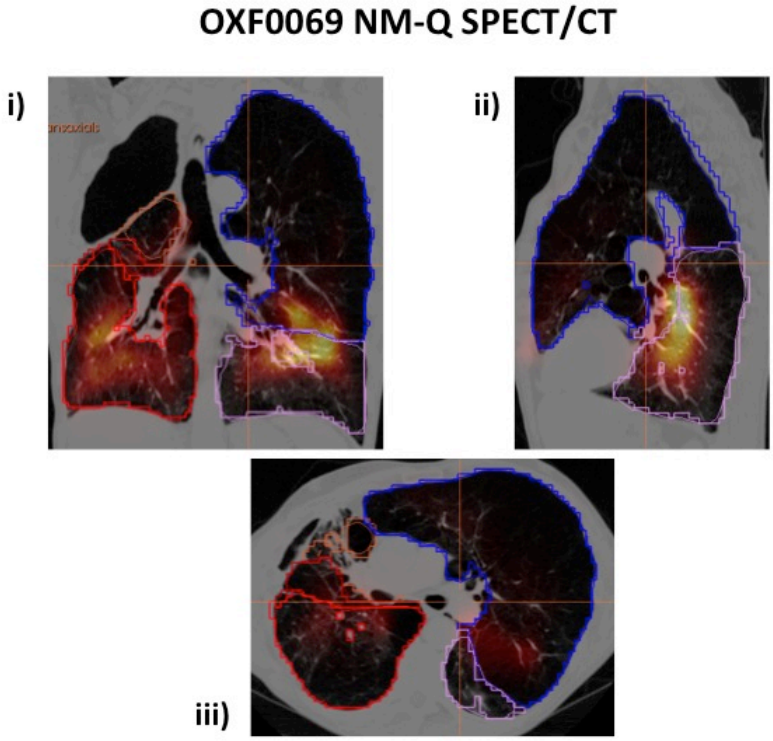

Figure 4.17: Selected NM-Q SPECT/CT images acquired from OXF0069.
Images are in the i) coronal, ii) sagittal and iii) axial plane and show perfusion limited predominantly to the lower lobes.

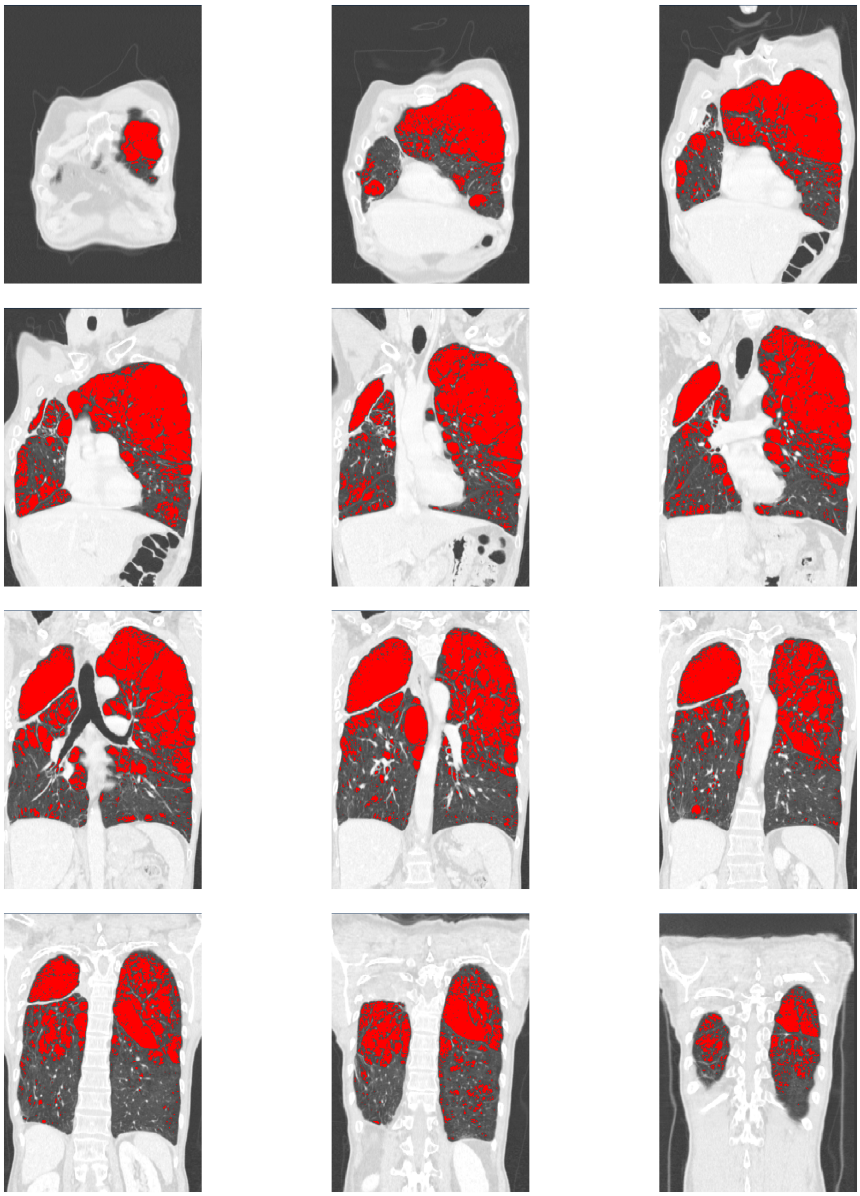

Figure 4.18: QCT-derived emphysema (% LAA) for patient OXF0069. Red areas correspond to regions with attenuation less than -950 HU. Images show severe upper lobe predominant emphysema.

Lobar HP ^{129}Xe-MRI percentage ventilated volume and lobar HP ^{129}Xe-MRI average ADC showed correlation with lobar QCT-derived %LAA (r=-0.32, $p<0.001$ and r=0.75, $p<0.0001$ respectively)[Figure 4.19]. There was no correlation between lobar HP ^{129}Xe-MRI parameters and lobar QCT Pi10 [Table 4.6].

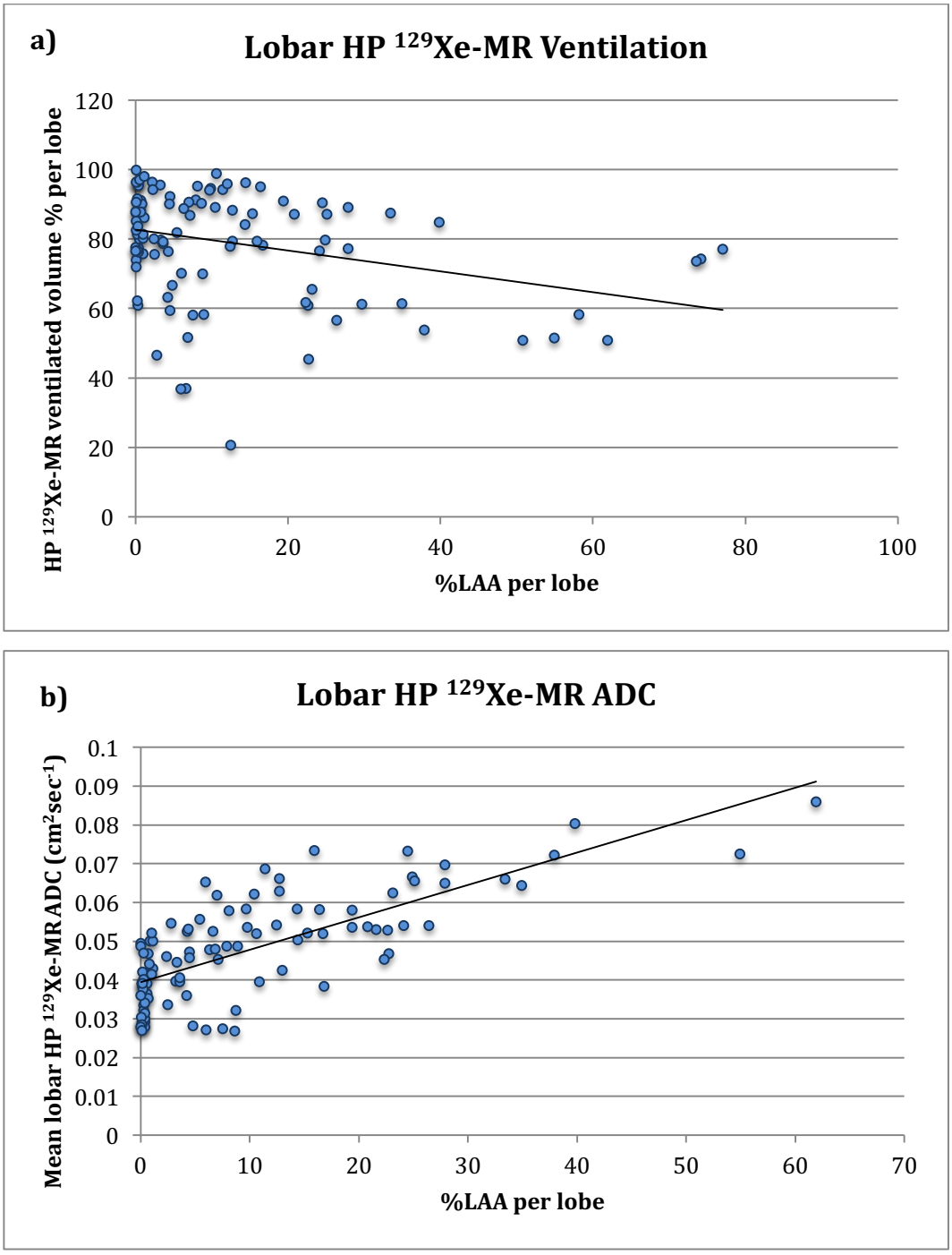

Figure 4.19: Scatter plots to show the correlation between lobar imaging parameters. a) Linear correlation between HP ^{129}Xe-MR ventilated volume (%) and percentage low-attenuation areas less than -950 HU (%LAA) per pulmonary lobe. b) Linear correlation between HP ^{129}Xe-MR average ADC and %LAA per pulmonary lobe.

Table 4.6: Pearson's correlation of HP ^{129}Xe-MRI and QCT lobar imaging parameters

Pearson's correlation coefficient (*r*=)	HP ^{129}Xe-MRI ventilated volume (%)	HP ^{129}Xe-MRI average ADC (cm^2sec^{-1}) ξ
QCT-derived %LAA	-0.32 (p=0.00061)*	0.75 (p=7.71 x 10^{-20})*
QCT-derived Pi10 (mm)	-0.086 (p=0.38)	-0.051 (p=0.61)

ξ Data available for n=21
* Statistically significant p value
ADC = Apparent diffusion coefficient, %LAA = Percentage low-attenuation areas less than -950 HU, Pi10 = Square root of bronchial wall area for a "theoretical airway" with an internal perimeter of 10 mm

NM-Q SPECT relative percentage perfusion showed correlation with HP ^{129}Xe-MRI relative % ventilated volume [Figure 4.5], QCT-derived relative % LAA and QCT derived Pi10 [Table 4.7].

Table 4.7: Pearson's correlation of NM-Q SPECT lobar relative percentage perfusion with HP ^{129}Xe-MRI and QCT lobar measures

Pearson's correlation coefficient (*r*=)	HP ^{129}Xe-MRI (relative % ventilated volume)	HP ^{129}Xe-MRI average ADC (cm^2sec^{-1})	QCT-derived (relative %LAA)	QCT-derived Pi10 (mm)
NM-Q SPECTξ (relative % perfusion)	0.67 (p=7.99 x 10^{-13})*	0.16 (p=0.13)	0.41 (p=6.17 x 10^{-5})*	-0.25 (p=0.019)*

ξ Data available for n=18
* Statistically significant p value
ADC = Apparent diffusion coefficient, %LAA = Percentage low-attenuation areas less than -950 HU, Pi10 = Square root of bronchial wall area for a "theoretical airway" with an internal perimeter of 10 mm

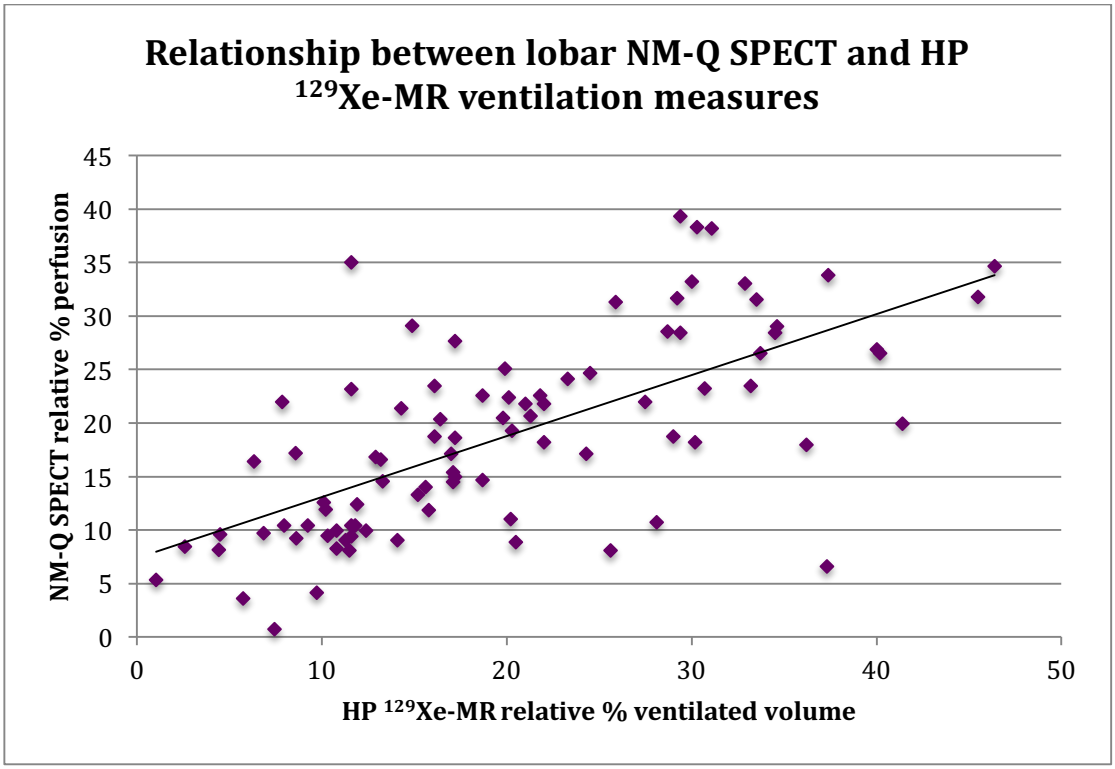

Figure 4.20: Scatter plot to show correlation between NM-Q SPECT relative percentage perfusion and HP ^{129}Xe-MR relative percentage ventilated volume.

Descriptive statistics for HP ^{129}Xe-MRI and QCT-derived metrics according to pulmonary lobe are provided in Table 4.8.

Table 4.8: Descriptive statistics of imaging parameters according to pulmonary lobe

Parameter	Pulmonary lobe				
	RUL	RML	RLL	LUL	LLL
HP ^{129}Xe-MRI ventilated volume (%)	74.81 (13.94)	85.52 (11.25)	79.06 (19.59)	76.88 (15.51)	80.67 (13.29)
HP ^{129}Xe-MRI average ADC (cm^2sec^{-1})ξ	0.050 (0.014)	0.045 (0.011)	0.047 (0.013)	0.050 (0.015)	0.045 (0.013)
QCT-derived %LAA	6.62 (0.84/21.89)	7.06 (0.50/12.03)	4.05 (0.45/11.81)	6.90 (1.11/15.87)	3.20 (0.41/9.3)
QCT-derived Pi10	6.17 (0.92)	6.82 (2.06)	6.42 (1.14)	6.04 (0.96)	5.84 (0.97)

If not otherwise stated, the figures are mean (SD)
ξ Data only available for n=21
RUL = Right upper lobe, RML = Right middle lobe, RLL = Right lower lobe, LUL = Left upper lobe, LLL = Left lower lobe, %LAA = Percentage low-attenuation areas less than -950 HU, Pi10 = Square root of bronchial wall area for a "theoretical airway" with an internal perimeter of 10 mm

Whole lung HP ^{129}Xe-MRI average ADC showed moderate correlation with PFTs: percentage predicted TLCO (r=-0.61, p<0.005) and percentage predicted FRC (r=0.47, p<0.05). Whole lung QCT-derived %LAA showed a similar correlation with percentage predicted TLCO (r=-0.65, p<0.005) and near statistically significant correlation with percentage predicted FRC (r=0.39, p=0.07). There was poor correlation between whole lung HP ^{129}Xe-MRI percentage ventilated volume and PFTs [Table 4.9]. There was similar weak correlation between whole lung QCT-derived Pi10 and PFTs (r=-0.34-0.24, p=0.13 - 0.86, Table 4.9). There was no correlation between any imaging parameters and spirometric indices (r=-0.37-0.24, p=0.092 - 0.29, Table 4.9).

A trend towards correlation between whole lung HP ^{129}Xe-MRI ventilated volume percentage and dyspnoea-12 questionnaire scores (r=-0.41, p=0.057) reaching near statistical significance was demonstrated. In contrast, there was

no correlation between dyspnoea-12 scores and spirometry (r=-0.19 - -0.28, p=0.21-0.39). Regarding PFTs; dyspneoa-12 scores showed significant correlation with RV/TLC (r=0.47, p=0.027) but not with FRC (r=0.14, p=0.54) or TLCO (r=-0.042, p=0.85).

Table 4.9: Pearson's correlation of whole lung imaging parameters, pulmonary function tests and dyspnoea-12 questionnaire scores

Pearson's correlation coefficient (r=)	HP ^{129}Xe-MRI ventilated volume (%)	HP ^{129}Xe-MRI average ADC (cm^2sec^{-1})ξ	QCT-derived %LAA	QCT-derived Pi10 (mm)
FEV_1 (L, % predicted	0.082 (p=0.72)	-0.15 (p=0.51)	-0.20 (p=0.37)	0.24 (p=0.29)
FEV_1/FVC (%)	0.097 (p=0.67)	-0.37 (p=0.092)	-0.22 (p=0.32)	0.040 (p=0.86)
RV/TLC (%)	-0.12 (p=0.59)	-0.094 (p=0.68)	-0.052 (p=0.82)	-0.27 (p=0.23)
FRC (% predicted)	0.11 (p=0.64)	0.47 (p=0.026)*	0.39 (p=0.072)	-0.34 (p=0.13)
TLCO (mmol/min/kPa, % predicted)	0.14 (p=0.52)	-0.61 (p=0.0024)*	-0.65 (p=0.0012)*	0.13 (p=0.56)
Dyspnoea-12 score	-0.41 (p=0.057)	-0.12 (p=0.59)	-0.20 (p=0.37)	0.10 (p=0.66)

ξ Data only available for n=21
* Statistically significant p value

The Bland Altman agreement plot [Figure 4.21] for repeated lobar HP ^{129}Xe-MR ventilation imaging shows a difference of up to 25% between repeated ventilated volume percentage measures. The variability of data points around the bias line appears relatively consistent with increasing mean lobar HP ^{129}Xe-MR ventilated volume percentage measurements.

The Bland Altman agreement plot [Figure 4.22] for repeated lobar HP ^{129}Xe-MR average ADC values shows that the majority of differences between repeated

measures lie below the mean absolute difference. The difference between repeated HP ^{129}Xe-MRI ADC values may be up to 0.04 cm^2sec^{-1}.

The mean absolute difference is above zero for both repeated lobar HP ^{129}Xe-MR ventilated volume percentage measurements and average ADC values indicating a consistent difference between repeated and baseline lobar HP ^{129}Xe-MRI measures and potential systematic error relating to the imaging technique itself. Reproducibility statistics are shown in Table 4.10.

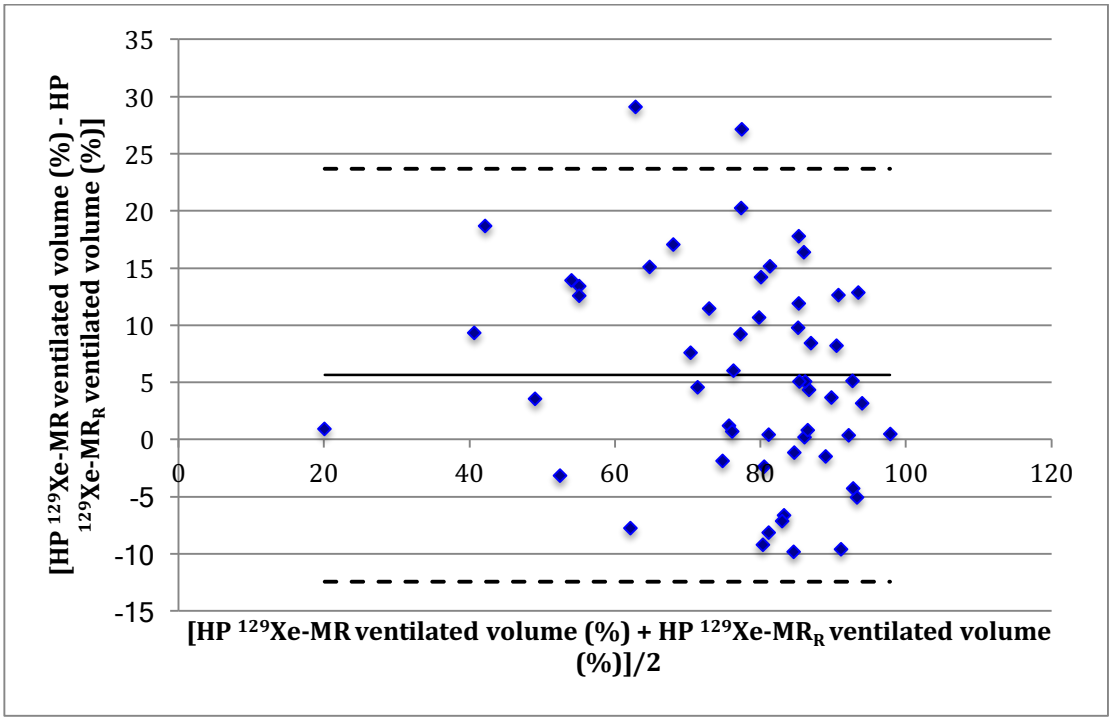

Figure 4.21: Bland Altman agreement plot to show reproducibility of lobar HP ^{129}Xe-MR ventilated volume (%) generated using automated PTK analysis tool. The solid line indicates mean absolute difference. Two outer dashed lines represent 95% confidence interval of the mean difference (limits of agreement).

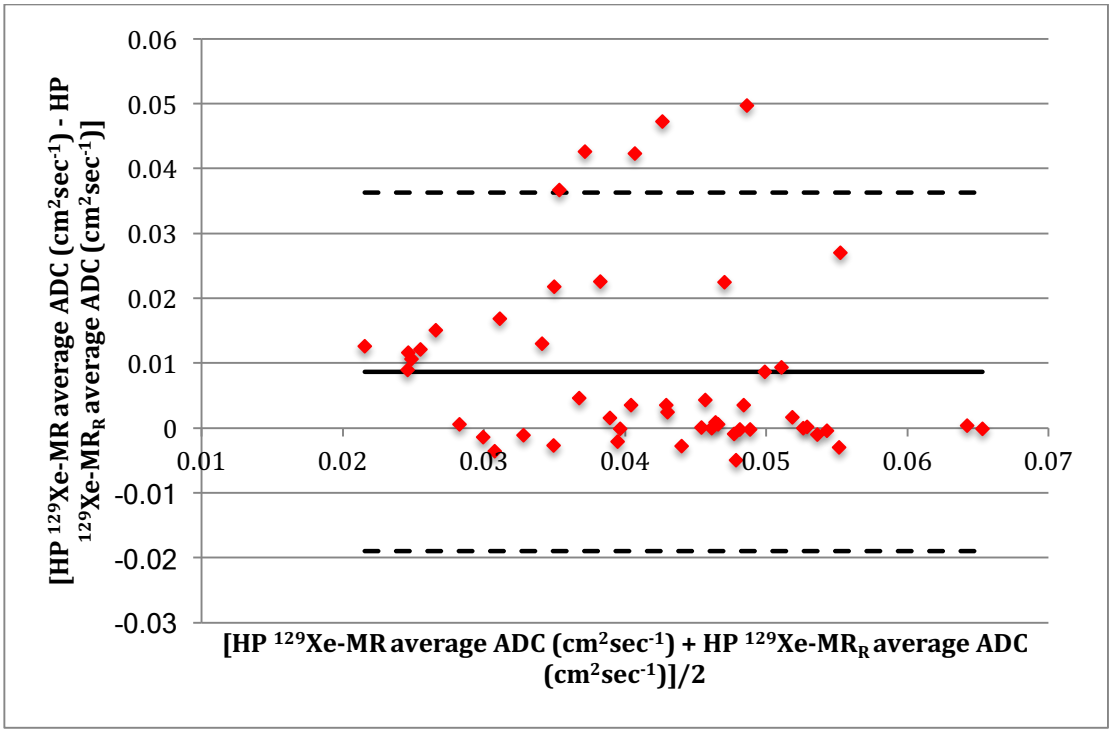

Figure 4.22: Bland Altman agreement plot to show reproducibility of lobar HP ^{129}Xe-MR average ADC (cm^{2}sec^{-1}) generated using automated PTK analysis tool. The solid line indicates mean absolute difference. Two outer dashed lines represent 95% confidence interval of the mean difference (limits of agreement).

Table 4.10: Reproducibility statistics of lobar HP ^{129}Xe-MR ventilated volume percentage and average ADC calculated from paired HP ^{129}Xe-MR ventilation and diffusion-weighted imaging

Imaging parameter	Mean ± Standard Deviation	Mean Difference*	Coefficient of repeatability
Lobar HP ^{129}Xe-MRI ventilated volume (%)¥	77.12±16.55	5.63 (-12.43-23.69)	18.06
Lobar HP ^{129}Xe-MR average ADC (cm^{2}sec^{-1})§	0.042±0.013	0.0087 (-0.019-0.036)	0.028

* Data in parentheses are 95% limits of agreement, ¥ Data available from n=11, § Data available from n=10

4.6 Discussion

4.6.1 HP ^{129}Xe-MRI measures are successfully quantified according to pulmonary lobes

This chapter has generated lobar measurements of ventilation and ADC using HP ^{129}Xe-MRI and demonstrated moderate correlation with lobar lung anatomy (QCT) and global functional transfer capability (TLCO). Although previous studies have shown the feasibility of hyperpolarised gas imaging to determine global functional parameters of the lung, translation of this technique from academic to routine clinical application has been limited to date. Accurate lobar quantification of HP ^{129}Xe-MRI is particularly relevant to the field of respiratory medicine with emerging regional treatments not adequately assessed by standard whole lung methods. These HP ^{129}Xe-MRI lobar analyses offer the potential for improved description of COPD regional functional heterogeneity and assessment for regional treatments such as LVRS or endobronchial valve placement. Unlike CT and NM-Q SPECT, HP ^{129}Xe-MRI does not involve exposure to ionising radiation and may therefore be performed repeatedly, potentially immediately after an intervention to determine its efficacy. This may allow early treatment modifications or enable clinicians to inform patients regarding the likely success of their intervention in real-time.

The feasibility of regional ventilation including lobar measures using HP ^{3}He-MRI in healthy volunteers and subjects with asthma has been reported(339, 340) but lobar ventilation and ADC measures using HP ^{129}Xe-MRI have not been

previously determined. This study has derived HP ^{129}Xe-MR ventilation and ADC per lobe following automated non-rigid registration to proton MRI and QCT. The software used to generate lobar HP ^{129}Xe-MRI measures has a GUI offering the potential for incorporation into the clinical workflow and providing external validity for use in other respiratory centres. Furthermore lobar HP ^{129}Xe-MRI measures could evaluate treatment effects in other obstructive diseases, for example, lobar HP ^{129}Xe-MRI ADC values in patients with α_1-antitrypsin deficiency and lobar HP ^{129}Xe-MRI ventilated volume percentage in asthma. This work may enable stratification of patients according to disease severity and COPD phenotype. Lobar HP ^{129}Xe-MRI may also help determine patient suitability for specific regional pulmonary treatments.

4.6.2 Lobar HP ^{129}Xe-MRI measures are reproducible

The reproducibility of generated lobar HP ^{129}Xe-MRI measurements was confirmed by Bland Altman analyses. Agreement plots [Figure 4.21 and 4.22] showed that the majority of differences between repeated lobar HP ^{129}Xe-MR percentage ventilated volume measurements and lobar HP ^{129}Xe-MR average ADC values lie within 95% limits of agreement. Review of the outlier data suggests despite radiographer training and coaching, small differences in lung inflation volume occurred during image acquisition leading to imperfect co-registration between HP ^{129}Xe-MRI, proton MRI and QCT in these cases. Variation in lung volumes during separate acquisition of MRI and QCT remains a recognised limitation of the method presented, although the non-rigid co-registration algorithm used adjusts for this.

4.6.3 Lobar HP ^{129}Xe-MRI correlates with QCT-derived emphysema

The lobar percentage ventilated volumes and average lobar ADC values as assessed by HP ^{129}Xe-MRI significantly correlated with QCT-derived emphysema (r=-0.32, p<0.05, r=0.75, p<0.01). These findings are consistent with Kirby *et al.*(308) who investigated HP ^{3}He-MR and HP ^{129}Xe-MR ventilation imaging in ten subjects with COPD and demonstrated significant correlation between regions of decreased HP ^{129}Xe-MRI ventilation with QCT-derived emphysema but not QCT airway wall measurement. Significant correlation between HP ^{3}He-MRI ADC and QCT-derived emphysema has been similarly reported(306). The relationship between whole lung HP ^{129}Xe-MRI ADC and QCT-derived emphysema in healthy volunteers and COPD subjects has also been demonstrated(310). The results confirm these findings and extend the correlation already demonstrated between HP ^{129}Xe-MRI and QCT on a lobar level.

4.6.4 HP ^{129}Xe-MRI ADC values are higher in patients with COPD compared with healthy volunteers

The whole lung mean ADC values from the study population [Table 4.2] are consistent with those of Kaushik *et al.* who reported a mean ADC of 0.056 ± 0.008 cm^2sec^{-1} for COPD subjects with emphysema(146). Moreover, the whole lung mean ADC value obtained from patients with COPD is much higher than that established for healthy volunteers (0.028 ± 0.007 cm^2sec^{-1}) detailed in Section

3.5 [Table 3.4]. The increased ADC values obtained in COPD are expected, since they relate to emphysematous tissue destruction and have been previously observed with both HP ^{3}He-MRI and HP ^{129}Xe-MRI(146, 310) and reported to be significantly higher to those obtained in healthy volunteers(146). These data confirm that elevated mean HP ^{129}Xe-MRI ADC values indicate the presence of emphysema and can therefore differentiate COPD from healthy lung tissue.

4.6.5 Lobar HP ^{129}Xe-MRI ventilation correlates with NM-Q SPECT lobar perfusion

Lobar HP ^{129}Xe-MRI relative percentage ventilated volume showed significant correlation with NM-Q SPECT lobar relative percentage perfusion (r=0.67, p=7.99 x 10^{-13}). Confirming a relationship with NM-Q, the conventional imaging modality for lung function assessment provides evidence to validate HP ^{129}Xe-MRI. These data are consistent with a previous study reporting good correlation between HP ^{3}He-MR ventilation imaging and NM-V SPECT using the radiotracer ^{81m}Kr(103). Four patients declined NM-Q SPECT, primarily due to the length required to lie still on the scanner table for image acquisition i.e. 20 minutes. Taking image acquisition time into account, HP ^{129}Xe-MRI would seem more appealing to patients, since images are acquired within a breath-hold, therefore requiring minimal time on the MRI scanner table.

4.6.6 Whole lung HP^{129}Xe-MRI ADC correlates with TLCO and FRC

Whole lung mean ADC values obtained from patients with COPD correlated with TLCO percentage predicted and FRC percentage predicted. Whole lung QCT-derived emphysema showed a similar correlation with TLCO providing evidence that HP ^{129}Xe-MRI ADC measurements accurately reflect emphysematous destruction of the pulmonary microstructure. The relationship between hyperpolarised gas MRI ADC values and TLCO is established in asymptomatic smokers(177) and subjects with COPD(306, 330). Previous investigation of 53 ex-smokers, including subjects with and without COPD, showed significant correlation between HP ^{3}He-MRI ADC and QCT-derived emphysema with TLCO (r=-0.55, p<0.0001, r=-0.31, p=0.03 respectively)(318), in keeping with the presented results.

4.6.7 HP ^{129}Xe-MRI does not correlate with spirometry

Spirometric indices did not correlate with HP ^{129}Xe-MRI. A possible explanation may be that HP ^{129}Xe-MRI provides regional measurements of lung function, accounts for disease heterogeneity and can be easily acquired at the same lung volume for all patients i.e. FRC+1 L ^{129}Xe gas. In contrast, spirometry alone, provides a global measure of lung function and depends on external factors including patient effort, which may confound results. There are conflicting reports within the literature regarding the relationship between hyperpolarised gas imaging and spirometry. Woodhouse *et al.* showed no relationship between

HP ^{3}He-MR ventilation imaging and spirometry (309). Other investigators have reported a significant correlation between spirometry and HP ^{3}He-MRI VDP(307) and with HP ^{129}Xe-MRI VDP(310). Similarly, contrasting significant correlation(169) and weak associations(307) between HP ^{3}He-MRI ADC and spirometry are published within the literature. These discrepant results may be explained by the relatively small sample sizes included, the varying patient disease severity and non-standardised analysis methods ranging from manual to semi-automated segmentation.

4.6.8 Whole lung HP ^{129}Xe-MRI ventilation demonstrates a trend towards correlation with dyspnoea-12 questionnaires

The correlation found between whole lung HP ^{129}Xe-MRI ventilated volume percentage and dyspnoea-12 questionnaire scores reached near statistical significance (r=-0.41, p=0.057). In contrast, poor correlation was observed between dyspnoea-12 scores and spirometry (r=-0.19 - -0.28, p=0.21-0.39). These data suggest that HP ^{129}Xe-MRI may have a stronger relationship with patient functional outcomes than spirometry, specifically the dyspneoa-12 questionnaire that captures both “physical” and “affective” aspects of breathlessness.

4.6.9 QCT-derived airway measurements do not correlate with other imaging or PFTs

QCT-derived Pi10 did not correlate with other imaging parameters or spirometry in the cohort studied. The small peripheral airways less than 2 mm in diameter are attributed to the site of airflow limitation in COPD but are not readily resolved on CT. Previous pathology studies have shown that the disease process occurring in COPD affects both large and small airways, and as such measurements of large airways on QCT could reflect the state of small airways(341). Nakano *et al.* supported this hypothesis by showing correlation of QCT-derived airway dimensions of the upper lobe segmental bronchus with spirometry(342) and histology(343). However, it has been reported that emphysema weakens the relationship between FEV_1 and QCT-derived peripheral airway wall measurements(344). Emphysema may cause a loss of airway tethering, attenuating peripheral airway dilatation during inspiration(345) and subsequently reducing the accuracy of QCT-derived airway wall measurements. It is plausible that Pi10, a measure derived from predominantly larger airways may not accurately reflect the smaller peripheral airways in the presence of emphysema, explaining why this parameter did not correlate with spirometry or HP ^{129}Xe-MRI in the cohort. Furthermore, evaluation of over 4000 smokers with and without COPD showed poor correlation of Pi10 with spirometry and QCT-derived emphysema(346) consistent with the current findings.

4.6.10 Limitations

There are a number of limitations of the presented work. Despite the relatively small sample size, the study cohort included subjects that comprise the majority of clinically relevant COPD cases (GOLD stage II-IV). Future work should include patients with milder COPD (GOLD I) to identify lobar abnormalities for early stage disease. The proton MRI, HP ^{129}Xe-MR ventilation and ADC images and QCT were acquired during separate breath-holds. Despite acquisition of all images following inhalation of 1 L from FRC, potential lung volume differences may have arisen as a result of subjects varying the amount of air exhaled to achieve FRC before inhalation for each breath-hold. Potential lung volume differences and body movement may have affected accurate image registration, although the non-rigid multi-modal registration performed by PTK corrects for this. The requirement for co-registration might be reduced in future studies by simultaneous acquisition of proton MRI and HP ^{129}Xe-MRI during a single breath-hold(347). The software employed for image data analysis (PTK) is open source and not currently available commercially. Further optimisation of the software is required before integration into the clinical workflow is possible. Another limitation of the study is that no comparison between HP ^{129}Xe-MRI and other emerging functional lung imaging techniques was made, for example with oxygen-enhanced MRI and ^{19}F –MRI.

4.6.11 Future work

Future work should extend the lobar HP ^{129}Xe-MRI data analyses to incorporate recently described whole lung HP ^{129}Xe-MR ventilation image analysis

modifications i.e. including a bias field correction for the inhomogeneous B_1 field produced by the flexible vest coil(305). A "vesselness" filter should also be used to remove pulmonary vasculature, which can cause ^{129}Xe signal voids and be misinterpreted as ventilation defects(305). There is potential for the lobar analysis method to be further optimised from binary ^{129}Xe signal segmentation to a complete comprehensive scale accounting for all ^{129}Xe signal levels. This would be a further improvement on previously employed clusters/bins(305, 334) to fully characterise all the information contained on a HP ^{129}Xe-MR image.

4.6.12 Conclusion

In conclusion, lobar measures of HP ^{129}Xe-MR ventilation and diffusion-weighted imaging have been derived using automated non-rigid co-registration and shown to correlate with lobar lung anatomy (QCT) and global functional transfer capability (TLCO). Future work is needed to determine if lobar HP ^{129}Xe-MRI ventilation and ADC provide an improved method for selecting patients for regional lung treatments, and whether it offers new insights into efficacy of regional lung treatment in patients with COPD or other obstructive lung diseases.

5 Chapter 5: Assessment of delayed ventilation with HP ^{129}Xe-MRI

5.1 Background

5.1.1 Emphysema

COPD is characterised by progressive airflow limitation caused by a combination of small airways disease (obstructive bronchiolitis) and parenchymal destruction (emphysema).

Emphysema is the abnormal, permanent enlargement of airspaces distal to the terminal bronchioles with associated destruction of walls and loss of elastic connective tissue. This causes a reduced area for gas exchange and lung elastic recoil. Collapsed airways during expiration result in increased airflow resistance and dynamic hyperinflation. Chest wall compliance and respiratory muscle function is reduced causing increased work of breathing and consequent symptoms of dyspnoea, decreased exercise capacity and poorer quality of life experienced by patients(8, 348-351).

Emphysema is a component of COPD that can be effectively treated with lung volume reduction therapy (LVRT) in selected patients. LVRT can be performed via a surgical or bronchoscopic approach and aims to reduce the residual volume (RV) through resection or induced collapse of hyperinflated regions of the lung.

Reduction of RV improves the RV: total lung capacity ratio (TLC) and aims to restore elastic recoil and radial traction on the terminal bronchioles, thereby improving lung function and chest wall mechanics(352-354).

5.1.2 Collateral ventilation

Three levels of collateral ventilation have been previously described in human lungs: 5-15 μm pores of Kohn(355, 356), 30 μm alveolar ducts described by Lambert(357) and accessory communication between terminal bronchioles described by Martin(358). The importance of collateral ventilation in the healthy lung is negligible since resistance to airflow is much higher in the collateral pathways than the normal branching airways(359, 360). However, in the presence of emphysema, collateral pathways are often low resistance channels partly due to the additional destruction of barriers between pulmonary lobes. In some emphysematous lung regions, these lower resistance collateral pathways encourage preferential airflow rather than via the normal branching airways(359-361). This may be a beneficial physiological response to improve gas exchange in respiratory diseases such as emphysema, bronchiectasis and bronchiolitis obliterans. Collateral ventilation may also be advantageous in airway bypass treatment(362) but it prevents collapse of the target lobe in LVRT(363) due to backfilling ventilation and is therefore a cause for treatment failure.

5.1.3 Lung volume reduction therapy (LVRT)

5.1.3.1 Lung volume reduction surgery (LVRS)

The surgical procedure of resecting emphysematous lung to reduce residual volume was initially proposed by Brantigan in 1956(364). Cooper *et al.*(365)reintroduced lung volume reduction surgery (LVRS) in 1995 inspiring renewed interest in the technique amongst the surgical community.

LVRS has been shown to provide benefit in terms of lung function, exercise capacity, oxygen therapy requirement(365-369) and quality of life(370). Durable effects of up to 5 years following surgery have been reported(366, 371). However the procedure is associated with significant mortality and morbidity(372, 373). The 90-day mortality is reported to be 4% even when LVRS is performed by the most experienced surgeons(371).

The National Emphysema Treatment Trial (NETT), a randomised controlled trial (RCT) comparing LVRS with best medical therapy, identified specific high-risk patients. Subjects with FEV_1 less than 20% of predicted and either homogeneous emphysema or DLCO less than 20% of predicted showed a 90-day mortality rate of 28% and were subsequently defined as candidates who should not be offered surgery (373). Following post-hoc subgroup analysis, it was concluded that the functional and physiological benefits from LVRS occurred in stringently selected patients with predominant upper lobe disease and poor exercise capacity(374).

The controversy surrounding the significant costs, and the associated mortality and morbidity of LVRS has encouraged the development of less invasive bronchoscopic techniques to induce lung volume reduction, as a therapeutic alternative for non-surgical candidates.

5.1.3.2 Endobronchial valve placement

Several less invasive bronchoscopic techniques ranging from airway bypass, endoscopic sealant, steam and lung volume reduction coils(375-380) have been developed to simulate the effects of LVRS but without the associated morbidity and mortality risk. Of these creative interventional bronchoscopy techniques, endobronchial valve placement has emerged as the leading treatment with the largest evidence base(381, 382).

One-way endobronchial valves reduce the flow of air into the treated lobe during inspiration but allow secretions and air to be expelled from the region during expiration. With effective isolation of the treated lobe, progressive expiration results in shrinkage of the lobar volume and eventual complete collapse. The reduction of lung volume improves the elastic recoil of the lung and chest wall dynamics. Even in the absence of collapse, some clinical benefit has been suggested to occur due to redirection of airflow away from more damaged bullous lung to less damaged lung regions(382).

Improved lung function was initially demonstrated in proof-of-principle case series, particularly in patients with endobronchial valve induced atelectasis(363,

383). Other positive benefits demonstrated following successful volume reduction included reduced chest-wall asynchrony(384), increased exercise capacity and reduction in the work of breathing(385).

The Endobronchial Valve for Emphysema Palliation Trial (VENT) was the main RCT conducted in the USA and Europe to evaluate safety and effectiveness of endobrochial valves compared with optimal medical management(386). There was statistically significant but clinically modest improvement in lung function, exercise capacity and symptoms in patients(386, 387). Moreover, the observed benefits of valves were associated with a higher risk of complications compared with medical therapy, which was most commonly exacerbation of COPD(386, 387). Despite this, the safety profile of endobronchial valves has been reported to be considerably more acceptable when compared to LVRS(386-390). Subsequent post-hoc analysis of the VENT data indicated that greater emphysema heterogeneity and intact interlobar fissures were potential predictors for clinically important functional and physiological response to endobronchial valve treatment. Improved outcomes in subjects with heterogeneous emphysema and a target lobe with intact interlobar fissures were confirmed in a recent double-blind sham-controlled trial for endobronchial valve treatment (the BeLieVeR-HIFi study)(391).

The long-term benefit(392) and improved survival following successful endobronchial valve therapy(393) have been previously reported.

Currently, potential LVRT subjects are assessed for the presence of collateral ventilation either indirectly with computed tomography (CT) or directly via a commercially available bronchoscopic system, the Chartis system (Pulmonx)(394, 395).

5.1.4 The Chartis system (Pulmonx)

The Chartis system is a commercially available tool to measure collateral ventilation during bronchoscopy. A balloon catheter is inserted into the selected airway for endobronchial valve placement. The balloon is then inflated to effectively isolate the target lobe where complete collapse aims to be induced. Expiratory airflow and pressure is measured through sensors in the Chartis console. A gradual decline in expiratory airflow after balloon occlusion indicates the absence of collateral ventilation, whereas persistence of flow suggests the presence of significant collateral ventilation.

The Chartis system showed 75% accuracy in the prediction of response to endobronchial valve placement(396) but is associated with disadvantages including: -

1. Low tolerance e.g. excessive coughing
2. Incorrect positioning of the catheter (operator dependent)
3. Presence of mucus blockages preventing assessment
4. False-negative collateral-ventilation results due to airway collapse associated with short duration of evaluation and reduced total exhaled volume(395, 397)

A failure rate of up to 16% has been reported in subjects that cannot be evaluated with the Chartis system(395).

5.1.5 Fissure integrity on CT

Although interlobar fissure integrity has been proposed as a surrogate for collateral ventilation and therefore predictor of successful LVRT outcome(386, 387), there are conflicting reports regarding the accuracy of CT fissure assessment. Interlobar fissure completeness is defined as having >90% fissure present on high resolution CT (HRCT) in at least one image plane. There are reports that CT tends to overestimate the integrity of fissures(398) and there is no correlation between collateral ventilation and interlobar fissure completeness on histology(399). Despite this, HRCT has been found to be equally effective as Chartis for prediction of response to endobronchial valve treatment(400). In contrast, fissure integrity has been reported to have no influence on outcome to LVRT using a polymer sealant(401).

Subjects have been reported to show significant collateral ventilation with Chartis despite intact interlobar fissures on CT and subsequent reduced response to endobronchial valve treatment(391). These data highlight the potential pitfall of employing CT fissure analysis alone as surrogate for collateral ventilation.

In a recent retrospective study, multiple QCT predictors of response to endobronchial valve placement were compared with the Chartis system. The

QCT model including measurements of fissure integrity, low attenuation clusters in the treated lobe and volumetric percentage of smallest vessels detected, provided comparable accuracy with Chartis(402). This study suggests that a multi-dimensional QCT model may provide an improved surrogate for collateral ventilation than CT analysis of fissure integrity alone.

Automated computer–based methods for fissure integrity assessment have been described(403) which can provide more robust and reproducible quantification but require specific expensive software not readily available in most LVRT centres.

5.1.6 Imaging delayed and collateral ventilation

Hogg *et al.* initially showed potential collateral ventilation in excised human lungs(359). Rosenberg and Lyons demonstrated interlobar collateral ventilation in five excised lungs with emphysema and pneumonia. Radioactive ^{133}Xe studies on the lung preparations showed activity in the lower lobe following administration of the tracer into the upper lobe suggesting the presence of collateral ventilation(404).

Collateral ventilation has been observed in animal and human studies using ^{133}Xe scintigraphy(405, 406) and xenon-enhanced dynamic dual-energy CT(407-410). However, these techniques incur exposure to ionising radiation and monitor the wash-in and wash-out of tracer gas over multiple breathing cycles. ^{133}Xe ventilation scintigraphy pre- and post- endoscopic placement of bronchial

prostheses in subjects with emphysema demonstrated delayed, persistent tracer wash-in into target upper lobes and accelerated wash-out from untreated lower lobes. The most likely explanation for the observed trend was reported as diffusion of ^{133}Xe into the upper lobes through interlobar collateral pathways(405).

5.1.7 HP ^{3}He-MR delayed ventilation imaging

There is a need for alternative non-invasive functional imaging methods to directly visualise collateral ventilation as the Chartis system is highly invasive. Furthermore, CT provides no functional information and identification of interlobar fissures in subjects with grossly distorted lung architecture can prove challenging but more importantly does not always correlate with LVRT response.

Hyperpolarised noble gas MR imaging has emerged as a promising technique to evaluate delayed ventilation. It offers the advantage of enabling assessment of gas diffusion to comprehensively evaluate both distribution of emphysema and delayed ventilation. Previous investigation has successfully demonstrated delayed ventilation in 8 COPD subjects using HP ^{3}He-MRI(411). The lower atomic mass of ^{3}He in air lends to increased diffusivity and potentially faster observation of delayed ventilation. In contrast, ^{129}Xe has a lower diffusivity and has not been previously employed for visualising delayed/collateral ventilation. It is therefore important to ensure that delayed ventilation can be imaged using HP ^{129}Xe-MR within a realistic single breath-hold time (~20 seconds) easily tolerated by patients.

Long range diffusion measurements with HP ^{3}He MRI may indicate that collateral ventilation is taking place(412, 413). Long-range ADC values are dependent on the lung structure at the acinar level and influenced by the passage of hyperpolarised gas through the peripheral airways. A high long-range ADC implies the presence of collateral ventilation since the hyperpolarised gas has diffused more quickly, taking a short circuit or bypassing the normal healthy airways(414-416). However, the measurement of long-range ADC does not provide direct visual evidence that collateral ventilation is actually taking place.

5.2 Hypothesis

This chapter will test the hypothesis that time-resolved single breath-hold HP ^{129}Xe-MR ventilation is feasible and can demonstrate delayed ventilation in subjects with COPD.

5.3 Aims

The aim of this chapter is to extend the *static* HP ^{129}Xe-MR ventilation sequence optimised in healthy volunteers and patients with COPD, in the previous chapters, to *dynamic* time-resolved HP ^{129}Xe-MR ventilation imaging. Specific aims are to: -

1. Determine the feasibility of time-resolved single breath-hold HP ^{129}Xe-MR ventilation imaging

2. Demonstrate delayed ventilation on a lobar basis in subjects with COPD using the new time-resolved HP ^{129}Xe-MR ventilation sequence
3. Determine the association between collateral ventilation predicted by CT fissure completeness and delayed ventilation observed with HP ^{129}Xe-MRI
4. Compare pulmonary lobes demonstrating delayed ventilation on HP ^{129}Xe-MRI with co-registered CT and NM-V images
5. Provide proof-of-principle that time-resolved HP ^{129}Xe-MR ventilation imaging could be further investigated in patients undergoing LVRT.

5.4 Materials and Methods

5.4.1 Subjects

The study was approved by the NRES South Central Committee (Berkshire) [REC reference 11/SC/0488] and written informed consent was obtained from study participants.

Thirteen patients diagnosed with COPD were prospectively enrolled between November 2014 and June 2015 from a tertiary referral centre with the following inclusion criteria: -

- At least mild disease (stage II-IV on GOLD criteria classification, FEV_1<80% predicted and FEV_1/ FVC <70%)
- Significant smoking history (>15 pack years)
- Over the age of 18-years-old and able to give informed consent.

Study exclusion criteria included the presence of co-existent cardio-pulmonary disease that predominated over COPD and might confound result interpretation (e.g. asthma, bronchiectasis, cystic fibrosis, lung cancer, uncontrolled heart failure, frequent unstable angina, respiratory muscle weakness). The study protocol is appended [Appendix 6].

The study population included nine males and four females [Table 5.1]. The mean±standard deviation and range of age in all participants was 67.4±9.0 years (52-84 years); in males, 68.4±9.6 years (52-84 years); and in females, 65.0±7.2 years (56-74 years). A Student's *t*-test was performed and showed no significant difference in age at baseline between males and females (p=0.57).

5.4.2 Study measures

Participants completed multi-modality imaging during a single study visit, including HP ^{129}Xe-MRI and combined nuclear medicine ventilation and computed tomography (NM-V SPECT/CT) [Section 2.8.1]. Two HP ^{129}Xe-MR sequences were acquired in each patient during the same scanning session: -

1. Static HP ^{129}Xe-MR ventilation imaging [Section 2.6.1]
2. Time-resolved ^{129}Xe-MR ventilation imaging [Section 2.6.3].

Details of the ^{129}Xe gas polarisation procedures, HP ^{129}Xe-MR sequences and NM-V SPECT/CT are provided in Section 2.

Study measures were completed during disease stability as defined by participants remaining exacerbation free for at least 4-weeks with no change to

their regular medications prior to completion of imaging and PFTs. Imaging was analysed blinded to clinical data and PFTs.

5.4.3 MRI analysis

Analysis of time-resolved HP ^{129}Xe-MR ventilation data was performed using PTK. Full details regarding the segmentation of pulmonary lobes on CT and non-rigid registration to proton and HP ^{129}Xe-MR by PTK is provided in Section 2.6.6. In brief, PTK performed automated non-rigid registration of corresponding CT and proton MR data to compute lobar masks, which were then used to establish the ventilation level (signal intensity) per pulmonary lobe on HP ^{129}Xe-MR for each time point. HP ^{129}Xe signal decay due to the imaging procedure and natural T_1 relaxation processes were accounted for by normalisation of images at each time point using a region of fully ventilated lung(243).

Delayed ventilation was defined as the quantifiable increase in ventilation level (signal intensity) in a lobe showing ventilation defects at baseline. The total number and percentage of pulmonary lobes demonstrating delayed ventilation with time-resolved HP ^{129}Xe-MRI were determined.

5.4.4 NM-V SPECT/CT analysis

Corresponding co-registered coronal image slices acquired with NM-V and CT were compared with time-resolved HP ^{129}Xe-MR image slices. NM-V and CT co-registered slices were reviewed for discernible differences that may contribute to delayed ventilation. Specifically, NM-V SPECT images were reviewed for the

presence of ventilation counts and CT for structural differences in lobes demonstrating delayed ventilation on HP ^{129}Xe-MRI.

Further analysis of CT included assessment of fissure integrity and lobar emphysema percentage. Interlobar fissure completeness was defined as the presence of >90% fissure on thin-slice CT in at least one plane (sagittal, axial or coronal views). CT prediction of collateral ventilation in pulmonary lobes was defined according to the integrity of adjacent interlobar fissures; for example, an incomplete right horizontal fissure on CT predicted collateral ventilation in the right upper and middle lobes, whereas a complete left oblique fissure predicted no collateral ventilation in the left upper and lower lobes. Since the middle lobe is adjacent to both right horizontal and oblique fissures, incompleteness of either fissure predicted the presence of collateral ventilation on CT.

The percentage of emphysema per lobe (%LAA) was calculated from CT using PTK as previously described in Section 2.7.1.

5.4.5 Statistical analysis

A priori analyses were completed to evaluate the relationship between HP ^{129}Xe-MR delayed ventilation and fissure integrity and percentage emphysema on CT. The McNemar's test (StatPlus:mac – statistical analysis program for Mac OS. Version v5, AnalystSoft.Inc.) was used to determine the association between CT predicted collateral ventilation and observed HP ^{129}Xe-MR delayed ventilation in each pulmonary lobe. Pearson's correlation coefficient was used to evaluate the relationship between CT-derived %LAA and increase in ventilation level (signal

intensity) in pulmonary lobes where delayed ventilation was detected with HP ^{129}Xe-MRI. P values less than 0.05 were considered significant.

5.5 Results

5.5.1 Subject demographics

Thirteen patients with COPD were prospectively enrolled over an 8-month period. Patient demographic data is provided in Table 5.1.

Time-resolved breath-hold HP ^{129}Xe-MR ventilation images were successfully acquired in all participants. The number of individual coronal image slices observed and number of time-points completed were determined by the subject's ability to breath-hold comfortably and are indicated in Table 5.1. The majority of subjects (n=10) were able to breath-hold for five separate time points (12 seconds).

One subject (OXF0069) completed study measures twice, once at baseline and then 6-months following a bronchoscopic procedure for coil placement to treat a right upper lobe pleural fistula. Data from both time points have therefore been included in the analysis. OXF0069 declined the NM-V SPECT scan at the 6-month follow-up and therefore HP ^{129}Xe-MRI and CT only were analysed for this study visit.

All subjects tolerated HP ^{129}Xe-MRI with no serious adverse events.

Table 5.1: Demographic data for each patient with COPD included in the study

Patient ID	Sex (M/F)	Age	Smoking status	Pack-year history	FEV_1	FEV_1/FVC	RV/TLC	FRC	TLCO	%LAA	Number of coronal HP ^{129}Xe-MR image slices	Number of time points
OXF0009	F	58	Ex-smoker	26	36	37	71	200	61	4.1	3	3
OXF0069	M	53	Ex-smoker	22	35	37	54	146	46	41.2	3	5
OXF0098	M	70	Ex-smoker	115	60	43	39	119	39	8.1	2	4
OXF0104	M	60	Ex-smoker	18	61	40	46	189	30	34	3	5
OXF0109	M	73	Ex-smoker	87	34	25	54	179	76	4.2	3	5
OXF0120	M	63	Ex-smoker	4	42	52	60	162	48	19.1	3	5
OXF0121	M	79	Ex-smoker	92	56	55	60	117	81	0.2	2	5
OXF0127	M	65	Current smoker	85	59	37	49	188	60	20.8	3	5
OXF0145	M	84	Ex-smoker	36	52	56	70	156	45	1.68	3	5

OXF0150	F	59	Ex-smoker	31	36	37	62	125	32	5.4	3	5
OXF0151	F	58	Ex-smoker	38	74	67	46	121	48	1.7	2	4
OXF0153	F	69	Ex-smoker	36	78	57	52	116	79	0.16	3	5
OXF0154	M	74	Ex-smoker	39	58	52	54	102	25	23.93	3	5
Group Mean (SD)	M: F 9:4	66.5 (8.8)	Ex: Current 12:1	48.4 (32.9)	52.4 (14.2)	45.8 (11.2)	55.2 (9.0)	147.7 (32.1)	51.5 (17.9)	5.4 (1.7/20.8)	2.8 (0.4)	4.7 (0.6)

If not otherwise stated, group mean (SD) are provided in the final row
Sex Given as M: F ratio
Smoking status Given as ex-smoker: current smoker ratio
FEV_1 = Forced expiratory volume in 1 second, FVC = Forced expiratory vital capacity, RV/TLC = Residual volume expressed as percentage of total lung capacity, FRC = Functional residual capacity, TLCO = Transfer factor of the lung for carbon monoxide, %LAA = Percentage low-attenuation areas less than -950 HU

5.5.2 HP ^{129}Xe-MR delayed ventilation

In total, 14 sets of time-resolved breath-hold HP ^{129}Xe-MR ventilation images were acquired and included in data analyses. Delayed ventilation was observed visually and quantified by an increase in ventilation level signal intensity in 13 of the 14 imaging sets acquired. Within the imaging sets where delayed ventilation was shown, an increase in ventilation level signal intensity was present in at least two and up to all five pulmonary lobes. In total, delayed ventilation was demonstrated in 42 pulmonary lobes.

HP ^{129}Xe-MR ventilation signal was not detected in pulmonary lobes on the selected coronal image slices for the following patients: -

- OXF0109 in the right middle lobe
- OXF0145 in the right middle lobe
- OXF0150 in the right middle and lower lobes
- OXF0151 in the right middle lobe.

Upon review of HP ^{129}Xe-MRI for these patients, the likely explanation is that the particular coronal image slices chosen to investigate delayed ventilation did not include coverage of those specific lobes. Accordingly, the absence of delayed ventilation in the lobes was reported in the results.

Table 5.2 provides summative results for the study cohort regarding the presence of delayed ventilation on time-resolved HP ^{129}Xe-MR ventilation imaging per pulmonary lobe and fissure integrity as assessed on CT. Individual

results, inclusive of co-registered corresponding coronal image slices from CT and NM-V are shown in Figures 5.1 – 5.12 and Appendix 8.

Table 5.2: Summative results for HP ^{129}Xe-MR delayed ventilation and CT fissure integrity

Subject	HP ^{129}Xe-MRI delayed ventilation					CT fissure completeness		
	RUL	RML	RLL	LUL	LLL	RH	RO	LO
OXF0009	Y	Y	Y	Y	Y	Y	Y	Y
OXF0069	N	Y	Y	N	Y	Y	Y	Y
OXF0069-2	Y	Y	Y	Y	Y	Y	Y	Y
OXF0098	Y	Y	N	N	Y	N	Y	Y
OXF0104	N	Y	N	N	Y	Y	Y	Y
OXF0109	N	N	Y	Y	Y	N	Y	Y
OXF0120	Y	Y	Y	Y	Y	N	Y	N
OXF0121	Y	N	N	Y	N	N	N	Y
OXF0127	Y	N	N	Y	Y	N	N	Y
OXF0145	N	N	N	N	N	N	Y	Y
OXF0150	N	N	N	Y	Y	Y	Y	Y
OXF0151	Y	N	N	Y	N	Y	Y	Y
OXF0153	N	Y	N	Y	N	N	N	Y
OXF0154	Y	Y	Y	Y	Y	N	Y	N

RUL = Right upper lobe, RML = Right middle lobe, RLL = Right lower lobe, LUL = Left upper lobe, LLL = Left lower lobe, RH = Right horizontal fissure, RO = Right oblique fissure, LO = Left oblique fissure, Y = Yes, N = No, OXF0069-***2*** = 6-month follow-up imaging

5.5.3 Co-registered NM-V and CT image slices

Corresponding co-registered coronal NM-V and CT image slices to selected time-resolved breath-hold HP ^{129}Xe-MRI slices are shown in Figures 5.2, 5.5, 5.8, 5.11 and Appendix 8. Review of NM-V imaging showed a lack of appreciable NM ventilation counts in regions where delayed ventilation was observed on

corresponding time-resolved breath-hold HP ^{129}Xe-MRI for all thirteen imaging sets. Review of CT did not reveal any differences in pulmonary structure to account for the observed HP ^{129}Xe-MR delayed ventilation. For example, the CT for OXF0150 [Figure 5.11] showed moderate centrilobular and paraseptal emphysema with upper lobe predominance. However, there was no difference in lung structure or emphysema distribution between the left upper lobe where significant delayed ventilation signal was observed after 3 seconds [Figure 5.10, slice 2] and the large ventilation defect in the right upper lobe, which did not ventilate at all.

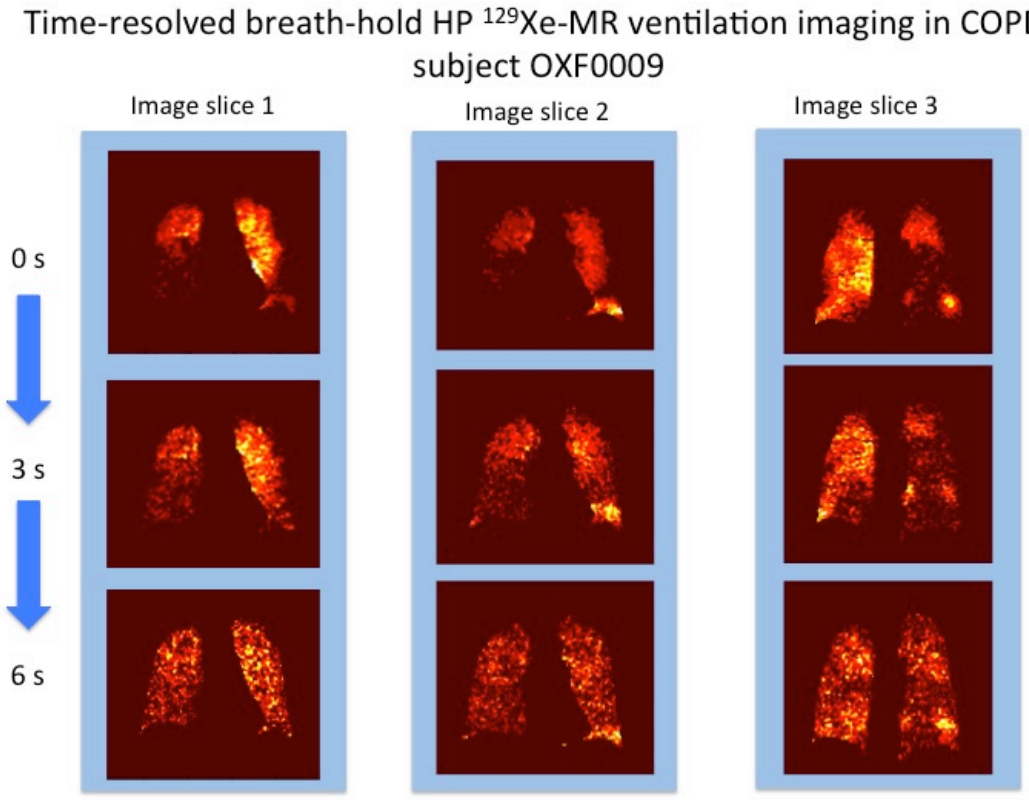

Figure 5.1: Coronal time-resolved breath-hold HP ^{129}Xe-MR ventilation imaging acquired from OXF0009. Delayed ventilation is observed in the right lower and left upper and lower zones.

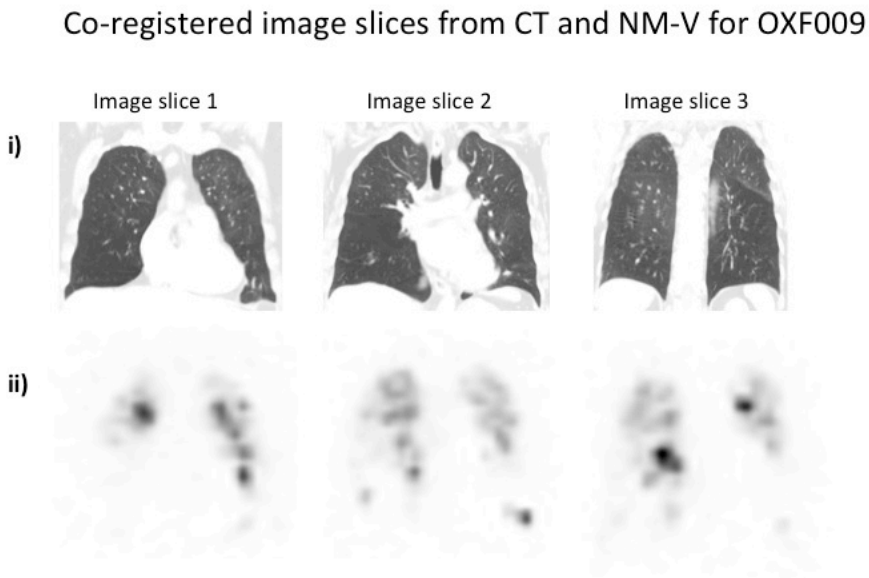

Figure 5.2: Coronal i) thoracic CT and ii) NM-V SPECT images acquired from OXF0009. Delayed ventilation is not observed with NM-V SPECT.

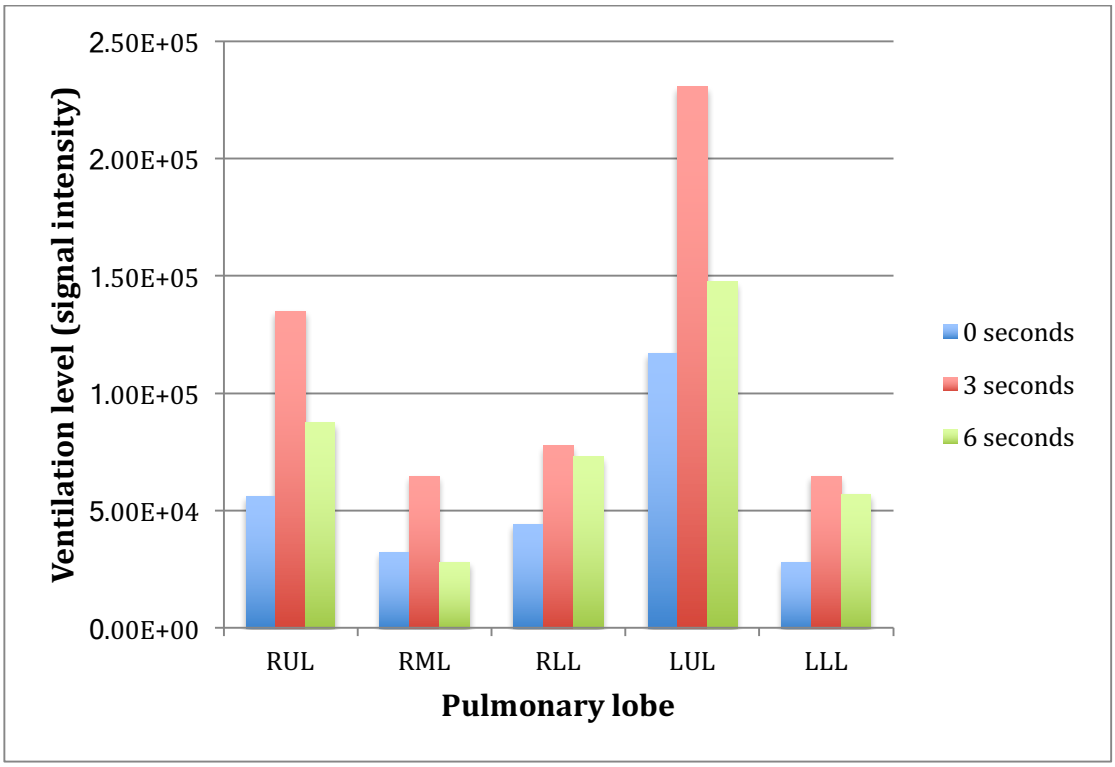

Figure 5.3: Histogram showing change in ventilation level signal intensity per pulmonary lobe during time-resolved breath-hold HP ^{129}Xe-MRI acquired from OXF0009. These data show delayed ventilation in all pulmonary lobes.

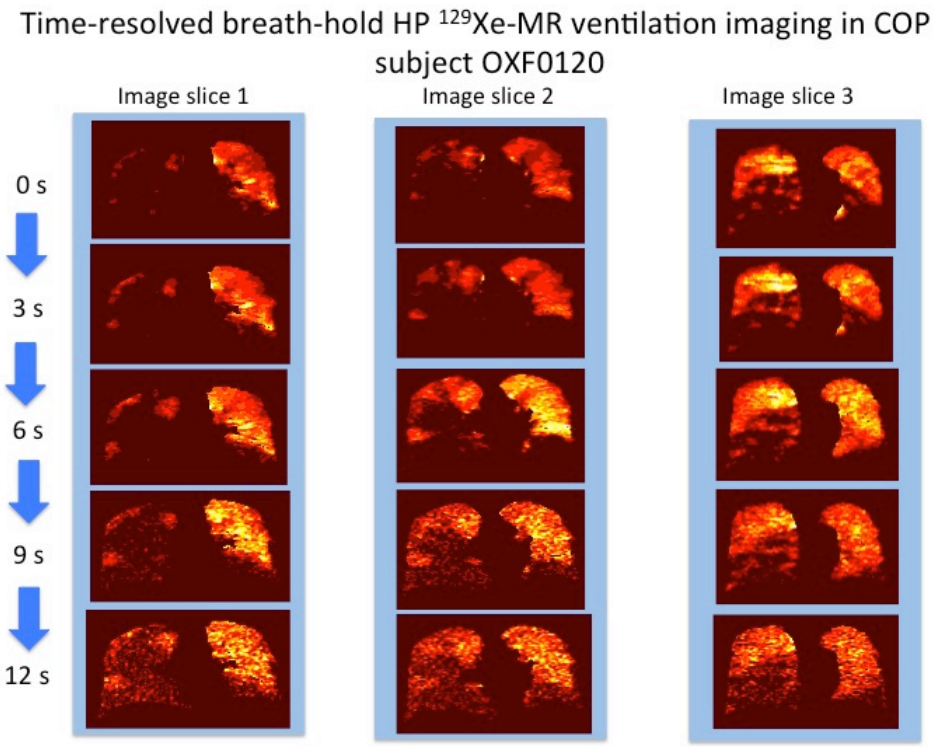

Figure 5.4: Coronal time-resolved breath-hold HP ^{129}Xe-MR ventilation imaging acquired from OXF0120. Delayed ventilation is observed in the right upper and lower and left lower zones.

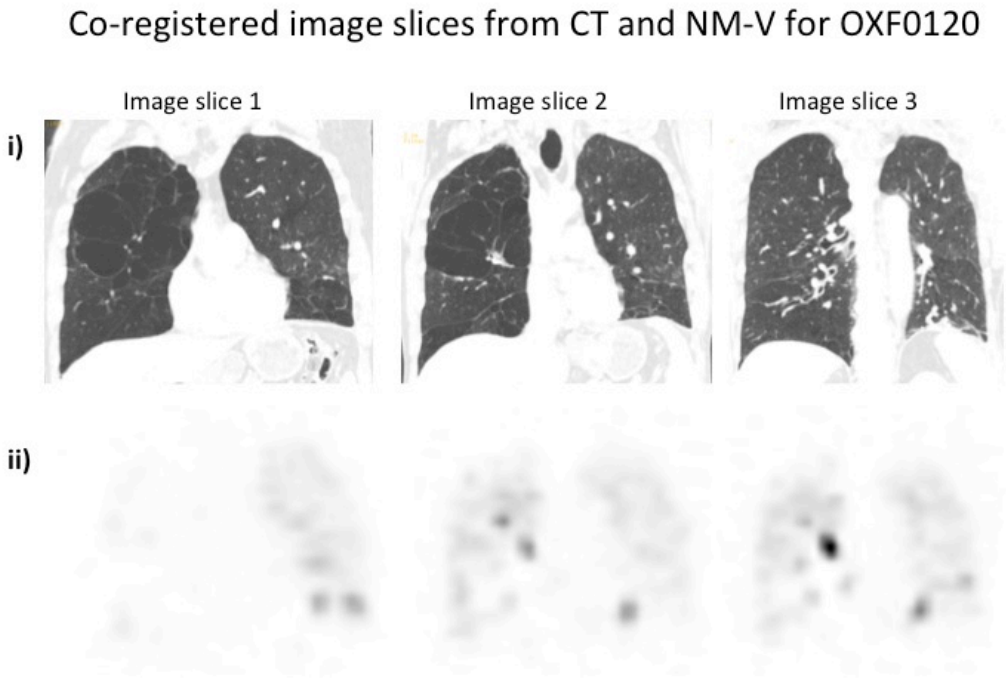

Figure 5.5: Coronal i) thoracic CT and ii) NM-V SPECT images acquired from OXF0120. Delayed ventilation is not observed with NM-V SPECT. There are

emphysematous bullae in the right mid and left lower zone on coronal CT image slice 1. However, on corresponding HP ^{129}Xe-MRI image slice 1 [Figure 5.4], delayed ventilation is appreciated in the right mid zone but not left lower zone.

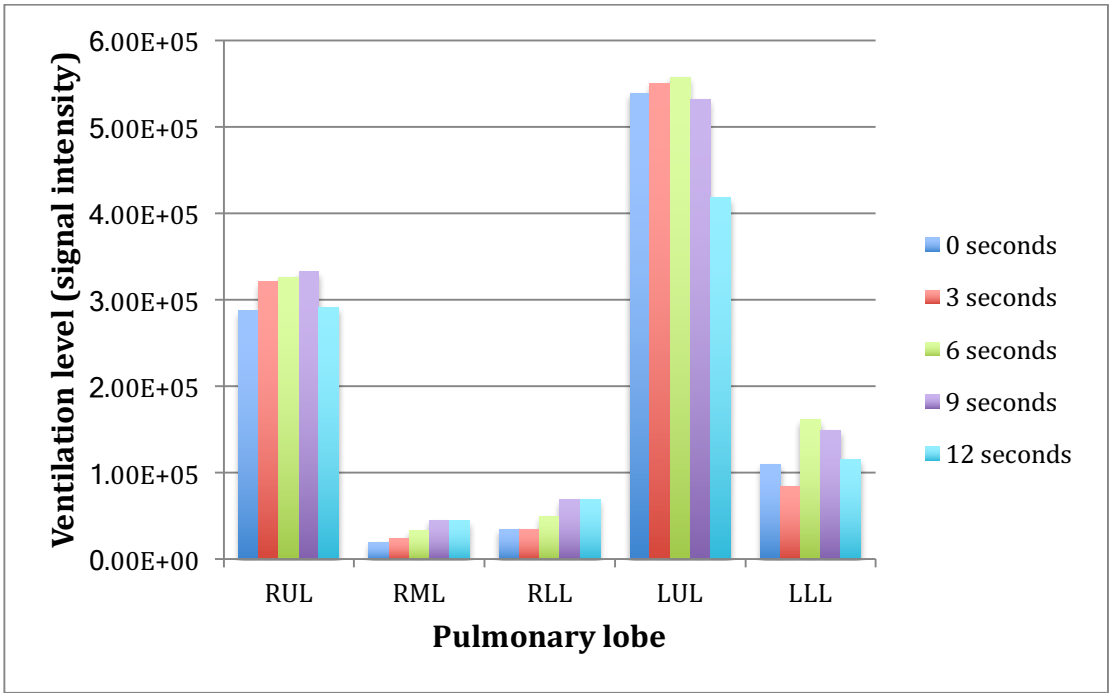

Figure 5.6: Histogram showing change in ventilation level signal intensity per pulmonary lobe during time-resolved breath-hold HP ^{129}Xe-MRI acquired from OXF0120. These data demonstrate delayed ventilation in all lobes.

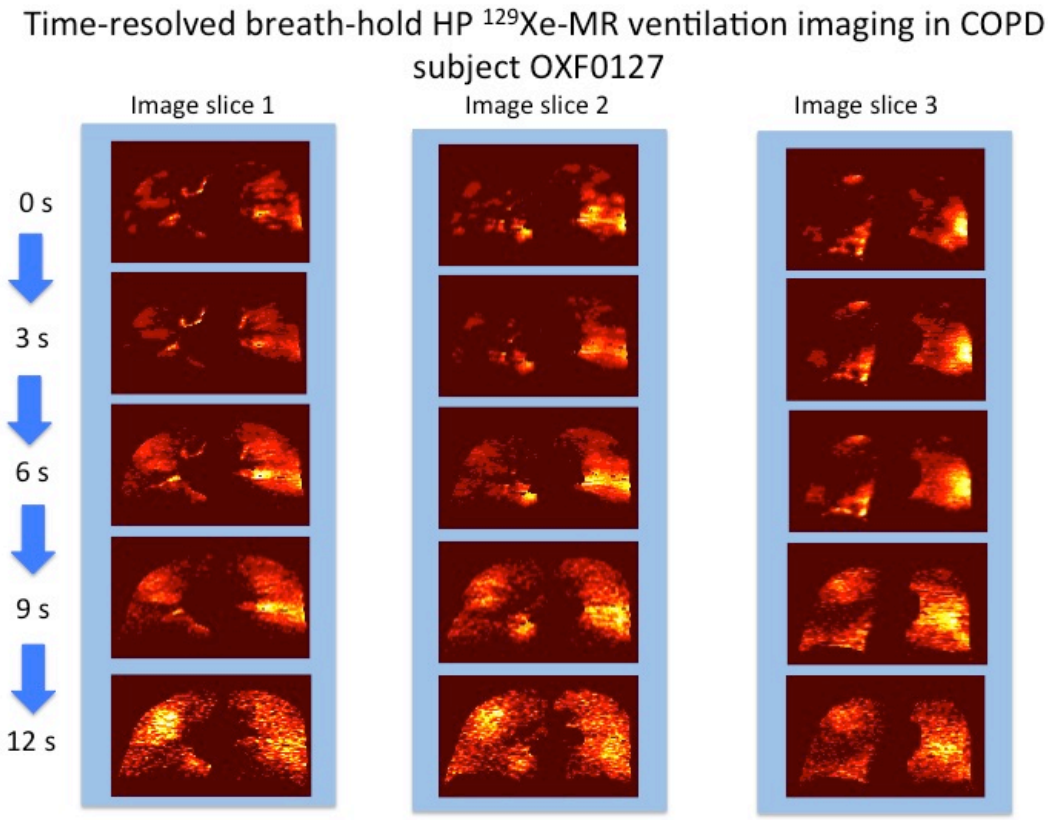

Figure 5.7: Coronal time-resolved breath-hold HP ^{129}Xe-MR ventilation imaging acquired from OXF0127. Delayed ventilation is observed in both upper zones.

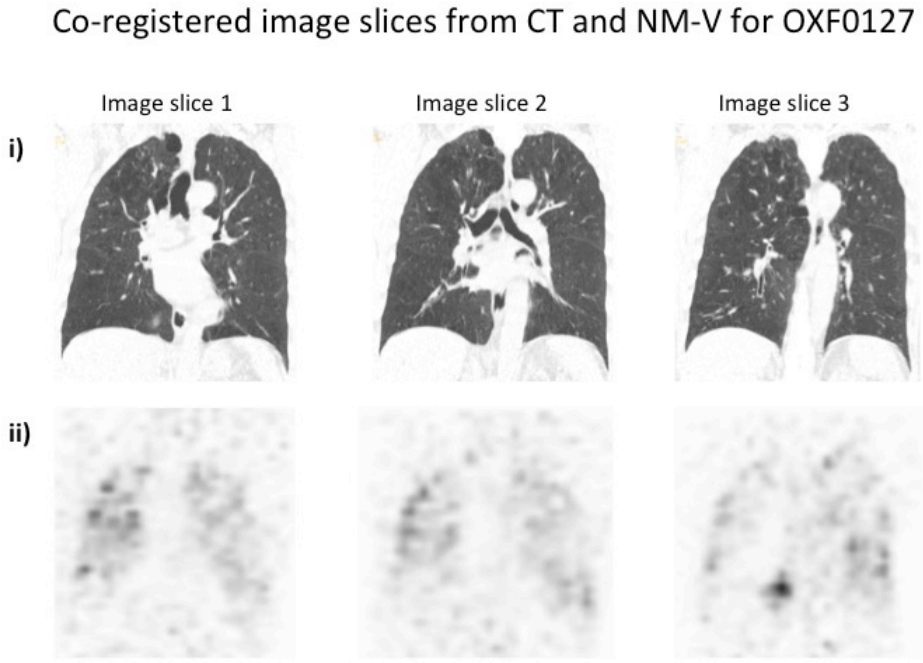

Figure 5.8: Coronal i) thoracic CT and ii) NM-V SPECT images acquired from OXF0127. Coronal CT shows moderate paraseptal and centrilobular emphysema in both upper lobes. Delayed ventilation is not observed with NM-V SPECT.

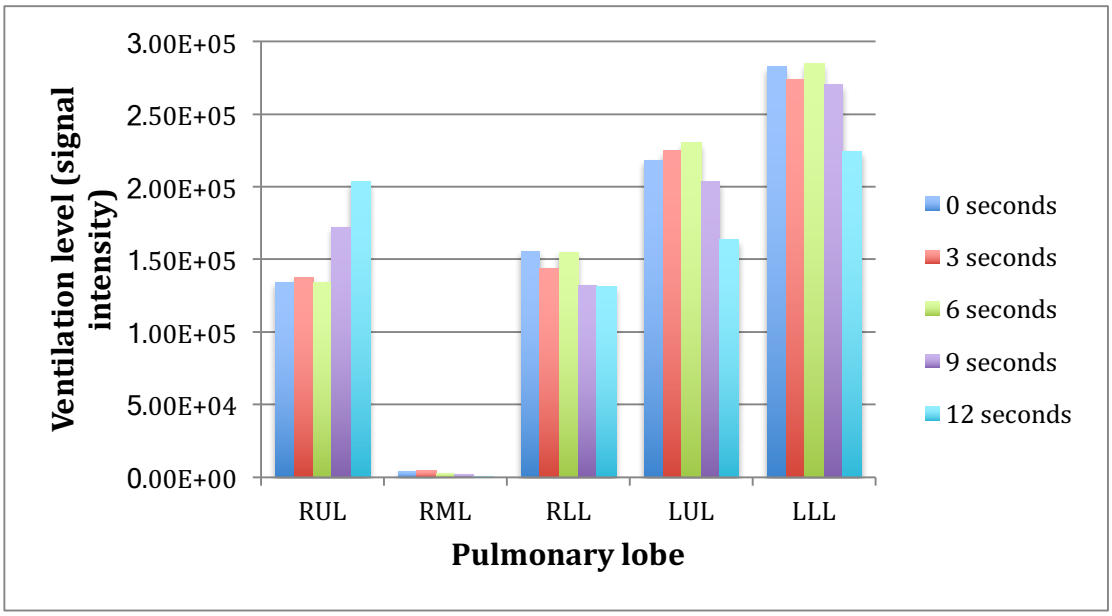

Figure 5.9: Histogram showing change in ventilation level signal intensity per pulmonary lobe during time-resolved breath-hold HP ^{129}Xe-MRI acquired from OXF0127. These data demonstrate delayed ventilation in the right and left upper lobes.

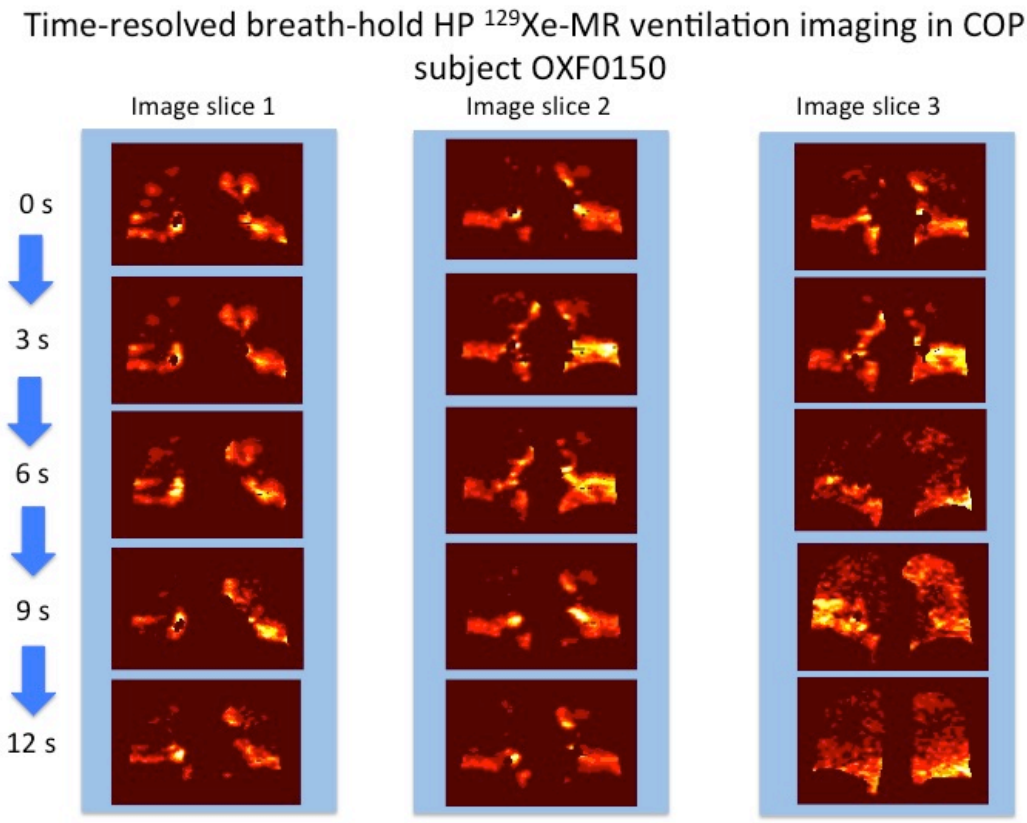

Figure 5.10: Coronal time-resolved breath-hold HP ^{129}Xe-MR ventilation imaging acquired from OXF0150. Delayed ventilation is observed in the left upper and lower lobes [Image slice 3].

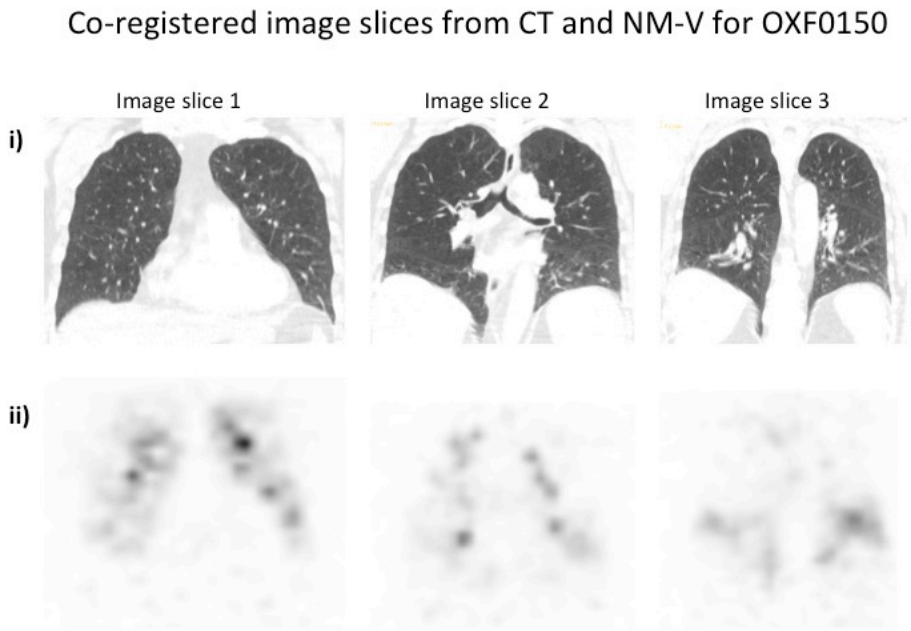

Figure 5.11: Coronal i) thoracic CT and ii) NM-V SPECT images acquired from OXF0150. The delayed ventilation observed with HP ^{129}Xe-MRI in left upper and lower zones is not appreciated with NM-V SPECT. Coronal CT showed moderate emphysema in both upper lobes.

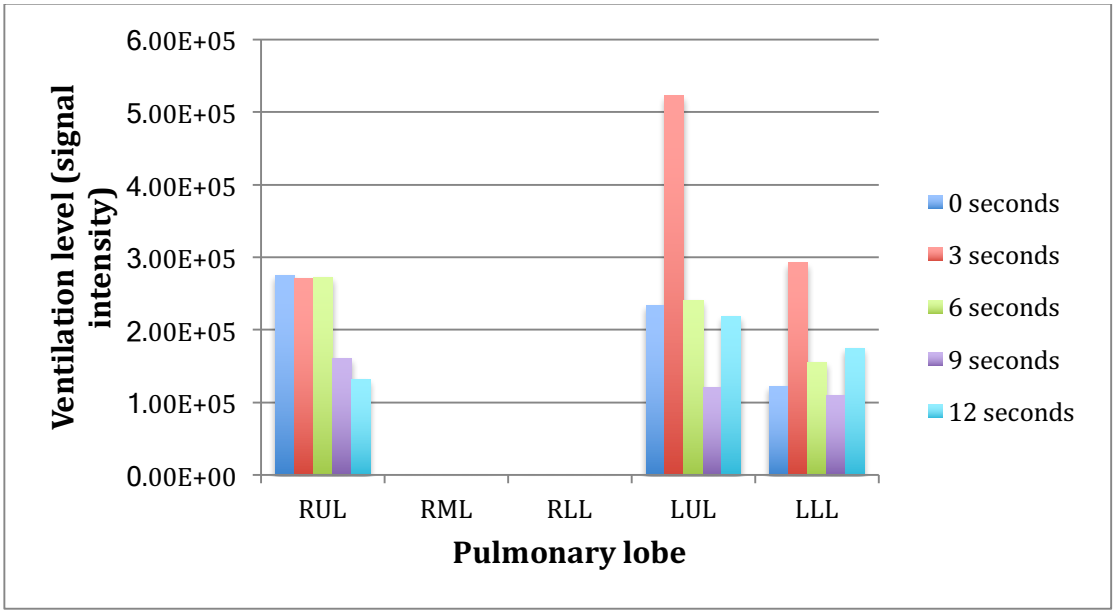

Figure 5.12: Histogram showing change in ventilation level signal intensity per pulmonary lobe during time-resolved breath-hold HP ^{129}Xe-MRI acquired from OXF0150. These data show delayed ventilation in the left lung.

5.5.4 CT fissure integrity

On the basis of CT fissure integrity evaluation alone, collateral ventilation was predicted in 23 (33%) pulmonary lobes and was not expected in 47 lobes (67%). However, in the 23 pulmonary lobes predicted to show collateral ventilation by CT, 13 (57%) actually demonstrated delayed ventilation on time-resolved HP ^{129}Xe-MR ventilation imaging. Similarly in the 47 pulmonary lobes where CT predicted no collateral ventilation, only 18 (38%) did not demonstrate delayed ventilation on HP ^{129}Xe-MRI.

Table 5.3 includes the results per pulmonary lobe from McNemar's test with continuity correction comparing collateral ventilation predicted from CT fissure integrity and delayed ventilation observed with HP ^{129}Xe-MRI. In the study cohort, there was no association between CT predicted collateral ventilation and HP ^{129}Xe-MRI delayed ventilation in the right upper, middle or lower lobes. However, there was a statistically significant association between CT predicted collateral ventilation and HP ^{129}Xe-MRI delayed ventilation in the left upper and lower lobes (χ^2 =6.13, p=0.01 and χ^2 =6.13, p=0.01).

Table 5.3: McNemar's test for association between collateral ventilation predicted by CT fissure integrity and observed HP ^{129}Xe-MR delayed ventilation

McNemar's test	Pulmonary lobe				
	RUL	RML	RLL	LUL	LLL
χ^2	0.17	0.13	0.444	6.13	6.13
Two-tailed P value	0.68	0.72	0.51	0.013*	0.013*

* Statistically significant P-value, RUL = Right upper lobe, RML = Right middle lobe, RLL = Right lower lobe, LUL = Left upper lobe, LLL = Left lower lobe

5.5.5 CT percentage emphysema

The Pearson's correlation coefficients between CT-derived emphysema and HP ^{129}Xe-MR delayed ventilation according to pulmonary lobe are shown in Table 5.4. There was no correlation between CT-derived emphysema and delayed ventilation in the pulmonary lobes where this was demonstrated with HP ^{129}Xe-MRI. The Pearson's correlation coefficient between emphysema and delayed ventilation in the right upper lobe was relatively high (r=0.6), however, this did not reach statistical significance.

Table 5.4: Pearson's correlation coefficients for CT-derived percentage emphysema and HP ^{129}Xe-MR delayed ventilation

Pearson's correlation coefficient (r=) between % LAA and HP ^{129}Xe-MR delayed ventilation (increase in ventilation level signal intensity)	**Pulmonary lobe**				
	RUL (n=8)	RML (n=8)	RLL (n=6)	LUL (n=10)	LLL (n=10)
	0.60 (p=0.12)	0.21 (p=0.62)	0.31 (p=0.55)	0.41 (p=0.23)	-0.065 (p=0.86)

RUL = Right upper lobe, RML = Right middle lobe, RLL = Right lower lobe, LUL = Left upper lobe, LLL = Left lower lobe

5.6 Discussion

This chapter has shown that time-resolved breath-hold HP ^{129}Xe-MR ventilation imaging is feasible in patients with COPD. The majority of patients (79%) successfully held their breath to allow image acquisition for five time-points over a 12-second duration.

5.6.1 Delayed ventilation is observed with HP ^{129}Xe-MRI

Delayed ventilation was demonstrated in 93% of the time-resolved HP ^{129}Xe-MR imaging sets completed. The delayed ventilation observed visually and objectively quantified may represent a number of processes including collateral ventilation, partial obstruction, gas trapping, narrowing of the peripheral airways or a combination of these. If the delayed ventilation observed does represent collateral ventilation, this may be due to gas moving freely between pulmonary lobules (intralobar) or between lobes (interlobar). The disease process of emphysema likely contributes to development of collateral pathways since destruction of alveolar walls and changes in mechanical strain(359) can lead to the formation of new channels or enlargement of existing channels thereby reducing their inherent resistance. Ventilation may occur preferentially via these collateral channels in emphysema, since they provide a pathway of much reduced airflow resistance when compared to the segmental airways where flow resistance in markedly increased due to expiratory collapse and mucus plugging(359, 360).

The current findings are consistent with the 8 out of 10 patients with COPD previously reported to show delayed ventilation with HP ^{3}He-MRI(411). In the previous study, time-resolved HP ^{3}He-MRI was used to determine the presence and pattern of delayed filling of ventilation defects. It was suggested that the pattern of ^{3}He filling with visible progression from edges towards the centre observed in 8 defects represented intersegmental collateral ventilation(411). Ventilation mapping using HP ^{3}He-MRI has shown a heterogeneous distribution of fractional ventilation in COPD patients, along with areas of high fractional ventilation parameter *r*, near ventilation defects, which has been suggested to indicate gas transport between well-ventilated and poorly ventilated regions of the lung(417).

The methodology employed in this chapter has quantified delayed ventilation according to pulmonary lobe rather than within a region-of-interest (ROI) representative of a ventilation defect. The rationale behind this was to objectively quantify ventilation signal increase within specific pulmonary lobes thereby providing potential evidence of interlobar collateral ventilation. Arguably interlobar collateral ventilation is of greatest significance in treatment planning for lung volume reduction(418). It is therefore possible that the method presented will provide a potentially clinically relevant assessment of delayed and collateral ventilation in subjects considered for LVRT. HP ^{129}Xe-MRI is non-invasive, exposes the patient to no radiation and may be performed repeatedly, potentially immediately after LVRT to determine its efficacy. This may allow early treatment modifications or allow thoracic surgeons to inform patients of the likely success of their intervention.

5.6.2 CT predicted collateral ventilation is associated with HP ^{129}Xe-delayed ventilation in the left lung

Additional analyses included the comparison of time-resolved HP ^{129}Xe-MR ventilation imaging with fissure integrity on CT. There was significant association between CT predicted collateral ventilation and delayed ventilation observed with HP ^{129}Xe-MRI in the left upper and lower lobes. However, no such association was found in the right upper, middle and lower lobes. The literature is conflicted about the accuracy of evaluation of fissures on HRCT and ability to predict collateral ventilation and LVRT outcome.

HRCT fissure analysis has been reported to be equally effective as Chartis assessment in the prediction of response to endobronchial valve treatment(400). In contrast, equivocal response to volume reduction therapy using a polymer sealant has been shown irrespective of fissure integrity(401).

In comparison with direct observation during thoracic surgery, CT was reported to overestimate integrity of the right horizontal fissure and underestimate right oblique fissure completeness(398). This supports the current finding of poor association between CT predicted collateral ventilation and HP ^{129}Xe-MR specifically within the right pulmonary lobes. No correlation between collateral ventilation and interlobar fissure integrity on histology has also been reported(399). Furthermore, poor inter-observer correlation has been shown between a respiratory physician, general radiologist and experienced chest radiologist for CT fissure evaluation in patients with emphysema(419).

Previous investigation has also shown a lack of correlation between CT fissure integrity with both GOLD criteria and pulmonary function test results, suggesting that the development of COPD is not specifically related to fissure integrity(420). It was suggested that collateral ventilation might in fact be a more complex process, not simply evaluated by fissure completeness. Consistent with this are reports of significant collateral ventilation demonstrated on Chartis despite intact interlobar fissures on CT and subsequent reduced response to endobronchial valve treatment in some patients(391). It is possible direct visualisation of delayed ventilation using HP ^{129}Xe-MRI may prove a more reliable imaging tool for assessment of collateral ventilation and subsequent LVRT response than CT.

5.6.3 CT-derived emphysema does not correlate with HP ^{129}Xe-MR delayed ventilation

There was no correlation between CT-derived percentage emphysema and delayed ventilation in the pulmonary lobes where this was demonstrated with HP ^{129}Xe-MRI. There are differing reports within the literature regarding the relationship between CT-derived emphysema and collateral ventilation and the ability of emphysema heterogeneity to predict LVRT outcome. Previous ex-vivo assessment of seventeen lungs from patients with smoking-related severe emphysema demonstrated greater collateral ventilation in patients with homogeneous emphysema(399). The results from the current study cannot be directly compared since %LAA and HP ^{129}Xe-MR delayed ventilation were

correlated on a lobar basis rather than evaluation of whole lung emphysema heterogeneity based on radiological scores and collateral ventilation determined via bronchoscopy. Despite this, qualitative evaluation of pulmonary structure on corresponding co-registered CT image slices showed no difference, specifically in emphysema distribution to account for the observed HP ^{129}Xe-MR delayed ventilation in some lobes and absence in others.

The general consensus is that LVRS outcomes are better in patients with heterogeneous emphysema, specifically involving the upper lobes, than in individuals with diffuse homogeneous emphysema(421, 422). In contrast, the importance of emphysema heterogeneity in bronchoscopic lung volume reduction remains uncertain(381, 423-425). It has been reported that emphysema heterogeneity is not critical for positive endobronchial valve placement outcomes(387). In contrast, a recent RCT has demonstrated significant improvements in lung function following unilateral endobronchial valve placement in patients with heterogeneous emphysema and intact interlobar fissures(391).

Although HP ^{129}Xe-MR diffusion-weighted imaging was not acquired in this chapter, the method for generating lobar HP ^{129}Xe-MR ADC values has been previously described [Section 2.6.6, Section 4]. Lobar ADC values would enable characterisation of pulmonary structure, specifically the heterogeneous or homogeneous distribution of emphysema in potential LVRT candidates. This would provide complementary information to the observed HP ^{129}Xe-MR delayed ventilation in these patients.

5.6.4 Delayed ventilation observed with HP ^{129}Xe-MRI is not appreciated on NM-V SPECT

Static HP ^{129}Xe-MR ventilation images were acquired during the same scanning session as time-resolved imaging. Static HP ^{129}Xe-MR ventilation imaging involves high-resolution, multislice acquisition of the whole lung during a single breath-hold. It does not therefore incorporate any time-resolved aspect and cannot determine changes over time. The delayed ventilation demonstrated with time-resolved HP ^{129}Xe-MRI was not present on static ventilation HP ^{129}Xe-MRI in any data set [Figures 5.1, 5.4, 5.7 and 5.10]. It is possible that the time a specific image slice is acquired during static HP ^{129}Xe-MRI will influence the detection of delayed ventilation. For example, if the slice is acquired at the start of the breath-hold it is likely no delayed ventilation is detected and ventilation defects remain void of signal. In contrast, if the same image slice is acquired later in the breath-hold, delayed ventilation may have occurred by then and be readily observed from the increase in signal intensity.

The delayed ventilation depicted by time-resolved HP ^{129}Xe-MR ventilation imaging is not appreciated on NM-V. NM-V has lower temporal and spatial resolution than HP ^{129}Xe-MRI. NM-V was acquired during tidal breathing whereas HP ^{129}Xe-MRI was acquired during a single breath-hold. In addition, the radiotracer (^{99m}Tc-DTPA) administered for NM-V SPECT is composed of a relatively large particle size resulting in the main pattern of ventilation being via convective flow rather than diffusion. These combined factors may have contributed to the lack of observation of delayed ventilation with NM-V.

Since NM-V images are acquired over an approximate 20-minute duration, it is unlikely that this technique would be sensitive to the maximal delayed ventilation observed in the majority of patients within 9 seconds. If the delayed ventilation detected by HP ^{129}Xe-MRI does represent collateral ventilation, it is also plausible that both increase and decrease in signal intensity may be observed over a longer period of time as HP ^{129}Xe gas moves in and out of initially non-ventilated regions via the dynamic process of collateral flow.

5.6.5 Technical factors

Previous investigation of delayed ventilation with HP ^{3}He-MRI included imaging up to 6 time-points over a 19.3 second breath-hold. In comparison, the method employed in the current study included fewer time-points (up to five) over a shorter breath-hold (12 seconds). Maximal delayed ventilation was observed in 71% of patients by time-point 3 (6 seconds) suggesting there is further potential to optimise the time-resolved HP ^{129}Xe-MR sequence. For example, the sequence could be developed to include more time-points with shorter intervals (<3 seconds) to focus on observed maximal delayed ventilation. Alternatively a reduced total number of time-points could be adopted to increase the spatial resolution of images instead.

Ventilation signal was not detected in particular lobes for four patients included in the study. Whilst the most likely reason for this is non-coverage of the lobes in the coronal HP ^{129}Xe-MR image slices selected for investigation, inaccurate

automated lobar segmentation may have also been a contributory factor. Review of time-resolved breath-hold HP 129Xe-MR imaging supported non-coverage of pulmonary lobes rationale, however potential technical limitations of the PTK automated segmentation algorithm should be considered for future work.

5.6.6 Limitations

There are a number of limitations associated with the study. Despite the small sample size, five patients included would have been considered for endobronchial valves according to criteria from previous randomised controlled trials(386, 391); FEV_1 <50% predicted, TLC >100% predicted, RV >150% predicted and TLCO >20% predicted.

Participants did not undergo direct measurement of collateral ventilation with the Chartis system. The HP ^{129}Xe-MR delayed ventilation observed cannot therefore be confirmed to exclusively represent collateral ventilation. However, the association between HP ^{129}Xe-MR delayed ventilation and CT fissure integrity in the left lung has been described providing supplementary evidence for the potential of the technique to demonstrate collateral ventilation.

Delayed ventilation was quantified according to pulmonary lobes in up to three selected coronal image slices per participant. Although coronal image slices were selected to incorporate the largest ventilation defects at baseline, the method could be improved by complete 3-D lung coverage. The HP ^{129}Xe-MR sequence

employed was restricted by breath-hold but optimisation may allow for full lung coverage in the future.

The single-breath-hold HP ^{129}Xe-MRI acquisition method may be criticised for incomplete assessment of collateral ventilation, which has been described as a dynamic process and therefore better assessed during a normal breathing cycle. Unfortunately due to the inherent limitations of HP ^{129}Xe-MRI, this is not currently feasible and would require continued administration of hyperpolarised ^{129}Xe gas to overcome signal loss associated with the imaging procedure and natural T_1 relaxation processes due to the presence of oxygen(243).

5.6.7 Future work

Future work should be aimed to demonstrate that the delayed ventilation shown using HP ^{129}Xe-MR corresponds to collateral ventilation measured directly using the Chartis system. Subsequent pre-assessment of patients considered for LVRT with time-resolved breath-hold HP ^{129}Xe-MR ventilation imaging may help stratify individuals more effectively. For example, extensive delayed ventilation on HP ^{129}Xe-MRI may indicate that patients should not proceed for treatment; whereas the absence of HP ^{129}Xe-MR delayed ventilation may identify individuals who should proceed to Chartis assessment and then LVRT. This strategy would potentially improve patient selection and reduce the number of invasive Chartis procedures performed in patients who are ultimately precluded from LVRT.

Although this chapter has quantified delayed ventilation per lobe using HP ^{129}Xe-MRI, collateral ventilation is a continuous variable as such the mere presence or absence is insufficient to improve patient selection for LVRT. Future work is needed to quantify a threshold of delayed/collateral ventilation above which LVRT is unlikely to be successful.

5.6.8 Conclusion

In conclusion, time-resolved breath-hold HP ^{129}Xe-MR ventilation imaging is a feasible technique to demonstrate delayed ventilation on a lobar basis in patients with COPD. The delayed ventilation demonstrated with HP ^{129}Xe-MRI was not observed with NM-V. A significant association between CT predicted collateral ventilation and delayed ventilation observed with HP ^{129}Xe-MRI was found in the left lung only. Future work may confirm that the observed delayed ventilation represents collateral ventilation and subsequently identify a potential role for HP ^{129}Xe-MRI to improve patient selection and treatment efficacy evaluation in LVRT.

6 Chapter 6: Measuring the effects of intervention with HP ^{129}Xe-MRI

6.1 Background

6.1.1 Management of COPD

According to National Institute for Health and Care Excellence (NICE) guidance, short-acting bronchodilators are recommended as the initial empirical treatment for relief of dyspnoea and exercise limitation in COPD(5). Despite characterisation of COPD by the presence of airflow limitation with limited or no reversibility, bronchodilators remain first line pharmacotherapy(426, 427). The most common bronchodilators used include short-acting ß$_2$-agonists and short-acting anticholinergics, also referred to as muscarinic antagonists. Short-acting ß$_2$-agonists, for example salbutamol, act directly on bronchial smooth muscle to cause bronchodilation, whereas anticholinergics act by inhibiting resting bronchomotor tone.

NICE guidance for bronchodilator use in COPD is based on studies showing improved daily dyspnoea scores(428) and quality of life(429) following short-acting ß$_2$-agonist administration. However, the guidance also acknowledges that "clinical benefits may be seen without clear changes in the FEV_1"(5). There is a significant body of evidence demonstrating poor correlation between spirometry and clinical measurements of COPD, particularly dyspnoea and exercise

tolerance(430-432) and conversely several studies have reported symptomatic relief in patients following bronchodilator use with only modest improvements in FEV_1(433-435).

6.1.2 Spirometry in diagnosis and reversibility testing of COPD

Post-bronchodilator spirometry is recommended for the diagnosis and assessment of severity of COPD(5). Although historically reversibility testing has also been advised in COPD(426, 436), this is no longer advocated. The inherent limitations of reversibility testing are now well recognised, including significant variation in FEV_1 change following bronchodilator both between patients and within patients tested on different days(437-439). Different inspiratory manoeuvres performed before and after bronchodilator administration also impact on FEV_1, leading to variable reversibility results(440). Reversibility testing to predict response to long-term treatment in COPD is no longer recommended(5, 75), since response to a short course of oral steroids does not predict long-term therapy outcomes(441). Despite, the acknowledged limitations of spirometry in reversibility testing, FEV_1 remains the most common end-point for clinical trials evaluating therapeutic response in COPD.

6.1.3 Methods for evaluating bronchodilator response

There are several published criteria for assessing FEV_1 bronchodilator responsiveness in COPD: $\geq$ 12% and $\geq$ 200 mL improvement(442-444); $\geq$ 15 %

increase over baseline(445, 446); and ≥ 10% absolute increase in the percentage predicted value(437, 447).

The discordance between spirometry, COPD symptoms and functional outcome measures prompted investigation into new methods(448, 449) and non-invasive imaging(450-453) as alternative end-points for bronchodilator response. Detailed information about regional pulmonary response rather than global, whole lung response is critical to treatment evaluation in heterogeneous lung diseases such as COPD, asthma and cystic fibrosis.

CT-derived airway morphology showed changes post-salbutamol(450, 451) and tiotropium(452, 453) and demonstrated greater post-bronchodilator response in COPD patients characterised by predominant airway disease compared with those with a predominant emphysema phenotype(454). Three dimensional-CT analysis of airway inner luminal area detected significant bronchodilation in COPD patients one-week post-combination inhaled therapy, when the average improvement in FEV_1 was a modest 180 mL(455).

The effects of tiotropium on ventilation heterogeneity have been observed using NM-V SPECT/CT and multiple breath nitrogen wash-out with significant change reported post-treatment(456).

Oxygen-enhanced MRI (O_2-MRI) can feasibly be used to detect changes in lung function after treatment in COPD(457). Changes in both FEV_1 and O_2-MRI biomarkers were reported following a single dose of long-acting ß$_2$-agonist and

8-week treatment with combined corticosteroid and bronchodilator(457). However, the statistical significance of therapeutic effect as measured by FEV_1 was greater than O_2-MRI biomarkers, indicating an inherent variability in the imaging technique.

6.1.4 Use of hyperpolarised gas MRI in assessment of therapeutic response

The majority of hyperpolarised gas MR imaging studies investigating effects of treatment in pulmonary disease have been with ^{3}He in cohorts of less than fifteen patients to date(158, 458-461).

6.1.5 Asthma

Previous HP ^{3}He-MR imaging studies in asthma have shown changes in ^{3}He gas distribution following bronchial provocation with methacholine and exercise(462, 463). Furthermore, the ventilation defects revealed by provocation were reversed by inhaled bronchodilator(462).

A prospective, double-blind controlled study of thirteen patients with exercise-induced bronchoconstriction compared HP ^{3}He-MRI with spirometry under challenge and therapy with oral montelukast(464). Expected decreases in HP ^{3}He-MR ventilation volume and FEV_1 occurred in response to exercise challenge after placebo, both of which were significantly mitigated after treatment with montelukast(464).

6.1.6 COPD

A small cohort of ex-smokers with COPD (n=10) was observed with HP ^{3}He-MRI pre and post-salbutamol to determine the effects on ventilation(335) and diffusion-weighted imaging(334). The effect of salbutamol on HP ^{3}He-MR ventilation imaging was compared with spirometry and although both significantly changed from pre- to post-treatment, the magnitude of treatment effect size was greater for HP ^{3}He-MRI(335).

The mean whole lung HP ^{3}He-MR ADC value was reported as unchanged post-salbutamol in ten patients with COPD(334). No significant difference was found between the mean ADC value of lung regions that were newly ventilated, and those that remained ventilated post-salbutamol(334). Taken together, the findings suggested that the lung regions probed post-salbutamol were not more emphysematous than those that were ventilated pre-salbutamol.

6.1.7 Cystic Fibrosis

Regional changes in ventilation have also been demonstrated with HP ^{3}He-MRI in patients with cystic fibrosis following interventions(465), ranging from bronchodilator(460), chest physiotherapy(461, 466) and a new drug treatment to target specific genetic mutations, Ivacaftor(467, 468).

6.1.8 Effects of salbutamol on HP ^{129}Xe-MRI

Published literature describing the effects of salbutamol on HP ^{129}Xe-MRI is sparse. A study comparing HP ^{3}He- and ^{129}Xe-MR ventilation imaging pre- and post-bronchodilator in seven patients with asthma, showed significantly greater ventilation defect percentage (VDP) with ^{129}Xe than ^{3}He before salbutamol administration(469). VDP improved post-salbutamol with both HP gases. The authors suggested HP ^{129}Xe-MRI might reveal ventilation abnormalities that are otherwise not observed with HP ^{3}He-MRI(469).

6.2 Hypothesis

The reproducibility of static ^{129}Xe-MR ventilation imaging and analysis according to pulmonary lobes has been described in Section 4.5, 4.6.2. The proposed work in this chapter will extend these findings to determine whether ^{129}Xe-MRI is sensitive to changes in regional lung function post-bronchodilator in COPD.

This chapter will test the hypothesis that HP ^{129}Xe-MRI can demonstrate regional changes in static ventilation post-salbutamol in patients with COPD.

6.3 Aims

The aim of this chapter is to evaluate the effects of inhaled salbutamol on regional ventilation in patients with COPD using HP ^{129}Xe-MRI.

6.4 Materials and Methods

6.4.1 Subjects

The study was approved by the NRES South Central Committee (Berkshire) [REC reference 11/SC/0488] and written informed consent was obtained from study participants.

Four patients diagnosed with COPD were prospectively enrolled between 20th January 2016 and 16th March 2016 from a tertiary referral centre.

Inclusion criteria: -

- At least mild disease (stage II-IV on GOLD criteria classification [Appendix 5], FEV_1<80% predicted and FEV_1/ FVC<70%)
- Significant smoking history (>15 pack years)
- Over the age of 18 and able to give informed consent.

Study exclusion criteria: -

- Known hypersensitivity to salbutamol or to any of its excipients
- Inability to omit long-acting bronchodilators for 24 hours prior to, and short-acting bronchodilators on the morning of, the study until measurements are complete
- Co-existent cardio-pulmonary disease that predominates over COPD and might confound results interpretation (for example asthma, bronchiectasis, cystic fibrosis, lung cancer, uncontrolled heart failure,

frequent unstable angina, respiratory muscle weakness).

Patients were required to omit long acting ß$_2$-agonists (e.g. serevent) and antimuscarinics (e.g. tiotropium) for 24 hours in advance of the study visit, and short acting ß$_2$-agonists (e.g. salbutamol and atrovent) on the day until study measures were complete. This temporary omission of bronchodilators is well tolerated without adverse symptoms in patients with stable COPD, given the minimal airway reversibility in this patient group(335). Safe refrainment from bronchodilators in patients with stable COPD has been reported previously in several imaging studies(334, 335, 455). The approved study protocol is appended [Appendix 6].

6.4.2 Study measures

Participants completed static HP ^{129}Xe-MR ventilation imaging, spirometry and dyspnoea-12 questionnaires pre- and a mean of 17 minutes ±4 (standard deviation) post-salbutamol. QCT was completed during the same study visit. Details of all study measures are provided in Section 2.

Study measures were completed during disease stability as defined by participants remaining exacerbation-free for at least 4-weeks with no change to their regular medications prior to completion of imaging and spirometry. Imaging was analysed blinded to clinical data, spirometry and time-point. The time point i.e. pre- and post-salbutamol imaging was randomised to reduce potential measurement bias.

6.4.3 Salbutamol

Ten puffs of salbutamol (AirSalb CFC-free inhaler 100 microgram/dose, Sandoz Limited, Frimley, Camberley, Surrey, UK) were administered from an MDI (metered dose inhaler) and inhaled by patients via a spacer device (AeroChamber plus, Trudell Medical International Europe Limited, Nottingham, UK).

6.4.4 Spirometry analysis

The absolute change (**Δ**) in FEV_1 and FVC was calculated by subtraction of pre-salbutamol from post-salbutamol volumes in litres. **Δ** FEV_1 and **Δ** FVC was also calculated as percentage change from baseline absolute value in litres.

6.4.5 MRI analysis

Analysis of static HP ^{129}Xe-MR ventilation data was performed using PTK as detailed previously in Section 2.6.6. Whole lung and lobar ventilated volume percentage was calculated for pre- and post-salbutamol HP ^{129}Xe-MR ventilation imaging. Reproducibility of automated lobar analysis of HP ^{129}Xe-MRI has been reported in Section 4.5, 4.6.2. The change in HP ^{129}Xe-MR ventilation imaging (**Δ** HP ^{129}Xe-MRI) was calculated by subtracting the percentage ventilated volume pre-salbutamol from post salbutamol on a whole lung and lobar basis.

6.4.6 QCT analysis

The percentage of emphysema per lung and according to pulmonary lobe (%LAA) was calculated from CT using PTK as previously described in Section 2.7.1.

6.4.7 Statistical analysis

The small sample size prevented conclusive formal statistical analyses. However, a priori Pearson's correlation coefficients (Excel 2011, Microsoft) were calculated to evaluate the trend between: -

1. Change in whole lung HP ^{129}Xe-MR ventilated volume percentage and change in FEV_1 and FVC from pre- to post-salbutamol
2. Change in whole lung HP ^{129}Xe-MR ventilated volume percentage and change in dyspnoea-12 questionnaire scores from pre- to post-salbutamol.

In these statistical analyses, results were considered significant when the probability of making a type I error was less than 5% (p values <0.05).

6.5 Results

Static HP ^{129}Xe-ventilation imaging pre- and post-salbutamol was completed in four patients with COPD with no serious adverse events. Demographic data for the four patients are shown in Table 6.1.

Table 6.1: Demographic data of patients with COPD included in the study

Parameter	**Participant ID**			
	OXF0068	**OXF0086**	**OXF0113**	**OXF0136**
Age (years)	74	72	67	72
Sex	Female	Male	Female	Female
Body mass index (kg/m^2)	27.9	31.6	29	33.2
GOLD classification	III	II	II	III
Smoking status	Ex-smoker	Ex-smoker	Current smoker	Ex-smoker
Pack-year history	111	62	81	69
FEV_1 (L)	0.85	1.64	1.24	0.68
FEV_1 (% predicted)	42	65	58	35
FVC (L)	1.54	3.55	2.22	1.31
FVC (% predicted)	63	108	87	55
FEV_1/FVC (%)	66	43	61	46
Whole lung % LAA	17.1	27.7	15.1	17.7

FEV_1 = Forced expiratory volume in 1 second, FVC = Forced expiratory vital capacity, %LAA = Percentage low-attenuation areas less than -950 HU

Patient specific whole lung [Table 6.2] and lobar [Table 6.4-6.7] pre- and post-salbutamol measures are given below. Three patients (OXF0068, OXF0113 and OXF0136) showed improvement in whole lung mean HP ^{129}Xe-MR % ventilated volume, FEV_1, FVC and dyspnoea-12 score post-salbutamol. In contrast, one patient (OXF0086) showed a decrease in whole lung mean HP ^{129}Xe-MR % ventilated volume, FVC and worsened dyspnoea-12 score post-salbutamol. In this patient, **Δ** FEV_1 post-salbutamol was also small (0.06 L). Although not statistically significant, moderate correlation was shown between the **Δ** HP ^{129}Xe-MRI and **Δ** FEV_1, **Δ** FVC and **Δ** dyspnoea-12 scores [Table 6.3].

Table 6.2: Whole lung HP ^{129}Xe-MRI, spirometry and dyspnoea-12 pre- and post-salbutamol administration

Participant ID	Pre-salbutamol				Post-salbutamol				Δ			
	HP ^{129}Xe-MRI ventilated volume (%)	FEV_1 (L/% pred)	FVC (L/% pred)	Dyspnoea-12 score	HP ^{129}Xe-MRI ventilated volume (%)	FEV_1 (L/% pred)	FVC (L/% pred)	Dyspnoea-12 score	HP ^{129}Xe-MRI ventilated volume (%)	FEV_1* (L/% change)	FVC* (L/% change)	Dyspnoea-12 score
OXF0068	70.51	0.85/42	1.54/63	2	78.65	1.11/55	2.33/95	0	8.14	0.26/30.6	0.79/51.3	-2
OXF0086	71.51	1.64/65	3.55/108	4	70.02	1.70/67	3.34/102	8	1.49	0.06/3.7	-0.21/-5.9	4
OXF0113	72.68	1.24/58	2.22/87	2	73.18	1.41/67	2.56/101	0	0.51	0.17/13.7	0.34/15.3	-2
OXF0136	62.59	0.68/35	1.31/55	4	64.31	1.00/51	2.14/90	2	1.72	0.32/47.1	0.83/63.4	-2

Δ Change in measurement (post-salbutamol minus pre-salbutamol)
* Data are in litres/percentage change from baseline absolute value in litres
FEV_1 = Forced expiratory volume in 1 second, FVC = Forced expiratory vital capacity

Table 6.3: Pearson's correlation coefficients between changes in whole lung measures pre- to post-salbutamol

Pearson's correlation coefficient (*r*=)	Δ HP ^{129}Xe-MRI ventilated volume (%)
Δ FEV_1 (L)	0.61 (*P*=0.39)
Δ FVC (L)	0.74 (*P*=0.26)
Δ Dyspnoea-12 score	-0.59 (*P*=0.41)

Δ Change in measurement (post-salbutamol minus pre-salbutamol)
FEV_1 = Forced expiratory volume in 1 second, FVC = Forced expiratory vital capacity

6.5.1 Data analysis from COPD patient OXF0068

Table 6.4: Lobar QCT-derived emphysema and pre- and post-salbutamol HP ^{129}Xe-MR ventilated volume percentage in OXF0068

Pulmonary lobe	OXF0068			
	% LAA	Pre-salbutamol HP ^{129}Xe-MRI ventilated volume (%)	Post-Salbutamol HP ^{129}Xe-MRI ventilated volume (%)	**Δ** HP ^{129}Xe-MRI ventilated volume (%)
RUL	16.1	75.7	77.18	1.48
RML	15.4	62.12	92.80	30.68
RLL	19.3	95.26	95.04	-0.23
LUL	18.2	84.39	88.26	3.86
LLL	14.5	85.50	85.48	-0.01

Δ Change in measurement (post-salbutamol minus pre-salbutamol)
RUL = Right upper lobe, RML = Right middle lobe, RLL = Right lower lobe, LUL = Left upper lobe, LLL = Left lower lobe, %LAA = percentage low attenuation areas less than -950HU

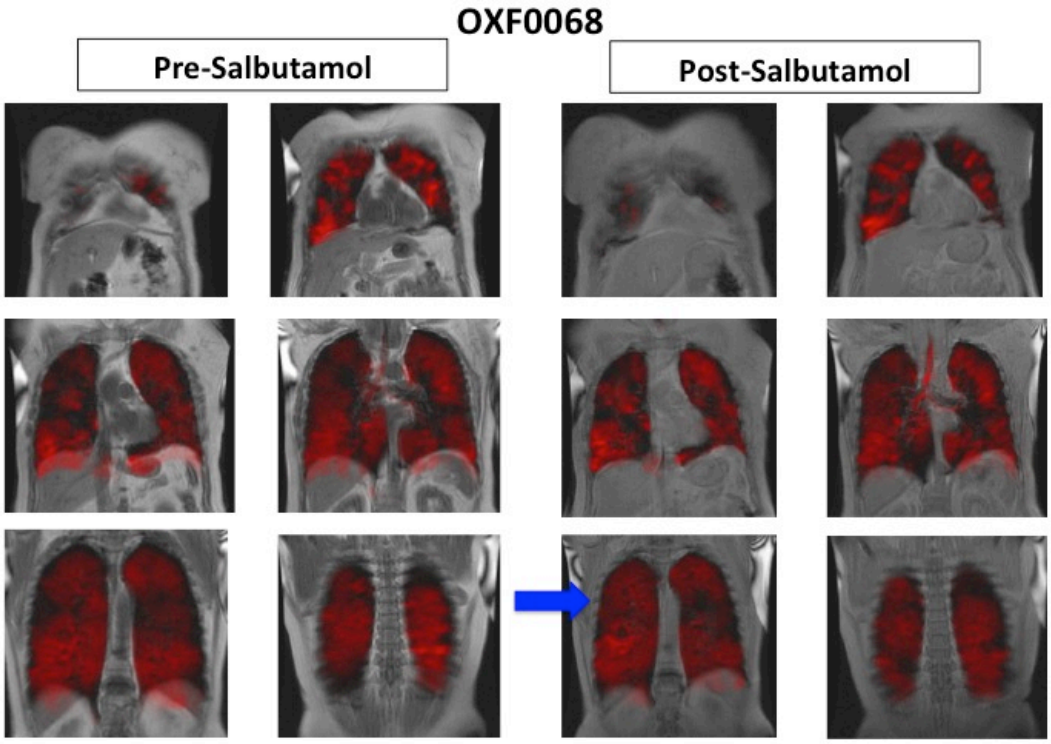

Figure 6.1: Coronal co-registered HP ^{129}Xe-MR ventilation and proton MR imaging acquired in OXF0068 pre- and post-salbutamol. The blue arrow indicates resolution of a right upper zone defect post-salbutamol.

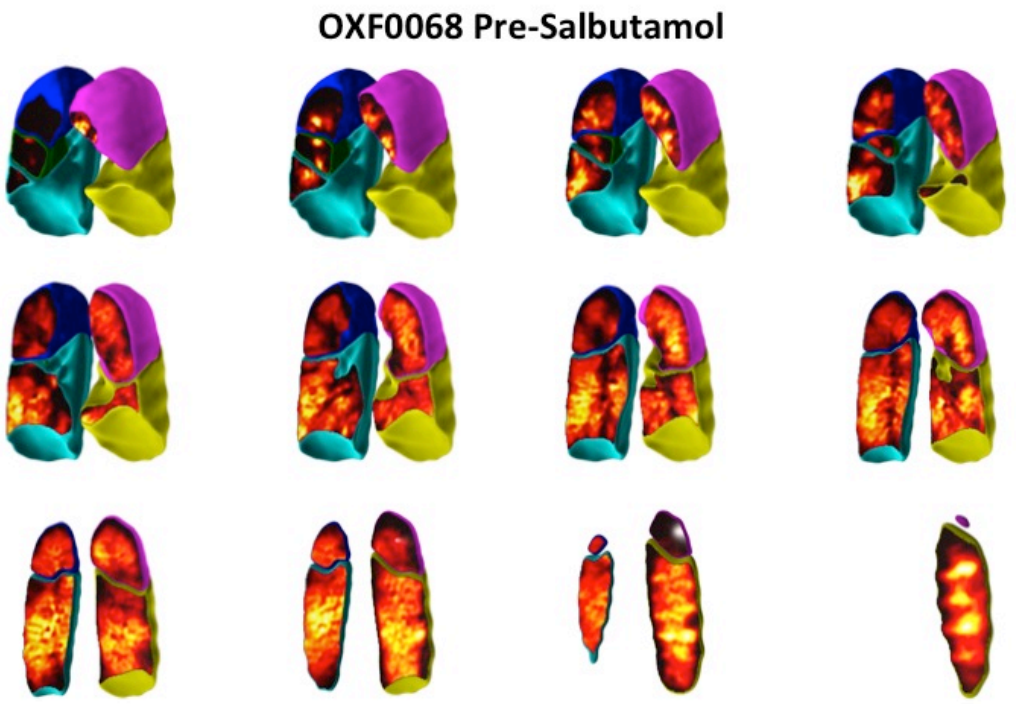

Figure 6.2: 3-D HP ^{129}Xe-MRI lobar ventilation imaging acquired from OXF0068 pre-salbutamol.

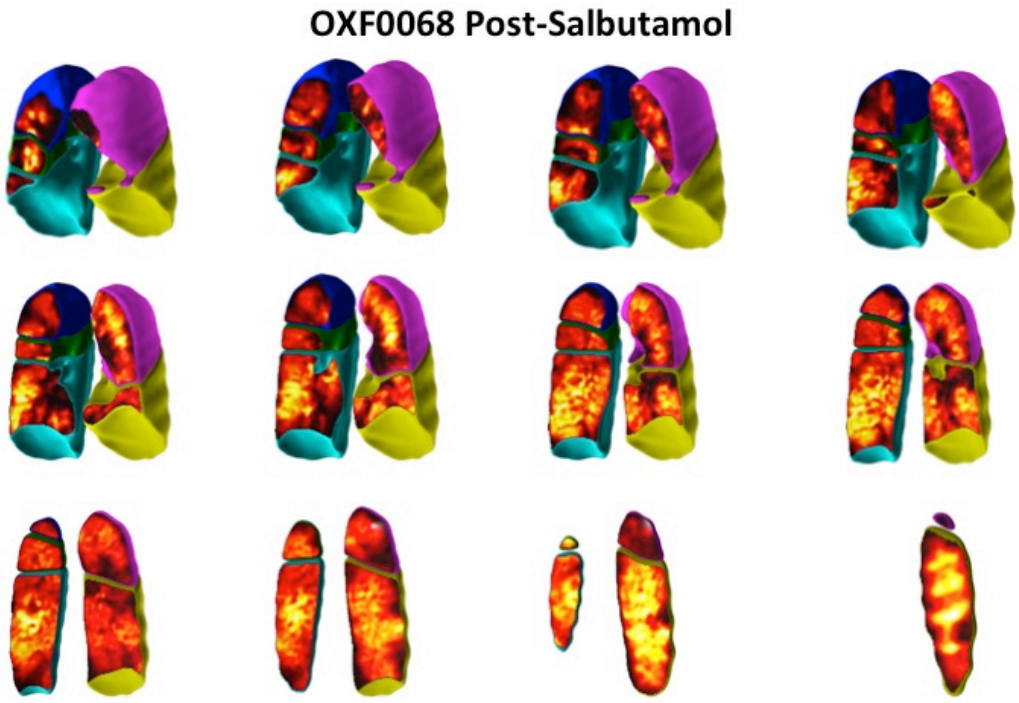

Figure 6.3: 3-D HP ^{129}Xe-MRI lobar ventilation imaging acquired from OXF0068 post-salbutamol. Images show appreciable increase in right upper (blue) and middle (green) lobe ventilation signal intensity.

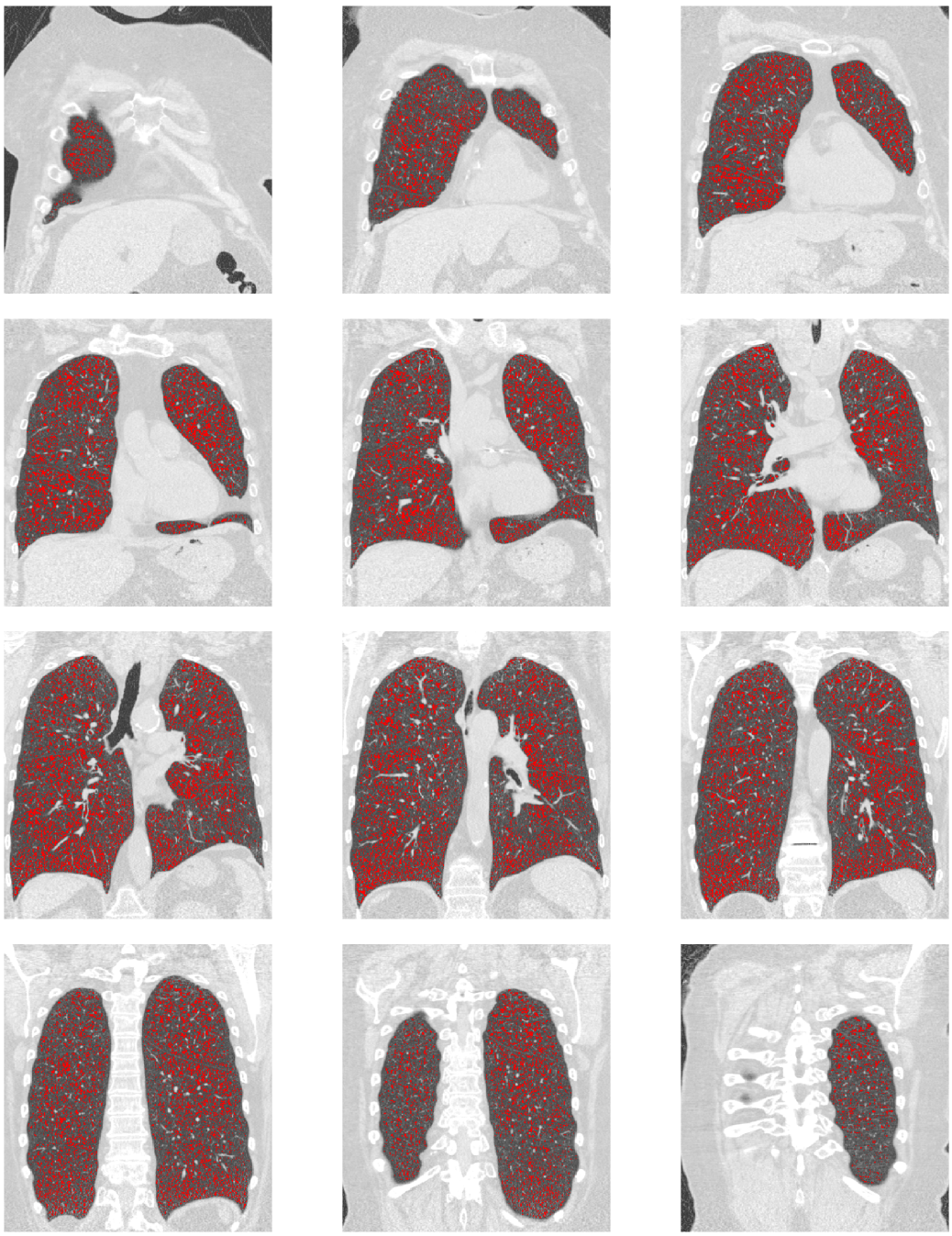

Figure 6.4: QCT-derived emphysema (% LAA) from patient OXF0068. Red areas correspond to regions with attenuation less than -950 HU.

6.5.2 Data analysis from COPD patient OXF0086

Table 6.5: Lobar QCT-derived emphysema and pre- and post-salbutamol HP ^{129}Xe-MR ventilated volume percentage in OXF0086

Pulmonary lobe	OXF0086			
	% LAA	Pre-Salbutamol HP ^{129}Xe-MRI ventilated volume (%)	Post-Salbutamol HP ^{129}Xe-MRI ventilated volume (%)	**Δ** HP ^{129}Xe-MRI ventilated volume (%)
RUL	37.3	93.78	83.18	-10.6
RML	27.1	64.19	72.29	8.1
RLL	19.1	77.46	76.98	-0.48
LUL	28.8	80.26	76.45	-3.81
LLL	20.6	73.45	84.78	11.33

Δ Change in measurement (post-salbutamol minus pre-salbutamol)
RUL = Right upper lobe, RML = Right middle lobe, RLL = Right lower lobe, LUL = Left upper lobe, LLL = Left lower lobe, %LAA = percentage low attenuation areas less than -950HU

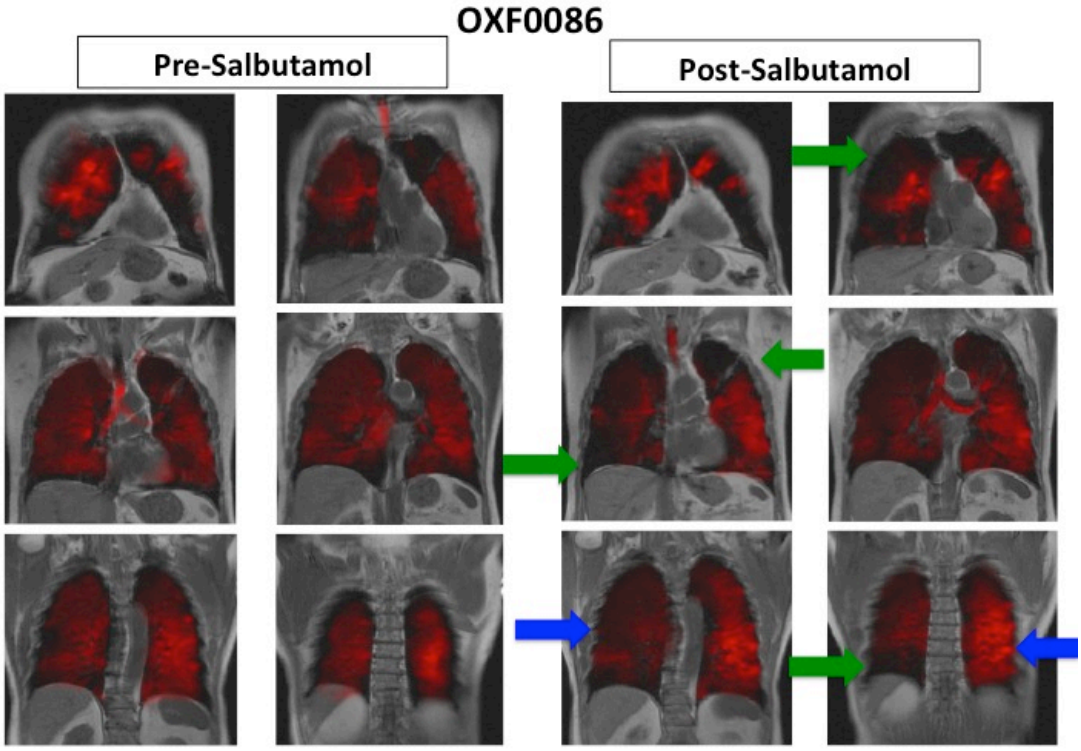

Figure 6.5: Coronal co-registered HP ^{129}Xe-MR ventilation and proton MR imaging acquired in OXF0086 pre- and post-salbutamol. The blue arrows indicate improvement in right mid zone and left lower zone ventilation signal intensity post-salbutamol. The green arrows indicate new ventilation defects in the left upper, right upper and right lower zones post-salbutamol.

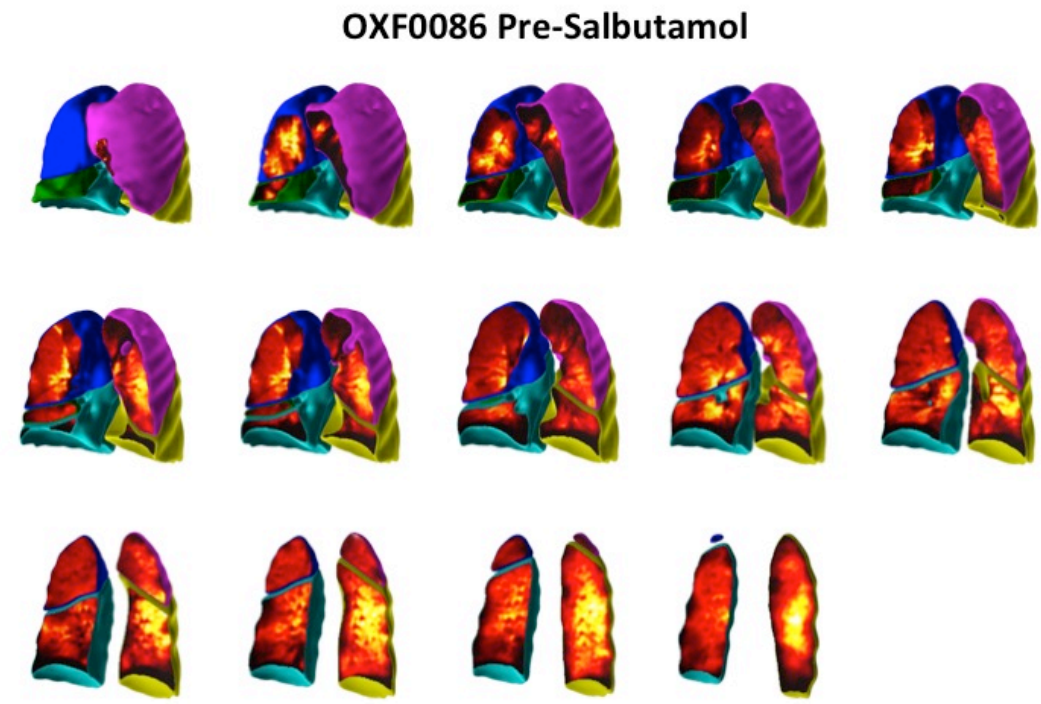

Figure 6.6: 3-D HP ^{129}Xe-MRI lobar ventilation imaging acquired from OXF0086 pre-salbutamol.

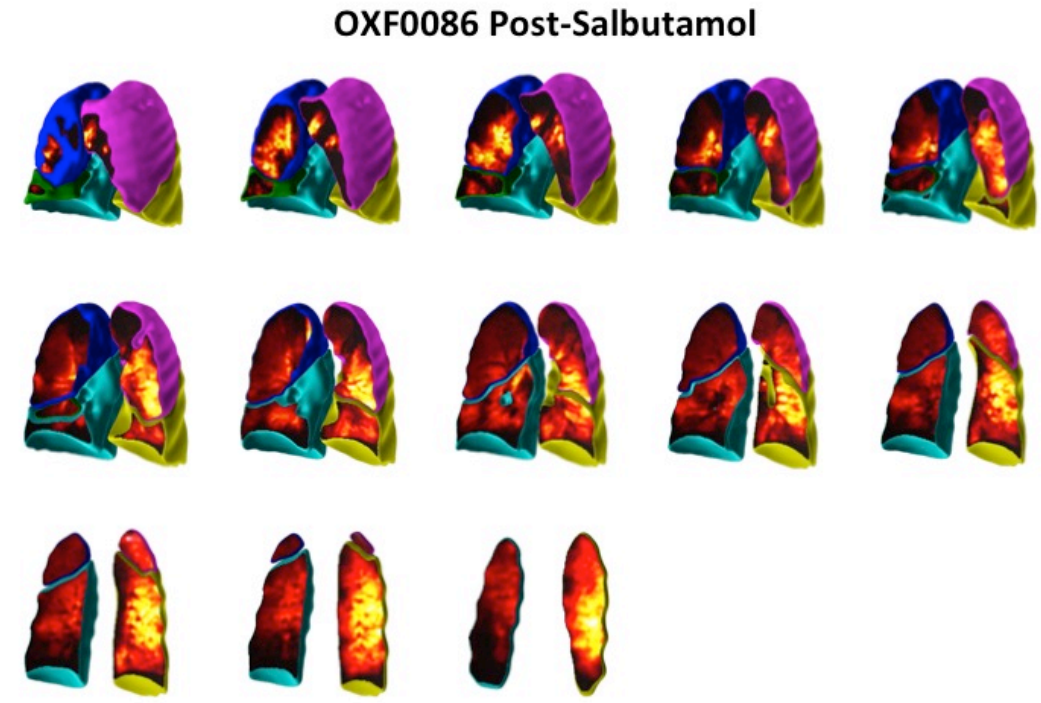

Figure 6.7: 3-D HP ^{129}Xe-MRI lobar ventilation imaging acquired from OXF0086 post-salbutamol. Images show increased ventilation signal in the left lower lobe (yellow) but also a new ventilation defect in the right lower lobe (cyan).

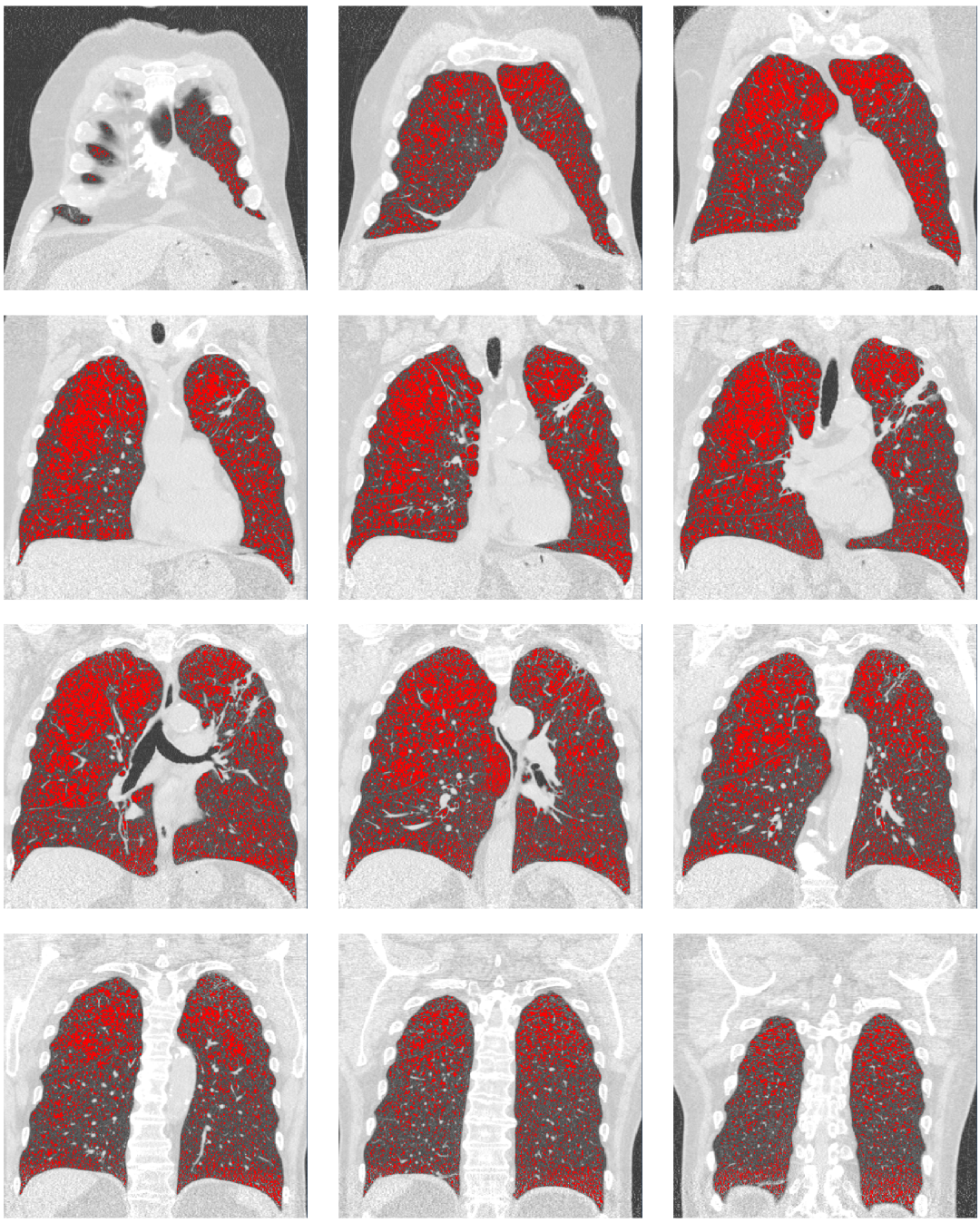

Figure 6.8: QCT-derived emphysema (% LAA) from patient OXF0086. Red areas correspond to regions with attenuation less than -950 HU.

6.5.3 Data analysis from COPD patient OXF0113

Table 6.6: Lobar QCT-derived emphysema and pre- and post-salbutamol HP ^{129}Xe-MR ventilated volume percentage in OXF0113

Pulmonary lobe	OXF0113			
	% LAA	Pre-Salbutamol HP ^{129}Xe-MRI ventilated volume (%)	Post-Salbutamol HP ^{129}Xe-MRI ventilated volume (%)	**Δ** HP ^{129}Xe-MRI ventilated volume (%)
RUL	15.2	95.51	94.42	-1.09
RML	15	84.31	82.61	-1.71
RLL	10.1	85.49	86.79	1.31
LUL	21.2	89.66	85.77	-3.89
LLL	15.5	75.01	80.45	5.44

Δ Change in measurement (post-salbutamol minus pre-salbutamol)
RUL = Right upper lobe, RML = Right middle lobe, RLL = Right lower lobe, LUL = Left upper lobe, LLL = Left lower lobe, %LAA = percentage low attenuation areas less than -950HU

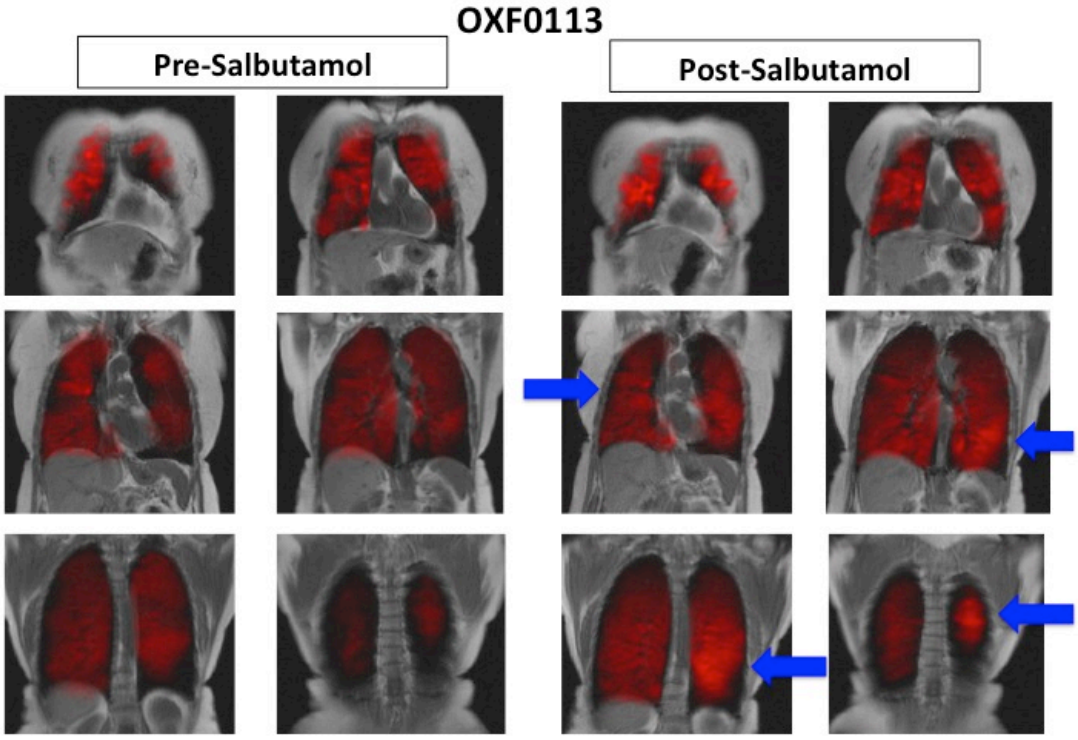

Figure 6.9: Coronal co-registered HP ^{129}Xe-MR ventilation and proton MR imaging acquired in OXF0113 pre- and post-salbutamol. The blue arrows indicate improvement in right mid zone and left lower zone ventilation signal intensity post-salbutamol.

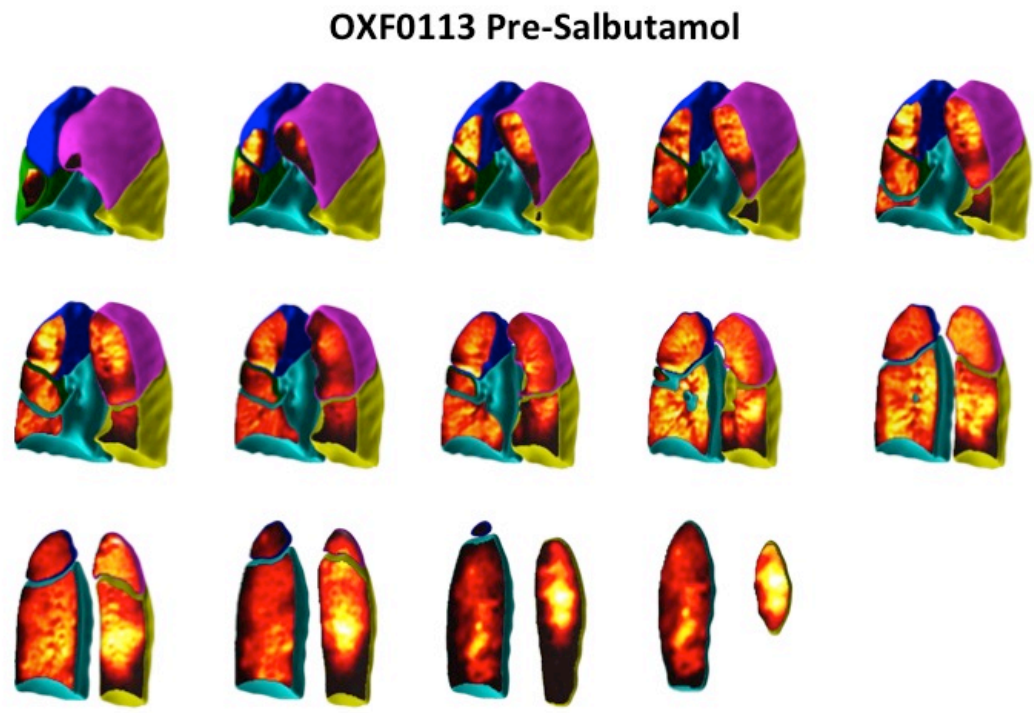

Figure 6.10: 3-D HP ^{129}Xe-MRI lobar ventilation imaging acquired from OXF0113 pre-salbutamol.

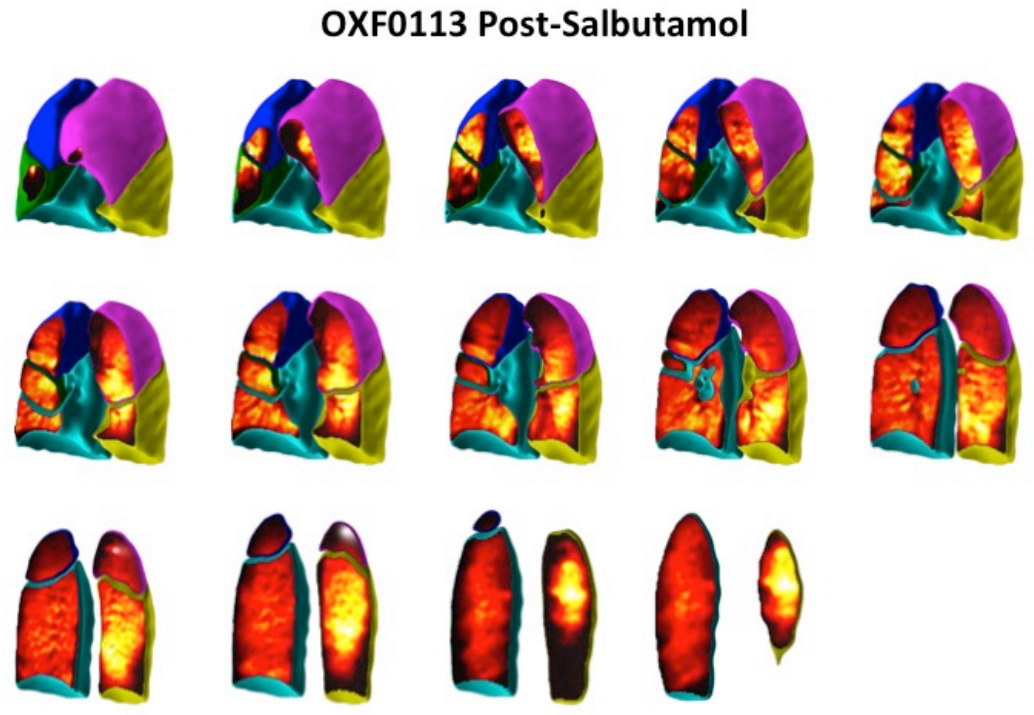

Figure 6.11: 3-D HP ^{129}Xe-MRI lobar ventilation imaging acquired from OXF0113 post-salbutamol. Images show appreciable increase in right lower (cyan) and left lower (yellow) lobe ventilation signal intensity.

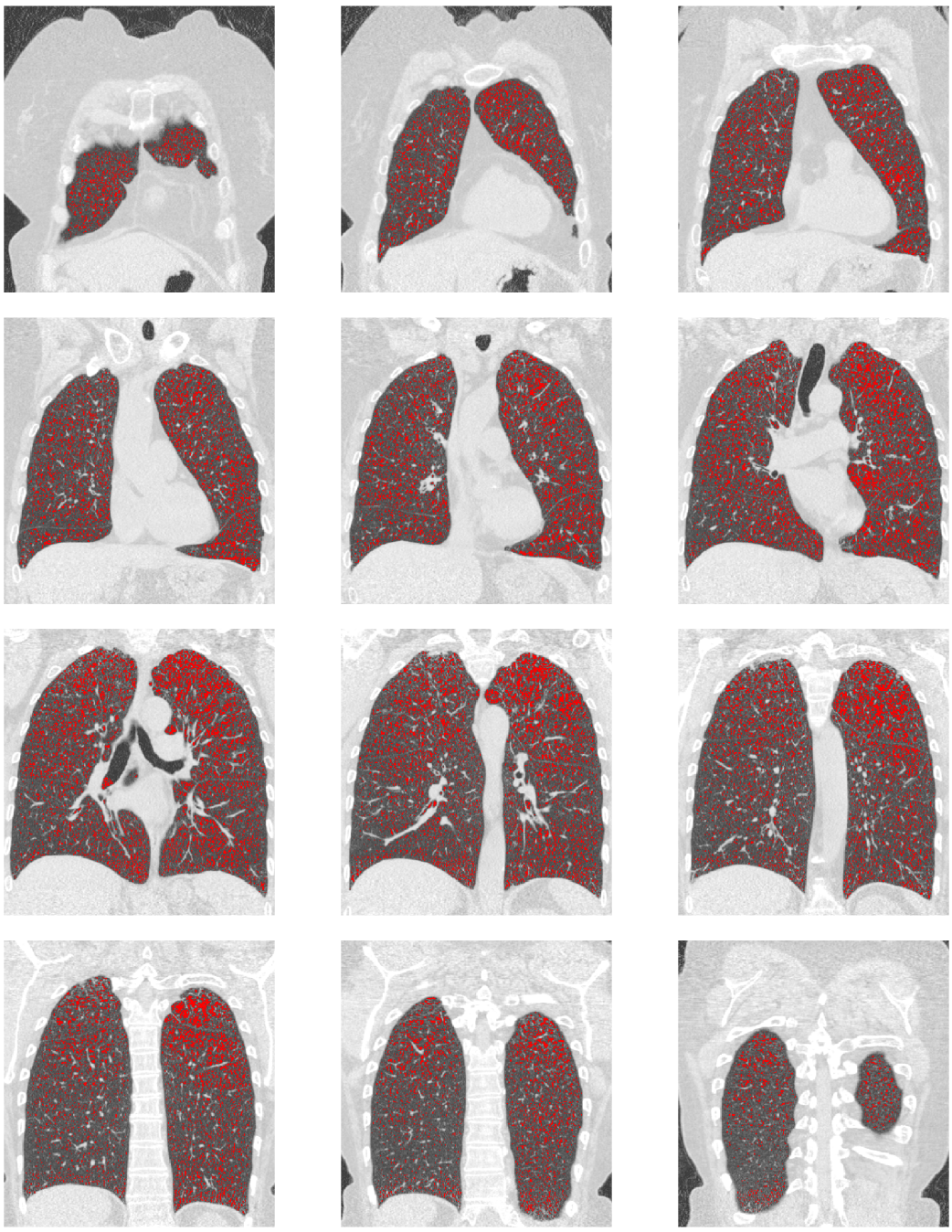

Figure 6.12: **QCT-derived emphysema (% LAA) from patient OXF0113.** Red areas correspond to regions with attenuation less than -950 HU.

6.5.4 Data analysis from COPD patient OXF0136

Table 6.7: Lobar QCT-derived emphysema and pre- and post-salbutamol HP ^{129}Xe-MR ventilated volume percentage in OXF0136

Pulmonary lobe	OXF0136			
	% LAA	Pre-Salbutamol HP ^{129}Xe-MRI ventilated volume (%)	Post-Salbutamol HP ^{129}Xe-MRI ventilated volume (%)	**Δ** HP ^{129}Xe-MRI ventilated volume (%)
RUL	18.5	90.46	97.52	7.06
RML	15.0	68.71	79.08	10.37
RLL	16.5	51.51	80.76	29.25
LUL	19.3	88.34	92.58	4.24
LLL	17.7	81.30	87.97	6.67

Δ Change in measurement (post-salbutamol minus pre-salbutamol)
RUL = Right upper lobe, RML = Right middle lobe, RLL = Right lower lobe, LUL = Left upper lobe, LLL = Left lower lobe, %LAA = percentage low attenuation areas less than -950HU

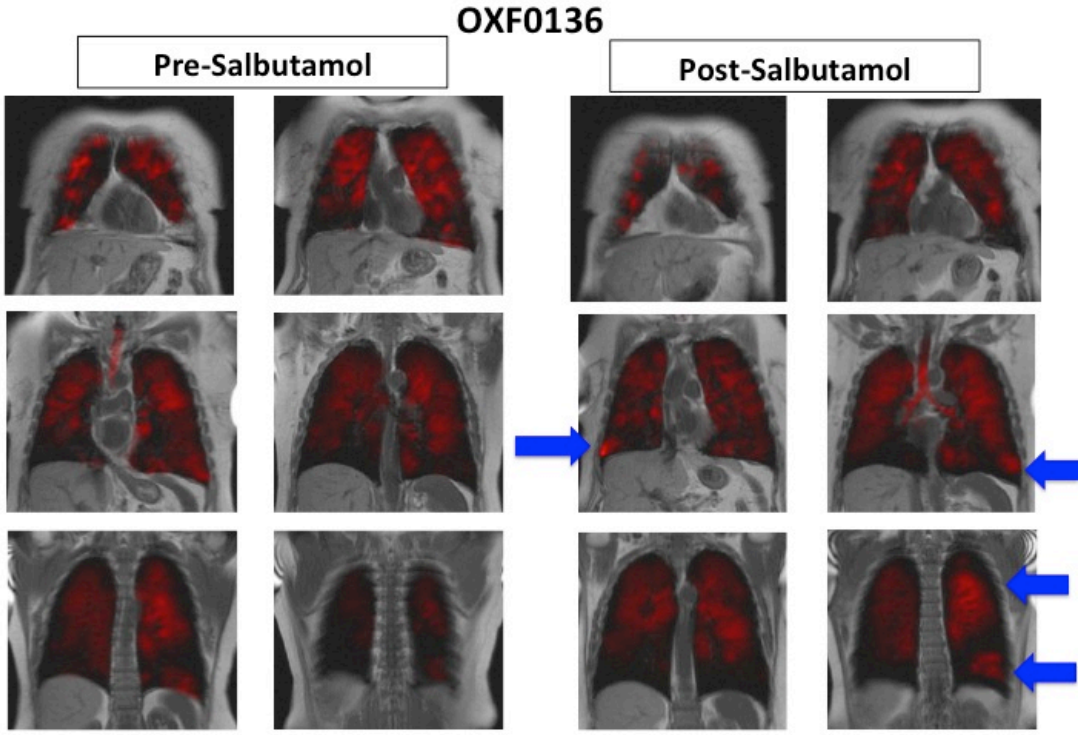

Figure 6.13: Coronal co-registered HP ^{129}Xe-MR ventilation and proton MR imaging acquired in OXF0136 pre- and post-salbutamol. The blue arrows indicate improvement in ventilation signal intensity within the right lower, left upper and lower zones post-salbutamol.

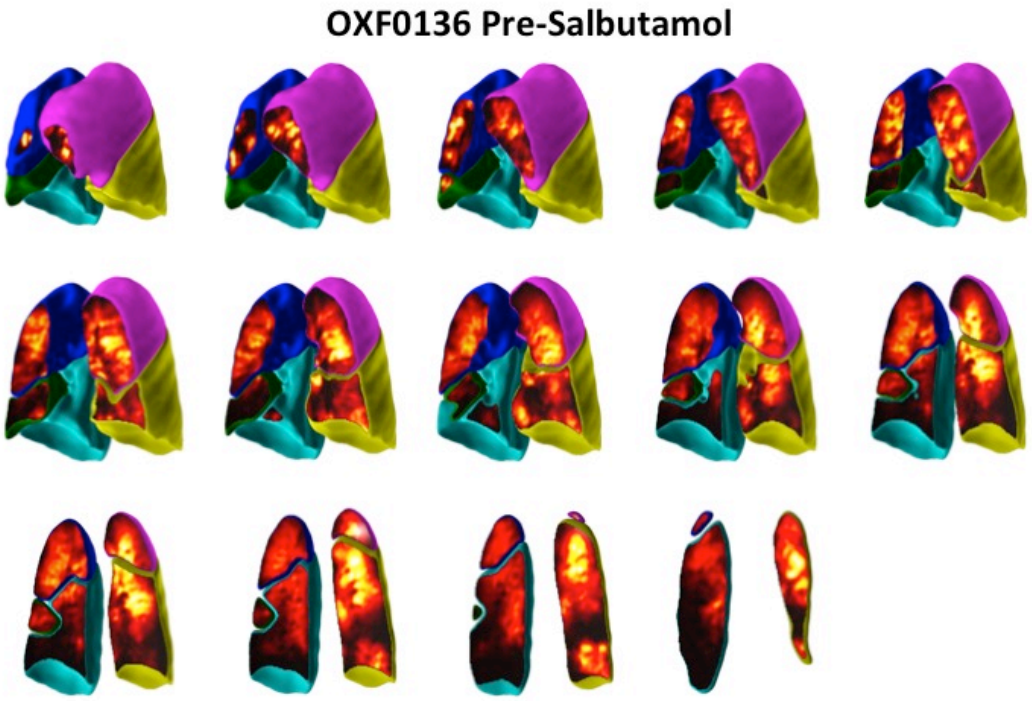

Figure 6.14: 3-D HP ^{129}Xe-MRI lobar ventilation imaging acquired from OXF0136 pre-salbutamol.

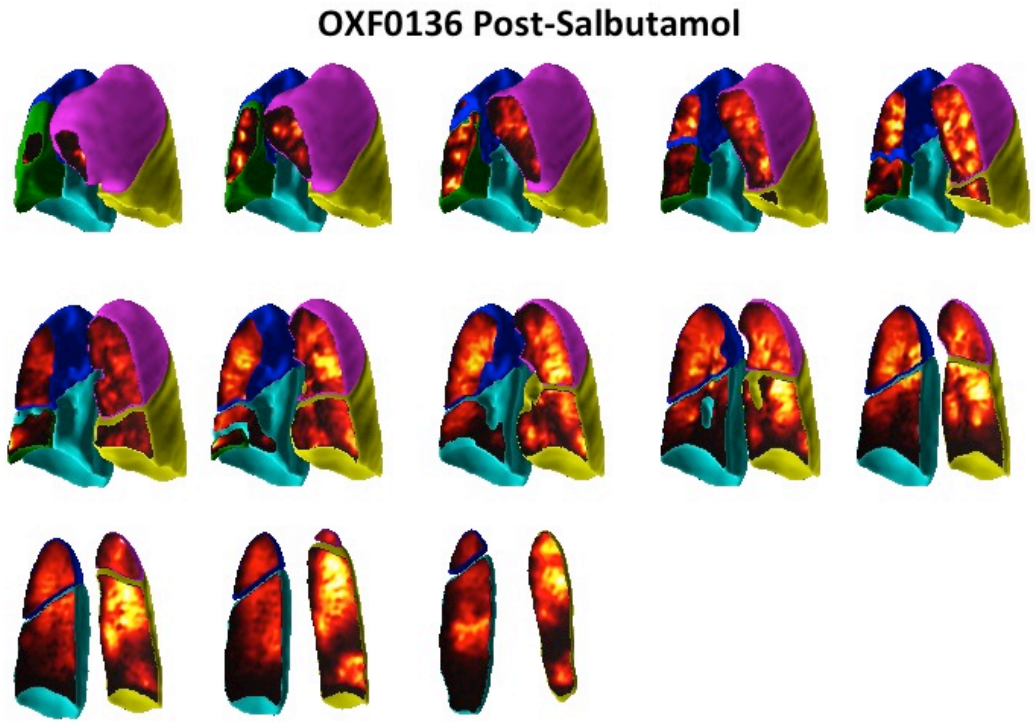

Figure 6.15: 3-D HP ^{129}Xe-MRI lobar ventilation imaging acquired from OXF0136 post-salbutamol. Images show improved ventilation signal intensity in the left upper (pink) and lower (yellow) lobes.

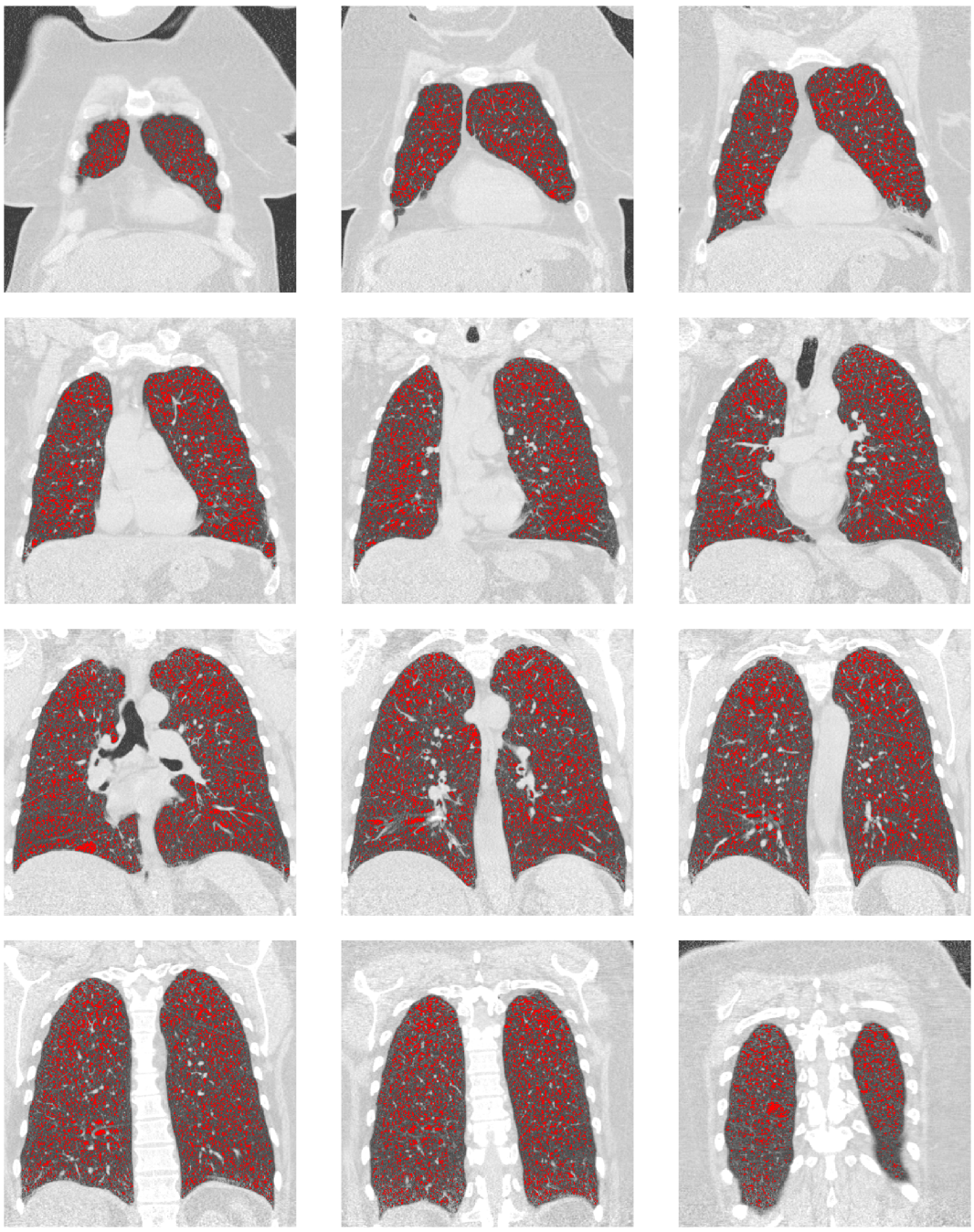

Figure 6.16: QCT-derived emphysema (% LAA) from patient OXF0136. Red areas correspond to regions with attenuation less than -950 HU.

6.6 Discussion

The preliminary findings from this pilot study measuring bronchodilator effects in COPD using HP ^{129}Xe-MRI showed: -

a) Post-bronchodilator change in spirometry, whole lung static HP ^{129}Xe-MR ventilation imaging and dyspnoea-12 questionnaire scores
b) A differential post-bronchodilator change in lobar HP ^{129}Xe-MR ventilated volume percentages for each patient.

6.6.1 Variable changes in post-salbutamol HP ^{129}Xe-MRI ventilation, spirometry and dyspnoea-12 scores are observed

Three patients (OXF0068, OXF0113, OXF0136) demonstrated an improvement in HP ^{129}Xe-MRI, spirometry and dyspnoea-12 scores post-salbutamol. According to published criteria(442-444), these patients would be classified as bronchodilator responders based on post-salbutamol FEV_1. OXF0068 showed the greatest overall improvement in whole lung HP ^{129}Xe-MR ventilated volume percentage with an increase of 8.1% post-salbutamol. However, further lobar analysis showed a differential response within pulmonary lobes, with an increase in HP ^{129}Xe-MR ventilation in the right upper, middle and left upper lobes but decreased ventilation in both lower lobes. This differential response within pulmonary lobes is not appreciated with global spirometric measures.

Despite minimal increase in whole lung HP ^{129}Xe-MR ventilated volume percentage post-salbutamol (1.7%) for OXF0136, regional analysis showed substantially increased lobar ventilation up to 29.2% in the right lower lobe. The additional information provided by regional analysis of HP ^{129}Xe-MRI post-salbutamol may therefore indicate a greater response in particular lobes than would be otherwise appreciated from whole lung HP ^{129}Xe-MRI parameters alone. Furthermore, in this patient there is no structural difference appreciated on CT between the right lower lobe (16.5% LAA) and left lower lobe (17.7% LAA) to account for the differential increase in lobar ventilation of 29.2% and 6.7% post-salbutamol respectively.

OXF0086 would be classified as a non-responder based on post-salbutamol FEV_1 and showed a similar reduced whole lung HP ^{129}Xe-MR ventilated volume percentage and dyspnoea-12 score post-salbutamol. Although post-salbutamol HP ^{129}Xe-MRI enables multiple new ventilation defects to be visually appreciated [Figure 6.5], lobar analysis again indicated a differential response including a decrease in right upper lobe ventilation (10.6%) but increase in left lower lobe ventilation (11.3%) [Table 6.5].

6.6.2 Differential change in post-salbutamol lobar HP ^{129}Xe-MRI ventilation is observed

The mean time elapsed between salbutamol administration and post-treatment HP ^{129}Xe-MRI acquisition was 17±4 minutes. The maximum effect of salbutamol has been reported to occur approximately 15-20 minutes(470) post-

administration. The changes in regional HP ^{129}Xe-MR ventilation were observed within this time frame and therefore likely to reflect maximal response.

The differential change in post-salbutamol ventilation volume percentage in different pulmonary lobes suggests that HP ^{129}Xe-MRI is capable of capturing regional treatment response. This is particularly relevant to heterogeneous lung diseases such as COPD, where the most common primary end-point for clinical trials evaluating new therapies remains global spirometric measures. HP ^{129}Xe-MRI is a non-ionising technique, offering the potential for repeated evaluation of treatments and description of response per lobe by employing the lobar analysis methods presented. Furthermore, it would be possible to integrate the graphical user interface (GUI) used to determine the lobar HP ^{129}Xe-MR ventilated volume percentages pre- and post-salbutamol into the clinical workflow and subsequently translate the technique to other respiratory centres for use in multicentre drug development clinical trials.

6.6.3 Observations are consistent with previous HP ^{3}He-MRI studies

These observations are consistent with previous reports evaluating the effects of salbutamol in COPD with HP ^{3}He-MRI(334, 335). HP ^{3}He-MRI demonstrated significant decrease in VDP in 14 ex-smokers with COPD post-salbutamol(335). The magnitude of treatment effect size was calculated to be greater for HP ^{3}He-MRI compared with FEV_1(335). Furthermore, the ^{3}He gas changes occurred in different image slices across patients, providing evidence of the regional

heterogeneity of bronchodilator response. The current study confirms the patient-specific regional response and extends findings to determine post-salbutamol HP ^{129}Xe-MR ventilation per lobe. The regional change in lobar HP ^{129}Xe-MR ventilation was both observed visually [Figures 6.1-6.4a, c] and was objectively quantified [Table 6.4-6.7]. Heterogeneous bronchodilation following inhaled anticholinergics in COPD has also been reported using three-dimensional CT analysis of fourth to sixth generation airway luminal area supporting these findings(453).

6.6.4 HP ^{129}Xe-MRI offers new insights into regional bronchodilator response

Determining bronchodilator response in patients with COPD has previously proved challenging due to a variety of factors including: -

- Diurnal and day-to-day variability in bronchomotor tone(471)
- Significant intra-individual variability in acute bronchodilator response between repeat testing(437)
- Adoption of differing criteria for acute responsiveness based on post-bronchodilator FEV_1.

FEV_1 responsiveness has been previously reported to differ substantially in a large cohort of COPD patients after administration of ipratropium and salbutamol depending upon the criteria used(471). It is also widely acknowledged that some patients derive benefit from bronchodilator use as a result of an isolated volume response(472) rather than increase in FEV_1. The improvement in exercise endurance and dyspnoea in these patients(473) has

been explained by a reduction in FRC and improved inspiratory capacity. The use of absolute terms to define responsiveness and non-responsiveness may not be optimal in the management of patients with COPD. In this respect, HP ^{129}Xe-MR ventilation, diffusion-weighted and dissolved phase imaging may offer new insights into the mechanism of bronchodilator response at a regional level enabling treatments to be tailored to the individual.

6.6.5 HP ^{129}Xe-MRI can act as a surrogate end-point in interventional studies

Previous HP ^{3}He-MR imaging studies have shown changes in both ventilation and ADC values(334) after an intervention in a number of obstructive lung diseases(158, 458-461). In patients with asthma, induced HP ^{3}He-MR ventilation defects were reported to show differential reversibility following an inhaled bronchodilator (albuterol)(462). The observed resolution of some ventilation defects and persistence of others post-albuterol is consistent with the current results presented. Investigation of HP ^{3}He- and ^{129}Xe-MRI in seven asthmatics before and after salbutamol inhalation demonstrated an improvement in both ^{129}Xe and ^{3}He ventilation defect percentage (VDP), however the improvement in HP ^{129}Xe-MR VDP was significantly greater(469). This suggests that HP ^{129}Xe-MRI may be more sensitive to bronchodilator response and therefore preferable as a surrogate end-point in interventional studies.

The bronchodilator effect on ADC values has also been investigated in ten COPD patients using HP ^{3}He-MR diffusion-weighted imaging(334). Although whole

lung ADC was unchanged, mean ADC values in ROIs that remained ventilated post-salbutamol significantly decreased indicating an improvement in gas trapping. It would be possible to extend the current study to determine post-salbutamol changes in lobar HP ^{129}Xe-MR ADC values to further evaluate the combination of reduced gas trapping and gas redistribution at a regional level.

The effect of intervention on HP ^{3}He-MRI has also been previously investigated in patients with cystic fibrosis(460, 461, 466). Evidence supporting the use of HP gas MRI in investigational drug treatment studies has been provided from preliminary HP ^{3}He-MRI findings in paediatric cystic fibrosis patients post-Ivacaftor(467, 468). HP ^{3}He-MRI demonstrated significant ventilation improvement post-Ivacaftor, a new class of drug targeting the genetic mutation G551D(467, 468).

Although the study did not include a control arm where patients completed HP ^{129}Xe-MR ventilation imaging pre- and post-placebo, reproducibility of lobar HP ^{129}Xe-MR ventilation has been confirmed [Section 4.5, 4.6.2]. In the COPD reproducibility study, differences between repeated lobar HP ^{129}Xe-MR ventilated volume percentage measurements were within the 95% limits of agreement for 11 patients [Bland Altman plot of agreement, Figure 4.21]. This provides supportive evidence that the observed increase in HP ^{129}Xe-MR ventilation post-salbutamol was not due to scan-rescan variability or measurement error. In addition, previous literature supports the reproducibility of hyperpolarised gas MRI in stable obstructive lung diseases imaged over different time points(175, 176, 324, 326, 474, 475).

6.6.6 Limitations

It is acknowledged that the small number of patients, effectively constituting a case report/series is a major limitation of this chapter. As such, formal statistical analyses were not possible and would be required to draw firm conclusions. These data represent proof-of-principle that the regional effects of intervention may be assessed in COPD using HP ^{129}Xe-MRI and a larger study should be undertaken to confirm results. In a larger sample size, the inclusion of the dyspnoea-12 questionnaire scores and QCT-derived emphysema measurements would allow for comparison of HP ^{129}Xe-MRI against clinical and imaging reference standards respectively. The prospective inclusion of a control arm to the study would strengthen findings, although HP ^{129}Xe-MRI reproducibility has been shown in Section 4.5.

The non-rigid multi-modal co-registration algorithm used for lobar HP ^{129}Xe-MR analysis accounts for potential patient motion and slightly different volumes of gas within the lungs during breath-hold imaging, which may contribute to measurement error. Patients were given extensive training and instruction for breath-hold imaging including practice breath-holds prior to imaging to improve technique and reproducibility of exhalation to FRC before inhalation of 1 L ^{129}Xe gas. Standardisation of breath-hold volumes, which is pertinent to treatment response studies, could be achieved by spirometric-gating. However, there is a body of literature supporting the reproducibility of self breath-holding in the

absence of respiratory monitoring devices following patient coaching and instruction(476-478).

6.6.7 Future work

Evaluation of pre-and post-salbutamol HP ^{129}Xe-MR ventilation imaging is required in a larger sample size of patients with COPD to validate the current findings and evaluate the relationship between change in HP ^{129}Xe-MR ventilated volume percentage, spirometry and dyspneoa-12 scores using Pearson's correlation coefficients. Formal statistical analyses using a repeated-measures analysis of variance are required to determine if the changes observed in HP ^{129}Xe-MR ventilation post-salbutamol are significant.

Future work may include HP ^{129}Xe-MR diffusion-weighted and dissolved-phase imaging pre-and post-salbutamol to assess the interaction between ventilation, gas trapping and gas exchange in COPD post-salbutamol. This may also elucidate the mechanism of action by which patients derive benefit from salbutamol despite limited change in FEV_1.

It is possible to complete HP ^{129}Xe-MRI pre- and post-inhaled interventions in a range of obstructive lung diseases to investigate applicability of current findings and potential for HP ^{129}Xe-MRI to act as a surrogate end-point in drug development trials. For example, in asthma patients with eosinophilic inflammation, changes in HP ^{129}Xe-MRI post-novel antibody treatments (e.g. omalizumab, monoclonal antibody to IgE) may be correlated with non-imaging

biomarkers of disease activity including exhaled nitric oxide levels, sputum and blood eosinophil level for a comprehensive structural, functional and physiological assessment.

6.6.8 Conclusion

Preliminary data from four COPD patients has demonstrated regional change in HP ^{129}Xe-MRI post-salbutamol. The ability of HP ^{129}Xe-MRI to capture a differential response according to pulmonary lobe suggests it may be of value in drug development studies for new obstructive lung disease treatments. This chapter provides proof-of-principle that HP ^{129}Xe-MRI can be used to evaluate regional effects of intervention and should lead to further studies with a larger sample size to confirm results.

7 Chapter 7: Concluding remarks

7.1 Summary of findings

7.1.1 HP ^{129}Xe-MRI demonstrates gravitational-dependent gradients

The potential clinical application of HP ^{129}Xe-MRI requires robust validation of the technique and definition of normal parameters, against which imaging in various respiratory disease cohorts can be compared. The normal HP ^{129}Xe-MR ventilation and diffusion-weighted imaging parameters were established for eleven healthy volunteers [Section 3]. In the supine posture (the position in which HP ^{129}Xe-MRI would most frequently be acquired) group mean ventilation signal intensity was 1.26±0.32 and ADC value was 0.028±0.006 cm^2sec^{-1}.

HP ^{129}Xe-MR ventilation and diffusion-weighted antero-posterior (AP) gradients were systematically evaluated in the supine and prone posture for healthy volunteers [Section 3.5.4]. HP ^{129}Xe-MR ventilation AP gradients were more marked in the supine than prone posture, whereas ADC AP gradients were more uniform. Although, an overall trend for negative HP ^{129}Xe-MR ADC AP gradients when supine and positive gradients when prone was found, the difference between postures did not reach statistical significance. These data were consistent with the current literature-base reporting increased ventilation in

dependent lung regions when supine and a more uniform ventilation distribution when prone(255, 257, 261-266, 317).

These data validate HP ^{129}Xe-MRI by demonstrating sensitivity to normal physiology. Furthermore, the findings support a role for HP ^{129}Xe-MRI in respiratory disease to reliably and accurately detect regional physiological disturbance and improve our understanding of underlying pathophysiological disease processes contributing to impaired gas exchange.

7.1.2 HP ^{129}Xe-MRI measures are successfully quantified according to pulmonary lobes

This is the first study to describe successful lobar quantification of HP ^{129}Xe-MRI ventilation and ADC in patients with COPD. The progression from qualitative radiological-based scoring(157) to quantitative methodology(325, 334, 336) has advanced HP gas MRI analysis; however no standardised method has yet been established. Direct comparison between imaging acquired at different HP gas MR centres necessitates consensus regarding an optimum analysis method. One of the unique advantages of HP ^{129}Xe-MRI is its capability for regional lung function assessment. The generation of lobar HP ^{129}Xe-MRI measurements enables regional information to be readily extracted. The automated analysis tool employed throughout this thesis, involves a graphic user interface (GUI), which could be easily incorporated into the clinical workflow.

Lobar HP ^{129}Xe-MRI parameters were successfully generated for 22 patients with COPD (GOLD II-IV criteria) [Section 4]. Both lobar HP ^{129}Xe-MR percentage ventilated volume and average ADC showed correlation with lobar QCT-derived emphysema (r=-0.32, p< 0.001 and r=0.75, p<0.0001). Furthermore, whole lung HP ^{129}Xe-MRI average ADC showed moderate correlation with PFTs: percentage predicted TLCO (r= -0.61, p<0.005) and percentage predicted FRC (r=0.47, p< 0.05). Taken together, these data substantiate the lobar HP ^{129}Xe-MRI analysis method presented by confirming a relationship with established pulmonary structural and functional measures.

The reproducibility of lobar HP ^{129}Xe-MR percentage ventilated volume and average ADC parameters were confirmed in 11 and 10 patients, respectively, during disease stability. This provides supplementary evidence to validate the automated lobar HP ^{129}Xe-MRI analysis method.

7.1.3 HP ^{129}Xe-MRI demonstrates delayed ventilation

The feasibility of time-resolved single breath-hold HP ^{129}Xe-MR ventilation imaging was demonstrated in thirteen patients with COPD [Section 5]. Delayed ventilation was observed visually and quantified by an increase in ventilation signal intensity in 93% of imaging sets acquired. Within the imaging sets where delayed ventilation was detected, a differential increase in ventilation signal was observed in different pulmonary lobes i.e. affecting between two and five pulmonary lobes. HP ^{129}Xe-MR delayed ventilation may represent collateral ventilation, partial obstruction, gas trapping, narrowing of the peripheral

airways or a combination of processes. If the delayed ventilation observed does represent collateral ventilation, this may be due to gas moving freely between pulmonary lobules (intralobar) or between lobes (interlobar).

Analysis of CT fissure integrity in these patients, demonstrated significant association between CT predicted collateral ventilation and delayed ventilation observed with HP ^{129}Xe-MRI in the left lung but no association was demonstrated in the right lung. The literature is conflicted about the accuracy of evaluation of fissures on HRCT and ability to predict collateral ventilation(398-400). Direct observation and quantification of delayed ventilation with HP ^{129}Xe-MRI may be preferable to other indirect methods that are only capable of predicting collateral ventilation with variable accuracy.

In addition, the delayed ventilation depicted by time-resolved HP ^{129}Xe-MR ventilation imaging was not appreciated on co-registered NM-V SPECT images, which may be due to lower spatial and temporal resolution [Section 5.6.4]. Detailed review of co-registered CT images also failed to identify differences in pulmonary structure, particularly regions of emphysema in lobes that did and did not demonstrate delayed ventilation.

Further work is required to determine the aetiology of the delayed ventilation observed and to develop the technique for potential non-invasive detection of collateral ventilation.

7.1.4 HP ^{129}Xe-MRI demonstrates regional lung function change post-therapeutic intervention

Preliminary findings from four patients with COPD showed regional change in static HP ^{129}Xe-MR ventilation post-salbutamol inhalation [Section 6]. Post-salbutamol changes in whole lung static HP ^{129}Xe-MR ventilation imaging, spirometry and dyspnoea-12 questionnaire scores provide complementary evidence of both functional and symptomatic change following intervention. Importantly, the differential change in post-salbutamol ventilation volume percentage according to pulmonary lobe suggests that HP ^{129}Xe-MRI is capable of capturing regional treatment response. This is particularly relevant to heterogeneous lung diseases such as COPD, where the most common primary end-point for clinical trials evaluating new therapies remains global spirometric measures(479, 480), which fail to provide detailed regional information.

Unfortunately due to the small sample size, formal statistical analyses could not be performed and extension to a larger cohort should be undertaken to validate the preliminary data. Nevertheless, these results suggest a promising role for HP ^{129}Xe-MRI in drug development studies to assess therapeutic response. HP ^{129}Xe-MRI may be adopted as a surrogate end-point in interventional studies, potentially enabling earlier and more detailed detection of regional response to novel obstructive lung disease treatments than current standard end-points (FEV_1).

7.1.5 Summary

Data presented in this thesis demonstrate how the technical acquisition of HP ^{129}Xe-MRI in healthy volunteers and patients with COPD has been optimised. Establishing the normal parameters of HP ^{129}Xe-MRI in healthy volunteers and demonstrating sensitivity to normal physiology have further validated potential clinical application. The successful generation of lobar HP ^{129}Xe-MRI parameters with confirmed reproducibility offers an automated analysis method that may be easily adopted into the clinical workflow and translated to other imaging centres. Demonstration of the feasibility of detecting delayed ventilation and regional change in lung function following intervention has identified specific roles for HP ^{129}Xe-MRI in evaluating regional treatments and assessing therapeutic response. Larger, multicentre studies focussed on the specific potential HP ^{129}Xe-MRI roles identified in this thesis are critical to propel the translation of the technique from bench to bedside. Future work should focus on well-designed, multicentre trials to evaluate the role of HP ^{129}Xe-MRI in COPD patient selection for LVRT. HP ^{129}Xe-MRI also has a possible role as a surrogate end-point in obstructive lung drug development studies. Data presented in this thesis primarily supports these clinical applications and other applications which could be explored are detailed below [Section 7.2 - 7.4].

7.2 Potential utility of HP ^{129}Xe-MRI

7.2.1 Challenges to overcome

When considering an ideal modality to evaluate lung function and quantify V/Q relationships, the following criteria have been suggested: -

- Non-invasive
- Able to be implemented in most clinical settings
- Offer high-resolution spatial information
- Minimal exposure to ionising radiation

HP ^{129}Xe-MRI fulfils most criteria and while it is feasible for the technique to be implemented in most clinical settings, there are still challenges to be overcome. The rapid clinical uptake of HP ^{129}Xe-MRI has been impeded by a number of factors: -

- Initial research efforts focussed solely on HP ^{3}He-MRI with subsequent ^{3}He resource becoming scarce and very expensive
- Regulation of hyperpolarised ^{129}Xe gas as a drug and therefore requirement for Medicines and Healthcare products regulatory authority (MHRA)/Food and Drug administration (FDA) approvals
- Slow commercialisation efforts of hyperpolarised gas technology.

Before 2012, HP gas MR research was restricted to only a few sites worldwide that had access to a small number of commercially available GE polarisers or the in-house expertise to build their own. Access to polariser technology is likely to

improve following the recent GE spin-off of intellectual property to Polarean (Research Triangle Park, NC)(481) and upcoming expiration of a key patent. The combined efforts of Polarean, Xemed LLC (Durham, NH)(137) as well as "open-source" polarisers(482, 483) aim to overcome barriers to accessing hyperpolarised gas technology and encourage multicentre translational research.

The cost associated with HP ^{129}Xe-MRI is another factor for consideration since the overheads of polariser installation/maintenance and purchase of ^{129}Xe gas supply are significant. The cost of 1 L of isotopically enriched ^{129}Xe gas has been reported as approximately US$ 200-250(484). In a resource-scarce NHS, delivery of routine lung function assessment with HP ^{129}Xe-MRI in all NHS hospitals across the UK is highly unlikely. However, as the evidence-base for clinical translation of HP ^{129}Xe-MRI is generated through multicentre trials and potential sponsorship from the pharmaceutical industry, it is anticipated that the associated costs will reduce as result of increasing market demand.

7.3 Clinical applications

7.3.1 Improving pathophysiological understanding of cardiorespiratory disease

7.3.1.1 Acute Respiratory Distress Syndrome

By demonstrating that HP ^{129}Xe-MRI is sensitive to gravitational-dependent gradients and thus normal physiology [Section 3], the reliable description of regional physiological disturbance with HP ^{129}Xe-MRI has been proposed. The findings, similar to previous animal(255, 257) and human studies(222), of a ventilation gravitational-dependent gradient more marked in the supine than prone position has direct implications for improving gas exchange in mechanically ventilated patients(485). Specifically the more homogeneous distribution of inflation in the prone posture, decreases ventilator-induced lung injury(486, 487), improves oxygenation(488) and in patients with acute respiratory distress syndrome (ARDS) provides a significant survival advantage(489).

7.3.1.2 Heart failure

HP ^{129}Xe-MRI may provide detailed information about the physiological imbalance that occurs during heart failure. Improved understanding of the interaction between the heart and lungs in heart failure may allow new therapeutic targets to be identified which are aimed at restoring altered V/Q gradients and consequently improve symptoms of dyspnoea. The distribution of

lung perfusion has been previously compared between healthy volunteers and patients with heart failure using a 2-dimensional gadolinium first-pass perfusion MR technique(280). In contrast to the significantly increased perfusion demonstrated in the dependent lung regions in healthy volunteers when lying supine, the gravitational gradient was blunted in heart failure, reduced in proportion to left ventricular end-diastolic pressure(280). The redistributed perfusion to non-dependent lung regions was likely due to increased pulmonary vasoconstriction in dependent lung areas.

HP ^{129}Xe-MRI offers the opportunity to observe the distribution of a wider range of lung function parameters i.e. ventilation, gas diffusion and gas transfer in heart failure. It may also enable the relationship between altered distribution of these parameters and symptoms, for example orthopnoea, to be delineated. It has been suggested that redistribution of perfusion from the lung periphery occurs in heart failure with prolonged supine positioning and may contribute to paroxysmal nocturnal dyspnoea and central sleep apnoea(490). Physiological studies using HP ^{129}Xe-MRI to demonstrate the alterations in regional lung function occurring after prolonged periods in the supine position and potentially during exercise would be valuable in patients with heart failure. Given the main cause for perfusion redistribution in heart failure has been suggested as pulmonary vasoconstriction, the mechanism of action and response to pulmonary vasodilator therapies may also be assessed using HP ^{129}Xe-MRI.

7.3.1.3 Pulmonary congestion in end-stage renal disease

The physiological disturbances occurring as a result of pulmonary congestion in end-stage renal disease (ESRD) patients undergoing dialysis could also be evaluated by HP ^{129}Xe-MRI. Pulmonary congestion is often incompletely resolved following ultrafiltration dialysis, with greater than 25% patients still having excessive lung water after dialysis(491). Moreover, in ESRD, pulmonary congestion may be asymptomatic or cause major deterioration in physical performance. Previous studies have reported chest ultrasound to reliably estimate extravascular lung water(492) and to help refine prognosis in dialysis patients(493, 494). By determining the alteration in pulmonary ventilation and gas transfer in pulmonary congestion and ESRD, HP ^{129}Xe-MRI may improve our understanding and act as a potential biomarker for early disease detection in asymptomatic patients.

7.3.2 Evaluation of regional treatments for obstructive lung diseases

The unique advantage of HP ^{129}Xe-MRI pertains to its ability to regionally describe ventilation, pulmonary microstructure, gas exchange and transfer. Although the regional distribution of the functional parameters may be easily visually appreciated from imaging, objective quantification is essential to extract this information. The generation and validation of an automated lobar analysis method for HP ^{129}Xe-MR ventilation and diffusion-weighted imaging is a significant step forward [Section 4]. The software used for lobar HP ^{129}Xe-MRI

analysis has a GUI, which would be easily integrated into the clinical workflow and thus translatable to other respiratory imaging centres. The method has several applications for patients with COPD, including quantification of regional disease severity and potential stratification and determination of patient suitability for particular treatments. The lobar analysis method may also be applied to other obstructive lung diseases, for example lobar HP ^{129}Xe-MRI ADC values in α_1 antitrypsin deficiency to determine regional air trapping and lobar HP ^{129}Xe-MR ventilated volume percentages in asthma to quantify regional airflow limitation. In these obstructive lung diseases, lobar HP ^{129}Xe-MRI analysis would be ideally placed to assess response to regional treatments, for example bronchial thermoplasty in asthma [Section 7.3.5].

With the emergence of regional treatments for many respiratory diseases, HP ^{129}Xe-MRI offers an approach to evaluate regional response, where previous standard global lung function measures have proven inadequate. Lobar HP ^{129}Xe-MR parameters may be employed for the assessment of a wide range of regional treatments including LVRS and endobronchial valve insertion in COPD, bronchial thermoplasty in asthma and radiotherapy in lung cancer. Unlike conventional CT follow-up after treatments, HP ^{129}Xe-MRI is non-ionising and can therefore be performed at multiple time points and earlier, potential immediately after an intervention. In this way, HP ^{129}Xe-MRI may provide evidence of likely treatment success or identify the need for modification, enabling the clinician to make judicious decisions about further management and share this information with patients earlier on the treatment pathway.

7.3.3 Improving patient selection for endobronchial valves

HP ^{129}Xe-MRI may enable comprehensive evaluation of COPD patients considered for endobronchial valve insertion or other similar regional treatments, for example airway bypass, endoscopic sealant, steam and lung volume reduction coils(375-380). HP ^{129}Xe-MR diffusion-weighted imaging enables the distribution of emphysema to be described in detail. Pulmonary lobes to be targeted for endobronchial valve insertion may be identified by an associated elevated mean lobar HP ^{129}Xe-MR ADC value. Furthermore, the detection of delayed ventilation with time-resolved or dynamic HP ^{129}Xe-MRI may help predict treatment outcome. Whilst HP ^{129}Xe-MR delayed ventilation may represent collateral ventilation, direct comparison with the Chartis system is still required to confirm this. The threshold of delayed/collateral ventilation above which endobronchial valves would fail also remains to be determined. Pre-assessment of individuals considered for endobronchial valves with time-resolved HP ^{129}Xe-MRI may allow patient stratification by rationalising the number of invasive Chartis procedures and patients demonstrating significant HP ^{129}Xe-MR delayed ventilation would not proceed to further treatment. In contrast, patients in whom significant HP ^{129}Xe-MR delayed ventilation is excluded would proceed to Chartis and for continued consideration for valve insertion. This strategy would improve patient selection for treatments and is aimed to reduce the number of invasive Chartis procedures in patients ultimately precluded from treatment.

7.3.4 Predicting post-LVRT lung function

There are a number of different techniques that have been used to predict post-operative lung function(495-498) in patients undergoing lung reduction surgery; all have difficulty in determining the precise contribution of individual lobes to the patients' lung function. Conventional nuclear medicine methods based on planar scintigraphy(97, 98, 100) are slowly being replaced by 3-D SPECT/CT techniques(101) to provide relative measurements of perfusion/ventilation per lobe. Disadvantages of nuclear medicine are the inherent low spatial and temporal resolution associated with images as well as exposure to ionising radiation. HP ^{129}Xe-MRI is an alternative non-ionising technique readily capable of quantifying lobar ventilation in patients considered for lung resection. In addition to estimating the impact of resection on pulmonary status, HP ^{129}Xe-MR offers dynamic ventilation and dissolved-phase imaging to provide complementary information on delayed/collateral ventilation and gas exchange/transfer in these patients. This may help determine patient suitability and also provide further insights into the physiological alterations occurring post-LVRT, specifically to identify the cause of treatment failures.

7.3.5 Evaluating bronchial thermoplasty

The lobar HP ^{129}Xe-MRI analysis methodology may be further extended to a segmental level with view to develop more effective image-guided treatments for obstructive lung diseases. Bronchial thermoplasty is a treatment for severe asthma that uses radiofrequency energy to reduce airway smooth muscle and decrease bronchoconstriction(499). Bronchial thermoplasty has been shown to

improve quality of life and decrease the rate of severe exacerbations(500) with no significant long-term complications(501). The specific group of patients with severe asthma who would benefit most from this treatment is not yet clearly defined. Previous investigation of seven patients with asthma using HP ^{3}He-MRI pre- and post-bronchial thermoplasty showed a decrease in ventilation defects as a function of time post-treatment(340). Further investigation using HP ^{129}Xe-MRI to both guide treatment and evaluate response, may help tailor treatments for individual patients. Ventilation defects demonstrated with HP ^{129}Xe-MRI may help localise specific bronchopulmonary segments to be targeted with bronchial thermoplasty. Subsequent HP ^{129}Xe-MRI post-thermoplasty may quantify the relative ventilation within different pulmonary lobes and segments. This regional information may be extremely valuable to the clinician, enabling careful decisions concerning radiofrequency dose, time interval between treatment sessions or whether all treatment sessions are even necessary, to be made.

7.3.6 Improving radiotherapy planning

The regional information provided by HP ^{129}Xe-MRI may be used to inform radiotherapy plans to preserve functional lung tissue whilst enabling delivery of high tumoricidal dose to target lung cancer. Previous research with HP ^{3}He-MRI has shown feasibility of the technique to aid radiotherapy planning in lung cancer patients(502) and evaluate radiation-induced lung injury in patients after thoracic radiation treatment(503). HP ^{3}He-MRI ventilated lung volumes have successfully been incorporated into conformal avoidance treatment-planning

paradigms(504) and used to reduced radiation exposure compared with planning based purely on anatomical information(505).

HP ^{129}Xe-MRI may allow evaluation of radiotherapy response beyond reduction in tumour size/volume conventionally assessed by CT follow-up, since improvements in regional ventilation or gas exchange/transfer may be detected. Ethical approval has been obtained for a study to investigate HP ^{129}Xe-MRI pre- and post-chemoradiotherapy in patients with non-small cell lung cancer [NRES South Central Committee (Berkshire) REC reference 13/SC/0473]. Patients are currently being recruited to this study despite the challenge of poor performance status limiting study visit attendance and high loss to follow-up. Preliminary data from a patient with non-small cell lung cancer where HP ^{129}Xe-MRI was successfully acquired pre- and post- combined chemoradiotherapy is shown in Figure 7.1. The initial right upper lobe ventilation defect is demonstrated to largely resolve by the final-day of treatment. The images are particularly encouraging for patients undergoing intensive daily radiotherapy schedules but further longitudinal investigation in a larger sample size is still needed. In the future, data acquired pre-chemoradiotherapy could be incorporated into the individual patient's radiotherapy plan to ensure optimal dose delivery whilst conserving functional lung tissue. Post-chemoradiotherapy HP ^{129}Xe-MRI may detect radiotherapy response or development of radiation-induced lung injury early. This may in turn allow clinical oncologists to make decisions about modifying chemoradiotherapy schedules earlier in the treatment pathway.

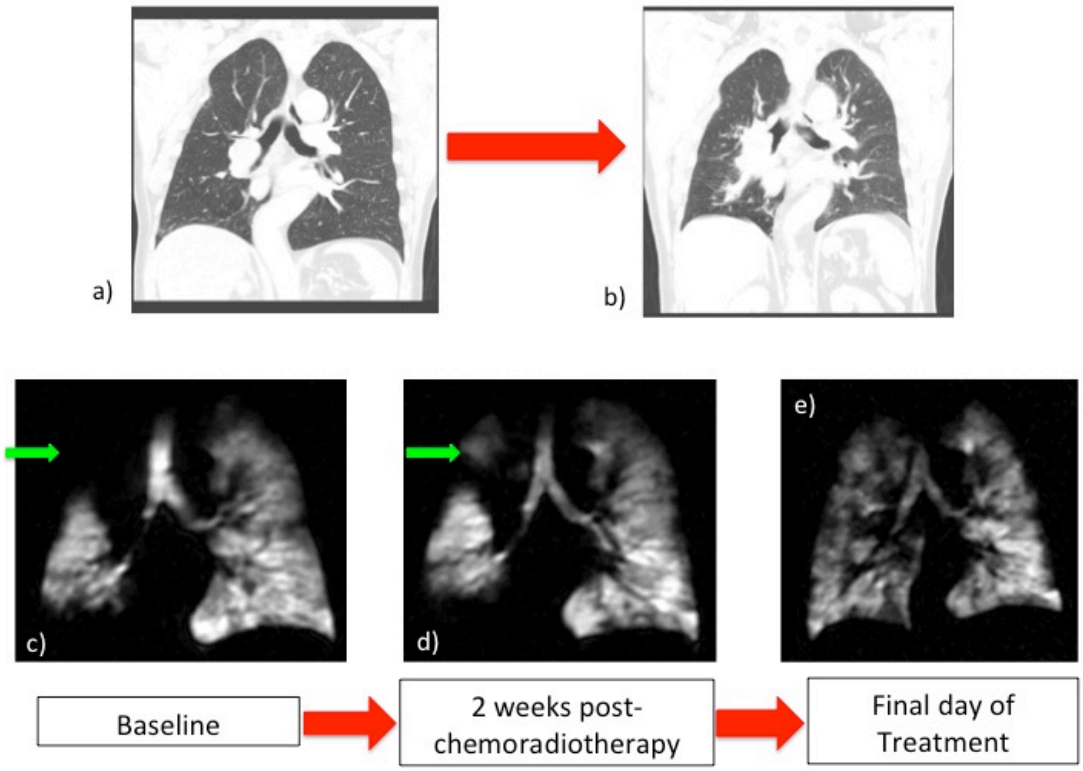

Figure 7.1: Coronal CT and HP ^{129}Xe-MR images from 72 year old female with non-small cell lung cancer. CT images show tumour centred at the right hilum a) pre-chemoradiotherapy and b) post-chemoradiotherapy with likely disease progression and subsequent new obstruction of the right upper lobe bronchus. In contrast, HP ^{129}Xe-MR ventilation images c) pre- d) two-week post- and e) on the final day of chemoradiotherapy treatment show gradual improvement and resolution of the right upper and lower lobe ventilation defects.

7.4 Research applications

7.4.1 Use as a surrogate end-point in drug development studies

Drug development studies present an imminent research application for HP ^{129}Xe-MRI. Clinical trials of new pharmacological treatments may benefit from

regional HP ^{129}Xe-MR parameters, as they appear more sensitive than global spirometric indices or PFTs particularly in heterogeneous respiratory disease. Furthermore, the use of HP ^{129}Xe-MRI may reduce the sample size needed for drug development studies as outcome may be based on surrogate measures.

HP ^{3}He-MRI has been used to investigate the efficacy of Ivacaftor, a new therapeutic agent for cystic fibrosis(506). Similar application of lobar HP ^{129}Xe-MR ventilation or ADC values as surrogate end-point measures in clinical trials for new COPD or asthma treatments is a clear translational use.

7.4.2 Assessment of gas transfer and exchange in interstitial lung disease

Although HP ^{129}Xe-MR dissolved phase imaging has not been investigated in this thesis, the unique property of ^{129}Xe to dissolve into the lung parenchyma and blood presents a significant advantage, allowing gas exchange dynamics to be probed. HP ^{129}Xe-MRI has the potential to play a significant role in the investigation of interstitial lung diseases, many of which can only be diagnosed by an invasive open or thoracoscopic lung biopsy. HP ^{129}Xe-MRI is non-invasive, may be performed repeatedly and dissolved-phase biomarkers; haematocrit, alveolar surface area per unit gas volume, capillary transit time(507, 508) and septal wall thickness may be used to monitor disease longitudinally and assess therapeutic response. There has been an explosion of potential therapies(509) in recent years driven by the need to improve prognosis of patients with interstitial lung diseases. HP ^{129}Xe-MRI may be used as a surrogate end-point in these drug

development trials and subsequently clinically to determine early therapeutic response. This will enable expensive therapies to be appropriately titrated up in patients who demonstrate a response or altered to different regimes if negligible response is shown.

7.5 Conclusion

Future efforts to advance HP ^{129}Xe-MRI should concentrate on well-designed multi-centre studies investigating its potential clinical utility in regional treatment evaluation, particularly LVRT for patients with COPD. Collaboration with industry would enable the role of HP ^{129}Xe-MRI in drug development to be further explored. Widespread adoption of HP ^{129}Xe-MRI across multiple clinical centres will require standardisation of parameters, including MR sequences, calibration of polarised ^{129}Xe gas concentrations and protocols for ^{129}Xe inhalation(510). The feasibility of performing a multinational, multicentre study using a central production facility has previously been accomplished with HP ^{3}He-MRI(330). The application of HP ^{129}Xe-MRI across multicentre sites in a similar approach would seem the next logistical step to progress towards clinical translation.

This thesis has contributed to the field of hyperpolarised noble gas MRI by further validating HP ^{129}Xe-MRI, improving methodology for regional analysis and determining its potential clinical utility in obstructive lung disease. Translation of this technique to the clinical arena will offer unique insights into the complex interaction between ventilation, diffusion and gas exchange at a

regional level and allow the true potential of HP ^{129}Xe-MRI in respiratory medicine to be realised.

8 Bibliography

1. The burden of lung disease 2nd Edition, A statistics report from the British Thoracic Society 2006.
2. World Health Organisation. World Health Report. Geneva: 2000.
3. Global Initiative for Chronic Obstructive Lung Disease (GOLD). Global strategy for the diagnosis, management and prevention of chronic obstructive pulmonary disease. Updated 2015.
4. Global Initiative for Chronic Obstructive Lung Disease; (GOLD). Global strategy for the diagnosis, management and prevention of COPD.2015. Available from: http://www.goldcopd.org/.
5. National Clinical Guideline Centre. Chronic obstructive pulmonary disease: management of chronic obstructive pulmonary disease in adults in primary and secondary care. London: National Clinical Guideline Centre; 2010.
6. Appendix D: Economics costs of COPD to the NHS. Thorax. 2004;59(Suppl 1):i192-i4.
7. Hogg JC, Chu F, Utokaparch S, Woods R, Elliott WM, Buzatu L, et al. The nature of small-airway obstruction in chronic obstructive pulmonary disease. The New England journal of medicine. 2004;350(26):2645-53.
8. McDonough JE, Yuan R, Suzuki M, Seyednejad N, Elliott WM, Sanchez PG, et al. Small-airway obstruction and emphysema in chronic obstructive pulmonary disease. The New England journal of medicine. 2011;365(17):1567-75.
9. Celli BR, Cote CG, Marin JM, Casanova C, Montes de Oca M, Mendez RA, et al. The body-mass index, airflow obstruction, dyspnea, and exercise capacity index in chronic obstructive pulmonary disease. The New England journal of medicine. 2004;350(10):1005-12.
10. Ong KC, Earnest A, Lu SJ. A multidimensional grading system (BODE index) as predictor of hospitalization for COPD. Chest. 2005;128(6):3810-6.
11. Pratt PC. Role of conventional chest radiography in diagnosis and exclusion of emphysema. The American journal of medicine. 1987;82(5):998-1006.
12. Thurlbeck WM, Muller NL. Emphysema: definition, imaging, and quantification. AJR American journal of roentgenology. 1994;163(5):1017-25.
13. Milne EN, Bass H. The roentgenologic diagnosis of early chronic obstructive pulmonary disease. Journal of the Canadian Association of Radiologists. 1969;20(1):3-15.
14. Katsura S, Martin CJ. The roenrgenologic diagnosis of anatomic emphysema. The American review of respiratory disease. 1967;96(4):700-6.
15. Nicklaus TM, Stowell DW, Christiansen WR, Renzetti AD, Jr. The accuracy of the roentgenologic diagnosis of chronic pulmonary emphysema. The American review of respiratory disease. 1966;93(6):889-99.
16. Reid L, Millard FJ. Correlation between Radiological Diagnosis and Structural Lung Changes in Emphysema. Clinical radiology. 1964;15:307-11.

17. Sutinen S, Christoforidis AJ, Klugh GA, Pratt PC. Roentgenologic Criteria for the Recognition of Nonsymptomatic Pulmonary Emphysema. Correlation between Roentgenologic Findings and Pulmonary Pathology. The American review of respiratory disease. 1965;91:69-76.
18. Thurlbeck WM, Simon G. Radiographic appearance of the chest in emphysema. AJR American journal of roentgenology. 1978;130(3):429-40.
19. Musk AW. Validation of the plain chest radiograph for epidemiologic studies of airflow obstruction. American journal of epidemiology. 1982;116(5):801-7.
20. Alderson PO, Secker-Walker RH, Forrest JV. Detection of obstructive pulmonary disease. Relative sensitivity of ventilation-perfusion studies and chest radiography. Radiology. 1974;112(3):643-8.
21. Herman PG. The chest roentgenogram: its role in evaluating cardiomegaly and chronic obstructive pulmonary disease. Chest. 1977;71(6):689-89.
22. Simon G. Radiology and Emphysema. Clinical radiology. 1964;15:293-306.
23. Phillips T. The Lateral Chest Radiograph and the Forced Expiratory Volume. British journal of diseases of the chest. 1965;59:39-40.
24. Andersen PE, Jr., Andersen LH, Jest P. The chest radiograph in chronic obstructive lung disease compared with measurements of single-breath nitrogen washout and spirometry. Clinical radiology. 1982;33(1):51-5.
25. Dull WL, Bohadana AB, Teculescu DB, Cereceda VJ. The standard chest roentgenogram for determining lung overinflation. Lung. 1982;160(6):311-4.
26. Simon G, Pride NB, Jones NL, Raimondi AC. Relation between abnormalities in the chest radiograph and changes in pulmonary function in chronic bronchitis and emphysema. Thorax. 1973;28(1):15-23.
27. Miniati M, Monti S, Stolk J, Mirarchi G, Falaschi F, Rabinovich R, et al. Value of chest radiography in phenotyping chronic obstructive pulmonary disease. Eur Respir J. 2008;31(3):509-15.
28. Burrows B, Fletcher CM, Heard BE, Jones NL, Wootliff JS. The emphysematous and bronchial types of chronic airways obstruction. A clinicopathological study of patients in London and Chicago. Lancet. 1966;1(7442):830-5.
29. Burrows B, Niden AH, Fletcher CM, Jones NL. Clinical Types of Chronic Obstructive Lung Disease in London and in Chicago. A Study of One Hundred Patients. The American review of respiratory disease. 1964;90:14-27.
30. Bergin C, Muller N, Nichols DM, Lillington G, Hogg JC, Mullen B, et al. The diagnosis of emphysema. A computed tomographic-pathologic correlation. The American review of respiratory disease. 1986;133(4):541-6.
31. Coddington R, Mera SL, Goddard PR, Bradfield JW. Pathological evaluation of computed tomography images of lungs. Journal of clinical pathology. 1982;35(5):536-40.
32. Foster WL, Jr., Pratt PC, Roggli VL, Godwin JD, Halvorsen RA, Jr., Putman CE. Centrilobular emphysema: CT-pathologic correlation. Radiology. 1986;159(1):27-32.
33. Gould GA, MacNee W, McLean A, Warren PM, Redpath A, Best JJ, et al. CT measurements of lung density in life can quantitate distal airspace enlargement--an essential defining feature of human emphysema. The American review of respiratory disease. 1988;137(2):380-92.

34. Hayhurst MD, MacNee W, Flenley DC, Wright D, McLean A, Lamb D, et al. Diagnosis of pulmonary emphysema by computerised tomography. Lancet. 1984;2(8398):320-2.
35. Hruban RH, Meziane MA, Zerhouni EA, Khouri NF, Fishman EK, Wheeler PS, et al. High resolution computed tomography of inflation-fixed lungs. Pathologic-radiologic correlation of centrilobular emphysema. The American review of respiratory disease. 1987;136(4):935-40.
36. Kuwano K, Matsuba K, Ikeda T, Murakami J, Araki A, Nishitani H, et al. The diagnosis of mild emphysema. Correlation of computed tomography and pathology scores. The American review of respiratory disease. 1990;141(1):169-78.
37. Miller RR, Muller NL, Vedal S, Morrison NJ, Staples CA. Limitations of computed tomography in the assessment of emphysema. The American review of respiratory disease. 1989;139(4):980-3.
38. Klein JS, Gamsu G, Webb WR, Golden JA, Muller NL. High-resolution CT diagnosis of emphysema in symptomatic patients with normal chest radiographs and isolated low diffusing capacity. Radiology. 1992;182(3):817-21.
39. Sanders C, Nath PH, Bailey WC. Detection of emphysema with computed tomography. Correlation with pulmonary function tests and chest radiography. Investigative radiology. 1988;23(4):262-6.
40. Ravin CE. Pulmonary vascularity: radiographic considerations. Journal of thoracic imaging. 1988;3(1):1-13.
41. Woodring JH. Pulmonary artery-bronchus ratios in patients with normal lungs, pulmonary vascular plethora, and congestive heart failure. Radiology. 1991;179(1):115-22.
42. Aysola RS, Hoffman EA, Gierada D, Wenzel S, Cook-Granroth J, Tarsi J, et al. Airway remodeling measured by multidetector CT is increased in severe asthma and correlates with pathology. Chest. 2008;134(6):1183-91.
43. Bankier AA, De Maertelaer V, Keyzer C, Gevenois PA. Pulmonary emphysema: subjective visual grading versus objective quantification with macroscopic morphometry and thin-section CT densitometry. Radiology. 1999;211(3):851-8.
44. Madani A, Keyzer C, Gevenois PA. Quantitative computed tomography assessment of lung structure and function in pulmonary emphysema. The European respiratory journal. 2001;18(4):720-30.
45. Muller NL, Staples CA, Miller RR, Abboud RT. "Density mask". An objective method to quantitate emphysema using computed tomography. Chest. 1988;94(4):782-7.
46. Nakano Y, Wong JC, de Jong PA, Buzatu L, Nagao T, Coxson HO, et al. The prediction of small airway dimensions using computed tomography. Am J Respir Crit Care Med. 2005;171(2):142-6.
47. Newman KB, Lynch DA, Newman LS, Ellegood D, Newell JD, Jr. Quantitative computed tomography detects air trapping due to asthma. Chest. 1994;106(1):105-9.
48. Hogg JC. Pathology of asthma. The Journal of allergy and clinical immunology. 1993;92(1 Pt 1):1-5.
49. McDonough JE, Yuan R, Suzuki M, Seyednejad N, Elliott WM, Sanchez PG, et al. Small-airway obstruction and emphysema in chronic obstructive

pulmonary disease. The New England journal of medicine. 2011;365(17):1567-75.
50. Madani A, Zanen J, de Maertelaer V, Gevenois PA. Pulmonary emphysema: objective quantification at multi-detector row CT--comparison with macroscopic and microscopic morphometry. Radiology. 2006;238(3):1036-43.
51. Gevenois PA, de Maertelaer V, De Vuyst P, Zanen J, Yernault JC. Comparison of computed density and macroscopic morphometry in pulmonary emphysema. Am J Respir Crit Care Med. 1995;152(2):653-7.
52. Heussel CP, Herth FJ, Kappes J, Hantusch R, Hartlieb S, Weinheimer O, et al. Fully automatic quantitative assessment of emphysema in computed tomography: comparison with pulmonary function testing and normal values. European radiology. 2009;19(10):2391-402.
53. Stolk J, Dirksen A, van der Lugt AA, Hutsebaut J, Mathieu J, de Ree J, et al. Repeatability of lung density measurements with low-dose computed tomography in subjects with alpha-1-antitrypsin deficiency-associated emphysema. Invest Radiol. 2001;36(11):648-51.
54. Murphy K, Pluim JP, van Rikxoort EM, de Jong PA, de Hoop B, Gietema HA, et al. Toward automatic regional analysis of pulmonary function using inspiration and expiration thoracic CT. Med Phys. 2012;39(3):1650-62.
55. Mets OM, Zanen P, Lammers JW, Isgum I, Gietema HA, van Ginneken B, et al. Early identification of small airways disease on lung cancer screening CT: comparison of current air trapping measures. Lung. 2012;190(6):629-33.
56. Grydeland TB, Dirksen A, Coxson HO, Eagan TM, Thorsen E, Pillai SG, et al. Quantitative computed tomography measures of emphysema and airway wall thickness are related to respiratory symptoms. Am J Respir Crit Care Med. 2010;181(4):353-9.
57. Washko GR, Dransfield MT, Estepar RS, Diaz A, Matsuoka S, Yamashiro T, et al. Airway wall attenuation: a biomarker of airway disease in subjects with COPD. J Appl Physiol (1985). 2009;107(1):185-91.
58. Lu GM, Zhao Y, Zhang LJ, Schoepf UJ. Dual-energy CT of the lung. AJR Am J Roentgenol. 2012;199(5 Suppl):S40-53.
59. Karcaaltincaba M, Aktas A. Dual-energy CT revisited with multidetector CT: review of principles and clinical applications. Diagn Interv Radiol. 2011;17(3):181-94.
60. Lee CW, Seo JB, Lee Y, Chae EJ, Kim N, Lee HJ, et al. A pilot trial on pulmonary emphysema quantification and perfusion mapping in a single-step using contrast-enhanced dual-energy computed tomography. Invest Radiol. 2012;47(1):92-7.
61. Pansini V, Remy-Jardin M, Faivre JB, Schmidt B, Dejardin-Bothelo A, Perez T, et al. Assessment of lobar perfusion in smokers according to the presence and severity of emphysema: preliminary experience with dual-energy CT angiography. European radiology. 2009;19(12):2834-43.
62. Chae EJ, Seo JB, Lee J, Kim N, Goo HW, Lee HJ, et al. Xenon ventilation imaging using dual-energy computed tomography in asthmatics: initial experience. Invest Radiol. 2010;45(6):354-61.
63. Jung JW, Kwon JW, Kim TW, Lee SH, Kim KM, Kang HR, et al. New insight into the assessment of asthma using xenon ventilation computed tomography. Ann Allergy Asthma Immunol. 2013;111(2):90-5 e2.

64. Goo HW, Yang DH, Hong SJ, Yu J, Kim BJ, Seo JB, et al. Xenon ventilation CT using dual-source and dual-energy technique in children with bronchiolitis obliterans: correlation of xenon and CT density values with pulmonary function test results. Pediatr Radiol. 2010;40(9):1490-7.
65. Bajc M, Neilly JB, Miniati M, Schuemichen C, Meignan M, Jonson B, et al. EANM guidelines for ventilation/perfusion scintigraphy : Part 1. Pulmonary imaging with ventilation/perfusion single photon emission tomography. European journal of nuclear medicine and molecular imaging. 2009;36(8):1356-70.
66. Freeman LM, Krynyckyi B, Zuckier LS. Enhanced lung scan diagnosis of pulmonary embolism with the use of ancillary scintigraphic findings and clinical correlation. Seminars in nuclear medicine. 2001;31(2):143-57.
67. Mariani G, Bruselli L, Kuwert T, Kim EE, Flotats A, Israel O, et al. A review on the clinical uses of SPECT/CT. European journal of nuclear medicine and molecular imaging. 2010;37(10):1959-85.
68. Gutte H, Mortensen J, Jensen CV, Johnbeck CB, von der Recke P, Petersen CL, et al. Detection of pulmonary embolism with combined ventilation-perfusion SPECT and low-dose CT: head-to-head comparison with multidetector CT angiography. Journal of nuclear medicine : official publication, Society of Nuclear Medicine. 2009;50(12):1987-92.
69. Gutte H, Mortensen J, Jensen CV, von der Recke P, Petersen CL, Kristoffersen US, et al. Comparison of V/Q SPECT and planar V/Q lung scintigraphy in diagnosing acute pulmonary embolism. Nuclear medicine communications. 2010;31(1):82-6.
70. Phillips JJ, Straiton J, Staff RT. Planar and SPECT ventilation/perfusion imaging and computed tomography for the diagnosis of pulmonary embolism: A systematic review and meta-analysis of the literature, and cost and dose comparison. Eur J Radiol. 2015;84(7):1392-400.
71. Inmai T, Sasaki Y, Shinkai T, Ohishi H, Nezu K, Nishimoto Y, et al. Clinical evaluation of 99mTc-Technegas SPECT in thoracoscopic lung volume reduction surgery in patients with pulmonary emphysema. Annals of nuclear medicine. 2000;14(4):263-9.
72. Xu J, Moonen M, Johansson A, Gustafsson A, Bake B. Quantitative analysis of inhomogeneity in ventilation SPET. European journal of nuclear medicine. 2001;28(12):1795-800.
73. Pellegrino R, Biggi A, Papaleo A, Camuzzini G, Rodarte JR, Brusasco V. Regional expiratory flow limitation studied with Technegas in asthma. Journal of applied physiology. 2001;91(5):2190-8.
74. Sasaki Y, Imai T, Shinkai T, Ohishi H, Otsuji H, Uchida H, et al. Estimation of regional lung function in interstitial pulmonary disease using 99mTc-technegas and 99mTc-macroaggregated albumin single-photon emission tomography. European journal of nuclear medicine. 1998;25(12):1623-9.
75. Celli BR, MacNee W, Force AET. Standards for the diagnosis and treatment of patients with COPD: a summary of the ATS/ERS position paper. Eur Respir J. 2004;23(6):932-46.
76. Taplin GV, Tashkin DP, Chopra SK, Anselmi OE, Elam D, Calvarese B, et al. Early detection of chronic obstructive pulmonary disease using radionuclide lung-imaging procedures. Chest. 1977;71(5):567-75.

77. Santolicandro A, Ruschi S, Fornai E, Giuntini C. Imaging of ventilation in chronic obstructive pulmonary disease. Journal of thoracic imaging. 1986;1(2):36-53.
78. Jogi J, Ekberg M, Jonson B, Bozovic G, Bajc M. Ventilation/perfusion SPECT in chronic obstructive pulmonary disease: an evaluation by reference to symptoms, spirometric lung function and emphysema, as assessed with HRCT. European journal of nuclear medicine and molecular imaging. 2011;38(7):1344-52.
79. Palmaz JC, Barnett CA, Reich SB, Krumpe PE, Farrer PA. Reverse ventilation--perfusion mismatch. Clinical nuclear medicine. 1984;9(1):6-9.
80. Jogi J, Palmer J, Jonson B, Bajc M. Heart failure diagnostics based on ventilation/perfusion single photon emission computed tomography pattern and quantitative perfusion gradients. Nuclear medicine communications. 2008;29(8):666-73.
81. Investigators P. Value of the ventilation/perfusion scan in acute pulmonary embolism. Results of the prospective investigation of pulmonary embolism diagnosis (PIOPED). Jama. 1990;263(20):2753-9.
82. Roach PJ, Gradinscak DJ, Schembri GP, Bailey EA, Willowson KP, Bailey DL. SPECT/CT in V/Q scanning. Seminars in nuclear medicine. 2010;40(6):455-66.
83. Satoh K, Nakano S, Tanabe M, Nishiyama Y, Takahashi K, Kobayashi T, et al. A clinical comparison between Technegas SPECT, CT, and pulmonary function tests in patients with emphysema. Radiation medicine. 1997;15(5):277-82.
84. Petersson J, Sanchez-Crespo A, Rohdin M, Montmerle S, Nyren S, Jacobsson H, et al. Physiological evaluation of a new quantitative SPECT method measuring regional ventilation and perfusion. Journal of applied physiology. 2004;96(3):1127-36.
85. Hogg JC. Pathophysiology of airflow limitation in chronic obstructive pulmonary disease. Lancet. 2004;364(9435):709-21.
86. Van Muylem A, Antoine M, Yernault JC, Paiva M, Estenne M. Inert gas single-breath washout after heart-lung transplantation. American journal of respiratory and critical care medicine. 1995;152(3):947-52.
87. Nagao M, Murase K, Ichiki T, Sakai S, Yasuhara Y, Ikezoe J. Quantitative analysis of technegas SPECT: evaluation of regional severity of emphysema. Journal of nuclear medicine : official publication, Society of Nuclear Medicine. 2000;41(4):590-5.
88. Chung HW, Huang YH. Fractal analysis of nuclear medicine images for the diagnosis of pulmonary emphysema: interpretations, implications, and limitations. AJR American journal of roentgenology. 2000;174(4):1055-9.
89. Christian JA, Partridge M, Nioutsikou E, Cook G, McNair HA, Cronin B, et al. The incorporation of SPECT functional lung imaging into inverse radiotherapy planning for non-small cell lung cancer. Radiotherapy and oncology : journal of the European Society for Therapeutic Radiology and Oncology. 2005;77(3):271-7.
90. Lavrenkov K, Singh S, Christian JA, Partridge M, Nioutsikou E, Cook G, et al. Effective avoidance of a functional spect-perfused lung using intensity modulated radiotherapy (IMRT) for non-small cell lung cancer (NSCLC): an update of a planning study. Radiotherapy and oncology : journal of the European Society for Therapeutic Radiology and Oncology. 2009;91(3):349-52.

91. Seppenwoolde Y, Engelsman M, De Jaeger K, Muller SH, Baas P, McShan DL, et al. Optimizing radiation treatment plans for lung cancer using lung perfusion information. Radiotherapy and oncology : journal of the European Society for Therapeutic Radiology and Oncology. 2002;63(2):165-77.
92. Shioyama Y, Jang SY, Liu HH, Guerrero T, Wang X, Gayed IW, et al. Preserving functional lung using perfusion imaging and intensity-modulated radiation therapy for advanced-stage non-small cell lung cancer. Int J Radiat Oncol Biol Phys. 2007;68(5):1349-58.
93. Kong FM, Hayman JA, Griffith KA, Kalemkerian GP, Arenberg D, Lyons S, et al. Final toxicity results of a radiation-dose escalation study in patients with non-small-cell lung cancer (NSCLC): predictors for radiation pneumonitis and fibrosis. Int J Radiat Oncol Biol Phys. 2006;65(4):1075-86.
94. Roeder F, Friedrich J, Timke C, Kappes J, Huber P, Krempien R, et al. Correlation of patient-related factors and dose-volume histogram parameters with the onset of radiation pneumonitis in patients with small cell lung cancer. Strahlentherapie und Onkologie : Organ der Deutschen Rontgengesellschaft [et al]. 2010;186(3):149-56.
95. Kong FM, Ten Haken RK, Schipper MJ, Sullivan MA, Chen M, Lopez C, et al. High-dose radiation improved local tumor control and overall survival in patients with inoperable/unresectable non-small-cell lung cancer: long-term results of a radiation dose escalation study. Int J Radiat Oncol Biol Phys. 2005;63(2):324-33.
96. Bolliger CT, Guckel C, Engel H, Stohr S, Wyser CP, Schoetzau A, et al. Prediction of functional reserves after lung resection: comparison between quantitative computed tomography, scintigraphy, and anatomy. Respiration. 2002;69(6):482-9.
97. Chandra D, Lipson DA, Hoffman EA, Hansen-Flaschen J, Sciurba FC, Decamp MM, et al. Perfusion scintigraphy and patient selection for lung volume reduction surgery. American journal of respiratory and critical care medicine. 2010;182(7):937-46.
98. Giordano A, Calcagni ML, Meduri G, Valente S, Galli G. Perfusion lung scintigraphy for the prediction of postlobectomy residual pulmonary function. Chest. 1997;111(6):1542-7.
99. Hunsaker AR, Ingenito EP, Reilly JJ, Costello P. Lung volume reduction surgery for emphysema: correlation of CT and V/Q imaging with physiologic mechanisms of improvement in lung function. Radiology. 2002;222(2):491-8.
100. Thurnheer R, Engel H, Weder W, Stammberger U, Laube I, Russi EW, et al. Role of lung perfusion scintigraphy in relation to chest computed tomography and pulmonary function in the evaluation of candidates for lung volume reduction surgery. American journal of respiratory and critical care medicine. 1999;159(1):301-10.
101. Toney LK, Wanner M, Miyaoka RS, Alessio AM, Wood DE, Vesselle H. Improved prediction of lobar perfusion contribution using technetium-99m-labeled macroaggregate of albumin single photon emission computed tomography/computed tomography with attenuation correction. J Thorac Cardiovasc Surg. 2014;148(5):2345-52.
102. Matin TN, Xu X, McGowan DR, Doel T, Grau V, Bradley KM, et al. Novel single photon emission tomography/computed tomography (SPECT/CT) methodology for accurate determination of lobar lung function in chronic

obstructive pulmonary disease (COPD). Clinical radiology. 2016;[In press - submitted October 2016].
103. Stavngaard T, Sogaard LV, Mortensen J, Hanson LG, Schmiedeskamp J, Berthelsen AK, et al. Hyperpolarized 3He MRI and 81mKr SPECT in chronic obstructive pulmonary disease. European journal of nuclear medicine and molecular imaging. 2005;32(4):448-57.
104. King GG, Harris B, Mahadev S. V/Q SPECT: utility for investigation of pulmonary physiology. Seminars in nuclear medicine. 2010;40(6):467-73.
105. Verbanck S, Paiva M. Model simulations of gas mixing and ventilation distribution in the human lung. Journal of applied physiology. 1990;69(6):2269-79.
106. Satoh K, Takahashi K, Sasaki M, Kobayashi T, Honjo N, Ohkawa M, et al. Comparison of 99mTc-Technegas SPECT with 133Xe dynamic SPECT in pulmonary emphysema. Annals of nuclear medicine. 1997;11(3):201-6.
107. Hatabu H, Alsop DC, Listerud J, Bonnet M, Gefter WB. T2* and proton density measurement of normal human lung parenchyma using submillisecond echo time gradient echo magnetic resonance imaging. European journal of radiology. 1999;29(3):245-52.
108. Johnson KM, Fain SB, Schiebler ML, Nagle S. Optimized 3D ultrashort echo time pulmonary MRI. Magn Reson Med. 2013;70(5):1241-50.
109. Bauman G, Puderbach M, Deimling M, Jellus V, Chefd'hotel C, Dinkel J, et al. Non-contrast-enhanced perfusion and ventilation assessment of the human lung by means of fourier decomposition in proton MRI. Magn Reson Med. 2009;62(3):656-64.
110. Couch MJ, Blasiak B, Tomanek B, Ouriadov AV, Fox MS, Dowhos KM, et al. Hyperpolarized and inert gas MRI: the future. Molecular imaging and biology : MIB : the official publication of the Academy of Molecular Imaging. 2015;17(2):149-62.
111. Mayo JR, MacKay A, Muller NL. MR imaging of the lungs: value of short TE spin-echo pulse sequences. AJR American journal of roentgenology. 1992;159(5):951-6.
112. Hoffman EA, Lynch DA, Barr RG, van Beek EJ, Parraga G, Investigators I. Pulmonary CT and MRI phenotypes that help explain chronic pulmonary obstruction disease pathophysiology and outcomes. J Magn Reson Imaging. 2016;43(3):544-57.
113. Takahashi M, Togao O, Obara M, van Cauteren M, Ohno Y, Doi S, et al. Ultra-short echo time (UTE) MR imaging of the lung: comparison between normal and emphysematous lungs in mutant mice. J Magn Reson Imaging. 2010;32(2):326-33.
114. Zurek M, Boyer L, Caramelle P, Boczkowski J, Cremillieux Y. Longitudinal and noninvasive assessment of emphysema evolution in a murine model using proton MRI. Magn Reson Med. 2012;68(3):898-904.
115. Capaldi DP, Sheikh K, Guo F, Svenningsen S, Etemad-Rezai R, Coxson HO, et al. Free-breathing pulmonary 1H and Hyperpolarized 3He MRI: comparison in COPD and bronchiectasis. Acad Radiol. 2015;22(3):320-9.
116. Mayo JR. Thoracic magnetic resonance imaging: physics and pulse sequences. Journal of thoracic imaging. 1993;8(1):1-11.

117. Weiger M, Wu M, Wurnig MC, Kenkel D, Jungraithmayr W, Boss A, et al. Rapid and robust pulmonary proton ZTE imaging in the mouse. NMR Biomed. 2014;27(9):1129-34.
118. Bauman G, Lutzen U, Ullrich M, Gaass T, Dinkel J, Elke G, et al. Pulmonary functional imaging: qualitative comparison of Fourier decomposition MR imaging with SPECT/CT in porcine lung. Radiology. 2011;260(2):551-9.
119. Bauman G, Scholz A, Rivoire J, Terekhov M, Friedrich J, de Oliveira A, et al. Lung ventilation- and perfusion-weighted Fourier decomposition magnetic resonance imaging: in vivo validation with hyperpolarized 3He and dynamic contrast-enhanced MRI. Magn Reson Med. 2013;69(1):229-37.
120. Abraham MH, Kamlet MJ, Taft RW, Doherty RM, Weathersby PK. Solubility properties in polymers and biological media. 2. The correlation and prediction of the solubilities of nonelectrolytes in biological tissues and fluids. J Med Chem. 1985;28(7):865-70.
121. Miller KW, Reo NV, Schoot Uiterkamp AJ, Stengle DP, Stengle TR, Williamson KL. Xenon NMR: chemical shifts of a general anesthetic in common solvents, proteins, and membranes. Proc Natl Acad Sci U S A. 1981;78(8):4946-9.
122. Sakai K, Bilek AM, Oteiza E, Walsworth RL, Balamore D, Jolesz FA, et al. Temporal dynamics of hyperpolarized 129Xe resonances in living rats. J Magn Reson B. 1996;111(3):300-4.
123. Ruppert K, Brookeman JR, Hagspiel KD, Driehuys B, Mugler JP, 3rd. NMR of hyperpolarized (129)Xe in the canine chest: spectral dynamics during a breath-hold. NMR in biomedicine. 2000;13(4):220-8.
124. Ruppert K, Brookeman JR, Hagspiel KD, Mugler JP, 3rd. Probing lung physiology with xenon polarization transfer contrast (XTC). Magn Reson Med. 2000;44(3):349-57.
125. Mansson S, Wolber J, Driehuys B, Wollmer P, Golman K. Characterization of diffusing capacity and perfusion of the rat lung in a lipopolysaccaride disease model using hyperpolarized 129Xe. Magn Reson Med. 2003;50(6):1170-9.
126. Driehuys B, Cofer GP, Pollaro J, Mackel JB, Hedlund LW, Johnson GA. Imaging alveolar-capillary gas transfer using hyperpolarized 129Xe MRI. Proceedings of the National Academy of Sciences of the United States of America. 2006;103(48):18278-83.
127. Abdeen N, Cross A, Cron G, White S, Rand T, Miller D, et al. Measurement of xenon diffusing capacity in the rat lung by hyperpolarized 129Xe MRI and dynamic spectroscopy in a single breath-hold. Magn Reson Med. 2006;56(2):255-64.
128. Patz S, Hersman FW, Muradian I, Hrovat MI, Ruset IC, Ketel S, et al. Hyperpolarized (129)Xe MRI: a viable functional lung imaging modality? European journal of radiology. 2007;64(3):335-44.
129. Patz S, Muradian I, Hrovat MI, Ruset IC, Topulos G, Covrig SD, et al. Human pulmonary imaging and spectroscopy with hyperpolarized 129Xe at 0.2T. Academic radiology. 2008;15(6):713-27.
130. Driehuys B, Moller HE, Cleveland ZI, Pollaro J, Hedlund LW. Pulmonary perfusion and xenon gas exchange in rats: MR imaging with intravenous injection of hyperpolarized 129Xe. Radiology. 2009;252(2):386-93.
131. Albert MS, Cates GD, Driehuys B, Happer W, Saam B, Springer CS, Jr., et al. Biological magnetic resonance imaging using laser-polarized 129Xe. Nature. 1994;370(6486):199-201.

132. MacFall JR, Charles HC, Black RD, Middleton H, Swartz JC, Saam B, et al. Human lung air spaces: potential for MR imaging with hyperpolarized He-3. Radiology. 1996;200(2):553-8.
133. Kouzes RT, Ely JH, Erikson LE, Kernan WJ, Lintereur AT, Siciliano ER, et al. Neutron detection alternatives to 3He for national security applications. Nuclear Instruments and Methods in Physics Research Section A: Accelerators, Spectrometers, Detectors and Associated Equipment. 2010;623(3):1035-45.
134. Woods JC. Mine the moon for 3He MRI? Not yet. Journal of applied physiology. 2013;114(6):705-6.
135. de Lange EE, Mugler JP, 3rd, Brookeman JR, Knight-Scott J, Truwit JD, Teates CD, et al. Lung air spaces: MR imaging evaluation with hyperpolarized 3He gas. Radiology. 1999;210(3):851-7.
136. Patz S, Hersman FW, Muradian I, Hrovat MI, Ruset IC, Ketel S, et al. Hyperpolarized (129)Xe MRI: a viable functional lung imaging modality? Eur J Radiol. 2007;64(3):335-44.
137. Hersman FW, Ruset IC, Ketel S, Muradian I, Covrig SD, Distelbrink J, et al. Large production system for hyperpolarized 129Xe for human lung imaging studies. Acad Radiol. 2008;15(6):683-92.
138. Cho A. Physics. Helium-3 shortage could put freeze on low-temperature research. Science. 2009;326(5954):778-9.
139. Nambu K, Suzuki R, Hirakawa K. Cerebral blood flow: measurement with xenon-enhanced dynamic helical CT. Radiology. 1995;195(1):53-7.
140. Suga K, Nishigauchi K, Kume N, Takano K, Koike S, Shimizu K, et al. Ventilation abnormalities in obstructive airways disorder: detection with pulmonary dynamic densitometry by means of spiral CT versus dynamic Xe-133 SPECT. Radiology. 1997;202(3):855-62.
141. Salerno M, Altes TA, Mugler JP, 3rd, Nakatsu M, Hatabu H, de Lange EE. Hyperpolarized noble gas MR imaging of the lung: potential clinical applications. Eur J Radiol. 2001;40(1):33-44.
142. Moller HE, Chen XJ, Saam B, Hagspiel KD, Johnson GA, Altes TA, et al. MRI of the lungs using hyperpolarized noble gases. Magnetic resonance in medicine : official journal of the Society of Magnetic Resonance in Medicine / Society of Magnetic Resonance in Medicine. 2002;47(6):1029-51.
143. van Beek EJ, Wild JM, Kauczor HU, Schreiber W, Mugler JP, 3rd, de Lange EE. Functional MRI of the lung using hyperpolarized 3-helium gas. J Magn Reson Imaging. 2004;20(4):540-54.
144. Matsuoka S, Patz S, Albert MS, Sun Y, Rizi RR, Gefter WB, et al. Hyperpolarized gas MR Imaging of the lung: current status as a research tool. J Thorac Imaging. 2009;24(3):181-8.
145. O'Halloran RL, Holmes JH, Wu YC, Alexander A, Fain SB. Helium-3 MR q-space imaging with radial acquisition and iterative highly constrained back-projection. Magn Reson Med. 2010;63(1):41-50.
146. Kaushik SS, Cleveland ZI, Cofer GP, Metz G, Beaver D, Nouls J, et al. Diffusion-weighted hyperpolarized 129Xe MRI in healthy volunteers and subjects with chronic obstructive pulmonary disease. Magn Reson Med. 2011;65(4):1154-65.
147. Shukla Y, Wheatley A, Kirby M, Svenningsen S, Farag A, Santyr GE, et al. Hyperpolarized 129Xe magnetic resonance imaging: tolerability in healthy

volunteers and subjects with pulmonary disease. Acad Radiol. 2012;19(8):941-51.
148. Qing K, Ruppert K, Jiang Y, Mata JF, Miller GW, Shim YM, et al. Regional mapping of gas uptake by blood and tissue in the human lung using hyperpolarized xenon-129 MRI. J Magn Reson Imaging. 2013.
149. Wang C, Mugler JP, 3rd, de Lange EE, Patrie JT, Mata JF, Altes TA. Lung injury induced by secondhand smoke exposure detected with hyperpolarized helium-3 diffusion MR. J Magn Reson Imaging. 2013.
150. Kauczor HU, Hofmann D, Kreitner KF, Nilgens H, Surkau R, Heil W, et al. Normal and abnormal pulmonary ventilation: visualization at hyperpolarized He-3 MR imaging. Radiology. 1996;201(2):564-8.
151. McMahon CJ, Dodd JD, Hill C, Woodhouse N, Wild JM, Fichele S, et al. Hyperpolarized 3helium magnetic resonance ventilation imaging of the lung in cystic fibrosis: comparison with high resolution CT and spirometry. Eur Radiol. 2006;16(11):2483-90.
152. Donnelly LF, MacFall JR, McAdams HP, Majure JM, Smith J, Frush DP, et al. Cystic fibrosis: combined hyperpolarized 3He-enhanced and conventional proton MR imaging in the lung--preliminary observations. Radiology. 1999;212(3):885-9.
153. Kauczor HU, Ebert M, Kreitner KF, Nilgens H, Surkau R, Heil W, et al. Imaging of the lungs using 3He MRI: preliminary clinical experience in 18 patients with and without lung disease. J Magn Reson Imaging. 1997;7(3):538-43.
154. Altes TA, Powers PL, Knight-Scott J, Rakes G, Platts-Mills TA, de Lange EE, et al. Hyperpolarized 3He MR lung ventilation imaging in asthmatics: preliminary findings. J Magn Reson Imaging. 2001;13(3):378-84.
155. Gast KK, Viallon M, Eberle B, Lill J, Puderbach MU, Hanke AT, et al. MRI in lung transplant recipients using hyperpolarized 3He: comparison with CT. J Magn Reson Imaging. 2002;15(3):268-74.
156. Zaporozhan J, Ley S, Gast KK, Schmiedeskamp J, Biedermann A, Eberle B, et al. Functional analysis in single-lung transplant recipients: a comparative study of high-resolution CT, 3He-MRI, and pulmonary function tests. Chest. 2004;125(1):173-81.
157. de Lange EE, Altes TA, Patrie JT, Gaare JD, Knake JJ, Mugler JP, 3rd, et al. Evaluation of asthma with hyperpolarized helium-3 MRI: correlation with clinical severity and spirometry. Chest. 2006;130(4):1055-62.
158. Samee S, Altes T, Powers P, de Lange EE, Knight-Scott J, Rakes G, et al. Imaging the lungs in asthmatic patients by using hyperpolarized helium-3 magnetic resonance: assessment of response to methacholine and exercise challenge. J Allergy Clin Immunol. 2003;111(6):1205-11.
159. Deninger AJ, Mansson S, Petersson JS, Pettersson G, Magnusson P, Svensson J, et al. Quantitative measurement of regional lung ventilation using 3He MRI. Magn Reson Med. 2002;48(2):223-32.
160. Mansson S, Deninger AJ, Magnusson P, Pettersson G, Olsson LE, Hansson G, et al. 3He MRI-based assessment of posture-dependent regional ventilation gradients in rats. J Appl Physiol. 2005;98(6):2259-67.
161. Spector ZZ, Emami K, Fischer MC, Zhu J, Ishii M, Vahdat V, et al. Quantitative assessment of emphysema using hyperpolarized 3He magnetic resonance imaging. Magn Reson Med. 2005;53(6):1341-6.

162. Santyr GE, Lam WW, Ouriadov A. Rapid and efficient mapping of regional ventilation in the rat lung using hyperpolarized 3He with Flip Angle Variation for Offset of RF and Relaxation (FAVOR). Magn Reson Med. 2008;59(6):1304-10.
163. Emami K, Cadman RV, Woodburn JM, Fischer MC, Kadlecek SJ, Zhu J, et al. Early changes of lung function and structure in an elastase model of emphysema--a hyperpolarized 3He MRI study. J Appl Physiol. 2008;104(3):773-86.
164. Cai J, Altes TA, Miller GW, Sheng K, Read PW, Mata JF, et al. MR grid-tagging using hyperpolarized helium-3 for regional quantitative assessment of pulmonary biomechanics and ventilation. Magn Reson Med. 2007;58(2):373-80.
165. Deppe MH, Parra-Robles J, Marshall H, Lanz T, Wild JM. A flexible 32-channel receive array combined with a homogeneous transmit coil for human lung imaging with hyperpolarized 3He at 1.5 T. Magn Reson Med. 2011;66(6):1788-97.
166. Mugler JP, 3rd, Driehuys B, Brookeman JR, Cates GD, Berr SS, Bryant RG, et al. MR imaging and spectroscopy using hyperpolarized 129Xe gas: preliminary human results. Magn Reson Med. 1997;37(6):809-15.
167. Driehuys B, Martinez-Jimenez S, Cleveland ZI, Metz GM, Beaver DM, Nouls JC, et al. Chronic obstructive pulmonary disease: safety and tolerability of hyperpolarized 129Xe MR imaging in healthy volunteers and patients. Radiology. 2012;262(1):279-89.
168. Saam BT, Yablonskiy DA, Kodibagkar VD, Leawoods JC, Gierada DS, Cooper JD, et al. MR imaging of diffusion of (3)He gas in healthy and diseased lungs. Magn Reson Med. 2000;44(2):174-9.
169. Salerno M, de Lange EE, Altes TA, Truwit JD, Brookeman JR, Mugler JP, 3rd. Emphysema: hyperpolarized helium 3 diffusion MR imaging of the lungs compared with spirometric indexes--initial experience. Radiology. 2002;222(1):252-60.
170. Swift AJ, Wild JM, Fichele S, Woodhouse N, Fleming S, Waterhouse J, et al. Emphysematous changes and normal variation in smokers and COPD patients using diffusion 3He MRI. Eur J Radiol. 2005;54(3):352-8.
171. Woods JC, Yablonskiy DA, Choong CK, Chino K, Pierce JA, Hogg JC, et al. Long-range diffusion of hyperpolarized 3He in explanted normal and emphysematous human lungs via magnetization tagging. J Appl Physiol. 2005;99(5):1992-7.
172. Mata JF, Altes TA, Cai J, Ruppert K, Mitzner W, Hagspiel KD, et al. Evaluation of emphysema severity and progression in a rabbit model: comparison of hyperpolarized 3He and 129Xe diffusion MRI with lung morphometry. J Appl Physiol. 2007;102(3):1273-80.
173. Peces-Barba G, Ruiz-Cabello J, Cremillieux Y, Rodriguez I, Dupuich D, Callot V, et al. Helium-3 MRI diffusion coefficient: correlation to morphometry in a model of mild emphysema. Eur Respir J. 2003;22(1):14-9.
174. Chen XJ, Hedlund LW, Moller HE, Chawla MS, Maronpot RR, Johnson GA. Detection of emphysema in rat lungs by using magnetic resonance measurements of 3He diffusion. Proc Natl Acad Sci U S A. 2000;97(21):11478-81.
175. Morbach AE, Gast KK, Schmiedeskamp J, Dahmen A, Herweling A, Heussel CP, et al. Diffusion-weighted MRI of the lung with hyperpolarized helium-3: a study of reproducibility. J Magn Reson Imaging. 2005;21(6):765-74.
176. Diaz S, Casselbrant I, Piitulainen E, Pettersson G, Magnusson P, Peterson B, et al. Hyperpolarized 3He apparent diffusion coefficient MRI of the lung:

reproducibility and volume dependency in healthy volunteers and patients with emphysema. J Magn Reson Imaging. 2008;27(4):763-70.
177. Fain SB, Panth SR, Evans MD, Wentland AL, Holmes JH, Korosec FR, et al. Early emphysematous changes in asymptomatic smokers: detection with 3He MR imaging. Radiology. 2006;239(3):875-83.
178. Fain SB, Altes TA, Panth SR, Evans MD, Waters B, Mugler JP, 3rd, et al. Detection of age-dependent changes in healthy adult lungs with diffusion-weighted 3He MRI. Acad Radiol. 2005;12(11):1385-93.
179. Altes TA, Mata J, de Lange EE, Brookeman JR, Mugler JP, 3rd. Assessment of lung development using hyperpolarized helium-3 diffusion MR imaging. J Magn Reson Imaging. 2006;24(6):1277-83.
180. Yablonskiy DA, Sukstanskii AL, Leawoods JC, Gierada DS, Bretthorst GL, Lefrak SS, et al. Quantitative in vivo assessment of lung microstructure at the alveolar level with hyperpolarized 3He diffusion MRI. Proc Natl Acad Sci U S A. 2002;99(5):3111-6.
181. Yablonskiy DA, Sukstanskii AL, Woods JC, Gierada DS, Quirk JD, Hogg JC, et al. Quantification of lung microstructure with hyperpolarized 3He diffusion MRI. J Appl Physiol (1985). 2009;107(4):1258-65.
182. Shanbhag DD, Altes TA, Miller GW, Mata JF, Knight-Scott J. q-Space analysis of lung morphometry in vivo with hyperpolarized 3He spectroscopy. J Magn Reson Imaging. 2006;24(1):84-94.
183. Chen XJ, Moller HE, Chawla MS, Cofer GP, Driehuys B, Hedlund LW, et al. Spatially resolved measurements of hyperpolarized gas properties in the lung in vivo. Part I: diffusion coefficient. Magn Reson Med. 1999;42(4):721-8.
184. Saam B, Happer W, Middleton H. Nuclear relaxation of 3He in the presence of O2. Phys Rev A. 1995;52(1):862-5.
185. Eberle B, Weiler N, Markstaller K, Kauczor H, Deninger A, Ebert M, et al. Analysis of intrapulmonary O(2) concentration by MR imaging of inhaled hyperpolarized helium-3. J Appl Physiol. 1999;87(6):2043-52.
186. Rizi RR, Baumgardner JE, Ishii M, Spector ZZ, Edvinsson JM, Jalali A, et al. Determination of regional VA/Q by hyperpolarized 3He MRI. Magn Reson Med. 2004;52(1):65-72.
187. Butler JP, Mair RW, Hoffmann D, Hrovat MI, Rogers RA, Topulos GP, et al. Measuring surface-area-to-volume ratios in soft porous materials using laser-polarized xenon interphase exchange nuclear magnetic resonance. J Phys Condens Matter. 2002;14(13):L297-304.
188. Guenther D, Hanisch G, Kauczor HU. Functional MR imaging of pulmonary ventilation using hyperpolarized noble gases. Acta radiologica. 2000;41(6):519-28.
189. Wild JM, Paley MN, Kasuboski L, Swift A, Fichele S, Woodhouse N, et al. Dynamic radial projection MRI of inhaled hyperpolarized 3He gas. Magn Reson Med. 2003;49(6):991-7.
190. Holmes JH, Korosec FR, Du J, O'Halloran RL, Sorkness RL, Grist TM, et al. Imaging of lung ventilation and respiratory dynamics in a single ventilation cycle using hyperpolarized He-3 MRI. J Magn Reson Imaging. 2007;26(3):630-6.
191. Koumellis P, van Beek EJ, Woodhouse N, Fichele S, Swift AJ, Paley MN, et al. Quantitative analysis of regional airways obstruction using dynamic hyperpolarized 3He MRI-preliminary results in children with cystic fibrosis. J Magn Reson Imaging. 2005;22(3):420-6.

192. Horn FC, Deppe MH, Marshall H, Parra-Robles J, Wild JM. Quantification of regional fractional ventilation in human subjects by measurement of hyperpolarized 3He washout with 2D and 3D MRI. Journal of applied physiology. 2014;116(2):129-39.
193. Mugler JP, 3rd, Driehuys B, Brookeman JR, Cates GD, Berr SS, Bryant RG, et al. MR imaging and spectroscopy using hyperpolarized 129Xe gas: preliminary human results. Magnetic resonance in medicine : official journal of the Society of Magnetic Resonance in Medicine / Society of Magnetic Resonance in Medicine. 1997;37(6):809-15.
194. Wagshul ME, Button TM, Li HF, Liang Z, Springer CS, Zhong K, et al. In vivo MR imaging and spectroscopy using hyperpolarized 129Xe. Magn Reson Med. 1996;36(2):183-91.
195. Ruppert K, Mata JF, Brookeman JR, Hagspiel KD, Mugler JP, 3rd. Exploring lung function with hyperpolarized (129)Xe nuclear magnetic resonance. Magn Reson Med. 2004;51(4):676-87.
196. Patz S, Muradian I, Hrovat MI, Ruset IC, Topulos G, Covrig SD, et al. Human pulmonary imaging and spectroscopy with hyperpolarized 129Xe at 0.2T. Acad Radiol. 2008;15(6):713-27.
197. Driehuys B, Cofer GP, Pollaro J, Mackel JB, Hedlund LW, Johnson GA. Imaging alveolar-capillary gas transfer using hyperpolarized 129Xe MRI. Proc Natl Acad Sci U S A. 2006;103(48):18278-83.
198. Kaushik SS, Freeman MS, Cleveland ZI, Davies J, Stiles J, Virgincar RS, et al. Probing the regional distribution of pulmonary gas exchange through single-breath gas- and dissolved-phase 129Xe MR imaging. J Appl Physiol (1985). 2013;115(6):850-60.
199. Mugler JP, 3rd, Altes TA, Ruset IC, Dregely IM, Mata JF, Miller GW, et al. Simultaneous magnetic resonance imaging of ventilation distribution and gas uptake in the human lung using hyperpolarized xenon-129. Proc Natl Acad Sci U S A. 2010;107(50):21707-12.
200. Cleveland ZI, Cofer GP, Metz G, Beaver D, Nouls J, Kaushik SS, et al. Hyperpolarized Xe MR imaging of alveolar gas uptake in humans. PLoS One. 2010;5(8):e12192.
201. Couch MJ, Ball IK, Li T, Fox MS, Littlefield SL, Biman B, et al. Pulmonary ultrashort echo time 19F MR imaging with inhaled fluorinated gas mixtures in healthy volunteers: feasibility. Radiology. 2013;269(3):903-9.
202. Halaweish AF, Moon RE, Foster WM, Soher BJ, McAdams HP, MacFall JR, et al. Perfluoropropane gas as a magnetic resonance lung imaging contrast agent in humans. Chest. 2013;144(4):1300-10.
203. Couch MJ, Ball IK, Li T, Fox MS, Ouriadov AV, Biman B, et al. Inert fluorinated gas MRI: a new pulmonary imaging modality. NMR Biomed. 2014;27(12):1525-34.
204. Chang YV, Conradi MS. Relaxation and diffusion of perfluorocarbon gas mixtures with oxygen for lung MRI. J Magn Reson. 2006;181(2):191-8.
205. Wolf U, Scholz A, Terekhov M, Muennemann K, Kreitner K, Werner C, et al. Fluorine-19 MRI of the lung: first human experiment. International Society for Magnetic Resonance Imaging Proceedings. 2008.
206. Schreiber WG, Eberle B, Laukemper-Ostendorf S, Markstaller K, Weiler N, Scholz A, et al. Dynamic (19)F-MRI of pulmonary ventilation using sulfur hexafluoride (SF(6)) gas. Magn Reson Med. 2001;45(4):605-13.

207. Wolf U, Scholz A, Heussel CP, Markstaller K, Schreiber WG. Subsecond fluorine-19 MRI of the lung. Magn Reson Med. 2006;55(4):948-51.
208. Wolf U, Scholz A, Terekhov M, Koebrich R, David M, Schreiber LM. Visualization of inert gas wash-out during high-frequency oscillatory ventilation using fluorine-19 MRI. Magn Reson Med. 2010;64(5):1478-83.
209. Halaweish AF, Foster WM, Moon RE, MacIntyre NR, MacFall JR, Charles HC, editors. Dynamics of pulmonary ventilation distribution at steady state via 19fluorine-enhanced MRI: initial experiences and future developments. Proceedings of the 21st Annual Meeting ISMRM; 2013; Salt Lake City, UT.
210. Scholz AW, Wolf U, Fabel M, Weiler N, Heussel CP, Eberle B, et al. Comparison of magnetic resonance imaging of inhaled SF6 with respiratory gas analysis. Magnetic resonance imaging. 2009;27(4):549-56.
211. Jacob RE, Chang YV, Choong CK, Bierhals A, Zheng Hu D, Zheng J, et al. 19F MR imaging of ventilation and diffusion in excised lungs. Magn Reson Med. 2005;54(3):577-85.
212. Ohno Y, Hatabu H. Basics concepts and clinical applications of oxygen-enhanced MR imaging. Eur J Radiol. 2007;64(3):320-8.
213. Edelman RR, Hatabu H, Tadamura E, Li W, Prasad PV. Noninvasive assessment of regional ventilation in the human lung using oxygen-enhanced magnetic resonance imaging. Nature medicine. 1996;2(11):1236-9.
214. Stadler A, Stiebellehner L, Jakob PM, Arnold JF, Eisenhuber E, von Katzler I, et al. Quantitative and o(2) enhanced MRI of the pathologic lung: findings in emphysema, fibrosis, and cystic fibrosis. International journal of biomedical imaging. 2007;2007:23624.
215. Hopkins SR, Levin DL, Emami K, Kadlecek S, Yu J, Ishii M, et al. Advances in magnetic resonance imaging of lung physiology. Journal of applied physiology. 2007;102(3):1244-54.
216. Kruger SJ, Nagle SK, Couch MJ, Ohno Y, Albert M, Fain SB. Functional imaging of the lungs with gas agents. J Magn Reson Imaging. 2016;43(2):295-315.
217. Dietrich O, Losert C, Attenberger U, Fasol U, Peller M, Nikolaou K, et al. Fast oxygen-enhanced multislice imaging of the lung using parallel acquisition techniques. Magn Reson Med. 2005;53(6):1317-25.
218. Kruger SJ, Fain SB, Johnson KM, Cadman RV, Nagle SK. Oxygen-enhanced 3D radial ultrashort echo time magnetic resonance imaging in the healthy human lung. NMR Biomed. 2014;27(12):1535-41.
219. Ohno Y, Hatabu H, Takenaka D, Adachi S, Van Cauteren M, Sugimura K. Oxygen-enhanced MR ventilation imaging of the lung: preliminary clinical experience in 25 subjects. AJR American journal of roentgenology. 2001;177(1):185-94.
220. Miller GW, Mugler JP, 3rd, Sa RC, Altes TA, Prisk GK, Hopkins SR. Advances in functional and structural imaging of the human lung using proton MRI. NMR Biomed. 2014;27(12):1542-56.
221. Bolar DS, Levin DL, Hopkins SR, Frank LF, Liu TT, Wong EC, et al. Quantification of regional pulmonary blood flow using ASL-FAIRER. Magn Reson Med. 2006;55(6):1308-17.
222. Henderson AC, Sa RC, Theilmann RJ, Buxton RB, Prisk GK, Hopkins SR. The gravitational distribution of ventilation-perfusion ratio is more uniform in prone

than supine posture in the normal human lung. J Appl Physiol (1985). 2013;115(3):313-24.
223. Ohno Y, Iwasawa T, Seo JB, Koyama H, Takahashi H, Oh YM, et al. Oxygen-enhanced magnetic resonance imaging versus computed tomography: multicenter study for clinical stage classification of smoking-related chronic obstructive pulmonary disease. American journal of respiratory and critical care medicine. 2008;177(10):1095-102.
224. Ohno Y, Hatabu H, Higashino T, Nogami M, Takenaka D, Watanabe H, et al. Oxygen-enhanced MR imaging: correlation with postsurgical lung function in patients with lung cancer. Radiology. 2005;236(2):704-11.
225. Ohno Y, Koyama H, Nogami M, Takenaka D, Matsumoto S, Obara M, et al. Dynamic oxygen-enhanced MRI versus quantitative CT: pulmonary functional loss assessment and clinical stage classification of smoking-related COPD. AJR American journal of roentgenology. 2008;190(2):W93-9.
226. Ohno Y, Koyama H, Yoshikawa T, Matsumoto K, Aoyama N, Onishi Y, et al. Comparison of capability of dynamic O(2)-enhanced MRI and quantitative thin-section MDCT to assess COPD in smokers. Eur J Radiol. 2012;81(5):1068-75.
227. Ohno Y, Nishio M, Koyama H, Seki S, Yoshikawa T, Matsumoto S, et al. Asthma: comparison of dynamic oxygen-enhanced MR imaging and quantitative thin-section CT for evaluation of clinical treatment. Radiology. 2014;273(3):907-16.
228. Renne J, Hinrichs J, Schonfeld C, Gutberlet M, Winkler C, Faulenbach C, et al. Noninvasive quantification of airway inflammation following segmental allergen challenge with functional MR imaging: a proof of concept study. Radiology. 2015;274(1):267-75.
229. Ohno Y, Nishio M, Koyama H, Yoshikawa T, Matsumoto S, Seki S, et al. Oxygen-enhanced MRI for patients with connective tissue diseases: comparison with thin-section CT of capability for pulmonary functional and disease severity assessment. Eur J Radiol. 2014;83(2):391-7.
230. Zeng X, Wu Z, Call T, Miron E, Schreiber D, Happer W. Experimental determination of the rate constants for spin exchange between optically pumped K, Rb, and Cs atoms and 129Xe nuclei in alkali-metal-noble-gas van der Waals molecules. Phys Rev A. 1985;31(1):260-78.
231. Kastler A. Optical Methods of Atomic Orientation and of Magnetic Resonance*. J Opt Soc Am. 1957;47(6):460-5.
232. Goodson BM. Nuclear magnetic resonance of laser-polarized noble gases in molecules, materials, and organisms. J Magn Reson. 2002;155(2):157-216.
233. Happer W ME, Schaefer S, Schreiber D, van Wijngaarden WA, Zeng X. . Polarization of the nuclear spins of noble-gas atoms by spin exchange with optically pumped alkali-metal atoms. Phys Rev A. 1984;29:3092-110.
234. Kauczor H, Surkau R, Roberts T. MRI using hyperpolarized noble gases. Eur Radiol. 1998;8(5):820-7.
235. Guenther D, Hanisch G, Kauczor HU. Functional MR imaging of pulmonary ventilation using hyperpolarized noble gases. Acta Radiol. 2000;41(6):519-28.
236. Kauczor HU, Chen XJ, van Beek EJ, Schreiber WG. Pulmonary ventilation imaged by magnetic resonance: at the doorstep of clinical application. Eur Respir J. 2001;17(5):1008-23.

237. Moller HE, Chen XJ, Saam B, Hagspiel KD, Johnson GA, Altes TA, et al. MRI of the lungs using hyperpolarized noble gases. Magn Reson Med. 2002;47(6):1029-51.
238. Mugler JP, 3rd, Altes TA. Hyperpolarized 129Xe MRI of the human lung. J Magn Reson Imaging. 2013;37(2):313-31.
239. Doel T. Available from: https://github.com/tomdoel/pulmonarytoolkit.
240. Plotkowiak M. Hyperpolarised gas MRI as a promising technique for regional chronic lung diseases assessment. [Thesis]: University of Oxford; 2010.
241. Matin TN, Rahman N, Nickol AH, Chen M, Xu X, Stewart NJ, et al. Lobar analysis of hyperpolarised xenon magnetic resonance lung imaging (HP 129Xe-MRI) in chronic obstructive pulmonary disease (COPD). Radiology. 2016;[In Press].
242. Kaushik R, Yeltiwar RK, Pushpanshu K. Salivary interleukin-1beta levels in patients with chronic periodontitis before and after periodontal phase I therapy and healthy controls: a case-control study. J Periodontol. 2011;82(9):1353-9.
243. Driehuys B, Cates GD, Miron E, Sauer K, Walter DK, Happer W. High-volume production of laser-polarized 129Xe. Applied Physics Letters. 1996;69/12:1668-70.
244. Hu S, Hoffman EA, Reinhardt JM. Automatic lung segmentation for accurate quantitation of volumetric X-ray CT images. IEEE transactions on medical imaging. 2001;20(6):490-8.
245. Kuhnigk JM, Dicken V, Zidowitz S, Bornemann L, Kuemmerlen B, Krass S, et al. Informatics in radiology (infoRAD): new tools for computer assistance in thoracic CT. Part 1. Functional analysis of lungs, lung lobes, and bronchopulmonary segments. Radiographics : a review publication of the Radiological Society of North America, Inc. 2005;25(2):525-36.
246. Doel T, Matin TN, Gleeson FV, Gavaghan DJ, Grau V, editors. Pulmonary lobe segmentation from CT images using fissureness, airways, vessels, and multilevel B-splines. IEEE International Symposium on Biomedical Imaging; 2012; Barcelona, Spain.
247. Murphy K, van Ginneken B, Reinhardt JM, Kabus S, Ding K, Deng X, et al. Evaluation of registration methods on thoracic CT: the EMPIRE10 challenge. IEEE transactions on medical imaging. 2011;30(11):1901-20.
248. Grydeland TB, Dirksen A, Coxson HO, Pillai SG, Sharma S, Eide GE, et al. Quantitative computed tomography: emphysema and airway wall thickness by sex, age and smoking. The European respiratory journal. 2009;34(4):858-65.
249. Patel BD, Coxson HO, Pillai SG, Agusti AG, Calverley PM, Donner CF, et al. Airway wall thickening and emphysema show independent familial aggregation in chronic obstructive pulmonary disease. American journal of respiratory and critical care medicine. 2008;178(5):500-5.
250. Yorke J, Moosavi SH, Shuldham C, Jones PW. Quantification of dyspnoea using descriptors: development and initial testing of the Dyspnoea-12. Thorax. 2010;65(1):21-6.
251. Yorke J, Swigris J, Russell AM, Moosavi SH, Ng Man Kwong G, Longshaw M, et al. Dyspnea-12 is a valid and reliable measure of breathlessness in patients with interstitial lung disease. Chest. 2011;139(1):159-64.
252. West J. Respiratory physiology - the essentials. Baltimore, MD: Lipincott; 2005.

253. Glenny RW, Robertson HT. Spatial distribution of ventilation and perfusion. Comprehensive physiology. New York: Wiley; 2011.
254. Tawhai MH, Nash MP, Lin CL, Hoffman EA. Supine and prone differences in regional lung density and pleural pressure gradients in the human lung with constant shape. Journal of applied physiology. 2009;107(3):912-20.
255. Mure M, Domino KB, Lindahl SG, Hlastala MP, Altemeier WA, Glenny RW. Regional ventilation-perfusion distribution is more uniform in the prone position. Journal of applied physiology. 2000;88(3):1076-83.
256. Galvin I, Drummond GB, Nirmalan M. Distribution of blood flow and ventilation in the lung: gravity is not the only factor. British journal of anaesthesia. 2007;98(4):420-8.
257. Treppo S, Mijailovich SM, Venegas JG. Contributions of pulmonary perfusion and ventilation to heterogeneity in V(A)/Q measured by PET. Journal of applied physiology. 1997;82(4):1163-76.
258. Glenny RW, Bernard S, Robertson HT, Hlastala MP. Gravity is an important but secondary determinant of regional pulmonary blood flow in upright primates. Journal of applied physiology. 1999;86(2):623-32.
259. Glenny RW, Lamm WJ, Albert RK, Robertson HT. Gravity is a minor determinant of pulmonary blood flow distribution. Journal of applied physiology. 1991;71(2):620-9.
260. West JB. Gravity and pulmonary blood flow distribution. Journal of applied physiology. 1992;73(5):2201-2.
261. Hoffman EA. Effect of body orientation on regional lung expansion: a computed tomographic approach. Journal of applied physiology. 1985;59(2):468-80.
262. Hoffman EA, Ritman EL. Effect of body orientation on regional lung expansion in dog and sloth. Journal of applied physiology. 1985;59(2):481-91.
263. Marcucci C, Nyhan D, Simon BA. Distribution of pulmonary ventilation using Xe-enhanced computed tomography in prone and supine dogs. Journal of applied physiology. 2001;90(2):421-30.
264. Pelosi P, D'Andrea L, Vitale G, Pesenti A, Gattinoni L. Vertical gradient of regional lung inflation in adult respiratory distress syndrome. American journal of respiratory and critical care medicine. 1994;149(1):8-13.
265. Wilson TA, Beck KC. Contributions of ventilation and perfusion inhomogeneities to the VA/Q distribution. Journal of applied physiology. 1992;72(6):2298-304.
266. Yang QH, Kaplowitz MR, Lai-Fook SJ. Regional variations in lung expansion in rabbits: prone vs. supine positions. Journal of applied physiology. 1989;67(4):1371-6.
267. Musch G, Layfield JD, Harris RS, Melo MF, Winkler T, Callahan RJ, et al. Topographical distribution of pulmonary perfusion and ventilation, assessed by PET in supine and prone humans. Journal of applied physiology. 2002;93(5):1841-51.
268. Nyren S, Radell P, Lindahl SG, Mure M, Petersson J, Larsson SA, et al. Lung ventilation and perfusion in prone and supine postures with reference to anesthetized and mechanically ventilated healthy volunteers. Anesthesiology. 2010;112(3):682-7.
269. Petersson J, Rohdin M, Sanchez-Crespo A, Nyren S, Jacobsson H, Larsson SA, et al. Posture primarily affects lung tissue distribution with minor effect on

blood flow and ventilation. Respiratory physiology & neurobiology. 2007;156(3):293-303.
270. Jones AT, Hansell DM, Evans TW. Pulmonary perfusion in supine and prone positions: an electron-beam computed tomography study. Journal of applied physiology. 2001;90(4):1342-8.
271. Kaneko K, Milic-Emili J, Dolovich MB, Dawson A, Bates DV. Regional distribution of ventilation and perfusion as a function of body position. J Appl Physiol. 1966;21(3):767-77.
272. Prisk GK, Yamada K, Henderson AC, Arai TJ, Levin DL, Buxton RB, et al. Pulmonary perfusion in the prone and supine postures in the normal human lung. Journal of applied physiology. 2007;103(3):883-94.
273. Nyren S, Mure M, Jacobsson H, Larsson SA, Lindahl SG. Pulmonary perfusion is more uniform in the prone than in the supine position: scintigraphy in healthy humans. Journal of applied physiology. 1999;86(4):1135-41.
274. Amis TC, Jones HA, Hughes JM. Effect of posture on inter-regional distribution of pulmonary ventilation in man. Respiration physiology. 1984;56(2):145-67.
275. Hughes JM, Glazier JB, Maloney JE, West JB. Effect of lung volume on the distribution of pulmonary blood flow in man. Respiration physiology. 1968;4(1):58-72.
276. Brudin LH, Rhodes CG, Valind SO, Jones T, Hughes JM. Interrelationships between regional blood flow, blood volume, and ventilation in supine humans. Journal of applied physiology. 1994;76(3):1205-10.
277. Brudin LH, Rhodes CG, Valind SO, Wollmer P, Hughes JM. Regional lung density and blood volume in nonsmoking and smoking subjects measured by PET. Journal of applied physiology. 1987;63(4):1324-34.
278. Erwin WS, Zolov D, Bickerman HA. The effect of posture on respiratory function in patients with obstructive pulmonary emphysema. The American review of respiratory disease. 1966;94(6):865-72.
279. Kosuda S, Kobayashi H, Kusano S. Change in regional pulmonary perfusion as a result of posture and lung volume assessed using technetium-99m macroaggregated albumin SPET. European journal of nuclear medicine. 2000;27(5):529-35.
280. Cao JJ, Wang Y, McLaughlin J, Rhee P, Passick M, Ngai N, et al. Effects of hemodynamics on global and regional lung perfusion: a quantitative lung perfusion study by magnetic resonance imaging. Circulation Cardiovascular imaging. 2012;5(6):693-9.
281. Ball WC, Jr., Stewart PB, Newsham LG, Bates DV. Regional pulmonary function studied with xenon 133. The Journal of clinical investigation. 1962;41:519-31.
282. Berdine GG, Lehr JL, McKinley DS, Drazen JM. Nonuniformity of canine lung washout by high-frequency ventilation. Journal of applied physiology. 1986;61(4):1388-94.
283. Bunow B, Line BR, Horton MR, Weiss GH. Regional ventilatory clearance by xenon scintigraphy: a critical evaluation of two estimation procedures. Journal of nuclear medicine : official publication, Society of Nuclear Medicine. 1979;20(7):703-10.
284. Gur D, Shabason L, Borovetz HS, Herbert DL, Reece GJ, Kennedy WH, et al. Regional pulmonary ventilation measurements by xenon enhanced dynamic

computed tomography: an update. Journal of computer assisted tomography. 1981;5(5):678-83.
285. Kreck TC, Krueger MA, Altemeier WA, Sinclair SE, Robertson HT, Shade ED, et al. Determination of regional ventilation and perfusion in the lung using xenon and computed tomography. Journal of applied physiology. 2001;91(4):1741-9.
286. Hoffman EA, Olson LE. Characterisics of respiratory system complexity captured via X-ray computed tomography: image acquisition, display, and analysis. In: Hlastala MP, Robertson HT, editors. Complexity in structure and function of the lung. New York: Marcel Dekker; 1998. p. 325-78.
287. Mansson S, Deninger AJ, Magnusson P, Pettersson G, Olsson LE, Hansson G, et al. 3He MRI-based assessment of posture-dependent regional ventilation gradients in rats. J Appl Physiol (1985). 2005;98(6):2259-67.
288. Lam WW, Holdsworth DW, Du LY, Drangova M, McCormack DG, Santyr GE. Micro-CT imaging of rat lung ventilation using continuous image acquisition during xenon gas contrast enhancement. Journal of applied physiology. 2007;103(5):1848-56.
289. Burnham KJ, Arai TJ, Dubowitz DJ, Henderson AC, Holverda S, Buxton RB, et al. Pulmonary perfusion heterogeneity is increased by sustained, heavy exercise in humans. Journal of applied physiology. 2009;107(5):1559-68.
290. Hopkins SR, Garg J, Bolar DS, Balouch J, Levin DL. Pulmonary blood flow heterogeneity during hypoxia and high-altitude pulmonary edema. American journal of respiratory and critical care medicine. 2005;171(1):83-7.
291. Henderson AC, Levin DL, Hopkins SR, Olfert IM, Buxton RB, Prisk GK. Steep head-down tilt has persisting effects on the distribution of pulmonary blood flow. Journal of applied physiology. 2006;101(2):583-9.
292. Sa RC, Cronin MV, Henderson AC, Holverda S, Theilmann RJ, Arai TJ, et al. Vertical distribution of specific ventilation in normal supine humans measured by oxygen-enhanced proton MRI. Journal of applied physiology. 2010;109(6):1950-9.
293. Albert RK, Hubmayr RD. The prone position eliminates compression of the lungs by the heart. American journal of respiratory and critical care medicine. 2000;161(5):1660-5.
294. Kauczor HU, Hast J, Heussel CP, Schlegel J, Mildenberger P, Thelen M. Focal airtrapping at expiratory high-resolution CT: comparison with pulmonary function tests. Eur Radiol. 2000;10(10):1539-46.
295. Verschakelen JA, Van fraeyenhoven L, Laureys G, Demedts M, Baert AL. Differences in CT density between dependent and nondependent portions of the lung: influence of lung volume. AJR American journal of roentgenology. 1993;161(4):713-7.
296. Mata J, Altes T, Christopher JM, Mugler JP, 3rd, Brookeman JR, de Lange EE, editors. Transient, position dependent ventilation defects of the lung in healthy volunteers: demonstration with hyperpolarized helium-3 MR imaging. ISMRM; 2002; Honolulu, HI.
297. Guenther D, Eberle B, Hast J, Lill J, Markstaller K, Puderbach M, et al. (3)He MRI in healthy volunteers: preliminary correlation with smoking history and lung volumes. NMR Biomed. 2000;13(4):182-9.

298. Fichele S, Woodhouse N, Swift AJ, Said Z, Paley MN, Kasuboski L, et al. MRI of helium-3 gas in healthy lungs: posture related variations of alveolar size. J Magn Reson Imaging. 2004;20(2):331-5.
299. Evans A, McCormack D, Ouriadov A, Etemad-Rezai R, Santyr G, Parraga G. Anatomical distribution of 3He apparent diffusion coefficients in severe chronic obstructive pulmonary disease. J Magn Reson Imaging. 2007;26(6):1537-47.
300. Bink A, Hanisch G, Karg A, Vogel A, Katsaros K, Mayer E, et al. Clinical aspects of the apparent diffusion coefficient in 3He MRI: results in healthy volunteers and patients after lung transplantation. J Magn Reson Imaging. 2007;25(6):1152-8.
301. Salerno M, Brookeman JR, de Lange EE, Knight-Scott J, Mugler JP, 3rd, editors. Demonstration of an alveolar-size gradient in the healthy human lung: a study of the reproducibility of hyperpolarized 3 He diffusion MRI. ISMRM; 2000; Denver, Colorado, USA.
302. Gevenois PA, Scillia P, de Maertelaer V, Michils A, De Vuyst P, Yernault JC. The effects of age, sex, lung size, and hyperinflation on CT lung densitometry. AJR American journal of roentgenology. 1996;167(5):1169-73.
303. Irion KL, Marchiori E, Hochhegger B, Porto Nda S, Moreira Jda S, Anselmi CE, et al. CT quantification of emphysema in young subjects with no recognizable chest disease. AJR American journal of roentgenology. 2009;192(3):W90-6.
304. Zach JA, Newell JD, Jr., Schroeder J, Murphy JR, Curran-Everett D, Hoffman EA, et al. Quantitative computed tomography of the lungs and airways in healthy nonsmoking adults. Investigative radiology. 2012;47(10):596-602.
305. He M, Kaushik SS, Robertson SH, Freeman MS, Virgincar RS, McAdams HP, et al. Extending semiautomatic ventilation defect analysis for hyperpolarized (129)Xe ventilation MRI. Acad Radiol. 2014;21(12):1530-41.
306. Diaz S, Casselbrant I, Piitulainen E, Magnusson P, Peterson B, Wollmer P, et al. Validity of apparent diffusion coefficient hyperpolarized 3He-MRI using MSCT and pulmonary function tests as references. Eur J Radiol. 2009;71(2):257-63.
307. Kirby M, Mathew L, Wheatley A, Santyr GE, McCormack DG, Parraga G. Chronic obstructive pulmonary disease: longitudinal hyperpolarized (3)He MR imaging. Radiology. 2010;256(1):280-9.
308. Kirby M, Svenningsen S, Kanhere N, Owrangi A, Wheatley A, Coxson HO, et al. Pulmonary ventilation visualized using hyperpolarized helium-3 and xenon-129 magnetic resonance imaging: differences in COPD and relationship to emphysema. J Appl Physiol (1985). 2013;114(6):707-15.
309. Woodhouse N, Wild JM, Paley MN, Fichele S, Said Z, Swift AJ, et al. Combined helium-3/proton magnetic resonance imaging measurement of ventilated lung volumes in smokers compared to never-smokers. J Magn Reson Imaging. 2005;21(4):365-9.
310. Kirby M, Svenningsen S, Owrangi A, Wheatley A, Farag A, Ouriadov A, et al. Hyperpolarized 3He and 129Xe MR imaging in healthy volunteers and patients with chronic obstructive pulmonary disease. Radiology. 2012;265(2):600-10.
311. Milic-Emili J. Ventilation distribution. In: Hamid Q, Shannon J, Martin J, editors. Physiologic basis of respiratory disease. 1st ed: BC Decker; 2005. p. 133-41.
312. Milic-Emili J, Henderson JA, Dolovich MB, Trop D, Kaneko K. Regional distribution of inspired gas in the lung. J Appl Physiol. 1966;21(3):749-59.

313. Hopkins SR, Henderson AC, Levin DL, Yamada K, Arai T, Buxton RB, et al. Vertical gradients in regional lung density and perfusion in the supine human lung: the Slinky effect. Journal of applied physiology. 2007;103(1):240-8.
314. Hulands GH, Greene R, Iliff LD, Nunn JF. Influence of anaesthesia on the regional distribution of perfusion and ventilation in the lung. Clinical science. 1970;38(4):451-60.
315. Eberle B, Weiler N, Markstaller K, Kauczor H, Deninger A, Ebert M, et al. Analysis of intrapulmonary O(2) concentration by MR imaging of inhaled hyperpolarized helium-3. J Appl Physiol (1985). 1999;87(6):2043-52.
316. Couch MJ, Ouriadov A, Santyr GE. Regional ventilation mapping of the rat lung using hyperpolarized (1)(2)(9)Xe magnetic resonance imaging. Magn Reson Med. 2012;68(5):1623-31.
317. West JB, Dollery CT. Distribution of blood flow and ventilation-perfusion ratio in the lung, measured with radioactive carbon dioxide. J Appl Physiol. 1960;15:405-10.
318. Kirby M, Owrangi A, Svenningsen S, Wheatley A, Coxson HO, Paterson NA, et al. On the role of abnormal DL(CO) in ex-smokers without airflow limitation: symptoms, exercise capacity and hyperpolarised helium-3 MRI. Thorax. 2013;68(8):752-9.
319. Wollmer P, Albrechtsson U, Brauer K, Eriksson L, Jonson B, Tylen U. Measurement of pulmonary density by means of X-ray computerized tomography. Relation to pulmonary mechanics in normal subjects. Chest. 1986;90(3):387-91.
320. Lopez AD, Shibuya K, Rao C, Mathers CD, Hansell AL, Held LS, et al. Chronic obstructive pulmonary disease: current burden and future projections. Eur Respir J. 2006;27(2):397-412.
321. Jones PW. Health status measurement in chronic obstructive pulmonary disease. Thorax. 2001;56(11):880-7.
322. de Torres JP, Pinto-Plata V, Casanova C, Mullerova H, Cordoba-Lanus E, Muros de Fuentes M, et al. C-reactive protein levels and survival in patients with moderate to very severe COPD. Chest. 2008;133(6):1336-43.
323. Marin JM, Carrizo SJ, Casanova C, Martinez-Camblor P, Soriano JB, Agusti AG, et al. Prediction of risk of COPD exacerbations by the BODE index. Respiratory medicine. 2009;103(3):373-8.
324. Mathew L, Evans A, Ouriadov A, Etemad-Rezai R, Fogel R, Santyr G, et al. Hyperpolarized 3He magnetic resonance imaging of chronic obstructive pulmonary disease: reproducibility at 3.0 tesla. Acad Radiol. 2008;15(10):1298-311.
325. Mathew L, Kirby M, Etemad-Rezai R, Wheatley A, McCormack DG, Parraga G. Hyperpolarized (3)He magnetic resonance imaging: preliminary evaluation of phenotyping potential in chronic obstructive pulmonary disease. Eur J Radiol. 2011;79(1):140-6.
326. Parraga G, Ouriadov A, Evans A, McKay S, Lam WW, Fenster A, et al. Hyperpolarized 3He ventilation defects and apparent diffusion coefficients in chronic obstructive pulmonary disease: preliminary results at 3.0 Tesla. Investigative radiology. 2007;42(6):384-91.
327. Choy S, Wheatley A, McCormack DG, Parraga G. Hyperpolarized (3)He magnetic resonance imaging-derived pulmonary pressure-volume curves. Journal of applied physiology. 2010;109(2):574-85.

328. Owrangi AM, Wang JX, Wheatley A, McCormack DG, Parraga G. Quantitative (1)H and hyperpolarized (3)He magnetic resonance imaging: comparison in chronic obstructive pulmonary disease and healthy never-smokers. Eur J Radiol. 2014;83(1):64-72.
329. Yu J, Law M, Kadlecek S, Emami K, Ishii M, Stephen M, et al. Simultaneous measurement of pulmonary partial pressure of oxygen and apparent diffusion coefficient by hyperpolarized 3He MRI. Magn Reson Med. 2009;61(5):1015-21.
330. van Beek EJ, Dahmen AM, Stavngaard T, Gast KK, Heussel CP, Krummenauer F, et al. Hyperpolarised 3He MRI versus HRCT in COPD and normal volunteers: PHIL trial. Eur Respir J. 2009;34(6):1311-21.
331. Diaz S, Casselbrant I, Piitulainen E, Magnusson P, Peterson B, Pickering E, et al. Progression of emphysema in a 12-month hyperpolarized 3He-MRI study: lacunarity analysis provided a more sensitive measure than standard ADC analysis. Acad Radiol. 2009;16(6):700-7.
332. Stavngaard T, Sogaard LV, Batz M, Schreiber LM, Dirksen A. Progression of emphysema evaluated by MRI using hyperpolarized (3)He (HP (3)He) measurements in patients with alpha-1-antitrypsin (A1AT) deficiency compared with CT and lung function tests. Acta Radiol. 2009;50(9):1019-26.
333. Woods JC, Choong CK, Yablonskiy DA, Bentley J, Wong J, Pierce JA, et al. Hyperpolarized 3He diffusion MRI and histology in pulmonary emphysema. Magn Reson Med. 2006;56(6):1293-300.
334. Kirby M, Heydarian M, Wheatley A, McCormack DG, Parraga G. Evaluating bronchodilator effects in chronic obstructive pulmonary disease using diffusion-weighted hyperpolarized helium-3 magnetic resonance imaging. Journal of applied physiology. 2012;112(4):651-7.
335. Kirby M, Mathew L, Heydarian M, Etemad-Rezai R, McCormack DG, Parraga G. Chronic obstructive pulmonary disease: quantification of bronchodilator effects by using hyperpolarized (3)He MR imaging. Radiology. 2011;261(1):283-92.
336. Tustison NJ, Cook TS, Song G, Gee JC. Pulmonary kinematics from image data: a review. Acad Radiol. 2011;18(4):402-17.
337. Sheikh K, Paulin GA, Svenningsen S, Kirby M, Paterson NA, McCormack DG, et al. Pulmonary ventilation defects in older never-smokers. Journal of applied physiology. 2014;117(3):297-306.
338. Virgincar RS, Cleveland ZI, Kaushik SS, Freeman MS, Nouls J, Cofer GP, et al. Quantitative analysis of hyperpolarized 129Xe ventilation imaging in healthy volunteers and subjects with chronic obstructive pulmonary disease. NMR Biomed. 2013;26(4):424-35.
339. Tahir BA, Van Holsbeke C, Ireland RH, Swift AJ, Horn FC, Marshall H, et al. Comparison of CT-based Lobar Ventilation with He MR Imaging Ventilation Measurements. Radiology. 2015:142278.
340. Thomen RP, Sheshadri A, Quirk JD, Kozlowski J, Ellison HD, Szczesniak RD, et al. Regional ventilation changes in severe asthma after bronchial thermoplasty with (3)He MR imaging and CT. Radiology. 2015;274(1):250-9.
341. Tiddens HA, Pare PD, Hogg JC, Hop WC, Lambert R, de Jongste JC. Cartilaginous airway dimensions and airflow obstruction in human lungs. American journal of respiratory and critical care medicine. 1995;152(1):260-6.
342. Nakano Y, Muro S, Sakai H, Hirai T, Chin K, Tsukino M, et al. Computed tomographic measurements of airway dimensions and emphysema in smokers.

Correlation with lung function. American journal of respiratory and critical care medicine. 2000;162(3 Pt 1):1102-8.
343. Nakano Y, Wong JC, de Jong PA, Buzatu L, Nagao T, Coxson HO, et al. The prediction of small airway dimensions using computed tomography. American journal of respiratory and critical care medicine. 2005;171(2):142-6.
344. Yahaba M, Kawata N, Iesato K, Matsuura Y, Sugiura T, Kasai H, et al. The effects of emphysema on airway disease: correlations between multi-detector CT and pulmonary function tests in smokers. Eur J Radiol. 2014;83(6):1022-8.
345. Diaz AA, Come CE, Ross JC, San Jose Estepar R, Han MK, Loring SH, et al. Association between airway caliber changes with lung inflation and emphysema assessed by volumetric CT scan in subjects with COPD. Chest. 2012;141(3):736-44.
346. Schroeder JD, McKenzie AS, Zach JA, Wilson CG, Curran-Everett D, Stinson DS, et al. Relationships between airflow obstruction and quantitative CT measurements of emphysema, air trapping, and airways in subjects with and without chronic obstructive pulmonary disease. AJR American journal of roentgenology. 2013;201(3):W460-70.
347. Wild JM, Ajraoui S, Deppe MH, Parnell SR, Marshall H, Parra-Robles J, et al. Synchronous acquisition of hyperpolarised 3He and 1H MR images of the lungs - maximising mutual anatomical and functional information. NMR Biomed. 2011;24(2):130-4.
348. Baraldo S, Turato G, Saetta M. Pathophysiology of the small airways in chronic obstructive pulmonary disease. Respiration. 2012;84(2):89-97.
349. Casanova C, Cote C, de Torres JP, Aguirre-Jaime A, Marin JM, Pinto-Plata V, et al. Inspiratory-to-total lung capacity ratio predicts mortality in patients with chronic obstructive pulmonary disease. Am J Respir Crit Care Med. 2005;171(6):591-7.
350. Clanton TL, Levine S. Respiratory muscle fiber remodeling in chronic hyperinflation: dysfunction or adaptation? J Appl Physiol (1985). 2009;107(1):324-35.
351. Hackx M, Bankier AA, Gevenois PA. Chronic obstructive pulmonary disease: CT quantification of airways disease. Radiology. 2012;265(1):34-48.
352. Cassart M, Hamacher J, Verbandt Y, Wildermuth S, Ritscher D, Russi EW, et al. Effects of lung volume reduction surgery for emphysema on diaphragm dimensions and configuration. Am J Respir Crit Care Med. 2001;163(5):1171-5.
353. Gelb AF, Brenner M, McKenna RJ, Jr., Fischel R, Zamel N, Schein MJ. Serial lung function and elastic recoil 2 years after lung volume reduction surgery for emphysema. Chest. 1998;113(6):1497-506.
354. Sciurba FC, Rogers RM, Keenan RJ, Slivka WA, Gorcsan J, 3rd, Ferson PF, et al. Improvement in pulmonary function and elastic recoil after lung-reduction surgery for diffuse emphysema. N Engl J Med. 1996;334(17):1095-9.
355. Bastacky J, Goerke J. Pores of Kohn are filled in normal lungs: low-temperature scanning electron microscopy. J Appl Physiol (1985). 1992;73(1):88-95.
356. Kohn HN. Zur Histologie der indurirenden fibrinosen Pneumonie. Munch med Wschr. 1893(40):42-5.
357. Lambert MW. Accessory bronchiolealveolar communications. J Pathol Bacteriol. 1955;70(2):311-4.

358. Martin HB. Respiratory bronchioles as the pathway for collateral ventilation. J Appl Physiol. 1966;21(5):1443-7.
359. Hogg JC, Macklem PT, Thurlbeck WM. The resistance of collateral channels in excised human lungs. J Clin Invest. 1969;48(3):421-31.
360. Terry PB, Traystman RJ, Newball HH, Batra G, Menkes HA. Collateral ventilation in man. N Engl J Med. 1978;298(1):10-5.
361. Tsai LW, Hoffman AM, Mazan MR, Ingenito EP. Bronchoscopic measurement of collateral ventilation in a sheep model of emphysema. Respiration. 2007;74(5):565-71.
362. Lausberg HF, Chino K, Patterson GA, Meyers BF, Toeniskoetter PD, Cooper JD. Bronchial fenestration improves expiratory flow in emphysematous human lungs. Ann Thorac Surg. 2003;75(2):393-7; discussion 8.
363. Toma TP, Hopkinson NS, Hillier J, Hansell DM, Morgan C, Goldstraw PG, et al. Bronchoscopic volume reduction with valve implants in patients with severe emphysema. Lancet. 2003;361(9361):931-3.
364. Brantigan OC, Mueller E. Surgical treatment of pulmonary emphysema. Am Surg. 1957;23(9):789-804.
365. Cooper JD, Trulock EP, Triantafillou AN, Patterson GA, Pohl MS, Deloney PA, et al. Bilateral pneumectomy (volume reduction) for chronic obstructive pulmonary disease. J Thorac Cardiovasc Surg. 1995;109(1):106-16; discussion 16-9.
366. Ciccone AM, Meyers BF, Guthrie TJ, Davis GE, Yusen RD, Lefrak SS, et al. Long-term outcome of bilateral lung volume reduction in 250 consecutive patients with emphysema. J Thorac Cardiovasc Surg. 2003;125(3):513-25.
367. Flaherty KR, Kazerooni EA, Curtis JL, Iannettoni M, Lange L, Schork MA, et al. Short-term and long-term outcomes after bilateral lung volume reduction surgery : prediction by quantitative CT. Chest. 2001;119(5):1337-46.
368. Geddes D, Davies M, Koyama H, Hansell D, Pastorino U, Pepper J, et al. Effect of lung-volume-reduction surgery in patients with severe emphysema. N Engl J Med. 2000;343(4):239-45.
369. Goldstein RS, Todd TR, Guyatt G, Keshavjee S, Dolmage TE, van Rooy S, et al. Influence of lung volume reduction surgery (LVRS) on health related quality of life in patients with chronic obstructive pulmonary disease. Thorax. 2003;58(5):405-10.
370. Cordova F, O'Brien G, Furukawa S, Kuzma AM, Travaline J, Criner GJ. Stability of improvements in exercise performance and quality of life following bilateral lung volume reduction surgery in severe COPD. Chest. 1997;112(4):907-15.
371. Yusen RD, Lefrak SS, Gierada DS, Davis GE, Meyers BF, Patterson GA, et al. A prospective evaluation of lung volume reduction surgery in 200 consecutive patients. Chest. 2003;123(4):1026-37.
372. Naunheim KS, Wood DE, Krasna MJ, DeCamp MM, Jr., Ginsburg ME, McKenna RJ, Jr., et al. Predictors of operative mortality and cardiopulmonary morbidity in the National Emphysema Treatment Trial. J Thorac Cardiovasc Surg. 2006;131(1):43-53.
373. National Emphysema Treatment Trial Research G. Patients at high risk of death after lung-volume-reduction surgery. N Engl J Med. 2001;345(15):1075-83.

374. Ware JH. The National Emphysema Treatment Trial--how strong is the evidence? N Engl J Med. 2003;348(21):2055-6.
375. Gompelmann D, Heussel CP, Eberhardt R, Snell G, Hopkins P, Baker K, et al. Efficacy of bronchoscopic thermal vapor ablation and lobar fissure completeness in patients with heterogeneous emphysema. Respiration. 2012;83(5):400-6.
376. Herth FJ, Ernst A, Baker KM, Egan JJ, Gotfried MH, Hopkins P, et al. Characterization of outcomes 1 year after endoscopic thermal vapor ablation for patients with heterogeneous emphysema. Int J Chron Obstruct Pulmon Dis. 2012;7:397-405.
377. Herth FJ, Gompelmann D, Stanzel F, Bonnet R, Behr J, Schmidt B, et al. Treatment of advanced emphysema with emphysematous lung sealant (AeriSeal(R)). Respiration. 2011;82(1):36-45.
378. Shah PL, Slebos DJ, Cardoso PF, Cetti E, Voelker K, Levine B, et al. Bronchoscopic lung-volume reduction with Exhale airway stents for emphysema (EASE trial): randomised, sham-controlled, multicentre trial. Lancet. 2011;378(9795):997-1005.
379. Shah PL, Zoumot Z, Singh S, Bicknell SR, Ross ET, Quiring J, et al. Endobronchial coils for the treatment of severe emphysema with hyperinflation (RESET): a randomised controlled trial. Lancet Respir Med. 2013;1(3):233-40.
380. Slebos DJ, Klooster K, Ernst A, Herth FJ, Kerstjens HA. Bronchoscopic lung volume reduction coil treatment of patients with severe heterogeneous emphysema. Chest. 2012;142(3):574-82.
381. Valipour A, Burghuber OC. An update on the efficacy of endobronchial valve therapy in the management of hyperinflation in patients with chronic obstructive pulmonary disease. Ther Adv Respir Dis. 2015.
382. Shah PL, Herth FJ. Current status of bronchoscopic lung volume reduction with endobronchial valves. Thorax. 2014;69(3):280-6.
383. Wan IY, Toma TP, Geddes DM, Snell G, Williams T, Venuta F, et al. Bronchoscopic lung volume reduction for end-stage emphysema: report on the first 98 patients. Chest. 2006;129(3):518-26.
384. Zoumot Z, LoMauro A, Aliverti A, Nelson C, Ward S, Jordan S, et al. Lung Volume Reduction in Emphysema Improves Chest Wall Asynchrony. Chest. 2015;148(1):185-95.
385. Hopkinson NS, Toma TP, Hansell DM, Goldstraw P, Moxham J, Geddes DM, et al. Effect of bronchoscopic lung volume reduction on dynamic hyperinflation and exercise in emphysema. Am J Respir Crit Care Med. 2005;171(5):453-60.
386. Sciurba FC, Ernst A, Herth FJ, Strange C, Criner GJ, Marquette CH, et al. A randomized study of endobronchial valves for advanced emphysema. N Engl J Med. 2010;363(13):1233-44.
387. Herth FJ, Noppen M, Valipour A, Leroy S, Vergnon JM, Ficker JH, et al. Efficacy predictors of lung volume reduction with Zephyr valves in a European cohort. Eur Respir J. 2012;39(6):1334-42.
388. Ninane V, Geltner C, Bezzi M, Foccoli P, Gottlieb J, Welte T, et al. Multicentre European study for the treatment of advanced emphysema with bronchial valves. Eur Respir J. 2012;39(6):1319-25.
389. Sterman DH, Mehta AC, Wood DE, Mathur PN, McKenna RJ, Jr., Ost DE, et al. A multicenter pilot study of a bronchial valve for the treatment of severe emphysema. Respiration. 2010;79(3):222-33.

390. Wood DE, McKenna RJ, Jr., Yusen RD, Sterman DH, Ost DE, Springmeyer SC, et al. A multicenter trial of an intrabronchial valve for treatment of severe emphysema. J Thorac Cardiovasc Surg. 2007;133(1):65-73.
391. Davey C, Zoumot Z, Jordan S, McNulty WH, Carr DH, Hind MD, et al. Bronchoscopic lung volume reduction with endobronchial valves for patients with heterogeneous emphysema and intact interlobar fissures (the BeLieVeR-HIFi study): a randomised controlled trial. Lancet. 2015;386(9998):1066-73.
392. Venuta F, Anile M, Diso D, Carillo C, De Giacomo T, D'Andrilli A, et al. Long-term follow-up after bronchoscopic lung volume reduction in patients with emphysema. Eur Respir J. 2012;39(5):1084-9.
393. Hopkinson NS, Kemp SV, Toma TP, Hansell DM, Geddes DM, Shah PL, et al. Atelectasis and survival after bronchoscopic lung volume reduction for COPD. Eur Respir J. 2011;37(6):1346-51.
394. Koenigkam-Santos M, Puderbach M, Gompelmann D, Eberhardt R, Herth F, Kauczor HU, et al. Incomplete fissures in severe emphysematous patients evaluated with MDCT: incidence and interobserver agreement among radiologists and pneumologists. Eur J Radiol. 2012;81(12):4161-6.
395. Gompelmann D, Eberhardt R, Michaud G, Ernst A, Herth FJ. Predicting atelectasis by assessment of collateral ventilation prior to endobronchial lung volume reduction: a feasibility study. Respiration. 2010;80(5):419-25.
396. Herth FJ, Eberhardt R, Gompelmann D, Ficker JH, Wagner M, Ek L, et al. Radiological and clinical outcomes of using Chartis to plan endobronchial valve treatment. Eur Respir J. 2013;41(2):302-8.
397. Gesierich W, Samitas K, Behr J. Determining collateral ventilation during bronchoscopy: unanswered questions. Thorax. 2014;69(3):289-90.
398. Kent MS, Ridge C, O'Dell D, Lo P, Whyte R, Gangadharan SP. The accuracy of computed tomography to predict completeness of pulmonary fissures. A prospective study. Ann Am Thorac Soc. 2015;12(5):696-700.
399. Higuchi T, Reed A, Oto T, Holsworth L, Ellis S, Bailey MJ, et al. Relation of interlobar collaterals to radiological heterogeneity in severe emphysema. Thorax. 2006;61(5):409-13.
400. Gompelmann D, Eberhardt R, Slebos DJ, Brown MS, Abtin F, Kim HJ, et al. Diagnostic performance comparison of the Chartis System and high-resolution computerized tomography fissure analysis for planning endoscopic lung volume reduction. Respirology. 2014;19(4):524-30.
401. Magnussen H, Kramer MR, Kirsten AM, Marquette C, Valipour A, Stanzel F, et al. Effect of fissure integrity on lung volume reduction using a polymer sealant in advanced emphysema. Thorax. 2012;67(4):302-8.
402. Schuhmann M, Raffy P, Yin Y, Gompelmann D, Oguz I, Eberhardt R, et al. Computed tomography predictors of response to endobronchial valve lung reduction treatment. Comparison with Chartis. Am J Respir Crit Care Med. 2015;191(7):767-74.
403. van Rikxoort EM, Goldin JG, Galperin-Aizenberg M, Abtin F, Kim HJ, Lu P, et al. A method for the automatic quantification of the completeness of pulmonary fissures: evaluation in a database of subjects with severe emphysema. Eur Radiol. 2012;22(2):302-9.
404. Rosenberg DE, Lyons HA. Collateral ventilation in excised human lungs. Respiration. 1979;37(3):125-34.

405. Salanitri J, Kalff V, Kelly M, Holsworth L, Williams T, Snell G. 133Xenon ventilation scintigraphy applied to bronchoscopic lung volume reduction techniques for emphysema: relevance of interlobar collaterals. Intern Med J. 2005;35(2):97-103.
406. Effmann EL, Freedman GS, Lange RC. 133Xe studies of collateral ventilation and air trapping following endobronchial occlusion. Radiology. 1972;105(1):85-91.
407. Chae EJ, Seo JB, Kim N, Song KS, Shin JH, Kim TH, et al. Collateral ventilation in a canine model with bronchial obstruction: assessment with xenon-enhanced dual-energy CT. Radiology. 2010;255(3):790-8.
408. Goo HW, Chae EJ, Seo JB, Hong SJ. Xenon ventilation CT using a dual-source dual-energy technique: dynamic ventilation abnormality in a child with bronchial atresia. Pediatr Radiol. 2008;38(10):1113-6.
409. Goo HW, Yang DH, Kim N, Park SI, Kim DK, Kim EA. Collateral ventilation to congenital hyperlucent lung lesions assessed on xenon-enhanced dynamic dual-energy CT: an initial experience. Korean J Radiol. 2011;12(1):25-33.
410. Park EA, Goo JM, Park SJ, Lee CH, Park CM. Collateral Ventilation Quantification Using Xenon-Enhanced Dynamic Dual-Energy CT: Differences between Canine and Swine Models of Bronchial Occlusion. Korean J Radiol. 2015;16(3):648-56.
411. Marshall H, Deppe MH, Parra-Robles J, Hillis S, Billings CG, Rajaram S, et al. Direct visualisation of collateral ventilation in COPD with hyperpolarised gas MRI. Thorax. 2012;67(7):613-7.
412. Owers-Bradley JR, Fichele S, Bennattayalah A, McGloin CJ, Bowtell RW, Morgan PS, et al. MR tagging of human lungs using hyperpolarized 3He gas. J Magn Reson Imaging. 2003;17(1):142-6.
413. Wang C, Altes TA, Mugler JP, 3rd, Miller GW, Ruppert K, Mata JF, et al. Assessment of the lung microstructure in patients with asthma using hyperpolarized 3He diffusion MRI at two time scales: comparison with healthy subjects and patients with COPD. J Magn Reson Imaging. 2008;28(1):80-8.
414. Woods JC, Yablonskiy DA, Chino K, Tanoli TS, Cooper JD, Conradi MS. Magnetization tagging decay to measure long-range (3)He diffusion in healthy and emphysematous canine lungs. Magn Reson Med. 2004;51(5):1002-8.
415. Conradi MS, Yablonskiy DA, Woods JC, Gierada DS, Jacob RE, Chang YV, et al. 3He diffusion MRI of the lung. Acad Radiol. 2005;12(11):1406-13.
416. Woods JC, Yablonskiy DA, Choong CK, Chino K, Pierce JA, Hogg JC, et al. Long-range diffusion of hyperpolarized 3He in explanted normal and emphysematous human lungs via magnetization tagging. J Appl Physiol (1985). 2005;99(5):1992-7.
417. Emami K, Hamedani H, Kadlececk S, Han B, Xin Y, Ishii M, et al., editors. A pilot fractional ventilation imaging study in healthy subjects, asymptomatic smokers and obstructive pulmonary disease patients. 21st Annual Meeting ISMRM; 2013; Salt Lake City, Utah, U.S.A.
418. Anile M, Diso D, Venuta F. Assessment of intraparenchymal lung collateral ventilation. Thorax. 2012;67(12):1111; author reply
419. Eberhardt R, Gompelmann D, Schuhmann M, Heussel CP, Herth FJ. Complete unilateral vs partial bilateral endoscopic lung volume reduction in patients with bilateral lung emphysema. Chest. 2012;142(4):900-8.

420. Pu J, Wang Z, Gu S, Fuhrman C, Leader JK, Meng X, et al. Pulmonary fissure integrity and collateral ventilation in COPD patients. PLoS One. 2014;9(5):e96631.
421. Fishman A, Martinez F, Naunheim K, Piantadosi S, Wise R, Ries A, et al. A randomized trial comparing lung-volume-reduction surgery with medical therapy for severe emphysema. N Engl J Med. 2003;348(21):2059-73.
422. Ingenito EP, Loring SH, Moy ML, Mentzer SJ, Swanson SJ, Reilly JJ. Interpreting improvement in expiratory flows after lung volume reduction surgery in terms of flow limitation theory. Am J Respir Crit Care Med. 2001;163(5):1074-80.
423. Klooster K, Ten Hacken NH, Franz I, Kerstjens HA, van Rikxoort EM, Slebos DJ. Lung volume reduction coil treatment in chronic obstructive pulmonary disease patients with homogeneous emphysema: a prospective feasibility trial. Respiration. 2014;88(2):116-25.
424. Valipour A, Herth FJ, Burghuber OC, Criner G, Vergnon JM, Goldin J, et al. Target lobe volume reduction and COPD outcome measures after endobronchial valve therapy. Eur Respir J. 2014;43(2):387-96.
425. Valipour A, Kramer MR, Stanzel F, Kempa A, Asadi S, Fruchter O, et al. Physiological modeling of responses to upper versus lower lobe lung volume reduction in homogeneous emphysema. Frontiers in physiology. 2012;3:387.
426. The COPD Guidelines Group of the Standards of Care Committee of the BTS. BTS guidelines for the management of chronic obstructive pulmonary disease. . Thorax. 1997;52 Suppl 5:S1-28.
427. Pauwels RA, Buist AS, Calverley PM, Jenkins CR, Hurd SS, Committee GS. Global strategy for the diagnosis, management, and prevention of chronic obstructive pulmonary disease. NHLBI/WHO Global Initiative for Chronic Obstructive Lung Disease (GOLD) Workshop summary. American journal of respiratory and critical care medicine. 2001;163(5):1256-76.
428. Ram FS, Sestini P. Regular inhaled short acting beta2 agonists for the management of stable chronic obstructive pulmonary disease: Cochrane systematic review and meta-analysis. Thorax. 2003;58(7):580-4.
429. Guyatt GH, Townsend M, Pugsley SO, Keller JL, Short HD, Taylor DW, et al. Bronchodilators in chronic air-flow limitation. Effects on airway function, exercise capacity, and quality of life. The American review of respiratory disease. 1987;135(5):1069-74.
430. Bauerle O, Chrusch CA, Younes M. Mechanisms by which COPD affects exercise tolerance. American journal of respiratory and critical care medicine. 1998;157(1):57-68.
431. Carlson DJ, Ries AL, Kaplan RM. Prediction of maximum exercise tolerance in patients with COPD. Chest. 1991;100(2):307-11.
432. O'Donnell DE, Webb KA. Exertional breathlessness in patients with chronic airflow limitation. The role of lung hyperinflation. The American review of respiratory disease. 1993;148(5):1351-7.
433. Belman MJ, Botnick WC, Shin JW. Inhaled bronchodilators reduce dynamic hyperinflation during exercise in patients with chronic obstructive pulmonary disease. American journal of respiratory and critical care medicine. 1996;153(3):967-75.

434. O'Donnell DE, Forkert L, Webb KA. Evaluation of bronchodilator responses in patients with "irreversible" emphysema. The European respiratory journal. 2001;18(6):914-20.
435. O'Donnell DE, Lam M, Webb KA. Measurement of symptoms, lung hyperinflation, and endurance during exercise in chronic obstructive pulmonary disease. American journal of respiratory and critical care medicine. 1998;158(5 Pt 1):1557-65.
436. Global Initiative for Chronic Obstructive Lung Disease. Global strategy for the diagnosis, management and prevention of COPD. 2001.
437. Anthonisen NR, Wright EC. Bronchodilator response in chronic obstructive pulmonary disease. The American review of respiratory disease. 1986;133(5):814-9.
438. Calverley PM, Burge PS, Spencer S, Anderson JA, Jones PW. Bronchodilator reversibility testing in chronic obstructive pulmonary disease. Thorax. 2003;58(8):659-64.
439. Tweeddale PM, Alexander F, McHardy GJ. Short term variability in FEV1 and bronchodilator responsiveness in patients with obstructive ventilatory defects. Thorax. 1987;42(7):487-90.
440. Santus P, Pecchiari M, Carlucci P, Boveri B, Di Marco F, Castagna F, et al. Bronchodilation test in COPD: effect of inspiratory manoeuvre preceding forced expiration. The European respiratory journal. 2003;21(1):82-5.
441. Burge PS, Calverley PM, Jones PW, Spencer S, Anderson JA. Prednisolone response in patients with chronic obstructive pulmonary disease: results from the ISOLDE study. Thorax. 2003;58(8):654-8.
442. Lung function testing: selection of reference values and interpretative strategies. American Thoracic Society. The American review of respiratory disease. 1991;144(5):1202-18.
443. Pellegrino R, Viegi G, Brusasco V, Crapo RO, Burgos F, Casaburi R, et al. Interpretative strategies for lung function tests. The European respiratory journal. 2005;26(5):948-68.
444. Tashkin D, Kesten S. Long-term treatment benefits with tiotropium in COPD patients with and without short-term bronchodilator responses. Chest. 2003;123(5):1441-9.
445. Criteria for the assessment of reversibility in airways obstruction. Report of the Committee on Emphysema American College of Chest Physicians. Chest. 1974;65(5):552-3.
446. Routine nebulized ipratropium and albuterol together are better than either alone in COPD. The COMBIVENT Inhalation Solution Study Group. Chest. 1997;112(6):1514-21.
447. Brand PL, Quanjer PH, Postma DS, Kerstjens HA, Koeter GH, Dekhuijzen PN, et al. Interpretation of bronchodilator response in patients with obstructive airways disease. The Dutch Chronic Non-Specific Lung Disease (CNSLD) Study Group. Thorax. 1992;47(6):429-36.
448. Borrill ZL, Houghton CM, Tal-Singer R, Vessey SR, Faiferman I, Langley SJ, et al. The use of plethysmography and oscillometry to compare long-acting bronchodilators in patients with COPD. British journal of clinical pharmacology. 2008;65(2):244-52.
449. Costa GM, Faria AC, Di Mango AM, Lopes AJ, Jansen JM, Melo PL. Bronchodilation in COPD: beyond FEV1-the effect of albuterol on resistive and

reactive properties of the respiratory system. Jornal brasileiro de pneumologia : publicacao oficial da Sociedade Brasileira de Pneumologia e Tisilogia. 2009;35(4):325-33.
450. Cerveri I, Pellegrino R, Dore R, Corsico A, Fulgoni P, van de Woestijne KP, et al. Mechanisms for isolated volume response to a bronchodilator in patients with COPD. Journal of applied physiology. 2000;88(6):1989-95.
451. De Luca N, Capuzi P, D'Angeli AL, D'Antoni L, Pavone P, De Santis M, et al. High resolution computed tomography (HRCT) assessment of beta 2-agonist induced bronchodilation in chronic obstructive pulmonary disease patients. European review for medical and pharmacological sciences. 1999;3(2):83-7.
452. Gelb AF, Taylor CF, Cassino C, Shinar CM, Schein MJ, Zamel N. Tiotropium induced bronchodilation and protection from dynamic hyperinflation is independent of extent of emphysema in COPD. Pulmonary pharmacology & therapeutics. 2009;22(3):237-42.
453. Hasegawa M, Makita H, Nasuhara Y, Odajima N, Nagai K, Ito Y, et al. Relationship between improved airflow limitation and changes in airway calibre induced by inhaled anticholinergic agents in COPD. Thorax. 2009;64(4):332-8.
454. Lee JH, Lee YK, Kim EK, Kim TH, Huh JW, Kim WJ, et al. Responses to inhaled long-acting beta-agonist and corticosteroid according to COPD subtype. Respiratory medicine. 2010;104(4):542-9.
455. Shimizu K, Makita H, Hasegawa M, Kimura H, Fuke S, Nagai K, et al. Regional bronchodilator response assessed by computed tomography in chronic obstructive pulmonary disease. European journal of radiology. 2015;84(6):1196-201.
456. Diba C, Salome CM, Berend N, Harris B, Bailey D, King GG. Effect of bronchodilator on ventilation hetergeneity in COPD. Am J Respir Crit Care Med; 2009. p. A5577.
457. Morgan AR, Parker GJ, Roberts C, Buonaccorsi GA, Maguire NC, Hubbard Cristinacce PL, et al. Feasibility assessment of using oxygen-enhanced magnetic resonance imaging for evaluating the effect of pharmacological treatment in COPD. European journal of radiology. 2014;83(11):2093-101.
458. de Lange EE, Altes TA, Patrie JT, Battiston JJ, Juersivich AP, Mugler JP, 3rd, et al. Changes in regional airflow obstruction over time in the lungs of patients with asthma: evaluation with 3He MR imaging. Radiology. 2009;250(2):567-75.
459. de Lange EE, Altes TA, Patrie JT, Parmar J, Brookeman JR, Mugler JP, 3rd, et al. The variability of regional airflow obstruction within the lungs of patients with asthma: assessment with hyperpolarized helium-3 magnetic resonance imaging. The Journal of allergy and clinical immunology. 2007;119(5):1072-8.
460. Mentore K, Froh DK, de Lange EE, Brookeman JR, Paget-Brown AO, Altes TA. Hyperpolarized HHe 3 MRI of the lung in cystic fibrosis: assessment at baseline and after bronchodilator and airway clearance treatment. Academic radiology. 2005;12(11):1423-9.
461. Woodhouse N, Wild JM, van Beek EJ, Hoggard N, Barker N, Taylor CJ. Assessment of hyperpolarized 3He lung MRI for regional evaluation of interventional therapy: a pilot study in pediatric cystic fibrosis. Journal of magnetic resonance imaging : JMRI. 2009;30(5):981-8.
462. Altes TA, Samee S, Ciambotti JM, Mata JF, Platts-Mills T, de Lange EE, editors. Hyperpolarized helium-3 MR imaging of asthma induction and reversal. Radiological Society of North America; 2002; Chicago, Illinois.

463. Altes TA, Samee S, Salerno M, Alford BA, Mata J, Menon A. Hyperpolarized helium-3 MR imaging of methacholine challenge testing in asthmatics. International Society Magnetic Resonance Medicine; Glasgow, Scotland2001.
464. Kruger SJ, Niles DJ, Dardzinski B, Harman A, Jarjour NN, Ruddy M, et al. Hyperpolarized Helium-3 MRI of exercise-induced bronchoconstriction during challenge and therapy. Journal of magnetic resonance imaging : JMRI. 2014;39(5):1230-7.
465. Sun Y, O'Sullivan BP, Roche JP, Walvick R, Reno A, Baker D, et al. Using hyperpolarized 3He MRI to evaluate treatment efficacy in cystic fibrosis patients. Journal of magnetic resonance imaging : JMRI. 2011;34(5):1206-11.
466. Bannier E, Cieslar K, Mosbah K, Aubert F, Duboeuf F, Salhi Z, et al. Hyperpolarized 3He MR for sensitive imaging of ventilation function and treatment efficiency in young cystic fibrosis patients with normal lung function. Radiology. 2010;255(1):225-32.
467. Altes TA, Johnson M, Mugler JP, 3rd, Froh D, Flors L, Miller GW, et al., editors. Hyperpolarized helium-3 MRI detects the effects of a CFTR potentiator (Ivacaftor) therapy in subjects with cystic fibrosis and the the G551D mutation. 20th Annual Meeting of ISMRM; 2012; Melbourne, Australia.
468. Altes TA, Johnson M, Mugler JP, 3rd, Miller GW, Flors L, Mata J, et al. The effect of ivacaftor, an investigational CFTR potentiator, on hyperpolarized noble gas magnetic resonance imaging in subjects with cystic fibrosis who has the G551d-CFTR mutation. American Thoracic Society San Francisco, California: Am. J. Respir Crit Care Med; 2012. p. A2814-A.
469. Svenningsen S, Kirby M, Starr D, Leary D, Wheatley A, Maksym GN, et al. Hyperpolarized (3) He and (129) Xe MRI: differences in asthma before bronchodilation. J Magn Reson Imaging. 2013;38(6):1521-30.
470. Larsson S, Svedmyr N. Bronchodilating effect and side effects of beta2-adrenoceptor stimulants by different modes of administration (tablets, metered aerosol, and combinations thereof). A study with salbutamol in asthmatics. The American review of respiratory disease. 1977;116(5):861-9.
471. Tashkin DP, Celli B, Decramer M, Liu D, Burkhart D, Cassino C, et al. Bronchodilator responsiveness in patients with COPD. The European respiratory journal. 2008;31(4):742-50.
472. Ramsdell JW, Tisi GM. Determination of bronchodilation in the clinical pulmonary function laboratory. Role of changes in static lung volumes. Chest. 1979;76(6):622-8.
473. O'Donnell DE, Fluge T, Gerken F, Hamilton A, Webb K, Aguilaniu B, et al. Effects of tiotropium on lung hyperinflation, dyspnoea and exercise tolerance in COPD. The European respiratory journal. 2004;23(6):832-40.
474. Niles DJ, Kruger SJ, Dardzinski BJ, Harman A, Jarjour NN, Ruddy M, et al. Exercise-induced bronchoconstriction: reproducibility of hyperpolarized 3He MR imaging. Radiology. 2013;266(2):618-25.
475. O'Sullivan B, Couch M, Roche JP, Walvick R, Zheng S, Baker D, et al. Assessment of repeatability of hyperpolarized gas MR ventilation functional imaging in cystic fibrosis. Academic radiology. 2014;21(12):1524-9.
476. Onishi H, Kuriyama K, Komiyama T, Tanaka S, Ueki J, Sano N, et al. CT evaluation of patient deep inspiration self-breath-holding: How precisely can patients reproduce the tumor position in the absence of respiratory monitoring devices? Medical Physics. 2003;30(6):1183-7.

477. Chong D, Brown MS, Kim HJ, van Rikxoort EM, Guzman L, McNitt-Gray MF, et al. Reproducibility of volume and densitometric measures of emphysema on repeat computed tomography with an interval of 1 week. European radiology. 2012;22(2):287-94.
478. Fukumitsu N, Hayashi Y. Application of a deformable registration technique to investigate breath-hold reproducibility. Japanese journal of radiology. 2014;32(12):700-7.
479. de Benedictis FM, Guidi R, Carraro S, Baraldi E, Excellence TENo. Endpoints in respiratory diseases. European journal of clinical pharmacology. 2011;67 Suppl 1:49-59.
480. Glaab T, Vogelmeier C, Buhl R. Outcome measures in chronic obstructive pulmonary disease (COPD): strengths and limitations. Respiratory research. 2010;11:79.
481. Driehuys B. CG, Miron E., Sauer K., Walter DK., Happer W. High-volume production of laser-polarized 129Xe. Appl Phys Lett. 1996;69(12):1668-70.
482. Korchak SE, Kilian W, Mitschang L. Configuration and Performance of a Mobile (129)Xe Polarizer. Applied magnetic resonance. 2013;44(1-2):65-80.
483. Nikolaou P, Coffey AM, Walkup LL, Gust BM, Whiting N, Newton H, et al. XeNA: an automated 'open-source' (129)Xe hyperpolarizer for clinical use. Magnetic resonance imaging. 2014;32(5):541-50.
484. Lilburn DM, Pavlovskaya GE, Meersmann T. Perspectives of hyperpolarized noble gas MRI beyond 3He. J Magn Reson. 2013;229:173-86.
485. Gattinoni L, Pesenti A, Carlesso E. Body position changes redistribute lung computed-tomographic density in patients with acute respiratory failure: impact and clinical fallout through the following 20 years. Intensive care medicine. 2013;39(11):1909-15.
486. Broccard A, Shapiro RS, Schmitz LL, Adams AB, Nahum A, Marini JJ. Prone positioning attenuates and redistributes ventilator-induced lung injury in dogs. Critical care medicine. 2000;28(2):295-303.
487. Du HL, Yamada Y, Orii R, Suzuki S, Sawamura S, Suwa K, et al. Beneficial effects of the prone position on the incidence of barotrauma in oleic acid-induced lung injury under continuous positive pressure ventilation. Acta anaesthesiologica Scandinavica. 1997;41(6):701-7.
488. Chatte G, Sab JM, Dubois JM, Sirodot M, Gaussorgues P, Robert D. Prone position in mechanically ventilated patients with severe acute respiratory failure. American journal of respiratory and critical care medicine. 1997;155(2):473-8.
489. Guerin C, Reignier J, Richard JC, Beuret P, Gacouin A, Boulain T, et al. Prone positioning in severe acute respiratory distress syndrome. The New England journal of medicine. 2013;368(23):2159-68.
490. Kasai T, Floras JS, Bradley TD. Sleep apnea and cardiovascular disease: a bidirectional relationship. Circulation. 2012;126(12):1495-510.
491. Zoccali C, Tripepi R, Torino C, Bellantoni M, Tripepi G, Mallamaci F. Lung congestion as a risk factor in end-stage renal disease. Blood purification. 2013;36(3-4):184-91.
492. Volpicelli G, Elbarbary M, Blaivas M, Lichtenstein DA, Mathis G, Kirkpatrick AW, et al. International evidence-based recommendations for point-of-care lung ultrasound. Intensive care medicine. 2012;38(4):577-91.

493. Siriopol D, Hogas S, Voroneanu L, Onofriescu M, Apetrii M, Oleniuc M, et al. Predicting mortality in haemodialysis patients: a comparison between lung ultrasonography, bioimpedance data and echocardiography parameters. Nephrology, dialysis, transplantation : official publication of the European Dialysis and Transplant Association - European Renal Association. 2013;28(11):2851-9.
494. Zoccali C, Torino C, Tripepi R, Tripepi G, D'Arrigo G, Postorino M, et al. Pulmonary congestion predicts cardiac events and mortality in ESRD. J Am Soc Nephrol. 2013;24(4):639-46.
495. Corris PA, Ellis DA, Hawkins T, Gibson GJ. Use of radionuclide scanning in the preoperative estimation of pulmonary function after pneumonectomy. Thorax. 1987;42(4):285-91.
496. Ohno Y, Koyama H, Nogami M, Takenaka D, Matsumoto S, Yoshimura M, et al. Postoperative lung function in lung cancer patients: comparative analysis of predictive capability of MRI, CT, and SPECT. AJR Am J Roentgenol. 2007;189(2):400-8.
497. Win T, Tasker AD, Groves AM, White C, Ritchie AJ, Wells FC, et al. Ventilation-perfusion scintigraphy to predict postoperative pulmonary function in lung cancer patients undergoing pneumonectomy. AJR Am J Roentgenol. 2006;187(5):1260-5.
498. Wu MT, Chang JM, Chiang AA, Lu JY, Hsu HK, Hsu WH, et al. Use of quantitative CT to predict postoperative lung function in patients with lung cancer. Radiology. 1994;191(1):257-62.
499. Sheshadri A, McKenzie M, Castro M. Critical review of bronchial thermoplasty: where should it fit into asthma therapy? Current allergy and asthma reports. 2014;14(11):470.
500. Wechsler ME, Laviolette M, Rubin AS, Fiterman J, Lapa e Silva JR, Shah PL, et al. Bronchial thermoplasty: Long-term safety and effectiveness in patients with severe persistent asthma. J Allergy Clin Immunol. 2013;132(6):1295-302.
501. Pavord ID, Thomson NC, Niven RM, Corris PA, Chung KF, Cox G, et al. Safety of bronchial thermoplasty in patients with severe refractory asthma. Annals of allergy, asthma & immunology : official publication of the American College of Allergy, Asthma, & Immunology. 2013;111(5):402-7.
502. Mathew L, Wheatley A, Castillo R, Castillo E, Rodrigues G, Guerrero T, et al. Hyperpolarized (3)He magnetic resonance imaging: comparison with four-dimensional x-ray computed tomography imaging in lung cancer. Acad Radiol. 2012;19(12):1546-53.
503. Mathew L, Gaede S, Wheatley A, Etemad-Rezai R, Rodrigues GB, Parraga G. Detection of longitudinal lung structural and functional changes after diagnosis of radiation-induced lung injury using hyperpolarized 3He magnetic resonance imaging. Med Phys. 2010;37(1):22-31.
504. Hodge CW, Tome WA, Fain SB, Bentzen SM, Mehta MP. On the use of hyperpolarized helium MRI for conformal avoidance lung radiotherapy. Med Dosim. 2010;35(4):297-303.
505. Cai J, McLawhorn R, Altes TA, de Lange E, Read PW, Larner JM, et al. Helical tomotherapy planning for lung cancer based on ventilation magnetic resonance imaging. Med Dosim. 2011;36(4):389-96.

506. Altes TA, Johnson M, Mugler JP, Froh D, Flors L, Miller GW, et al., editors. Hyperpolarized helium-3 MRI detects the effects of a CFTR potentiator (ivacaftor) therapy in subjects with cystic fibrosis and the g551d mutation.
507. Chang YV, Quirk JD, Ruset IC, Atkinson JJ, Hersman FW, Woods JC. Quantification of human lung structure and physiology using hyperpolarized 129Xe. Magn Reson Med. 2014;71(1):339-44.
508. Muradyan I, Butler JP, Dabaghyan M, Hrovat M, Dregely I, Ruset I, et al. Single-breath xenon polarization transfer contrast (SB-XTC): implementation and initial results in healthy humans. J Magn Reson Imaging. 2013;37(2):457-70.
509. King TE, Jr., Bradford WZ, Castro-Bernardini S, Fagan EA, Glaspole I, Glassberg MK, et al. A phase 3 trial of pirfenidone in patients with idiopathic pulmonary fibrosis. The New England journal of medicine. 2014;370(22):2083-92.
510. Fain S, Schiebler ML, McCormack DG, Parraga G. Imaging of lung function using hyperpolarized helium-3 magnetic resonance imaging: Review of current and emerging translational methods and applications. J Magn Reson Imaging. 2010;32(6):1398-408.